DO NOT DESTROY
RETURN TO LIBRARY

NASA CR-135446

DEFINITION OF MUTUALLY OPTIMUM NDI AND PROOF TEST CRITERIA FOR 2219 ALUMINUM PRESSURE VESSELS

VOLUME II OPTIMIZATION AND FRACTURE STUDIES

by Fred R. Schwartzberg, C. Toth, Jr.,
Richard G. King, and Paul H. Todd, Jr.

MARTIN MARIETTA CORPORATION

prepared for

NATIONAL AERONAUTICS AND SPACE ADMINISTRATION

NASA Lewis Research Center
Contract NAS3-17790

7 MAY 1979
MCDONNELL DOUGLAS
RESEARCH & ENGINEERING LIBRARY
ST. LOUIS

M79-13160

1. Report No.	2. Government Accession No.	3. Recipient's Catalog No.
NASA CR-135446		

4. Title and Subtitle	5. Report Date
Definition of Mutually Optimum NDI and Proof Test Criteria for 2219 Aluminum Pressure Vessels - Volume II Optimization and Fracture Studies	February 1979
	6. Performing Organization Code
7. Author(s) Fred R. Schwartzberg, C. Toth, Jr., Richard G. King and Paul H. Todd, Jr.	8. Performing Organization Report No.
9. Performing Organization Name and Address Martin Marietta Aerospace Denver Division P. O. Box 179 Denver, Colorado 80201	10. Work Unit No.
	11. Contract or Grant No. NAS 3-17790
	13. Type of Report and Period Covered Contractor Report
12. Sponsoring Agency Name and Address National Aeronautics and Space Administration Washington, D. C. 20546	14. Sponsoring Agency Code

15. Supplementary Notes

Project Manager, G. T. Smith, Materials and Structures Division, NASA Lewis Research Center, Cleveland, Ohio 44135

16. Abstract The results of this phase of the experimental program clearly demonstrated that the collimated ultrasonic pitch-catch inspection technique is a powerful tool that can be used in fracture-related studies. Certain behavioral aspects associated with fracture and crack extension that cannot be studied using other techniques have been evaluated with the ultrasonic method.

Characterization of collimated beam techniques showed that significant beam width reduction could be accomplished. Techniques for collimation are given.

The crack-opening displacement-gage correction-factor study showed that displacement resulting from crack opening and that from plasticity could be readily differentiated. It was shown that there appeared to be a threshold level for the initiation of subcritical growth.

Crack closure studies using both ultrasonic and crack-opening displacement measurements showed an opening and closing behavior associated with load-unload curves. The results of this work were in general agreement with the closure concepts of Elber.

Ultrasonic measurements used to study the nature of flaw extension characteristics associated with failure of the ligament between the flaw front and back surface showed that penetration could occur by an abrupt fracturing after subcritical growth or by continuous growth.

17. Key Words	18. Distribution Statement
NDI, Ultrasonic, Collimated, Pitch-Catch, Crack-Opening Displacement, Crack Closure, Ligament Penetration, Flaw Mapping	Unclassified - Unlimited

19. Security Classif. (of this report)	20. Security Classif. (of this page)	21. No. of Pages	22. Price
Unclassified	Unclassified	175	

Page intentionally left blank

FOREWORD

This report presents the results of the second phase of the program and deals with the application of the collimated pitch-catch ultrasonic inspection technique to study certain aspects of fracture behavior.

The work was performed under the management of NASA Project Manager Mr. Gordon T. Smith.

The Martin Marietta Program Manager for the activity was Fred R. Schwartzberg. Assisting in the performance of this work were Messrs. Richard G. King, Paul H. Todd, Jr., and Charles Toth, Jr.

For the benefit of technical readers, raw data and reductions of original engineering drawings are included in the figures.

TABLE OF CONTENTS

	Page
INTRODUCTION	2
COLLIMATED ULTRASONIC-BEAM PERFORMANCE CHARACTERISTICS AND OPTIMIZATION	3
Beam Energy Profiling	4
Surface Roughness Effects	15
Collimated-Beam Effectiveness	21
DETERMINATION OF CRACK-OPENING DISPLACEMENT GAGE CORRECTION FACTORS	28
Aluminum Data	34
Titanium Data	53
Steel Data	75
CRACK CLOSURE CHARACTERISTICS OF SURFACE-FLAWED SPECIMENS UNDER CYCLIC LOADING CONDITIONS	86
Background	86
Approach	90
Results	92
Discussion	132
DEEP SURFACE-FLAW EXTENSION CHARACTERISTICS	145
CONCLUSIONS	165
REFERENCES	167
APPENDIX	169

FIGURES

1.	Overall view of ultrasonic system	4
2.	Block diagram of sound-beam profiling system using ultrasonic pulse-echo	5
3.	Typical data plot for uncollimated ultrasonic beam	6
4.	Specifications for ultrasonic collimators	7
5.	Typical data plot for collimated ultrasonic beam	9
6.	Sketch of long cone	13
7.	Data from evaluation of collimator combinations	14
8.	Effect of roughness on ultrasonic reflections from front surface of aluminum	17
9.	Effect of roughness on ultrasonic reflections from front surface of steel	18
10.	Effect of roughness on ultrasonic reflections from back surface of aluminum	19
11.	Effect of roughness on ultrasonic reflections from back surface of steel	20

12. Ultrasonic data plots of defects in 1.3-mm (0.05-in.) titanium 23
13. Relationship of ultrasonic plot data to defect area for titanium 24
14. Ultrasonic data plots of defects in 0.5-mm (0.02-in.) aluminum 25
15. Ultrasonic data plots of defects in 0.8-mm (0.032-in.) aluminum (series 1) 26
16. Ultrasonic data plots of defects in 0.8-mm (0.032-in.) aluminum (series 2) 27
17. Ultrasonic apparatus in testing machine 29
18. Specifications for test specimen 29
19. Microdisplacement COD gage attached to surface-flawed specimen 30
20. Close-up view showing transducers, collimators, and COD gage housing 31
21. Typical data plot obtained using ultrasonic-signal-strength-versus-distance method 33
22. Typical flaw map using scanning approach 33
23. Schematic of ultrasonic path 34
24. Typical crack-opening displacement curves 37
25. Compliance calibration curve for 2219-T87 aluminum . . . 38
26. Ultrasonic calibration curve for aluminum 40
27. Schematic of components contributing to crack-opening displacement 43
28. Crack-opening displacement curves for aluminum-alloy specimen AOL-1 44
29. Crack-opening displacement curves for aluminum-alloy specimen AOL-2 45
30. Crack-opening displacement curves for aluminum-alloy specimen AOL-3 46
31. Crack-opening displacement curves for aluminum-alloy specimen AOL-4 47
32. Crack-opening displacement curves for aluminum-alloy specimen AOL-5 48
33. Crack-opening displacement curves for aluminum-alloy specimen AOL-6 49
34. Crack-opening displacement curves for aluminum-alloy specimen AOL-7 50
35. Crack-opening displacement curves for aluminum-alloy specimen AOL-8 51
36. Crack-opening displacement curves for aluminum-alloy specimen AOL-9 52
37. Subcritical growth threshold for aluminum 54
38. Fractograph and flaw map of specimen AOL-2 56
39. Fractograph and flaw map of specimen AOL-3 57
40. Fractograph and flaw map of specimen AOL-5 58
41. Fractograph and flaw map of specimen AOL-6 59
42. Fractograph and flaw map of specimen AOL-9 60
43. Ultrasonic calibration curve for titanium 61
44. Compliance calibration curve for titanium 62

45. Crack-opening displacement curves for titanium-alloy specimen TOL-4 63
46. Crack-opening displacement curves for titanium-alloy specimen TOL-5 64
47. Crack-opening displacement curves for titanium-alloy specimen TOL-9 65
48. Subcritical growth threshold for titanium 69
49. Fractograph and flaw map of specimen TOL-3 70
50. Fractograph and flaw map of specimen TOL-4 71
51. Fractograph and flaw map of specimen TOL-6 72
52. Fractograph and flaw map of specimen TOL-8 73
53. Fractograph and flaw map of specimen TOL-9 74
54. Ultrasonic calibration curve for steel 76
55. Compliance calibration curve for steel 77
56. Crack-opening displacement curves for steel specimen SOL-1 78
57. Crack-opening displacement curves for steel specimen SOL-6 79
58. Crack-opening displacement curves for steel specimen SOL-9 80
59. Subcritical growth threshold for steel 85
60. Basic principle of Wheeler crack-growth retardation model 87
61. Typical data record 91
62. Ultrasonic data illustrating effect of overload on crack closure for specimens ACC-1 and ACCO-1 93
63. Ultrasonic data illustrating effect of overload on crack closure for specimens ACC-2 and ACCO-2 94
64. Ultrasonic data illustrating effect of overload on crack closure for specimens ACC-3 and ACCO-2 95
65. Ultrasonic data illustrating effect of overload on crack closure for specimens ACC-4 and ACCO-4 96
66. Ultrasonic data illustrating effect of overload on crack closure for specimens ACC-5 and ACCO-5 97
67. Ultrasonic data illustrating effect of overload on crack closure for specimens ACC-6 and ACCO-6 98
68. Ultrasonic data illustrating effect of overload on crack closure for specimens ACC-7 and ACCO-7 99
69. Ultrasonic data illustrating effect of overload on crack closure for specimens ACC-8 and ACCO-8 100
70. Ultrasonic data illustrating effect of overload on crack closure for specimens ACC-9 and ACCO-9 101
71. Ultrasonic data illustrating effect of overload on crack closure for specimens ACC-10 and ACCO-10 102
72. Ultrasonic data illustrating effect of overload on crack closure for specimens ACC-11 and ACCO-11 103
73. Ultrasonic data illustrating effect of overload on crack closure for specimens ACC-12 and ACCO-12 104
74. COD data illustrating effect of overload on crack closure for specimens ACC-1 and ACCO-1 105

75. COD data illustrating effect of overload on crack closure for specimens ACC-2 and ACCO-2 106
76. COD data illustrating effect of overload on crack closure for specimens ACC-3 and ACCO-3 107
77. COD data illustrating effect of overload on crack closure for specimens ACC-4 and ACCO-4 108
78. COD data illustrating effect of overload on crack closure for specimens ACC-5 and ACCO-5 109
79. COD data illustrating effect of overload on crack closure for specimens ACC-6 and ACCO-6 110
80. COD data illustrating effect of overload on crack closure for specimens ACC-7 and ACCO-7 111
81. COD data illustrating effect of overload on crack closure for specimens ACC-8 and ACCO-8 112
82. COD data illustrating effect of overload on crack closure for specimens ACC-9 and ACCO-9 113
83. COD data illustrating effect of overload on crack closure for specimens ACC-10 and ACCO-10 114
84. COD data illustrating effect of overload on crack closure for specimens ACC-11 and ACCO-11 115
85. COD data illustrating effect of overload on crack closure for specimens ACC-12 and ACCO-12 116
86. Cyclic-flaw growth curves for specimens ACC-1 and ACCO-1 118
87. Cyclic-flaw growth curves for specimens ACC-9 and ACCO-9 118
88. Cyclic-flaw growth curves for specimens ACC-5 and ACCO-5 119
89. Cyclic-flaw growth curves for specimens ACC-2 and ACCO-2 119
90. Cyclic-flaw growth curves for specimens ACC-10 and ACCO-10 120
91. Cyclic-flaw growth curves for specimens ACC-6 and ACCO-6 120
92. Cyclic-flaw growth curves for specimens ACC-3 and ACCO-3 121
93. Cyclic-flaw growth curves for specimens ACC-11 and ACCO-11 121
94. Cyclic-flaw growth curves for specimens ACC-7 and ACCO-7 122
95. Cyclic-flaw growth curves for specimens ACC-4 and ACCO-4 122
96. Cyclic-flaw growth curves for specimens ACC-12 and ACCO-12 123
97. Cyclic-flaw growth curves for specimens ACC-8 and ACCO-8 123
98. Ultrasonic data illustrating effect of overload on crack closure for specimens TCC-1 and TCCO-1 124
99. Ultrasonic data illustrating effect of overload on crack closure for specimens TCC-2 and TCCO-2 125

100. COD data illustrating effect of overload on crack closure for specimens TCC-1 and TCCO-1 126
101. COD data illustrating effect of overload on crack closure for specimens TCC-2 and TCCO-2 127
102. Ultrasonic data illustrating effect of overload on crack closure for specimens SCC-1 and SCCO-1 128
103. Ultrasonic data illustrating effect of overload on crack closure for specimens SCC-2 and SCCO-2 129
104. COD data illustrating effect of overload on crack closure for specimens SCC-1 and SCCO-1 130
105. COD data illustrating effect of overload on crack closure for specimens SCC-2 and SCCO-2 131
106. Location of flaw in welded specimen 133
107. Sectioning of specimens 134
108. Welded 2219-T87 after original fatigue extension (W-2) 136
109. Welded 2219-T87 after 90-MN/m^2 (13-ksi) overload (W-3) 137
110. Welded 2219-T87 after 145-MN/m^2 (21-ksi) overload (W-4) 138
111. Welded 2219-T87 after 90-MN/m^2 (21-ksi) overload (W-5) 139
112. Welded 2219-T87 after 118-MN/m^2 (17-ksi) overload followed by 62-MN/m^2 (9-ksi) compressive load (W-6) . . 140
113. Base-metal 2219-T87 after original fatigue extension (BM-1) 141
114. Base-metal 2219-T87 after 206-MN/m^2 (30-ksi) overload and postoverload fatigue extension (BM-2) . . . 142
115. Base-metal 2219-T87 after 241-MN/m^2 (35-ksi) overload and postoverload fatigue extension (BM-3) . . . 143
116. Base-metal 2219-T87 after 276-MN/m^2 (40-ksi) overload and postoverload fatigue extension (BM-4) . . . 144
117. Ultrasonic data record for ligament penetration of specimen ACC-12 147
118. Crack-opening displacement curve for specimen ACC-12 148
119. Ultrasonic records for aluminum specimens exhibiting abrupt penetration 150
120. Ultrasonic records for aluminum specimens exhibiting rapid penetration 151
121. Ultrasonic records for aluminum specimens exhibiting gradual penetration 153
122. Crack-opening displacement curve for specimen ACC-5 . . 154
123. Crack-opening displacement curve for specimen ACCO-12. . 155
124. Crack-opening displacement curve for specimen ALP-1 . . 156
125. Effect of crack depth on growth rate before penetration in aluminum 157
126. Ultrasonic penetration records for welded aluminum specimens 158

127. Ultrasonic penetration records for welded titanium specimens 160
128. Crack-opening displacement curve for titanium specimen TCCO-1 161
129. Crack-opening displacement curve for titanium specimen TCC-1 162
130. Ultrasonic penetration records for steel specimens . . . 164

TABLES

I. TRANSDUCER BEAM CHARACTERISTICS 5
II. TRANSDUCER BEAM CHARACTERISTICS WITH 1.93-mm (0.076-in.) DIAMETER 8
III. COLLIMATOR GEOMETRY CHARACTERISTICS AT 13.2 MHz 10
IV. COLLIMATOR GEOMETRY CHARACTERISTICS AT 2.6 MHz 11
V. FOCUS TRANSDUCER DATA 11
VI. ACOUSTIC CONICAL-HORN COLLIMATOR DATA 13
VII. SURFACE ROUGHNESS DATA 16
VIII. SPECIMEN GEOMETRY DATA FOR BEAM EFFECTIVENESS STUDY . . 22
IX. SPECIFICATIONS FOR TRANSDUCER ADJUSTMENTS 32
X. ALUMINUM CALIBRATION DATA 35
XI. SUMMARIZED DATA FOR OVERLOADED ALUMINUM SPECIMENS . . . 41
XII. COMPARISON OF MEASUREMENT TECHNIQUES FOR ALUMINUM . . . 55
XIII. TITANIUM CALIBRATION DATA 61
XIV. SUMMARIZED DATA FOR OVERLOADED TITANIUM SPECIMENS . . . 66
XV. COMPARISON OF MEASUREMENT TECHNIQUES FOR TITANIUM . . . 68
XVI. STEEL CALIBRATION DATA 75
XVII. SUMMARIZED DATA FOR OVERLOADED STEEL SPECIMENS 81
XVIII. COMPARISON OF MEASUREMENT TECHNIQUES FOR STEEL 84
XIX. SUMMARY OF TEST DATA 134
XX. SUMMARY OF PARENT-METAL ALUMINUM-LIGAMENT PENETRATION DATA 149
XXI. SUMMARY OF WELDED ALUMINUM-LIGAMENT PENETRATION DATA 159
XXII. SUMMARY OF PARENT-METAL TITANIUM-LIGAMENT 159
XXIII. SUMMARY OF PARENT-METAL STEEL-LIGAMENT PENETRATION DATA 165

SUMMARY

The results of this phase of the experimental program clearly demonstrated that the collimated ultrasonic pitch-catch inspection technique is a powerful tool that can be used in fracture-related studies. Certain behavioral aspects associated with fracture and crack extension that cannot be studied using other techniques have been evaluated with the ultrasonic method.

The first part of the effort pertaining to performance characteristics and optimization of the collimated beam demonstrated that beam width could be reduced by at least 50%. Evaluation of various collimator designs, combinations, and frequencies showed that the combination of a cone collimator and cone receiver was the most effective in terms of maximizing signal strength.

The crack-opening displacement-gage correction-factor study showed that displacement resulting from crack opening and that from plasticity could be readily differentiated. It was shown that there appeared to be a threshold level for the initiation of subcritical growth in the three materials evaluated (aluminum, titanium, and steel). Plastic displacement of approximately 0.025 mm (0.001 in.) appeared to be required before subcritical growth was found.

Crack closure studies using both ultrasonic and crack-opening displacement measurements showed an opening and closing behavior associated with load-unload curves. The results of this work were in general agreement with the closure concepts of Elber. Ultrasonic measurements showed that changes in crack depth associated with loading and unloading occurred at the crack tip and would confirm the validity of Elber's contention of an effective stress intensity range.

Ultrasonic measurements used to study the nature of flaw extension characteristics associated with failure of the ligament between the flaw front and back surface showed that penetration could occur by an abrupt fracturing after subcritical growth or by continous growth. Differences in the nature of the process appear to be related to the toughness of the materials.

This program showed that the ultrasonic technique can readily be used to study crack growth and fracture-related phenomena in surface-flawed specimens with improved accuracy. Some of these measurements could not be made in any other way. The technique is particularly valuable in studies of flaw-front phenomena. Although the value of the crack-opening displacement gage has been criticized because it only measures surface compliance, the results of our studies show that a high-sensitivity gage can provide reliable information in many types of studies.

INTRODUCTION

The objective of this program was to provide a rational basis for selection of proof-test and nondestructive inspection (NDI) acceptance criteria for Space Shuttle 2219 aluminum weldments. The initial experimental effort (Vol I) consisted of:

1) Study of crack closure forces that obscure NDI visibility as functions of surface roughness and temperature;

2) Development and verification of experimental procedures for preparation of lack-of-fusion-defect (LFD) weld specimens with controlled crack geometries and representative residual stresses;

3) Establishment of NDI detection and characterization capabilities under various loading conditions;

4) Evaluation of the effects of preloads on crack opening and subsequent growth characteristics.

The effort described in this volume deals with use of an ultrasonic crack detection and characterization technique to study certain aspects of crack growth and fracture behavior.

The first activity in this phase was a study of the performance characteristics and optimization of collimated ultrasonic beams.

After the optimization activity, a study was performed to determine whether there is a usable correlation between surface-flaw depth measurements obtained with conventional clip-on-type crack-opening displacement (COD) gages and the collimated pitch-catch ultrasonic inspection technique.

The ultrasonic technique was also used to study crack opening and crack closure characteristics of surface-flawed specimens subject to cyclic loading.

Another aspect of fracture behavior studied using the ultrasonic inspection technique was establishment of flaw extension characteristics immediately before failure of the ligament between the flaw front and the back surface of the specimen.

COLLIMATED ULTRASONIC-BEAM PERFORMANCE CHARACTERISTICS AND OPTIMIZATION

The objective of this task was to construct a collimated ultrasonic shear-wave inspection system for delivery to NASA's Lewis Research Center at the end of the program and to perform a comprehensive evaluation of the system. The evaluation was intended to establish the limitations of the system in terms of flaw dimensions, study the effects of frequency and beam diameter, determine beam energy-profile characteristics for selected collimation techniques, and to characterize the effects of surface roughness on the dispersion of the beam from internal and external surfaces.

The conventional pitch-catch shear-wave ultrasonic technique was modified so that resolution capability for crack detection, crack mapping, crack opening, and determination of crack front profiles was improved. The basis for this approach is described in Volume I.

The major component of the system was the transducer mounting assembly. Ultrasonic fixture design provided for translation in three directions and angular adjustment of the two transducer housings. The system permitted 5.1-cm (2-in.) traverse in all three directions (X, Y, and Z). A housing and adjustment assembly for the transducer was attached to the three-axis table system that permitted ready change of transducers having different frequencies and for collimators with different apertures. Appendix A includes drawings of the transducer assembly. The mounting system permitted direct attachment to the upper friction grip of a closed-loop servo test machine or to a baseplate for bench-top examination.

Figure 1 is an overall view of the ultrasonic transducer assembly. After initial use of the ultrasonic apparatus, several modifications were made to permit speedier, simpler operation. The first change consisted of adding a linear variable differential transformer (LVDT) to the Y-axis feed mechanism to permit autographic data recording. By using the output signal from the Sonatest and the LVDT output, traces of signal amplitude versus distance were obtained. The second modification added a reversible drive motor equipped with drive limit switches to the Y-axis.

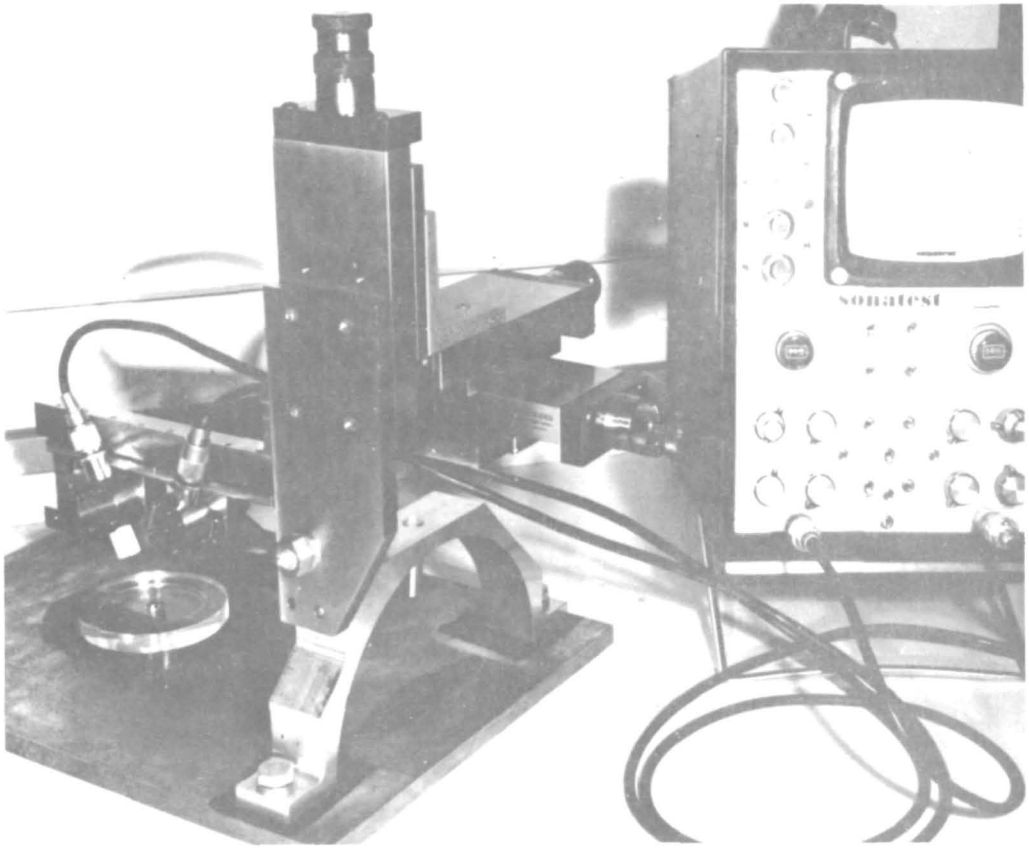

Figure 1. - Overall view of ultrasonic system.

Beam Energy Profiling

Evaluation of the system was initiated by plotting beam-energy profiles in the Fraunhofe and Fresnel zones, as described by McElroy (ref. 1), for eight transducers used during the program. The plots were a series of autographic records of reflected sound amplitude as the transducer was traversed across a reflector at a specified distance from the reflecting surface. A 3.2-mm (1/8-in.) diameter steel ball was used as the reflector. Figure 2 is a block diagram of the profiling scheme. The first series was without collimation. Table I summarizes individual transducer beam characteristics and presents the optimum transducer-to-reflector distance and associated beam width measured -6 dB from maximum amplitude. As anticipated, the reflection distance for maximum-amplitude signal increased with increasing frequency. The distance increased from approximately 32 mm (1.25 in.) at 2.5 MHz to more than 100 mm (4 in.) at 15 MHz. Beam widths were approximately 2.5 mm (0.1 in.). Figure 3 is a typical original data plot.

A second series used a 1.93-mm (0.076 in.) diameter exit-aperture Teflon cone-type collimator in front of each transducer. Figure 4 gives the specifications for two types of collimators. The data in table II summarize the results of this series of tests.

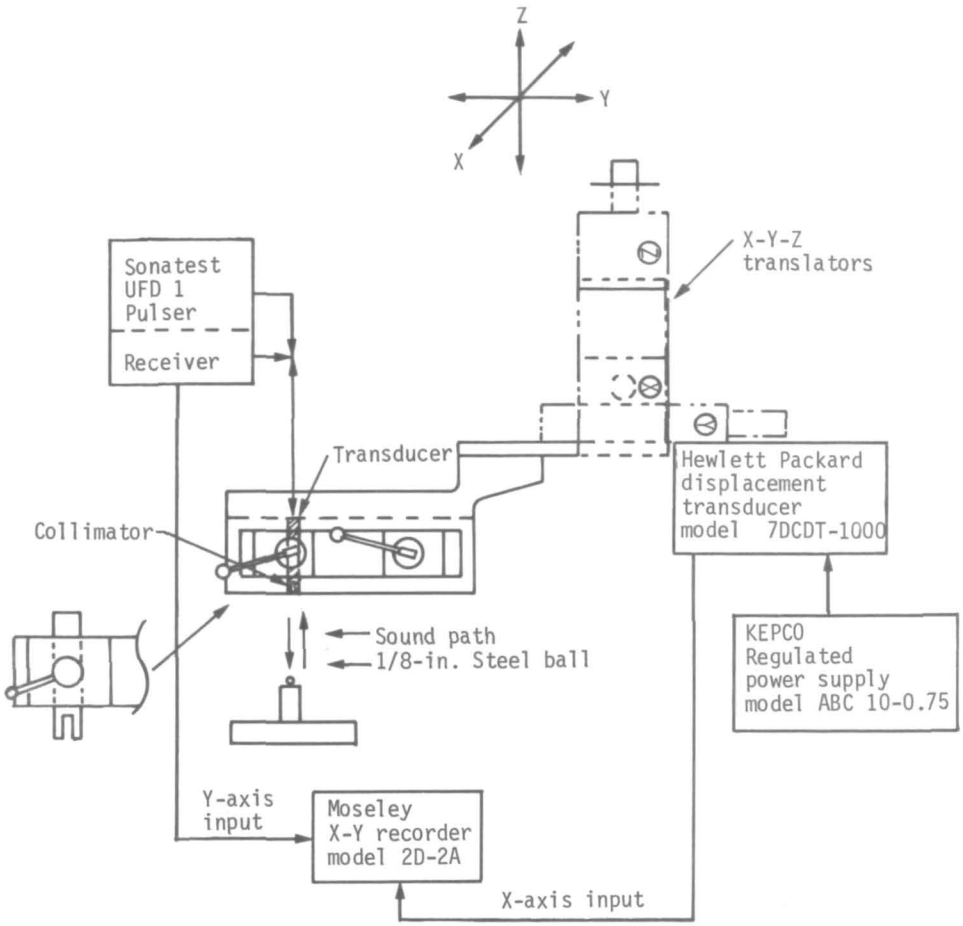

Figure 2. - Block diagram of sound-beam profiling system using ultrasonic pulse-echo.

TABLE I. - TRANSDUCER BEAM CHARACTERISTICS

Serial no.	Peak frequency, MHz	Sonatest gain setting, dB	Distance for max amplitude, $Y_o^+/2$,*		Beam width at -6 dB,	
			mm	(in.)	mm	(in.)
M1210	2.25	45	32	(1.2)	2.54	(0.100)
M1211	2.6	45	32	(1.2)	2.44	(0.096)
M1212	4.9	59	57	(2.2)	2.44	(0.096)
M1213	4.8	59	57	(2.2)	2.39	(0.094)
M1214	9.2	65	102	(4.0)	2.16	(0.085)
M1215	10.0	65	102	(4.0)	2.29	(0.090)
M1216	14.8	80	114	(4.5)	2.46	(0.097)
M1217	13.2	80	102	(4.0)	2.59	(0.102)

* Transducer-to-reflector distance

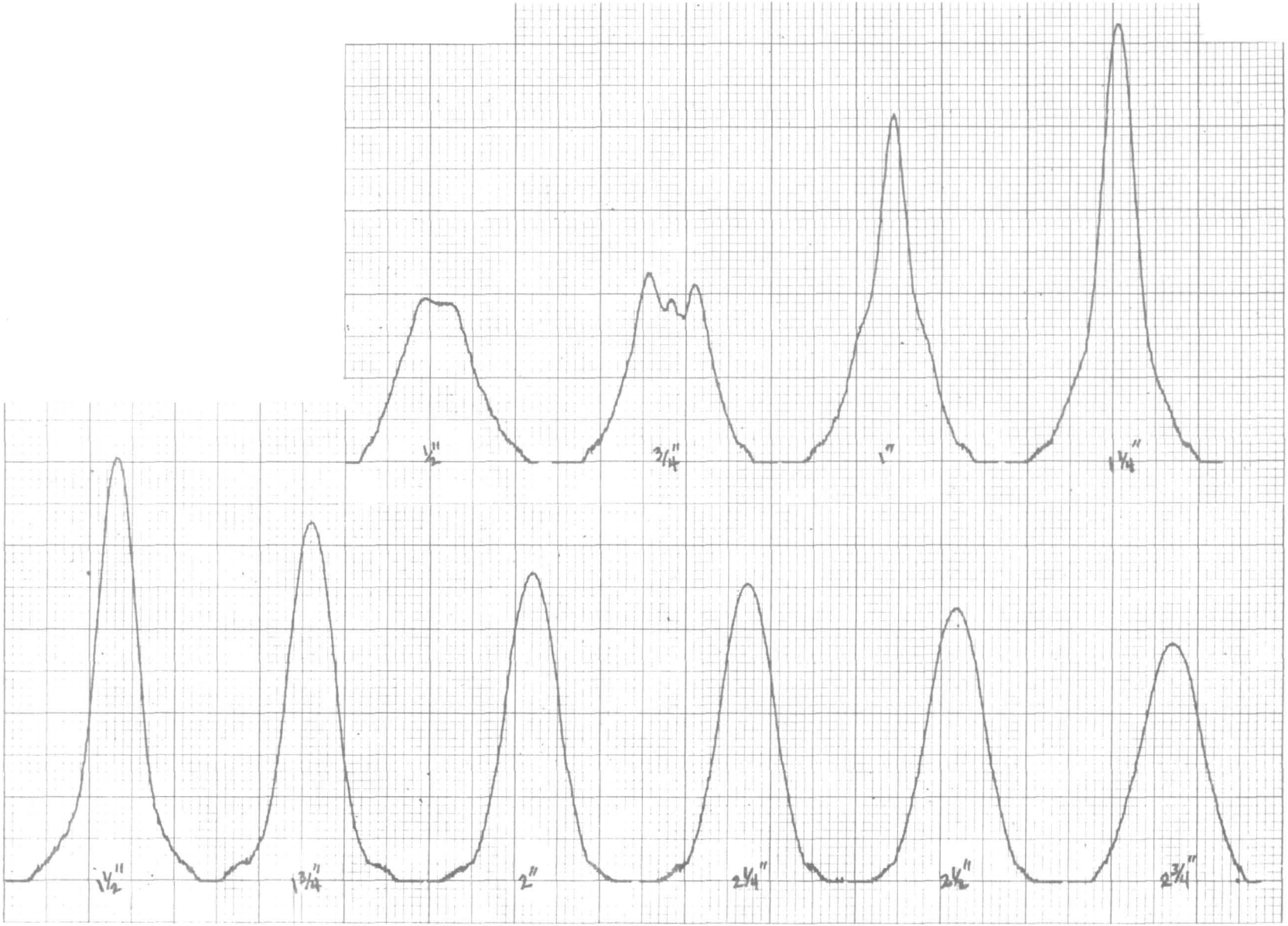

Figure 3. - Typical data plot for uncollimated ultrasonic beam.

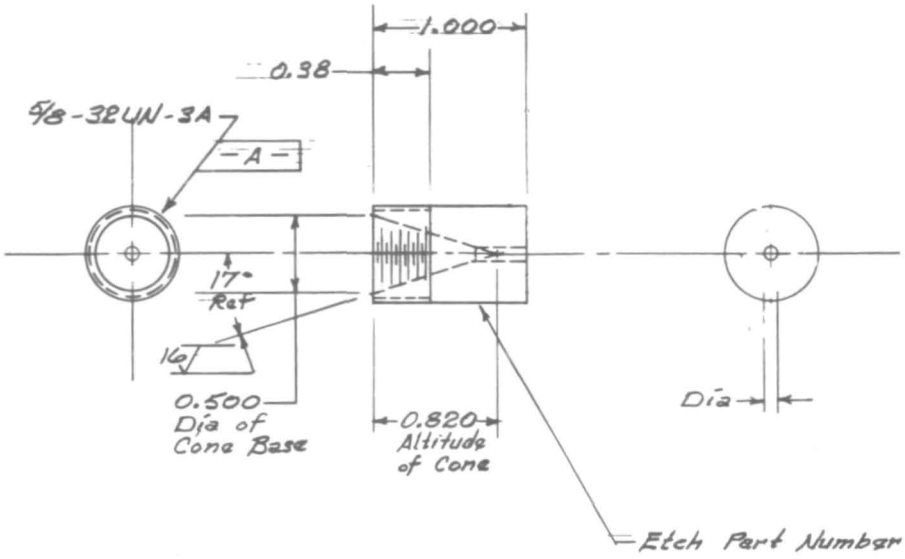

Cone collimator.

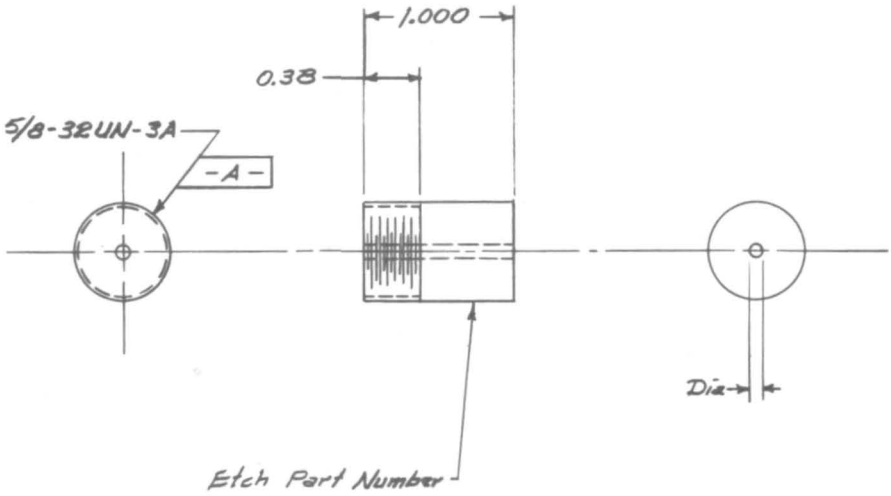

Straight collimator.

Figure 4. - Specifications for ultrasonic collimators.

TABLE II. - TRANSDUCER BEAM CHARACTERISTICS WITH 1.93-mm (0.076-in.) DIAMETER APERTURE TEFLON COLLIMATOR

Serial no.	Peak frequency, MHz	Sonatest gain setting, dB	Distance for max-amplitude signal				Beam width at -6 dB	
			Collimator to reflector		Transducer to reflector			
			mm	(in.)	mm	(in.)	mm	(in.)
M1210	2.25	61	0.25	(0.01)	28.7	(1.13)	1.42	(0.056)
M1211	2.6	61	0.25	(0.01)	28.7	(1.13)	1.42	(0.056)
M1212	4.9	62	0.25	(0.01)	28.7	(1.13)	1.12	(0.044)
M1213	4.8	62	0.25	(0.01)	28.7	(1.13)	1.12	(0.044)
M1214	9.2	57	0.25	(0.01)	28.7	(1.13)	0.64	(0.025)
M1215	10.0	57	0.25	(0.01)	28.7	(1.13)	0.64	(0.025)
M1216	14.8	68	0.51	(0.02)	33.5	(1.32)	0.51	(0.020)
M1217	13.2	68	1.25	(0.05)	29.7	(1.17)	0.51	(0.020)

The reflection distance for maximum amplitude was found to be independent of frequency and similar to that observed for the uncollimated transducers at 2.5 MHz. The beam width was greatly reduced from that of the uncollimated tests. Beam width decreased with increasing frequency. At 2.5 MHz, the beam width was approximately one-half of the uncollimated beam at 15 MHz; the width was approximately one-fifth of the uncollimated beam. At the higher frequency, the gain required to achieve maximum amplitude was lower than that required for an uncollimated beam. Figure 5 shows an original beam-profile series for a typical collimated signal.

As a result of these observations of the effect of frequency, investigations of other collimator designs used a 13.2-MHz transducer. Table III summarizes the results of collimator design studies. It was noted that, as aperture exit size increased for cone-shaped collimators, the exit-to-reflector distance for maximum $(Y_o^+/2)$*, increased. For straight collimators, Y_o^+ was greater when collimators were used; however, the Y_o^+ distance was always reduced when using collimation.

---

* Y_o^+ was defined as the axial position of the maximum value of the beam energy pattern as follows:

$Y_o^+ Z a^2/\lambda$

where: a = radius of aperture

g = wavelength of sound medium.

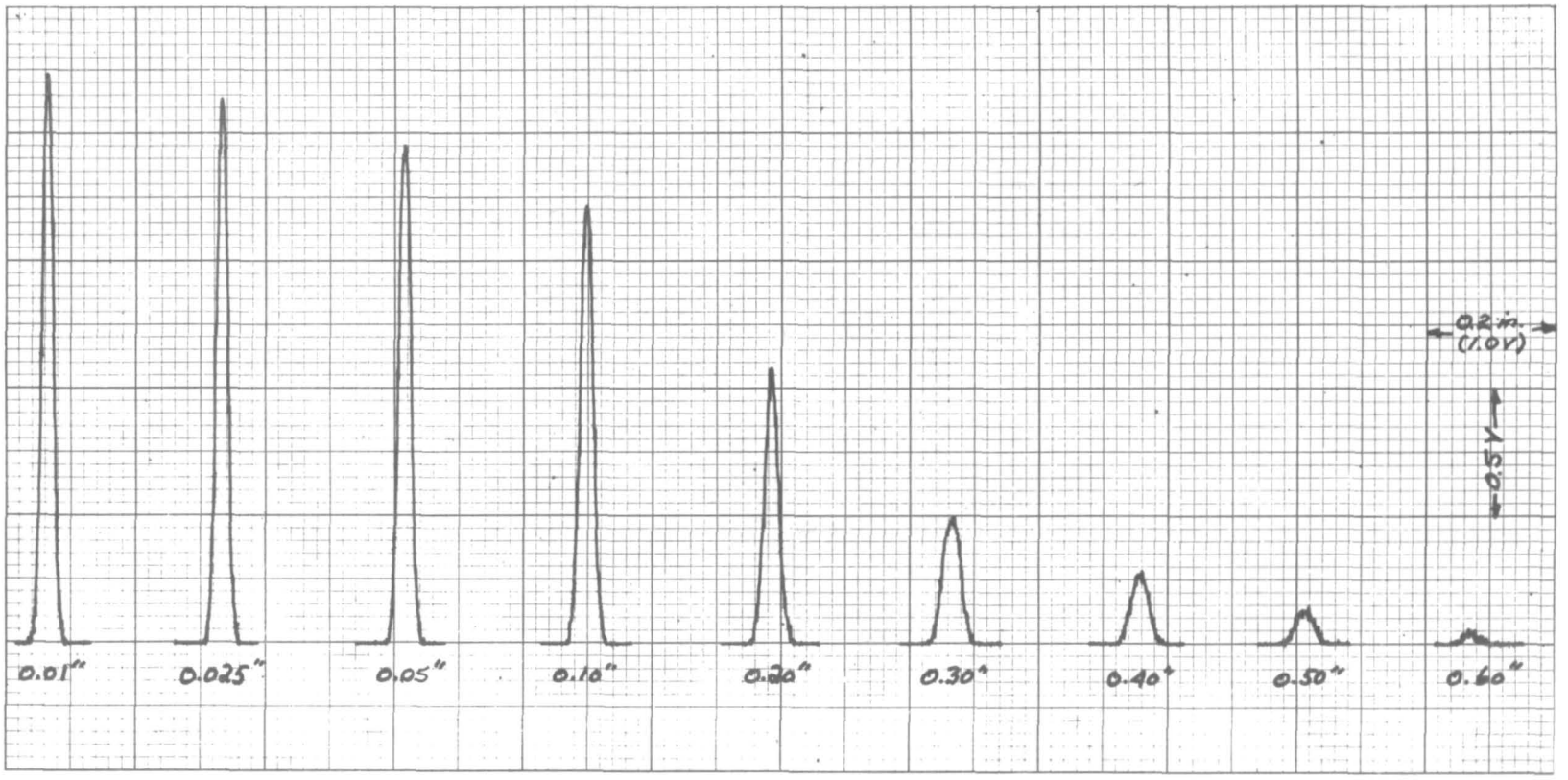

Figure 5. - Typical data plot for collimated ultrasonic beam.

TABLE III. - COLLIMATOR GEOMETRY CHARACTERISTICS AT 13.2 MHz

Collimator*			Sonatest gain setting, dB	Maximum amplitude for plot series,		Distance for maximum amplitude,† $Y_o^+/2$,		Beam width at -6 dB,	
Type	Aperture diameter,								
	mm	(in.)		mm	(in.)	mm	(in.)	mm	(in.)
Straight	0.97	(0.038)	80	56	(2.20)	0.25	(0.01)	0.43	(0.017)
	1.37	(0.054)	79	116	(4.55)	1.27	(0.05)	0.51	(0.020)
	2.01	(0.079)	74	109	(4.31)	0.25	(0.01)	0.81	(0.032)
	2.97	(0.117)	69	98	(3.85)	0.25	(0.01)	0.89	(0.035)
Cone	0.97	(0.038)	80	113	(4.45)	0.25	(0.01)	0.71	(0.028)
	1.45	(0.057)	69	114	(4.50)	0.25	(0.01)	0.51	(0.020)
	1.93	(0.076)	67	133	(5.25)	1.27	(0.05)	0.51	(0.020)
	2.06	(0.081)	69	118	(4.65)	1.27	(0.05)	0.51	(0.020)
	2.92	(0.115)	69	116	(4.55)	10.2	(0.40)	0.69	(0.027)
	3.78	(0.149)	69	124	(4.90)	16.5	(0.65)	0.76	(0.030)
	5.05	(0.199)	69	104	(4.10)	24.1	(0.95)	0.91	(0.036)
	6.25	(0.246)	69	114	(4.50)	41.9	(1.65)	1.09	(0.043)
No collimator			80	108	(4.25)	10.2	(4.00)	2.59	(0.102)

* 25.4-mm (1-in.) long Teflon.
† Distance from collimator exit to reflector transducer M1217.

Collimation effects at 2.6 MHz were studied with some of the collimators evaluated at 13.2 MHz. Table IV summarizes the results. Note that some collimators used successfully at the higher frequency could not provide enough energy to result in a detectable reflected signal. Maximum amplitude values were also lower and beam widths greater.

Beam energy profiles for a focus-type transudcer were made with and without collimation. The focus-type transducer exhibits a high energy profile with a small beam width. A significant variation in $Y_o^+/2$ distance was accomplished with only modest variation in signal amplitude. Collimating the focus transducer did not significantly affect performance. Although the maximum-amplitude signal was slightly higher for the collimated case, higher gain was required to achieve this level. The $Y_o^+/2$ distances were actually comparable because collimator length should be considered. Beam widths were comparable. The focus transducer appeared very promising for this type of work; however, collimation techniques provided similar results. Table V summarizes the data.

TABLE IV. - COLLIMATOR GEOMETRY CHARACTERISTICS AT 2.6 MHz

Collimator*			Sonatest gain setting, dB	Maximum amplitude for plot series,		Distance for maximum amplitude,† $Y_o^+/2$,		Beam width at -6 dB,	
Type	Aperture diameter,								
	mm	(in.)		mm	(in.)	mm	(in.)	mm	(in.)
Straight	1.37	(0.054)	80	Signal from reflector undetectable					
	2.01	(0.079)	80	79	(3.11)	0.25	(0.01)	1.24	(0.049)
Cone	0.97	(0.038)	80	Signal from reflector undetectable					
	1.45	(0.057)	76	100	(3.95)	0.25	(0.01)	1.52	(0.060)
	1.93	(0.076)	61	116	(4.56)	0.25	(0.01)	1.42	(0.056)
No collimator			45	129	(5.07)	31.8	1.25	2.44	(0.096)

* 25.4-mm (1-in.) long Teflon.
† Distance from collimator exit to reflector transducer M1217.

TABLE V. - FOCUS TRANSDUCER* DATA

Collimator*			Sonatest gain setting, dB	Maximum amplitude for plot series,		Distance for maximum amplitude,† $Y_o^+/2$,		Beam width at -6 dB,	
Type	Aperture diameter,								
	mm	(in.)		mm	(in.)	mm	(in.)	mm	(in.)
None			35	8.2	(3.22)	37.18	(1.25)†	0.61	(0.024)
Cone	1.93	(0.076)	47	14.0	(5.50)	0.25	(0.01)	0.81	(0.032)

* N128, focus type, 10.5-MHz peak frequency.
** 25.4-mm (1-in.) long Teflon.
† Transducer to reflector.

A series of profiles was made using a collimator that was much longer and contained a smaller cone angle than the collimators previously described. This collimator (fig. 6) approximated that described for an acoustic conical horn and was governed by the following equation (ref. 2):

$$S = S_o \left(1 + \frac{X}{X_o}\right)^2$$

where: S = the area of the entrance (large end),

S_o = the area of the exit (small end),

x = the entrance-to-exit distance,

x_o = the exit-to-cone-apex distance.

Data generated for this design were limited but showed that amplitude increased with decreasing $Y_o^+/2$ distance. No maximum value was obtained. High amplitude values were obtained with a significant variation in $Y_o^+/2$ distance. Table VI summarizes the data.

Up to this point data presented dealt with the pulse-echo mode of operation in which a single transducer and collimator were used for both transmitting and receiving. The following discussion describes evaluation of the pitch-catch mode. Based on pulse-echo data, an aperture value of 2.9 mm (0.115 in.) was selected to give a Y_o^+ value consistent with the requirements of inspecting thin-gage materials in the pitch-catch mode. Profiles were made for the four combinations of straight and cone collimators at the collimator-to-reflector distance $Y_o^+/2$ of 10 mm (0.4 in.) using transducers in the range of 13 to 15 MHz. Distance was optimum for the 25.4-mm (1-in.) long cone with the 2.9-mm (0.115-in.) aperture, but not for the straight collimator. The data showed that maximum signal amplitude and minimum beam widths (measured at -6 dB) were obtained using the cone-shaped collimators to both transmit and receive. The beam width [0.81 mm (0.032.)] was in close agreement with that shown for pulse-echo data. Figure 7 gives the data for the four combinations. For a given travel distance, the cone-cone combination resulted in the highest signal amplitude. The following table gives the ranking in order of decreasing maximum amplitude.

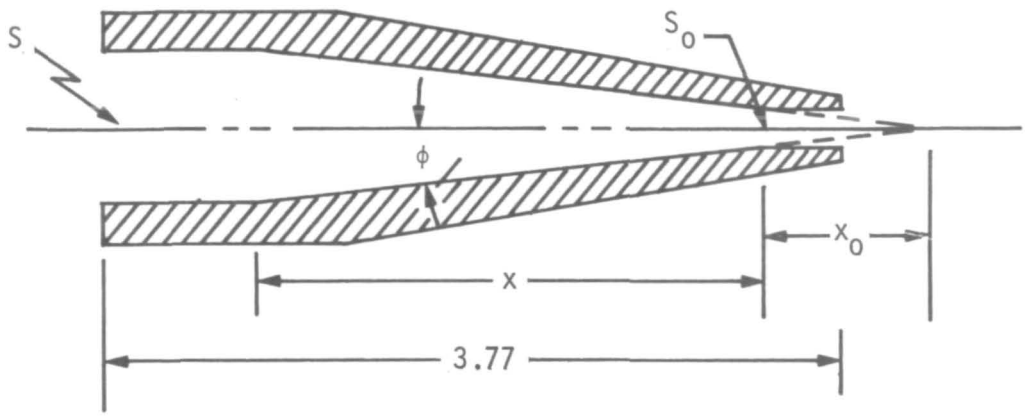

for S_0 = 0.108 and S = 0.366 in. dia $\phi \approx 2.6°$

Note: Dimensions in inches.

Figure 6. - Sketch of long cone.

TABLE VI. - ACOUSTIC CONICAL-HORN COLLIMATOR* DATA

Frequency, MHz	Sonatest gain setting, dB	Max amplitude for plot series,		Distance for max amplitude, $Y_o^+/2$,		Beam width at -6 dB,	
		mm	(in.)	mm	(in.)	mm	(in.)
13.2†	65	116	(4.55)	0	(0)	0.86	(0.034)
2.6§	55	116	(4.57)	0	(0)	1.52	(0.060)

* 96-mm (3.77-in.) long cone, 9.3-mm (0.366-in.) entrance aperture, 2.7-mm (0.108-in.) exit aperture.
† Transducer M1217.
§ Transducer M1211.

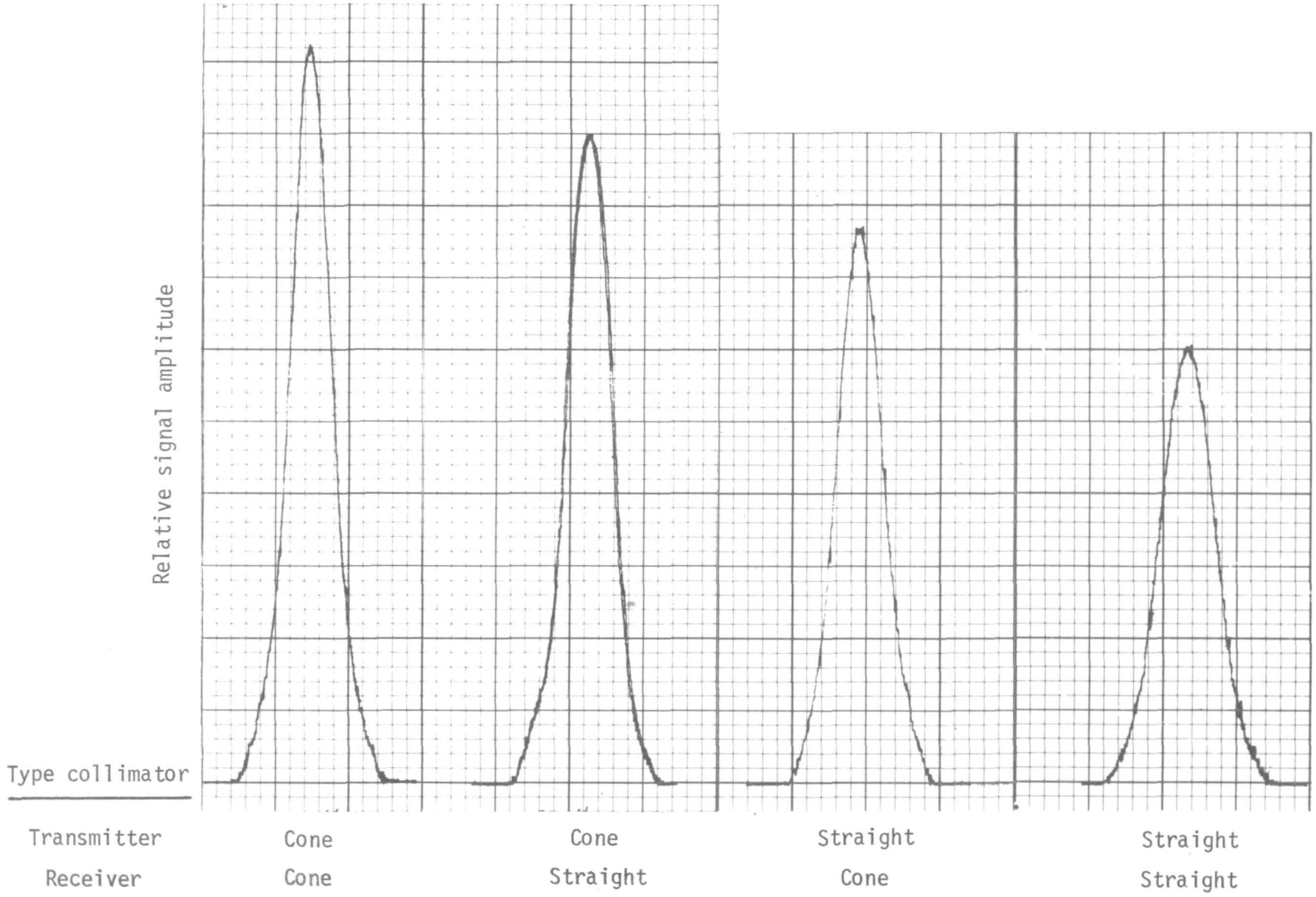

Figure 7. - Data from evaluation of collimator combinations.

Order	Collimator type		Relative amplitude
	Transmit	Receive	
1	Cone	Cone	1.00
2	Cone	Straight	0.88
3	Straight	Cone	0.76
4	Straight	Straight	0.59

Surface Roughness Effects

The effect of surface roughness on the ultrasonic signal was evaluated to determine the worst-case conditions that could be tolerated without danger of disguising defects.

Panels of 2219-T87 and 4340 steel 0.64-mm (0.25-in.) thick were machined to obtain varying degrees of surface roughness. Aluminum specimens were machined using a milling machine and fly cutter. Steel specimens were machined with a single-point fly cutter or surface ground. Surface finish readings were taken with a Gould surf-indicator model 21-1350, which provides an arithmetic average over the sampling distance. Table VII gives data for both alloys.

Ultrasonic measurements were made by traversing part of the specimen [approximately 30 mm (1.2 in.)] using a 23° incident angle and the pitch-catch technique. The front surface of the panel was used as the reflector. A 25-mm (1-in.) cone collimator with a 2.9-mm (0.115-in.) aperture was placed in front of the 14.8-MHz transmitter and a 25-mm (1-in.) straight collimator with a 3-mm (0.117-in.) aperture was used with the receiving transducer (13.2 MHz). A total travel distance of 20 mm (0.8 in.) was used.

Test results for front-face reflections showed that reflected-signal amplitude was sensitive to the degree of roughness. Amplitude variation increased with increasing roughness. For roughness values from 610 to 3048 nm (24 to 120 in.) rms in aluminum and from 254 to 3175 nm (10 to 125 μin.) rms in steel, traces were relatively flat. However, even for the highest roughness levels, the effect on the amplitude was minor compared to that produced by the presence of a defect. Figures 8 and 9 present the data for aluminum and steel, respectively.

The combination of parameters used for front-surface reflections was not satisfactory for back-surface reflections. To maintain the travel distance and incident angle, collimators with apertures of approximately 5 mm (0.2 in.) were used. Results were similar to those found from front-surface reflections (fig. 10 and 11).

TABLE VII. - SURFACE ROUGHNESS DATA

Alloy	Surface	Surface roughness, arithmetic average, nm (μin.)									
		Specimen number									
		1	2	3	4	5	6	7	8	9	10
Aluminum	A	457 (18)	610 (24)	610* (24*)	610 (24)	1143 (45)	1905 (75)	2921 (115)	3048 (120)	6350 (250)	6731 (285)
	B	5588 (220)	610 (24)	610* (24*)	3048 (120)	1397 (55)	1905 (75)	5588 (220)	3048 (120)	6350 (250)	7320 (300)
Steel	A	254 (10)	305 (12)	305 (12)	3556 (140)	3810 (150)	3810 (150)	4445 (175)	5715 (225)	6985 (275)	
	B	5842 (230)	305 (12)	3175 (125)	3810 (150)	3810 (150)	5715 (225)	4445 (175)	6350 (250)	6985 (275)	

* As-rolled surfaces.

Specimen no.	Roughness of reflecting surface, nm (μin.)	Maximum amplitude, cm (in.)	Gain, dB
A-2	610 (24)	10.7 (4.2)	47
A-5	1143 (45)	11.7 (4.6)	46
A-5	1397 (55)	11.2 (4.4)	44
A-6	1905 (75)	10.9 (4.3)	46
A-7	2921 (115)	10.9 (4.3)	45
A-8	5588 (220)	10.7 (4.2)	46
A-7	5588 (220)	10.7 (4.2)	46
A-9	6350 (250)	11.2 (4.4)	47
A-10	6731 (265)	10.9 (4.3)	47
A-10	7620 (300)	11.2 (4.4)	48
A-3	610 (24)	10.7 (4.2)	46

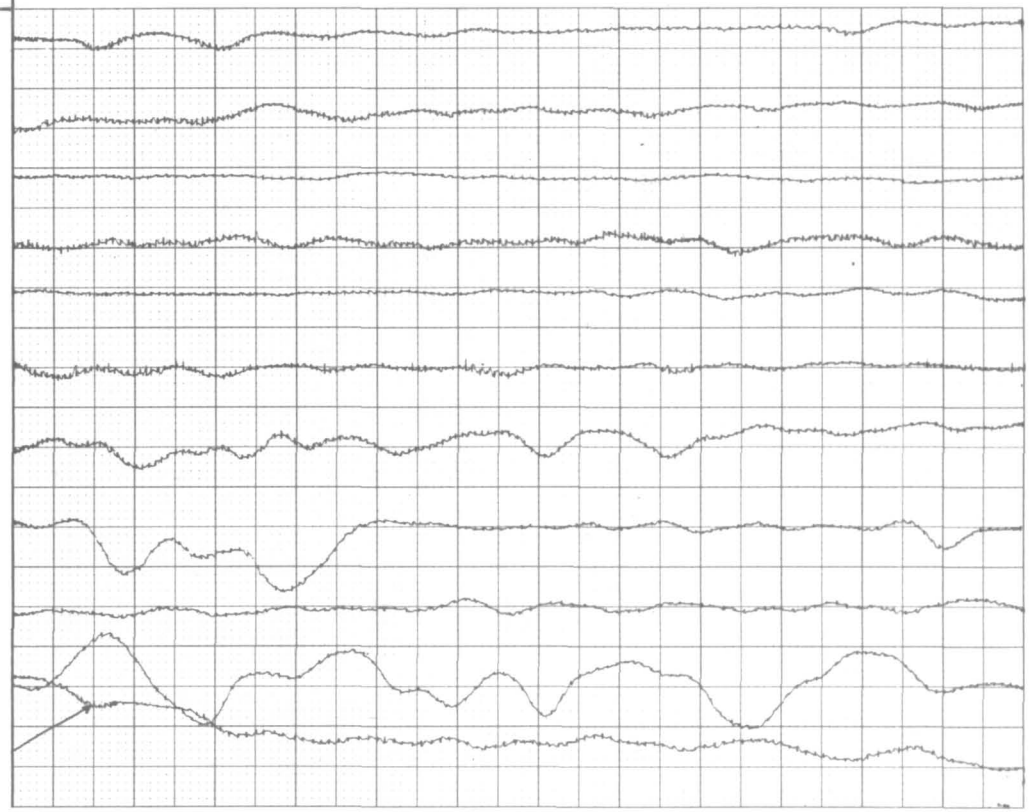

Figure 8. - Effect of roughness on ultrasonic reflections from front surface of aluminum.

Specimen no.	Roughness of reflecting surface, nm (μin.)	Maximum Maximum amplitude, cm (in.)	Gain, dB
S-1	254 (10)	10.9 (4.3)	45
S-2	305 (12)	11.2 (4.4)	45
S-3	3175 (125)	10.7 (4.2)	45
S-4	3556 (140)	10.7 (4.2)	47
S-4	3810 (150)	10.9 (4.3)	45
S-7	4445 (175)	11.2 (4.4)	46
S-8	5715 (225)	11.2 (4.4)	46
S-8	6350 (250)	10.7 (4.2)	47

Figure 9. - Effect of roughness on ultrasonic reflections from front surface of steel.

Specimen no.	Roughness of reflecting surface, nm (μin.)	Maximum amplitude, cm (in.)	Gain, dB
A-3	610 (24)	11.4 (4.5)	72
A-4	610 (24)	11.2 (4.4)	70
A-5	1143 (45)	10.9 (4.3)	70
A-5	1397 (55)	11.2 (4.4)	70
A-6	1905 (75)	11.7 (4.6)	72
A-7	2921 (115)	11.2 (4.4)	72
A-8	3048 (120)	11.2 (4.4)	72
A-7	5588 (220)	11.4 (4.5)	73
A-9	5350 (250)	11.2 (4.4)	74
A-10	6731 (265)	11.2 (4.4)	77
A-10	7320 (300)	11.2 (4.4)	77

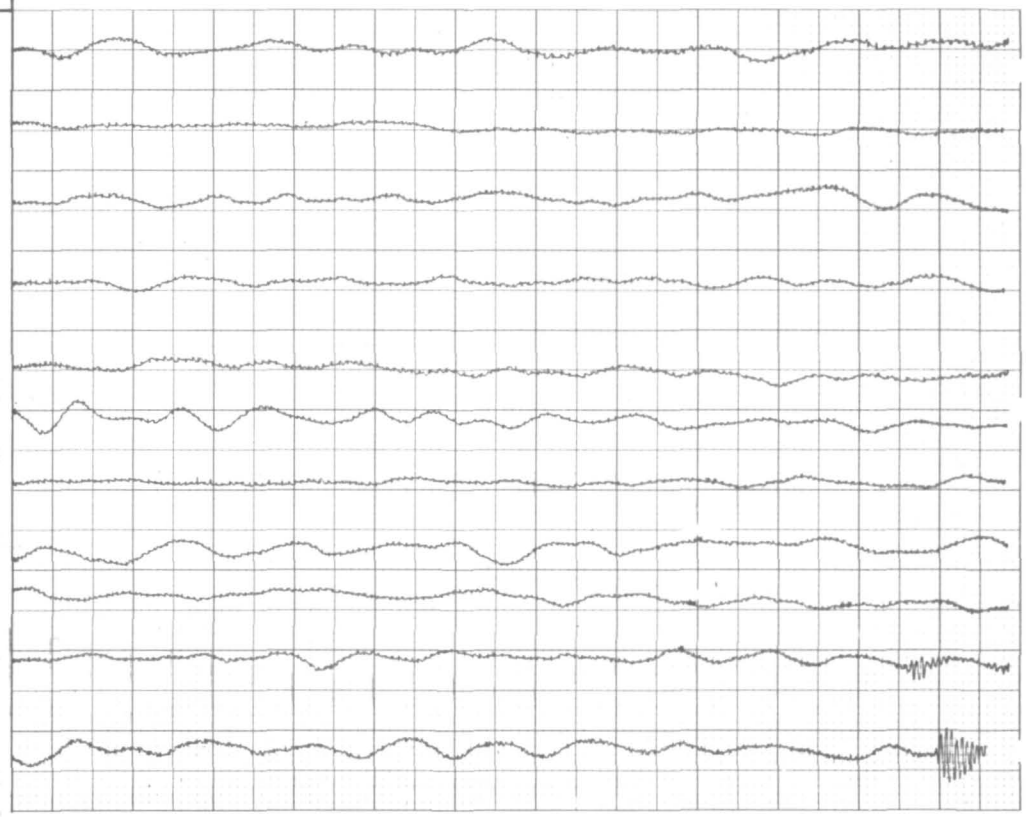

Figure 10. - Effect of roughness on ultrasonic reflections from back surface of aluminum.

Specimen no.	Roughness of reflecting surface, nm (μin.)	Maximum amplitude, cm (in.)	Gain, dB
S-1	254 (10)	10.7 (4.2)	69
S-2	305 (12)	11.4 (4.5)	68
S-3 (end)	3175 (125)	10.9 (4.3)	69
S-3 (center)	3175 (125)	10.9 (4.3)	69
S-4	3556 (140)	10.9 (4.3)	69
S-4	3810 (150)	11.2 (4.4)	69
S-7	4445 (175)	11.2 (4.4)	72
S-8	5715 (225)	10.7 (4.2)	68
S-8	6350 (250)	10.7 (4.2)	71

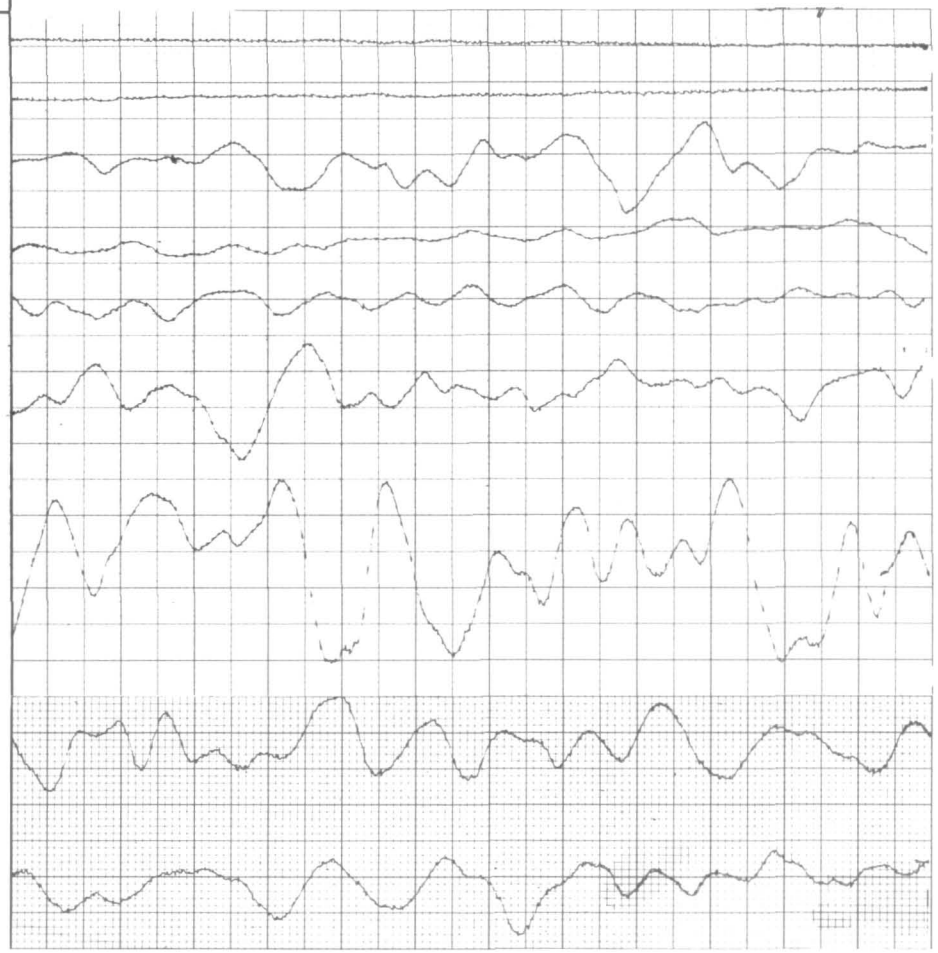

Figure 11. - Effect of roughness on ultrasonic reflections from back surface of steel.

Collimated-Beam Effectiveness

The final part of this task was to determine the effectiveness of the collimated-beam technique to sense the shape and location of small flaws in thin materials. Three specimens were fabricated with three small EDM flaws. Table VIII gives the geometry of the specimens and flaws.

Using the pitch-catch method, all flaws were monitored by traversing across the defect (perpendicular to the 2C direction). Starting at the center of the flaws, successive scans were made at 0.13-mm (0.005-in.) intervals from the center of the flaw to the edge.

The scans revealed that the smallest defect was readily discernible. Although the beam diameter was significantly greater than the defect size, the defect was well defined in the scan plot.

Figure 12 shows original plots for the three defects in the titanium alloy. The trace showing the greatest loss of signal strength (or largest dip) is that made by traversing the center of the flaw. The succeeding plot made by traversing at a small interval parallel to the first traverse shows a decreasing loss of signal strength and decreasing width of the affected area. The width of the dip and degree of loss of signal indicated the size of the defect. Because the beam was so large compared to the size of the defect, quantitative measurement of defect size could not be readily made. Comparison of the relative width of the largest dip was found to be an indicator of the size of the defect. The ratio of the width to the defect area was relatively constant. Figure 13 illustrates the data obtained.

Results for the two thicknesses of aluminum clearly show that a defect as small as 0.25 mm (0.01 in.) deep can be readily detected (fig. 14 and 15). To determine reproducibility of results, plots for the thicker-gage aluminum were repeated. The plots in figure 16 have the same width measurements as the first series and show excellent agreement.

Very small defects were shown to be readily detectable using the collimated ultrasonic pitch-catch technique. Because of the large ratio of beam width to defect size, direct determination of actual defect size from plotted data is difficult. However, through the use of standard defects, the size of an unknown defect can be readily estimated.

TABLE VIII. - SPECIMEN GEOMETRY DATA FOR BEAM EFFECTIVENESS STUDY

Alloy	Thickness		Flaw geometry				
			a		2C		
	mm	(in.)	mm	(in.)	mm	(in.)	a/t
Titanium	1.27	(0.050)	1.14	(0.045)	1.62	(0.064)	0.9
			1.02	(0.040)	1.62	(0.064)	0.8
			0.76	(0.030)	1.55	(0.061)	0.6
Aluminum	0.81	(0.032)	0.74	(0.029)	0.84	(0.033)	0.9
			0.56	(0.022)	0.84	(0.033)	0.7
	0.51	(0.020)	0.41	(0.016)	0.84	(0.033)	0.5
			0.46	(0.018)	0.79	(0.031)	0.9
			0.36	(0.014)	0.79	(0.031)	0.7
			0.25	(0.010)	0.79	(0.031)	0.5

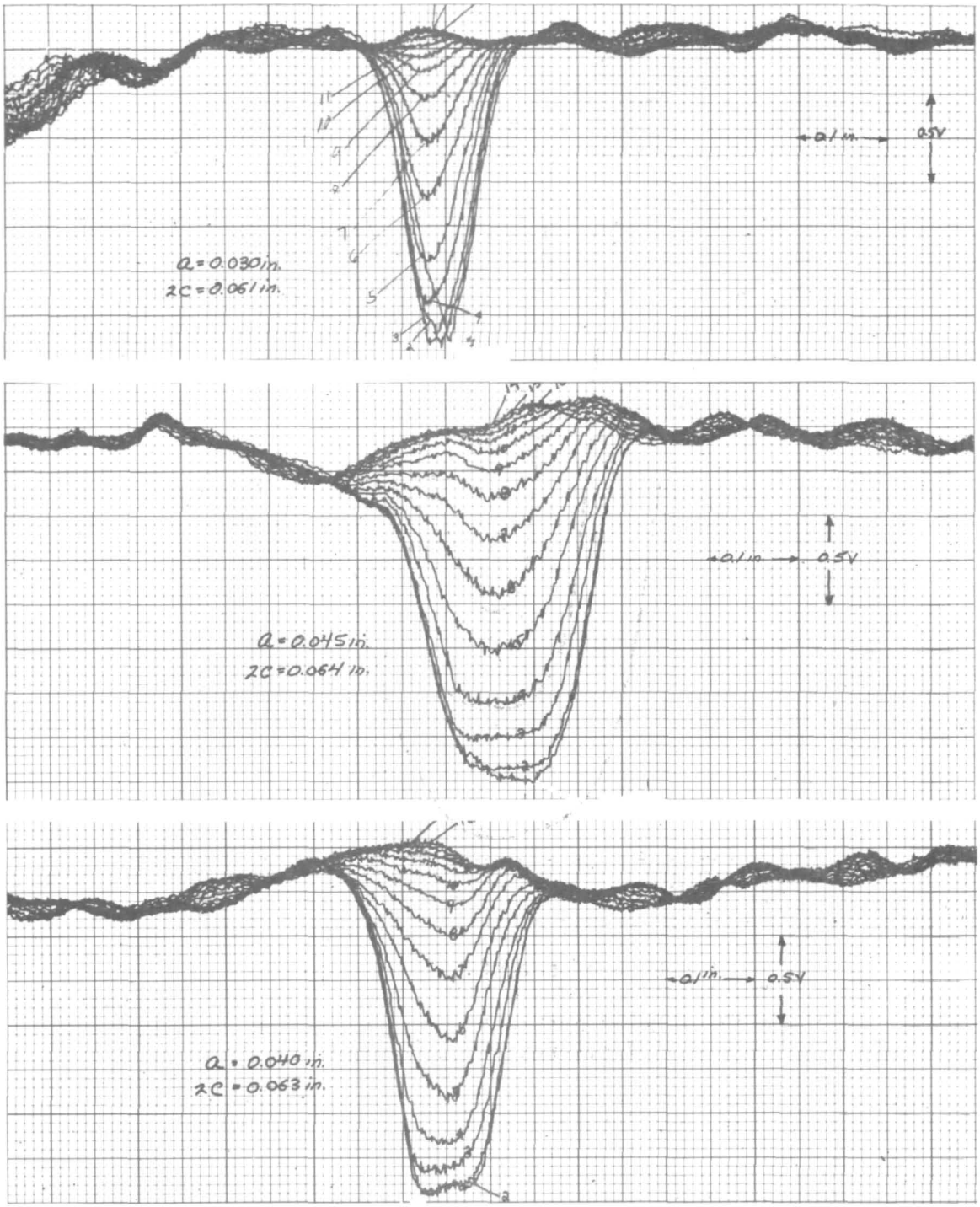

Figure 12. Ultrasonic data plots of defects in 1.3-mm (0.05-in.) titanium.

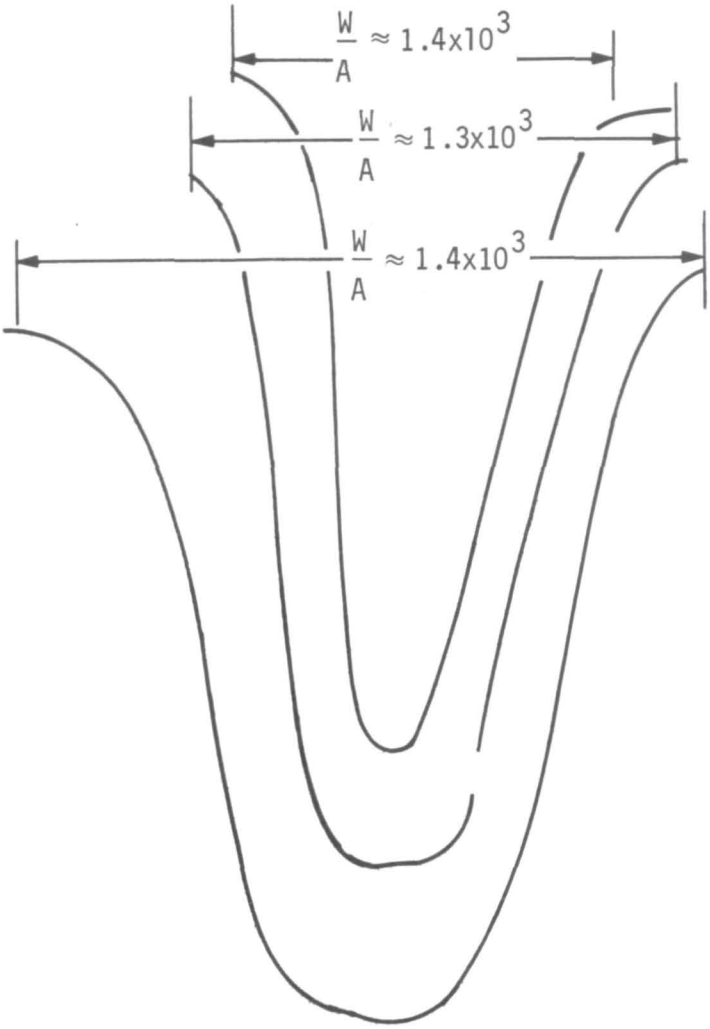

Legend:

W = width of dip from ultrasonic data

A = area of defect

Figure 13. - Relationship of ultrasonic plot data to defect area for titanium.

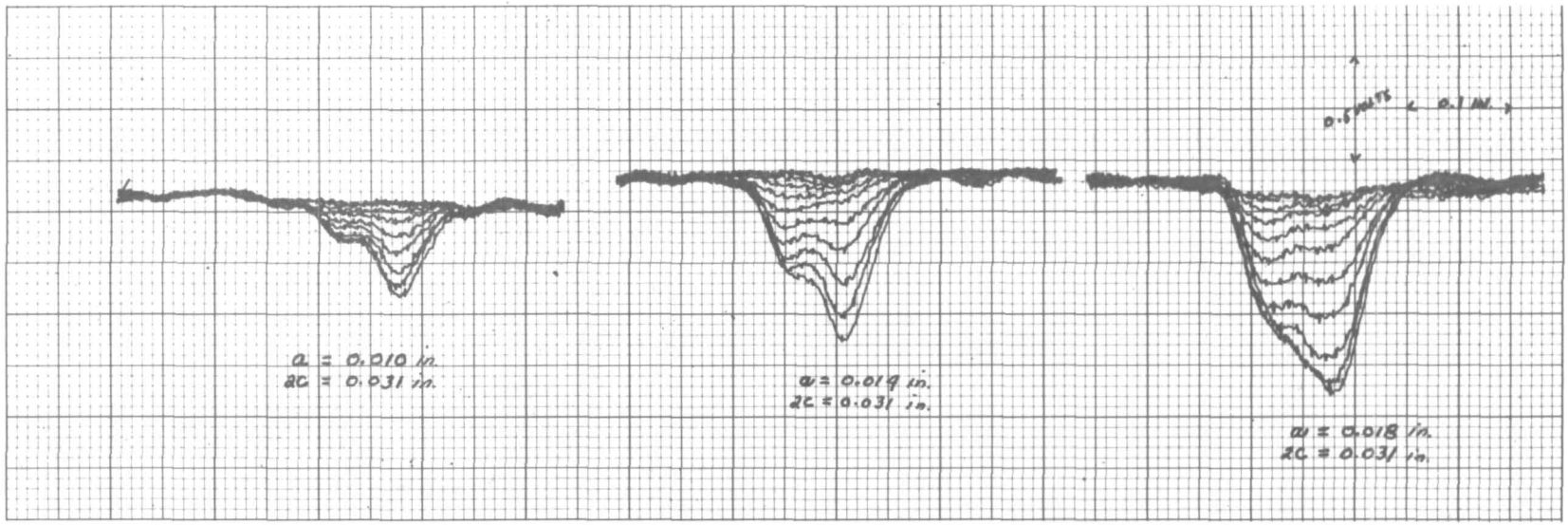

Figure 14. - Ultrasonic data plots of defects in 0.5-mm (0.020-in.) aluminum.

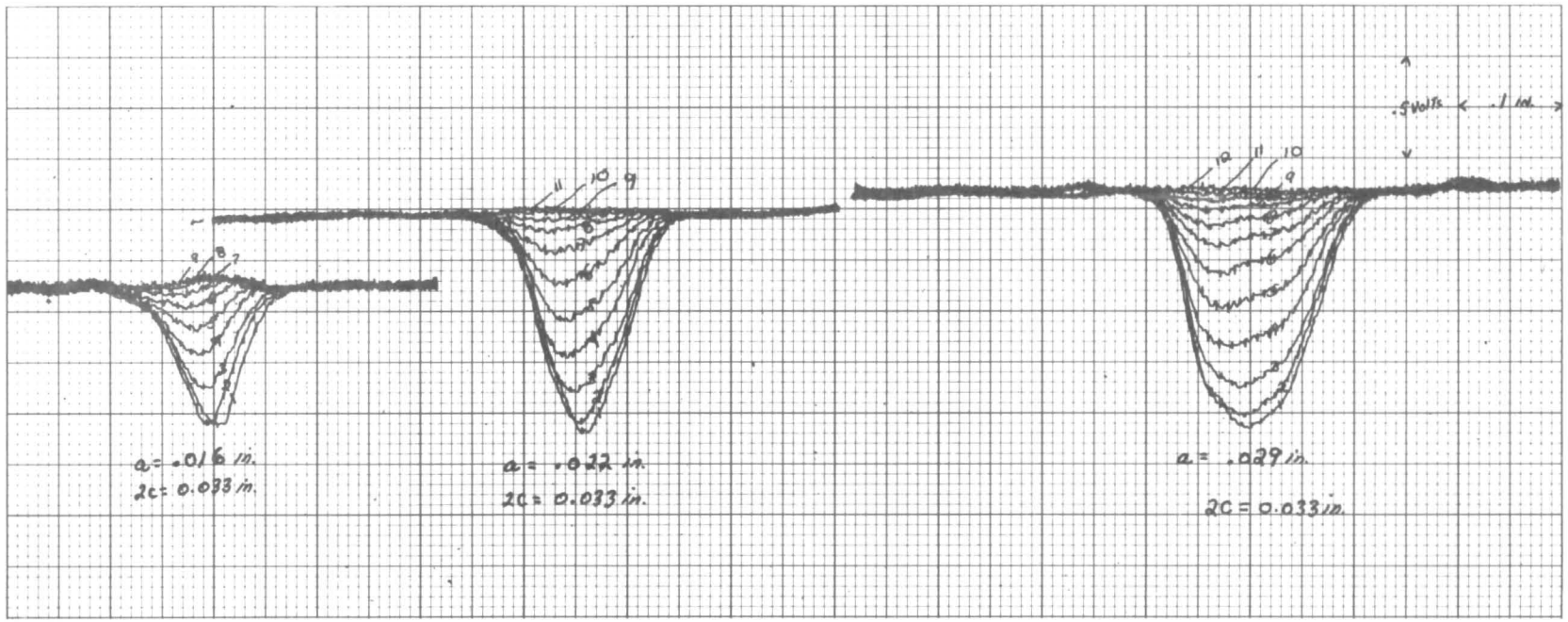

Figure 15. - Ultrasonic data plots of defects in 0.8-mm (0.032-in.) aluminum (series 1).

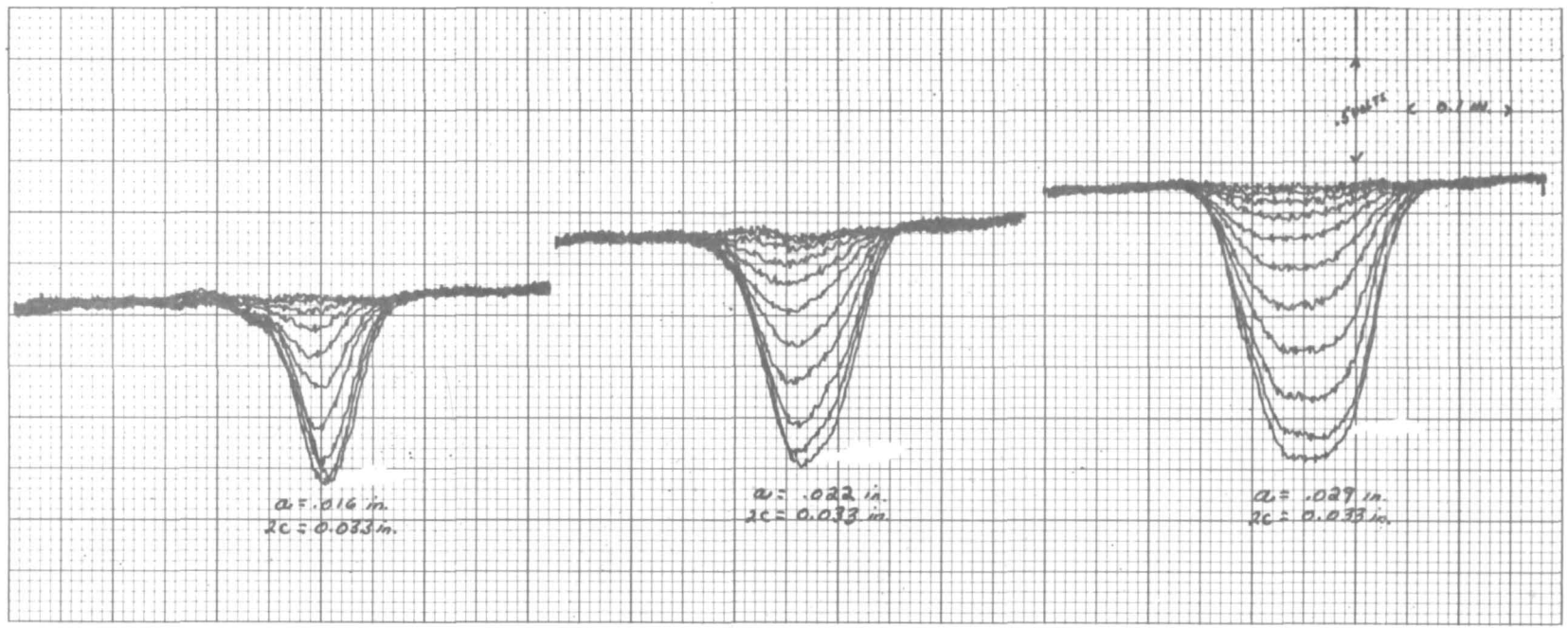

Figure 16. - Ultrasonic data plots of defects in 0.8-mm (0.032-in) aluminum (series 2).

DETERMINATION OF CRACK-OPENING-DISPLACEMENT GAGE CORRECTION FACTORS

The purpose of the crack-opening-displacement gage correction-factor task was to establish the correlation between flaw depth measurements obtained using conventional clip-on-type crack-opening displacement gages and the collimated pitch-catch ultrasonic technique, and to determine the nature of the plasticity associated with loading.

The ultrasonic apparatus was installed in a closed-loop servo-hydraulic testing machine as shown in figure 17. A large clear plastic container housed the water used as an ultrasonic transfer medium. The test specimen was pin loaded at one end and friction gripped at the other. Figure 18 gives the specifications for the test specimen.

To obtain crack-opening displacement (COD) data without the normal problems associated with a submersible gage, a watertight container was bonded to the specimen to house the COD gage.

The COD gage was a very short gage-length extensometer using a circular beam element. Several different attachment schemes have been developed. The simplest type uses needle points and is held in place by springs (fig. 19). A second type contains in-plane attachment points and is actually clipped into the crack surfaces. This gage rests flush with the surface and, like the spring-held gage, is sufficiently adherent to function satisfactorily for cyclic testing. The gages have also been used in cryogenic environments, are extremely sensitive to small crack openings, and have been demonstrated to be very reproducible. In most applications, the gage is used under conditions that give a displacement sensitivity of approximately 0.0005 cm/cm (0.0005 in./in.) of chart.

Figure 20 is a close-up view of the transducers and collimators and shows the watertight COD gage housing. Table IX gives the specifications for transducer adjustments.

Three materials were evaluated in this task. Thicknesses were:

Alloy	Thickness,	
	cm	(in.)
2219-T87 aluminum	0.64	(0.25)
6Aℓ-4V titanium	0.32	(0.125)
4130 steel	0.32	(0.125)

Surface-flaw specimens were prepared with aspect ratios varying from 0.20 to 0.50. Three sets were prepared and evaluated for each alloy. The first contained only an electrodischarge-machined (EDM) flaw and was used primarily for calibration. The second

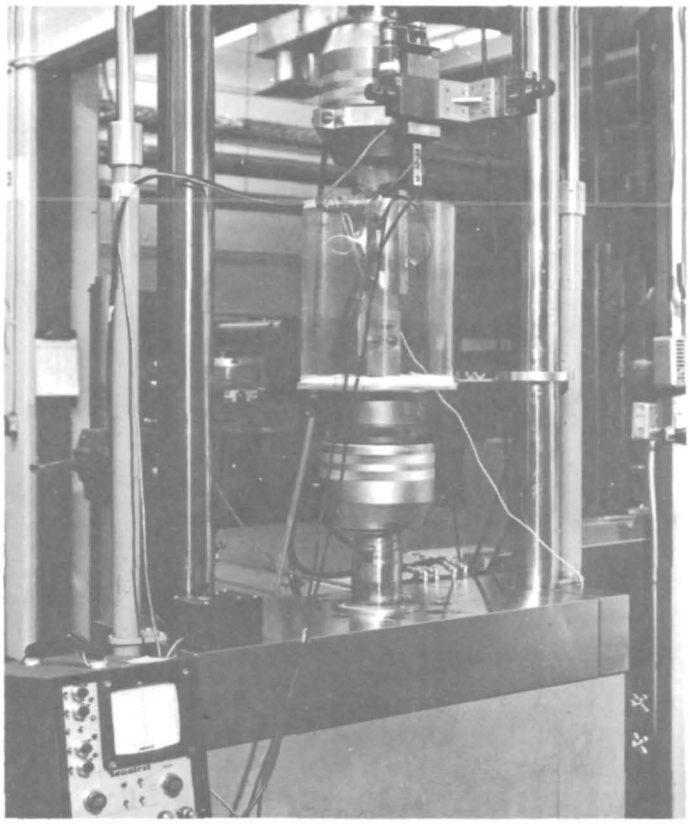

Figure 17. - Ultrasonic apparatus in testing machine.

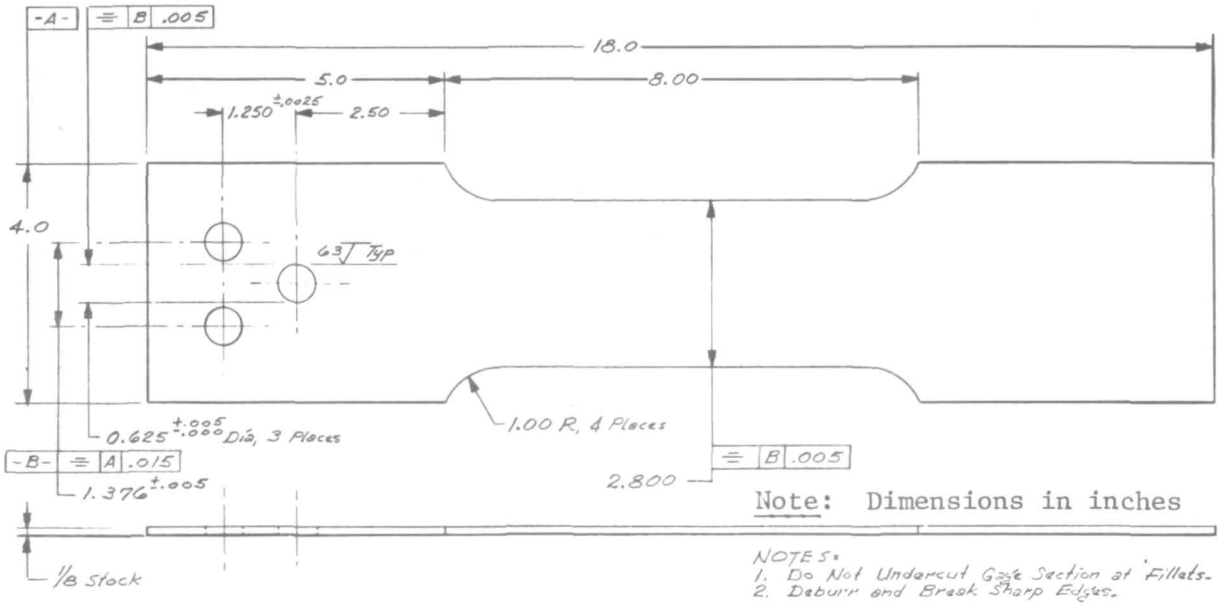

Figure 18. - Specifications for test specimen.

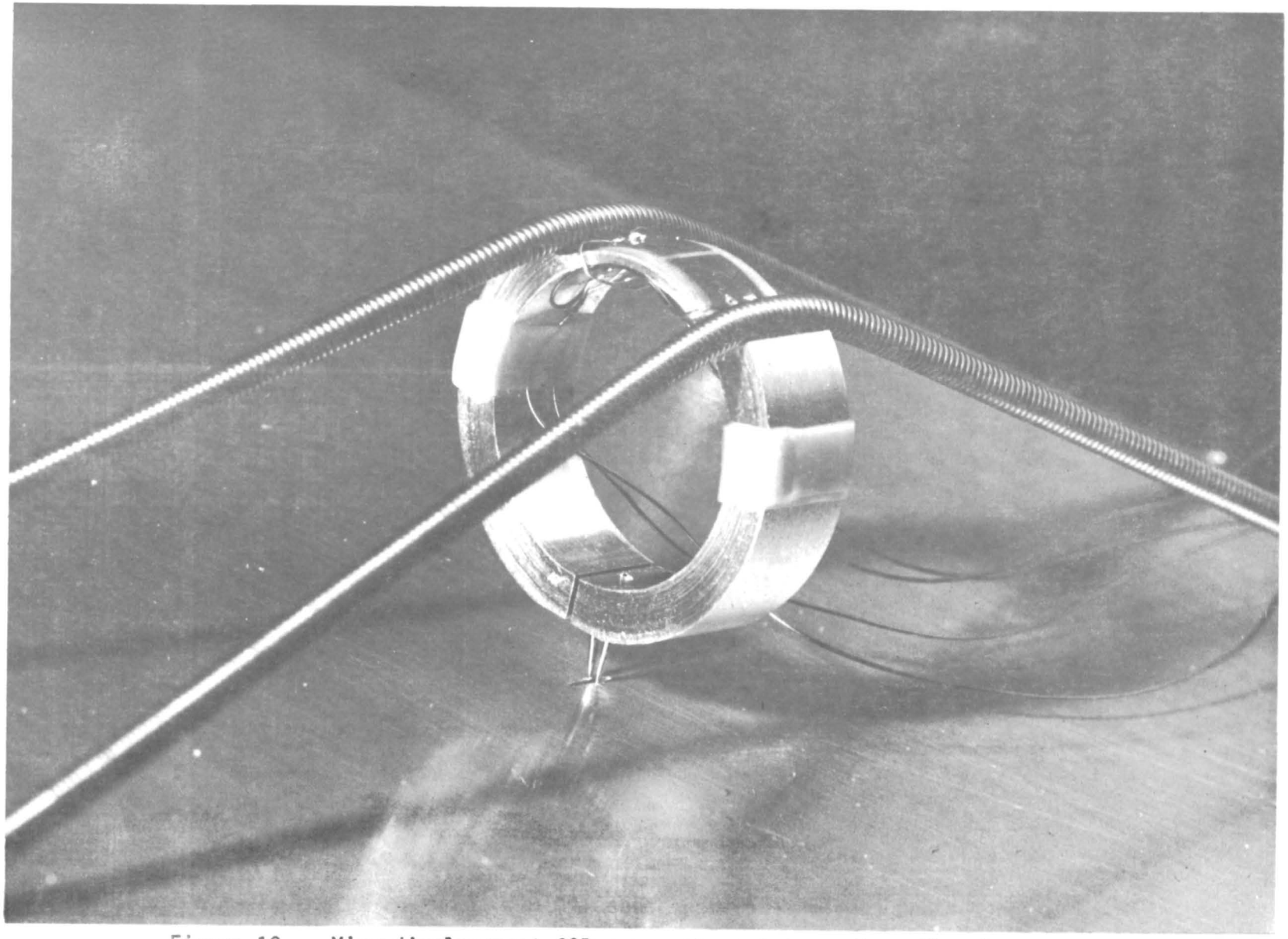

Figure 19. - Microdisplacement COD gage attached to surface-flawed specimen.

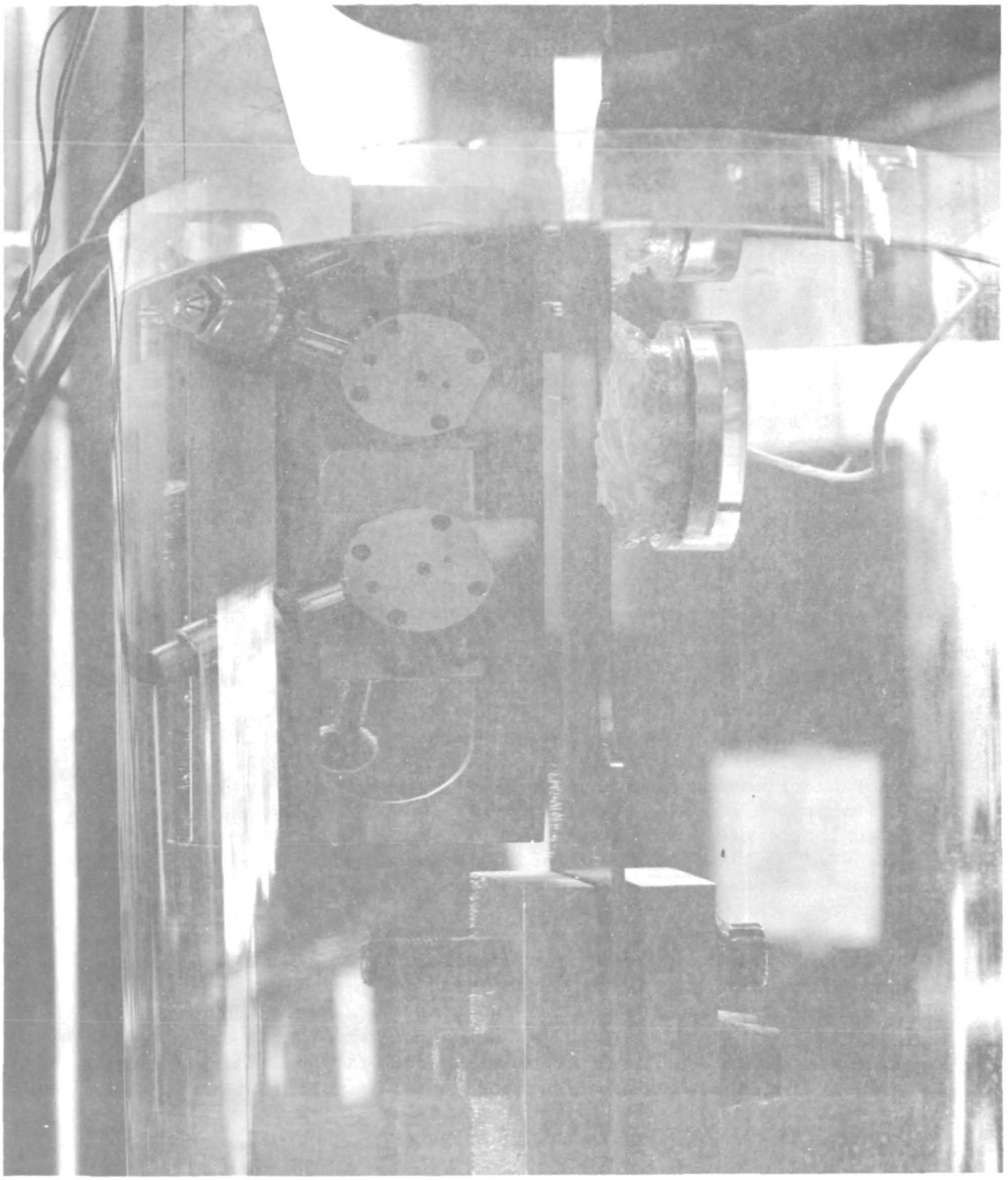

Figure 20. - Close-up view showing transducers, collimators, and COD gage housing.

TABLE XI. - SPECIFICATIONS FOR TRANSDUCER ADJUSTMENTS*

Material	Thickness,		Transducer inclination,† deg	Resultant shear angle, deg	Distance between transducer mounting blocks,	
	cm	(in.)			cm	(in.)
2219-T87 aluminum	0.64	(0.25)	25	61.6	2.01	(0.79)
6Aℓ-4V titanium	0.32	(0.125)	25	62.3	1.04	(0.41)
4130 steel	0.32	(0.125)	23.5	46.3	0.79	(0.31)

*10-MHz transducer; collimator diameter 0.505 cm (0.199 in.).
†Incident angle in water.

series contained a fatigue-sharpened flaw and was evaluated at stress levels up to 0.60 σ_{ys}. We expected that this series would not exhibit subcritical growth and would be used for additional calibration points. The third series also contained a fatigue-sharpened flaw but was loaded to levels that developed plastic deformation and, frequently, subcritical growth.

Several ultrasonic plots were made of the electrodischarge-machined defects at zero load. Data reduction techniques that would be required to obtain a map from these data would be prohibitively expensive. Figure 21 shows a typical data plot. This plot of ultrasonic amplitude versus distance requires determination of the location at which an arbitrary loss of ultrasonic signal strength occurs. A technique similar to C-scanning was selected so that the amount of data reduction required to obtain a flaw map would be minimized. Figure 22 is a map obtained in this manner. Before making a map, an amplitude scan was performed to obtain the signal-strength limits associated with the surface and complete signal loss. The gate level on the instrument was then set at a 50% loss of signal. The map was then prepared by traversing the ultrasonic transducers in a direction normal to the flaw. When the signal dropped to the gate level, the pen was automatically lifted. At the end of each traverse, the stage was advanced 0.64 mm (0.025 in.) and a return traverse made. The resulting plot gave a symmetrical image of the flaw, with the crack width as the axis of symmetry. The plot gives actual width dimensions and projections of the crack depth dimensions.

Figure 23 illustrates why a symmetrical image was obtained. As shown by the schematic diagram, the tip of the defect first interrupted the signal reflected from the back surface. As the transducer array traversed normal to the plane of the defect, the

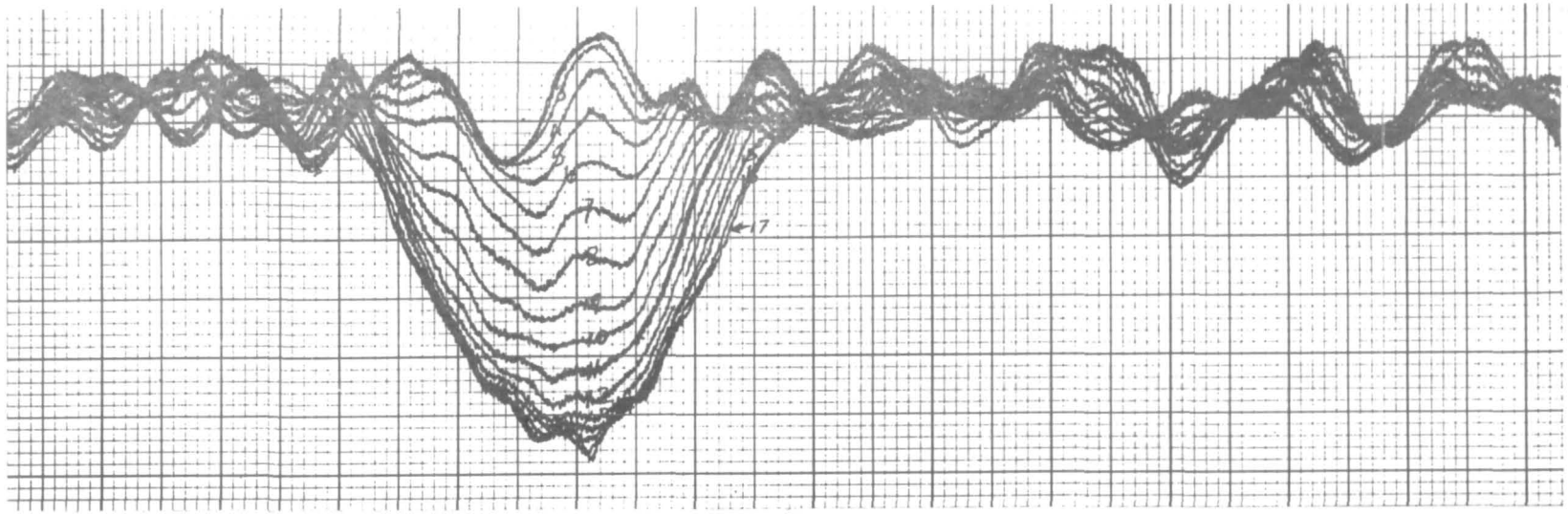

Figure 21. - Typical data plot obtained using ultrasonic signal-amplitude-versus-distance method.

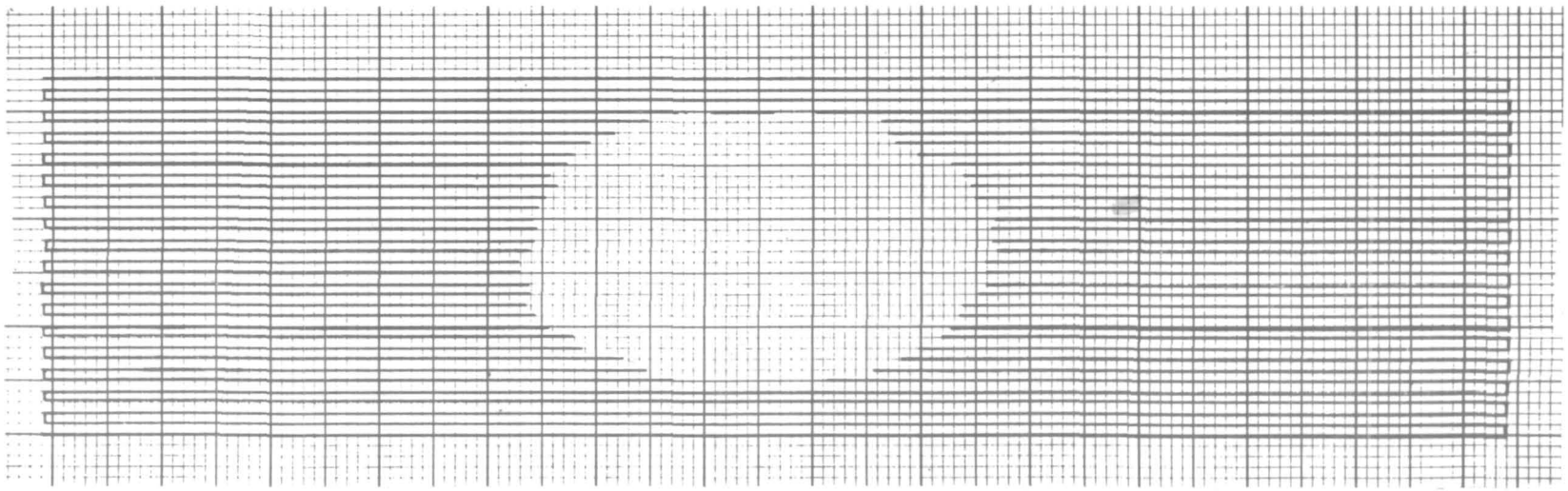

Figure 22. - Typical flaw map using scanning approach.

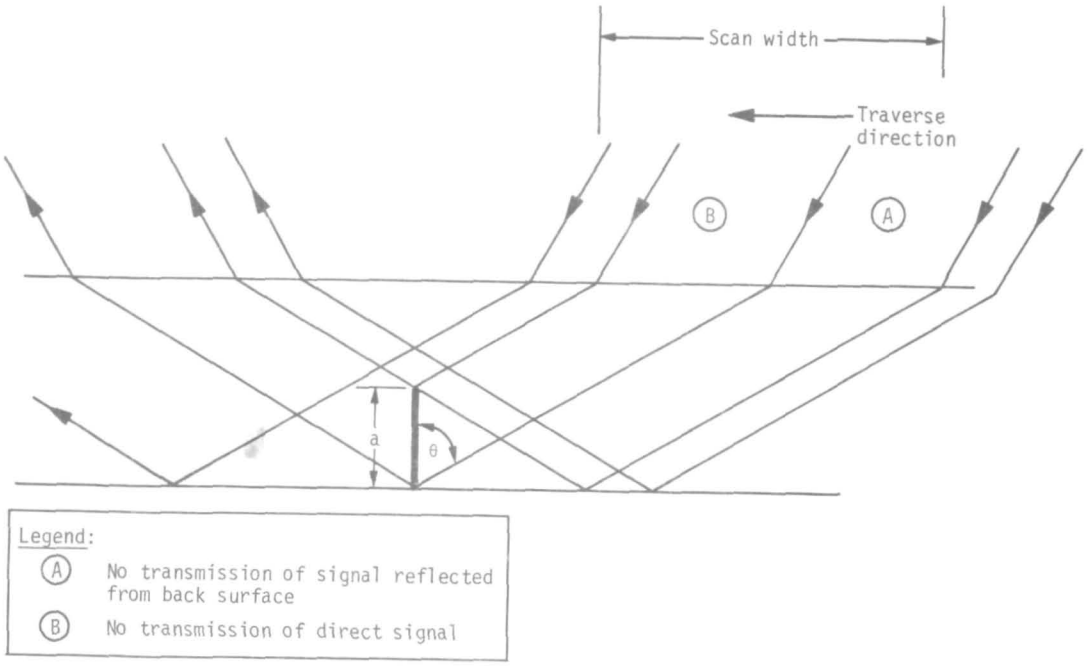

Scan width/2 = a (crack depth) x tan θ

Figure 23. - Schematic of ultrasonic path.

tip of the defect was the last interference to the direct signal. Scan width is a trigonometric function of the crack depth; the resulting relationship permits ready calculation of crack depth: scan width/2 = a (crack depth x tan θ).

Aluminum Data

Table X summarizes data for the aluminum calibration specimens. The table presents data describing flaw size and shape, crack depth information determined ultrasonically, and crack-opening displacement data obtained by loading to 30% and 60% of the yield strength. No evidence of subcritical growth was found by fracture surface examination after breaking open the specimens after loading to 60% of yield strength. Crack-opening displacement curves were sensitive enough to detect crack opening, as shown by a slightly greater slope during the first increment of loading. Curves obtained by loading to 30% of yield strength were generally linear, except for the initial crack opening. Loading to 60% of yield strength produced a very small deviation from linearity. Figure 24 shows typical crack-opening displacement curves.

Compliance calibration curves were obtained by using the data from the series described, plus data from initial crack-opening displacement measurements taken on specimens that were later loaded to exhibit subcritical growth. Figure 25 gives the compliance calibration curves obtained. Data are presented as three curves for crack shape ratios of 0.5, 0.35, and 0.2.

TABLE X. - ALUMINUM CALIBRATION DATA

Specimen no.*	Flaw geometry							Test condition	Stress level,	Ultrasonic scan width,		Compliance,	
	Depth, a,		Width, 2C,		a/2C	a/t	a/Q					nm/N	(μin./lb)
	cm	(in.)	cm	(in.)					% σ_{ys}	cm	(in.)		
AE-1	0.203	(0.080)	0.584	(0.230)	0.35	0.32	0.044	Static	0	6.99	(2.75)		
AE-2	0.213	(0.084)	0.744	(0.293)	0.29	0.34	0.053	Static	0	6.86	(2.70)		
AE-3	0.203	(0.080)	1.224	(0.482)	0.17	0.32	0.064	Static	0	5.97	(2.35)		
AE-4	0.333	(0.131)	0.813	(0.320)	0.41	0.52	0.064	Static	0	9.73	(3.83)		
AE-5	0.351	(0.138)	1.095	(0.431)	0.32	0.55	0.081	Static	0	11.23	(4.42)		
AE-6	0.351	(0.138)	1.842	(0.725)	0.19	0.55	0.106	Static	0	11.89	(4.68)		
								Loading	0-30			0.548	(0.096)
								Static	30	11.13	(4.38)		
								Unloading	30-0			0.542	(0.095)
								Loading	0-60			0.548	(0.096)
								Static	60	10.92	(4.30)		
								Unloading	60-0			0.554	(0.097)
AE-7	0.470	(0.185)	1.003	(0.395)	0.47	0.74	0.079	Static	0	14.78	(5.82)		
AE-8	0.490	(0.193)	1.407	(0.554)	0.35	0.77	0.107	Static	0	14.91	(5.87)		
								Loading	0-30			0.571	(0.100)
								Static	30	15.06	(5.93)		
								Unloading	30-0			0.577	(0.101)
								Loading	0-60			0.577	(0.101)
								Static	60	15.06	(5.93)		
								Unloading	60-0			0.588	(0.103)
AE-9	0.462	(0.182)	2.578	(1.015)	0.18	0.73	0.143	Static	0	14.17	(5.58)		
								Loading	0-30			0.765	(0.134)
								Static	30	13.79	(5.43)		
								Unloading	30-0			0.771	(0.135)
								Loading	0-60			0.771	(0.136)
								Static	60	13.74	(5.41)		
								Unloading	60-0			0.779	(0.140)
AF-1	0.272	(0.107)	0.635	(0.250)	0.43	0.43	0.50	Static	0	7.42	(2.92)		
								Loading	0-30			0.228	(0.040)
								Static	30	7.87	(3.10)		
								Unloading	30-0			0.228	(0.040)
								Static	0	6.65	(2.62)		
								Loading	0-60			0.228	(0.040)
								Static	60	7.47	(2.94)		
								Unloading	60-0			0.234	(0.041)
								Static	0	7.14	(2.81)		
AF-2	0.269	(0.106)	0.762	(0.300)	0.35	0.42	0.059	Static	0	7.87	(3.10)		
								Loading	0-30			0.211	(0.037)
								Static	30	9.45	(3.72)		
								Unloading	30-0			0.217	(0.038)
								Static	0	7.65	(3.01)		
								Loading	0-60			0.206	(0.036)
								Static	60	9.40	(3.70)		
								Unloading	60-0			0.211	(0.037)
								Static	0	9.19	(3.62)		
AF-3	0.442	(0.174)	1.341	(0.528)	0.33	0.70	0.100	Static	0	14.17	(5.58)		
								Loading	0-30			0.457	(0.080)
								Static	30	15.27	(6.01)		
								Unloading	30-0			0.463	(0.081)
								Static	0	13.77	(5.42)		
								Loading	0-60			0.463	(0.081)
								Static	60	15.67	(6.17)		
								Unloading	60-0			0.480	(0.084)
								Static	0	15.52	(6.11)		

* AE = electrodischarge-machined defect.
AF = fatigue-sharpened defect.

TABLE X. - Concluded.

Specimen no.*	Flaw geometry							Test condition	Stress level,	Ultrasonic scan width,		Compliance,	
	Depth, a,		Width, 2C,		a/2C	a/t	a/Q					nm/N	(μin./lb)
	cm	(in.)	cm	(in.)					% σ_{ys}	cm	(in.)		
AF-4	0.386	(0.152)	0.881	(0.347)	0.44	0.61	0.069	Static	0	10.57	(4.16)		
								Loading	0-30			0.354	(0.062)
								Static	30	12.60	(4.96)		
								Unloading	30-0			0.354	(0.062)
								Static	0	10.74	(4.23)		
								Loading	0-60			0.348	(0.061)
								Static	60	12.93	(5.09)		
								Unloading	60-0			0.365	(0.064)
								Static	0	12.37	(4.87)		
AF-5	0.460	(0.181)	1.214	(0.478)	0.38	0.72	0.094	Static	0	12.62	(4.97)		
								Loading	0-30			0.480	(0.084)
								Static	30	14.15	(5.57)		
								Unloading	30-0			0.480	(0.084)
								Static	0	12.19	(4.80)		
								Loading	0-60			0.480	(0.084)
								Static	60	14.17	(5.58)		
								Unloading	60-0			0.502	(0.088)
								Static	0	14.02	(5.52)		
AF-6	0.419	(0.165)	1.849	(0.728)	0.23	0.66	0.117	Static	0	12.32	(4.85)		
								Loading	0-30			0.600	(0.105)
								Static	30	13.49	(5.31)		
								Unloading	30-0			0.611	(0.107)
								Static	0	11.96	(4.71)		
								Loading	0-60			0.611	(0.107)
								Static	60	13.77	(5.42)		
								Unloading	60-0			0.600	(0.105)
								Static	0	12.95	(5.10)		
AF-7	0.523	(0.206)	1.095	(0.431)	0.48	0.82	0.087	Static	0	15.32	(6.03)		
								Loading	0-30			0.463	(0.081)
								Static	30	16.46	(6.48)		
								Unloading	30-0			0.463	(0.081)
								Static	0	14.78	(5.82)		
								Loading	0-60			0.463	(0.081)
								Static	60	16.33	(6.43)		
								Unloading	60-0			0.474	(0.083)
								Static	0	16.03	(6.31)		
AF-8	0.538	(0.212)	1.438	(0.566)	0.37	0.85	0.117	Static	0	14.86	(5.85)		
								Loading	0-30			0.531	(0.093)
								Static	30	15.95	(6.28)		
								Unloading	30-0			0.531	(0.093)
								Static	0	14.73	(5.80)		
								Loading	0-60			0.565	(0.099)
								Static	60	16.31	(6.42)		
								Unloading	60-0			0.571	(0.100)
								Static	0	15.54	(6.12)		
AF-9	0.635	(0.250)	2.614	(1.029)	0.24	1.0	0.174	Static	0	18.34	(7.22)		
								Loading	0-30			1.176	(0.206)
								Static	30	18.34	(7.22)		
								Unloading	30-0			1.205	(0.211)
								Static	0				
								Loading	0-60			1.199	(0.210)
								Static	60	19.56	(7.70)		
								Unloading	60-0			1.199	(0.210)
								Static	0	18.85	(7.42)		

* AE - electrodischarge-machines specimens.

AF = fatigue-sharpened defect.

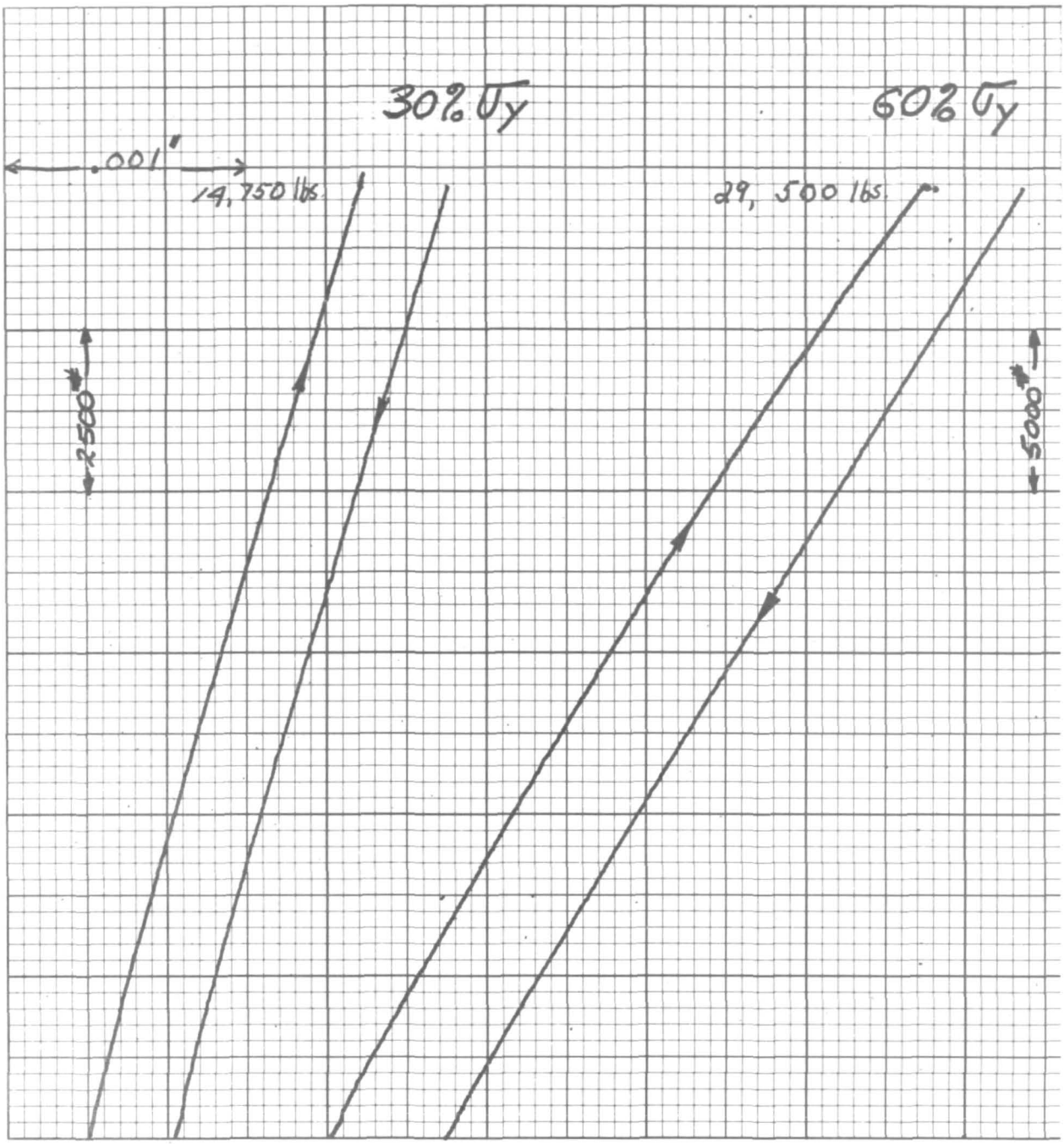

Figure 24. - Typical crack-opening displacement curves.

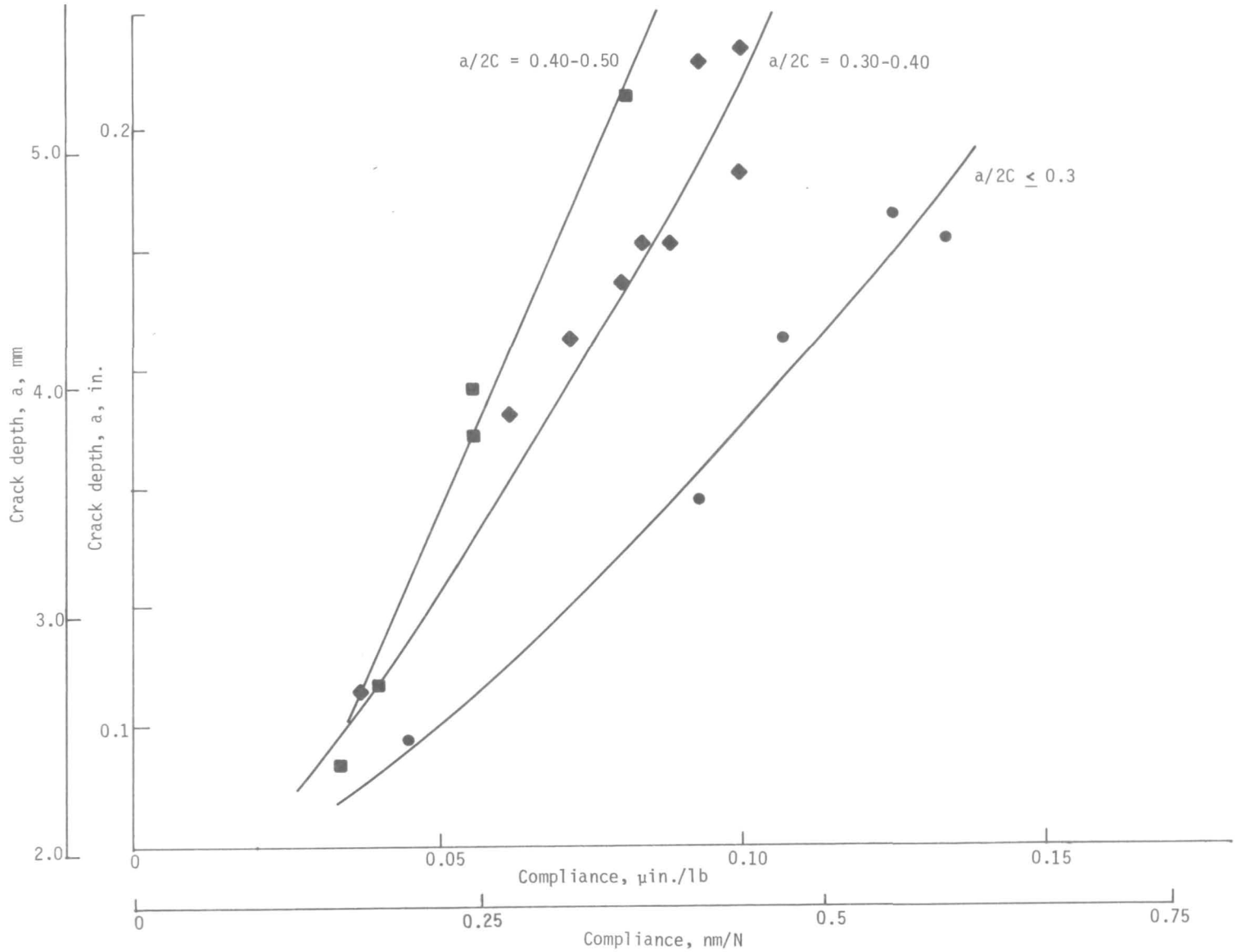

Figure 25. - Compliance calibration curve for 2219-T87 aluminum.

The relationship between scan width and crack depth can be established as previously shown in figure 23 if the refracted shear angle in the material is known.

Although the ultrasonic apparatus had a scale to permit reading the incident angle, the accuracy of such reading was no better than ±1°. For the incident angle setting of 25° in water, the refracted shear angle should be 61.6°. A calibration curve was prepared by plotting the measured flaw depth (a) versus the average of the scan widths obtained at 30 and 60% of yield strength for each fatigued specimen evaluated and for the unstressed electrodischarged-machined defects. As shown in figure 26, a different line can be drawn for each of the three groups of specimens. Each exhibits the same slope, but different intercepts. The reason for this behavior was not clear, but the scans were performed at different times and by different operators. Agreement was very good between the calculated refracted angle (62°) corresponding to the incident-angle adjustment and that obtained from the calibration curves (arc tan 0.51 = 63°).

A series of specimens was evaluated by loading to high percentages of the yield strength. The intent was to load to 30, 60, 90, and 100% of yield strength. However, the upper limit was adjusted to preclude failure or excessive subcritical growth. Table XI summarizes the data.

Eight of the nine specimens evaluated exhibited subcritical growth. As a result of selection of the initial defect and shape variations, growth behavior varying from a small amount of uniform growth to significant lateral growth or "tunneling" behavior was obtained. Table XI shows the geometry of the initial and final flaw as well as ultrasonic and crack-open displacement parameters.

In all cases, we found displacement due to plasticity. As shown by the schematic diagram (fig. 27), total displacement measured by the extensometer can be considered as the sum of the displacement associated with the existence of the initial defect, displacement caused by crack extension, and displacement caused by plastic deformation. Analysis of crack-opening displacement curves obtained at higher percentages of the yield strength (more than 82%) revealed an interesting relationship between plastic deformation and the onset of subcritical growth. For 2219-T87 aluminum alloy, a threshold plastic deformation of 0.02 to 0.025 mm (0.0008 to 0.001 in.) was required before subcritical growth was observed. The level at which subcritical growth began was estimated from crack-opening displacement curves using the scheme shown in figure 27.

Displacement measured at maximum load between the loading and unloading curves exceeding 178 nm (70 μin.) was considered to represent the beginning of subcritical growth. Figures 28 through 36 show actual crack-opening displacement curves.

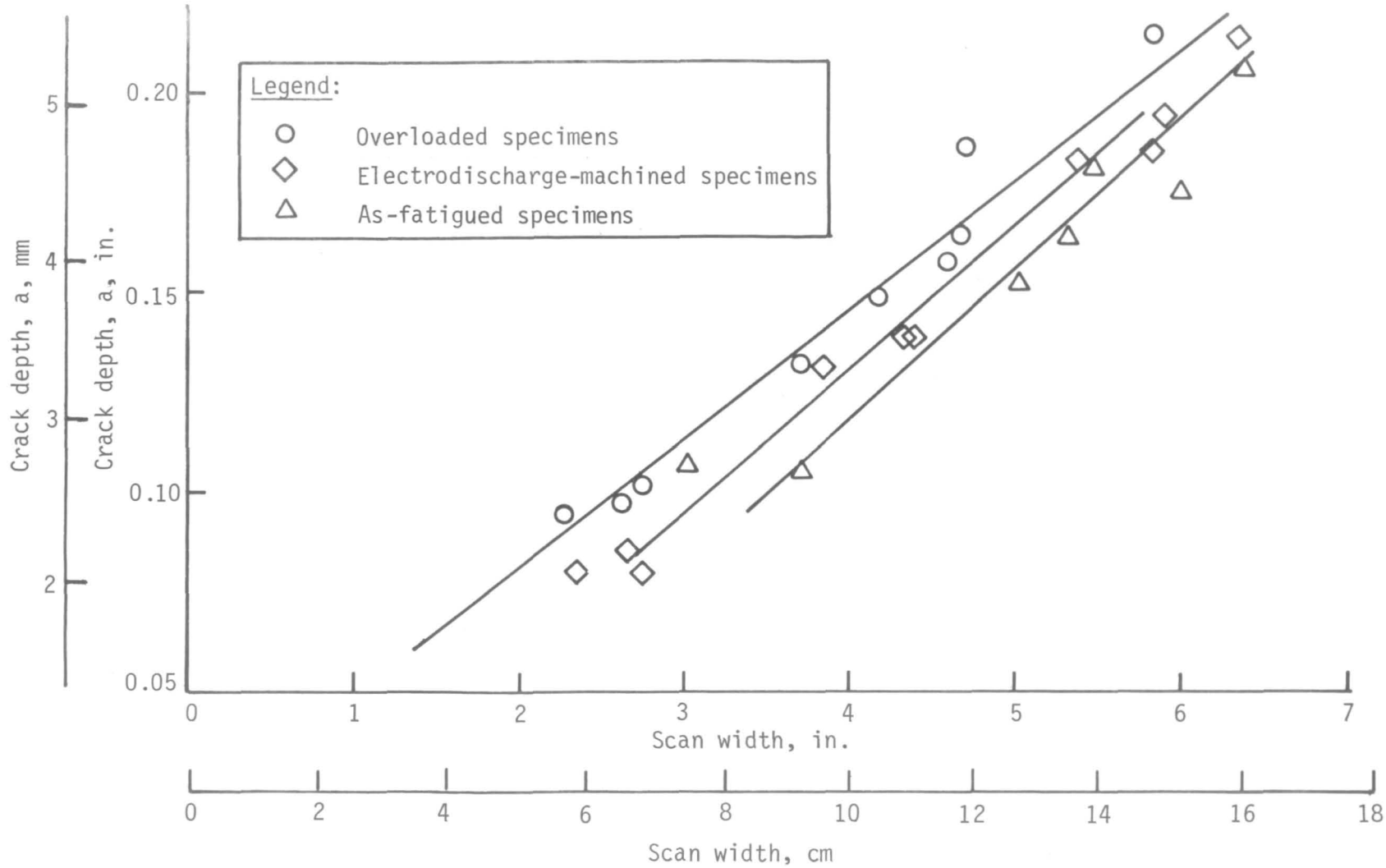

Figure 26. - Ultrasonic calibration curve for aluminum.

TABLE XI. - SUMMARIZED DATA FOR OVERLOADED ALUMINUM SPECIMENS

Specimen no.	Flaw geometry							Test condition	Stress level,	Ultrasonic scan width,		Compliance,	
	Depth, a,		Width, 2C,		a/2C	a/t	a/Q					nm/N	(μin./lb)
	cm	(in.)	cm	(in.)					% σ_{ys}	cm	(in.)		
AOL-1	0.249	(0.098)	1.026	(0.404)	0.24	0.39	0.068	Static	0	5.66	(2.23)		
								Loading	0-30			0.257	(0.045)
								Static	30	6.63	(2.61)		
								Unloading	30-0			0.257	(0.045)
								Loading	0-60			0.263	(0.046)
								Static	60	7.44	(2.93)		
								Unloading	60-0			0.251	(0.044)
								Loading	0-90			0.251	(0.044)
								Static	90	6.35	(2.50)		
								Unloading	90-0			0.263	(0.046)
								Loading	0-100			0.280	(0.049)
								Static	100	6.65	(2.62)		
								Unloading	100-0			0.286	(0.050)
	0.262	(0.103)	1.031	(0.406)	0.25	0.41	0.071	Static	0	6.81	(2.68)		
AOL-2	0.544	(0.214)	1.476	(0.581)	0.37	0.86	0.113	Static	0	12.57	(4.95)		
								Loading	0-30			0.577	(0.101)
								Static	30	15.06	(5.93)		
								Unloading	30-0			0.565	(0.099)
								Loading	0-60			0.594	(0.104)
								Static	60	14.83	(5.84)		
								Unloading	60-0			0.611	(0.107)
								Loading	0-90			0.588	(0.103)
								Static	90	15.75	(6.20)		
								Unloading	90-0			0.657	(0.115)
	0.569	(0.224)	1.476	(0.581)	0.39	0.90	0.114	Static	0	15.75	(6.20)		
AOL-3	0.472	(0.186)	1.991	(0.784)	0.24	0.74	0.129	Static	0	10.87	(4.28)		
								Loading	0-30			0.714	(0.125)
								Static	30	11.99	(4.72)		
								Unloading	30-0			0.714	(0.125)
								Loading	0-60			0.702	(0.123)
								Static	60	11.94	(4.70)		
								Unloading	60-0			0.708	(0.124)
								Loading	0-82			0.731	(0.128)
								Static	82	12.57	(4.95)		
								Unloading	82-0			0.771	(0.135)
	0.526	(0.207)	1.991	(0.784)	0.26	0.83	0.139	Static	0	12.45	(4.90)		
AOL-4	0.239	(0.094)	0.569	(0.224)	0.42	0.38	0.045	Static	0	4.37	(1.72)		
								Loading	0-30				
								Static	30	5.79	(2.28)		
								Unloading	30-0				
								Loading	0-60			0.194	(0.034)
								Static	60	5.77	(2.27)		
								Unloading	60-0			0.194	(0.034)
								Loading	0-90			0.188	(0.033)
								Static	90	5.64	(2.22)		
								Unloading	90-0			0.188	(0.033)
								Loading	0-100			0.188	(0.033)
								Static	100	5.66	(2.23)		
								Unloading	100-0			0.194	(0.034)
	0.249	(0.098)	0.569	(0.224)	0.44	0.39	0.045	Static	0	5.87	(2.31)		

TABLE XI. - Continued.

Specimen no.	Flaw geometry							Test condition	Stress level,	Ultrasonic scan width,		Compliance,	
	Depth, a,		Width, 2C,		a/2C	a/t	a/Q					nm/N	(μin./lb)
	cm	(in.)	cm	(in.)					% σ_{ys}	cm	(in.)		
AOL-5	0.378	(0.149)	0.841	(0.331)	0.45	0.60	0.067	Static	0	9.22	(3.63)		
								Loading	0-30			0.320	(0.056)
								Static	30	10.41	(4.10)		
								Unloading	30-0			0.320	(0.056)
								Loading	0-60			0.320	(0.056)
								Static	60	10.29	(4.05)		
								Unloading	60-0			0.308	(0.054)
								Loading	0-90			0.320	(0.056)
								Static	90	10.16	(4.00)		
								Unloading	90-0			0.325	(0.057)
								Loading	0-98.5			0.325	(0.057)
								Static	98.5	10.24	(4.03)		
								Unloading	98.5-0			0.325	(0.057)
	0.386	(0.152)	0.841	(0.331)	0.46	0.61	0.067	Static	0	10.87	(4.28)		
AOL-6	0.419	(0.165)	1.184	(0.466)	0.35	0.66	0.091	Static	0	11.02	(4.34)		
								Loading	0-30			0.411	(0.072)
								Static	30	11.94	(4.70)		
								Unloading	30-0			0.428	(0.075)
								Loading	0-60			0.428	(0.075)
								Static	60	11.76	(4.63)		
								Unloading	60-0			0.417	(0.073)
								Loading	0-90			0.411	(0.072)
								Static	90	11.96	(4.71)		
								Unloading	90-0			0.417	(0.073)
								Loading	0-95.6			0.411	(0.072)
								Static	95.6	12.24	(4.82)		
								Unloading	95.6-0			0.451	(0.079)
	0.445	(0.175)	1.184	(0.466)	0.38	0.70	0.091	Static	0	12.40	(4.88)		
AOL-7	0.259	(0.102)	0.414	(0.163)	0.63	0.41	0.041	Static	0	4.70	(1.85)		
								Loading	0-30			0.154	(0.027)
								Static	30	6.93	(2.73)		
								Unloading	30-0			0.154	(0.027)
								Loading	0-60			0.154	(0.027)
								Static	60	6.99	(2.75)		
								Unloading	60-0			0.154	(0.027)
								Loading	0-90			0.154	(0.027)
								Static	90	6.91	(2.72)		
								Unloading	90-0			0.160	(0.028)
								Loading	0-100			0.160	(0.028)
								Static	100	6.83	(2.69)		
								Unloading	100-0			0.177	(0.031)
	0.259	(0.102)	0.414	(0.163)	0.63	0.41	0.041	Static	0	7.06	(2.78)		
AOL-8	0.335	(0.132)	0.622	(0.245)	0.54	0.53	0.053	Static	0	9.40	(3.70)		
								Loading	0-30			0.263	(0.046)
								Static	30	9.45	(3.72)		
								Unloading	30-0			0.263	(0.046)
								Loading	0-60			0.268	(0.047)
								Static	60	9.45	(3.72)		
								Unloading	60-0			0.268	(0.047)
								Loading	0-90			0.274	(0.048)
								Static	90	9.32	(3.67)		
								Unloading	90-0			0.274	(0.048)
								Loading	0-98.5			0.274	(0.048)
								Static	98.5	9.32	(3.67)		
								Unloading	98.5-0			0.274	(0.048)
	0.343	(0.135)	0.645	(0.254)	0.53	0.54	0.053	Static	0	9.19	(3.62)		

TABLE XI. - Concluded.

Specimen no.	Flaw geometry							Test condition	Stress level, % σ_{ys}	Ultrasonic scan width,		Compliance,	
	Depth, a,		Width, 2C,		a/2C	a/t	a/Q					nm/N	(μin./lb)
	cm	(in.)	cm	(in.)						cm	(in.)		
AOL-9	0.399	(0.157)	0.798	(0.314)	0.50	0.63	0.063	Static	0	10.72	(4.22)		
								Loading	0-30			0.320	(0.056)
								Static	30	11.68	(4.60)		
								Unloading	30-0			0.320	(0.056)
								Loading	0-60			0.320	(0.056)
								Static	60	11.66	(4.59)		
								Unloading	60-0			0.337	(0.059)
								Loading	0-90			0.331	(0.058)
								Static	90	11.73	(4.62)		
								Unloading	90-0			0.331	(0.058)
								Loading	0-98.3			0.331	(0.058)
								Static	98.3	12.12	(4.77)		
								Unloading	98.3-0			0.354	(0.062)
	0.409	(0.161)	0.798	(0.314)	0.51	0.64	0.063	Static	0	12.24	(4.82)		

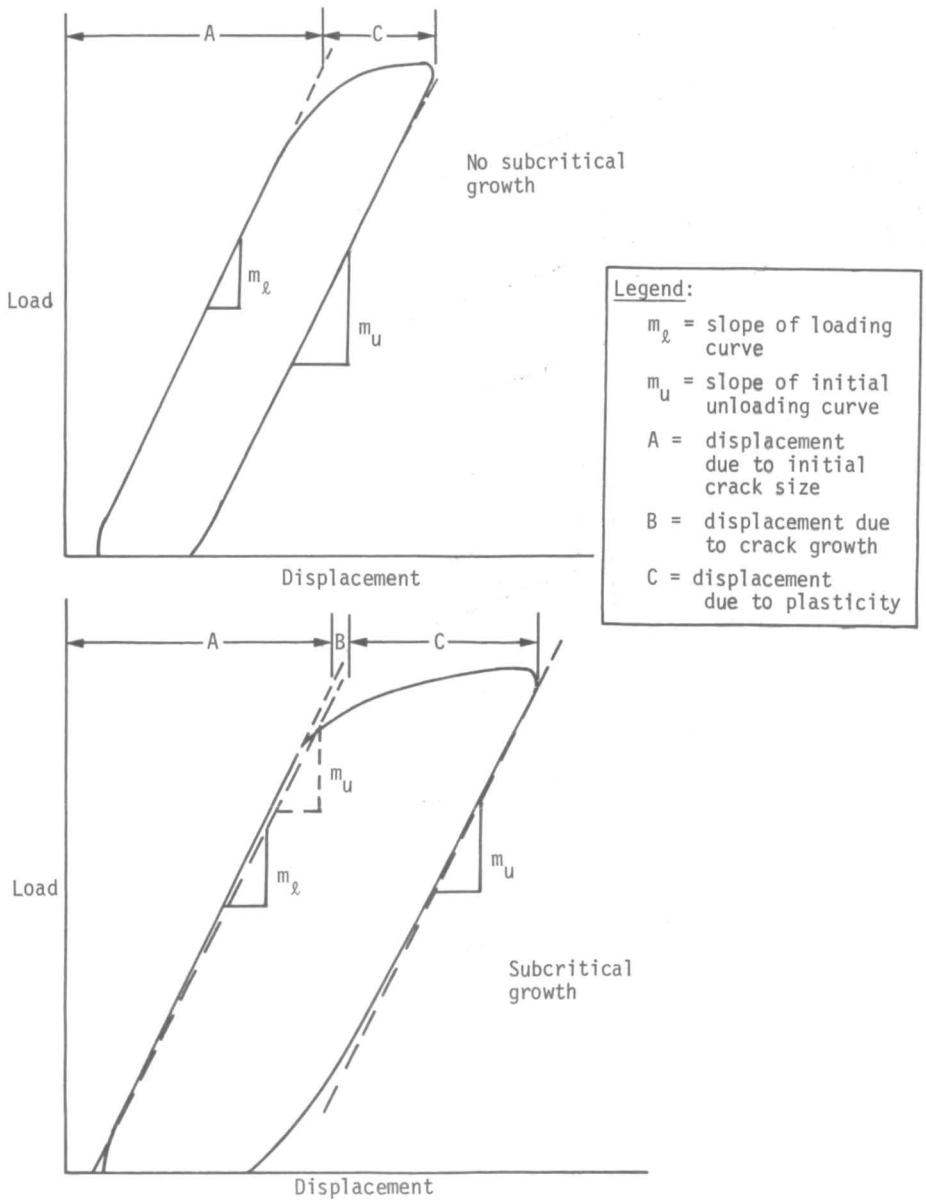

Figure 27. - Schematic of components contributing to crack-opening displacement.

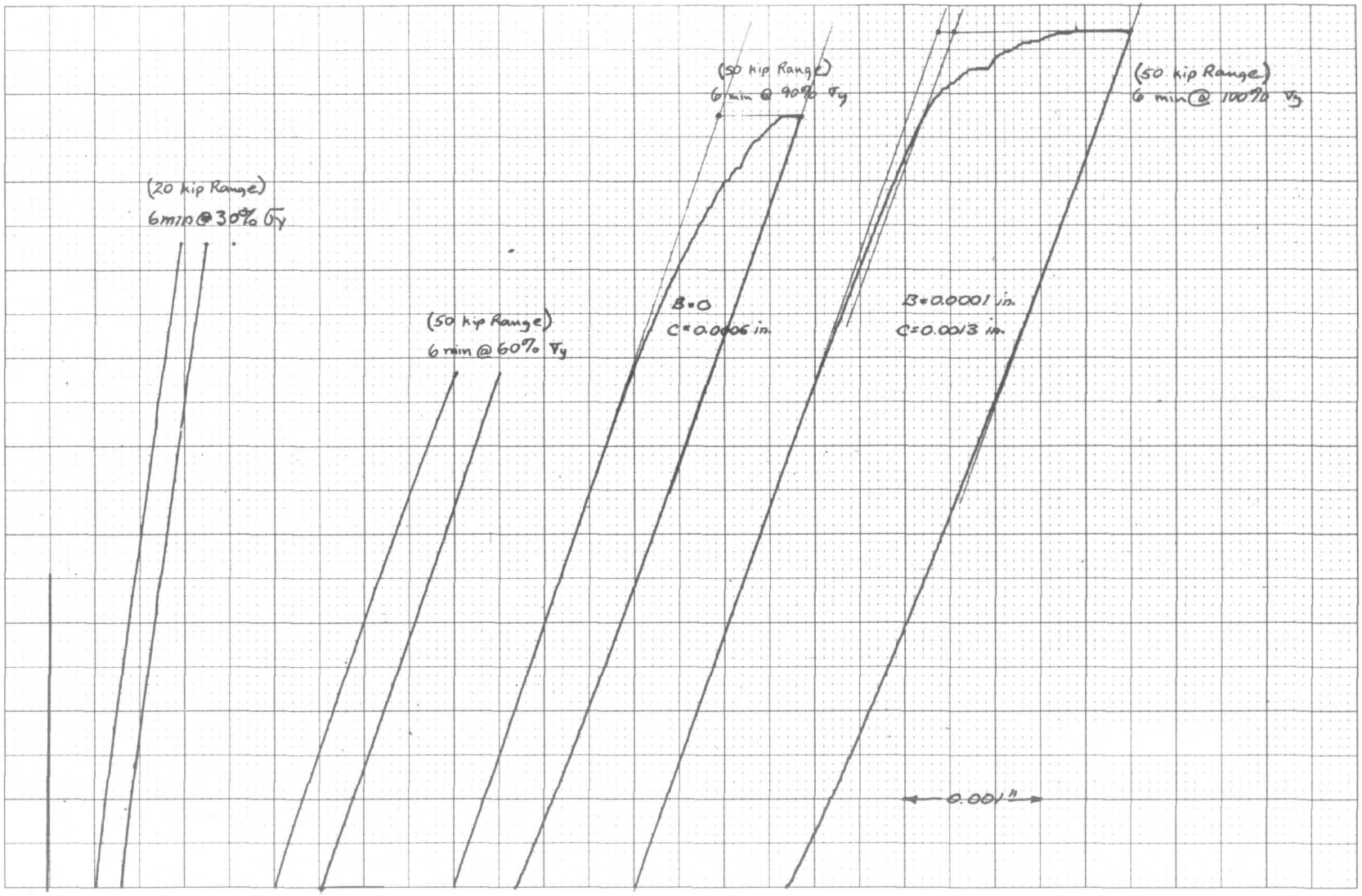

Figure 28. - Crack-opening displacement curves for aluminum-alloy specimen AOL-1.

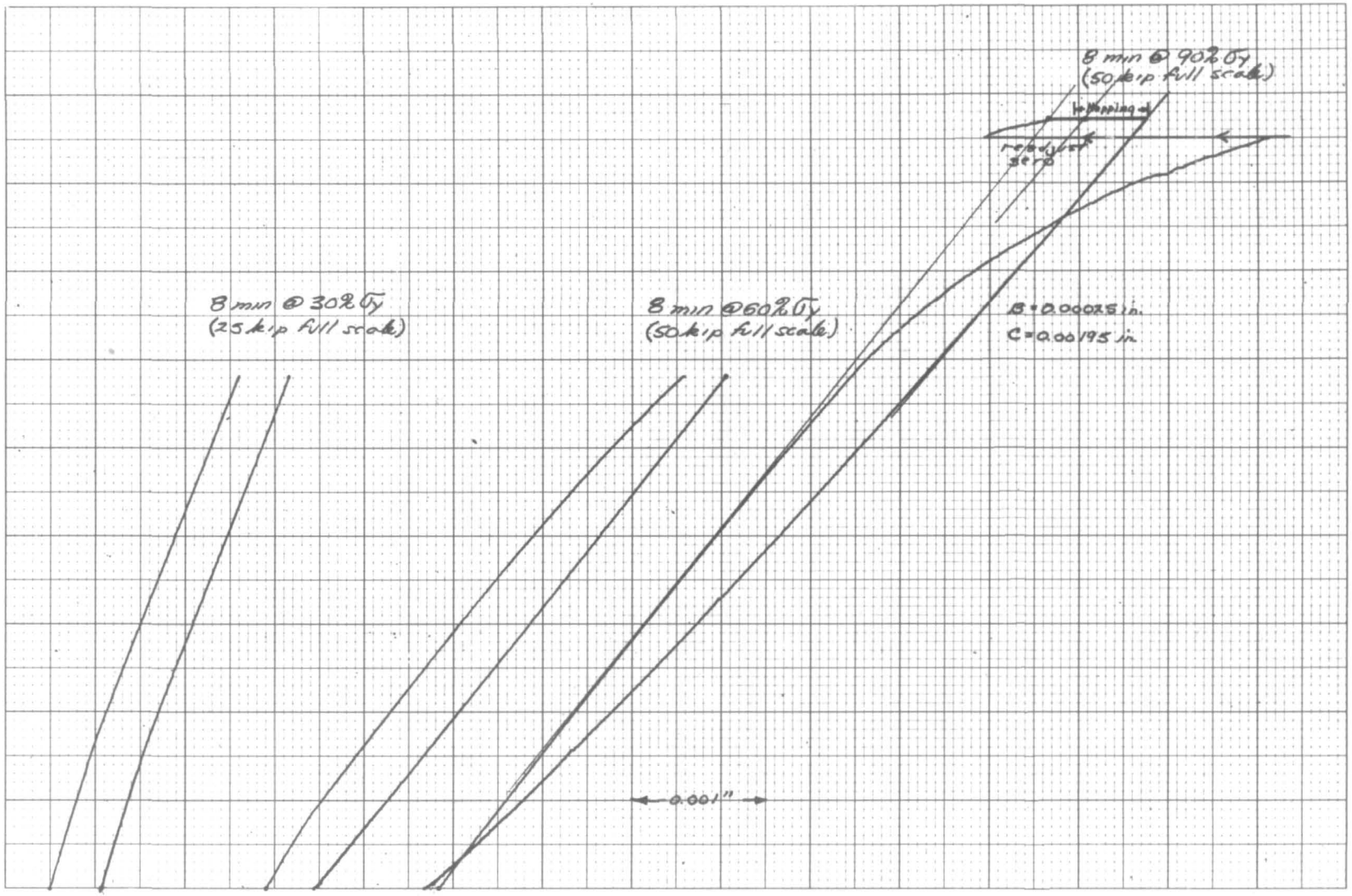

Figure 29. - Crack-opening displacement curves for aluminum-alloy specimen AOL-2.

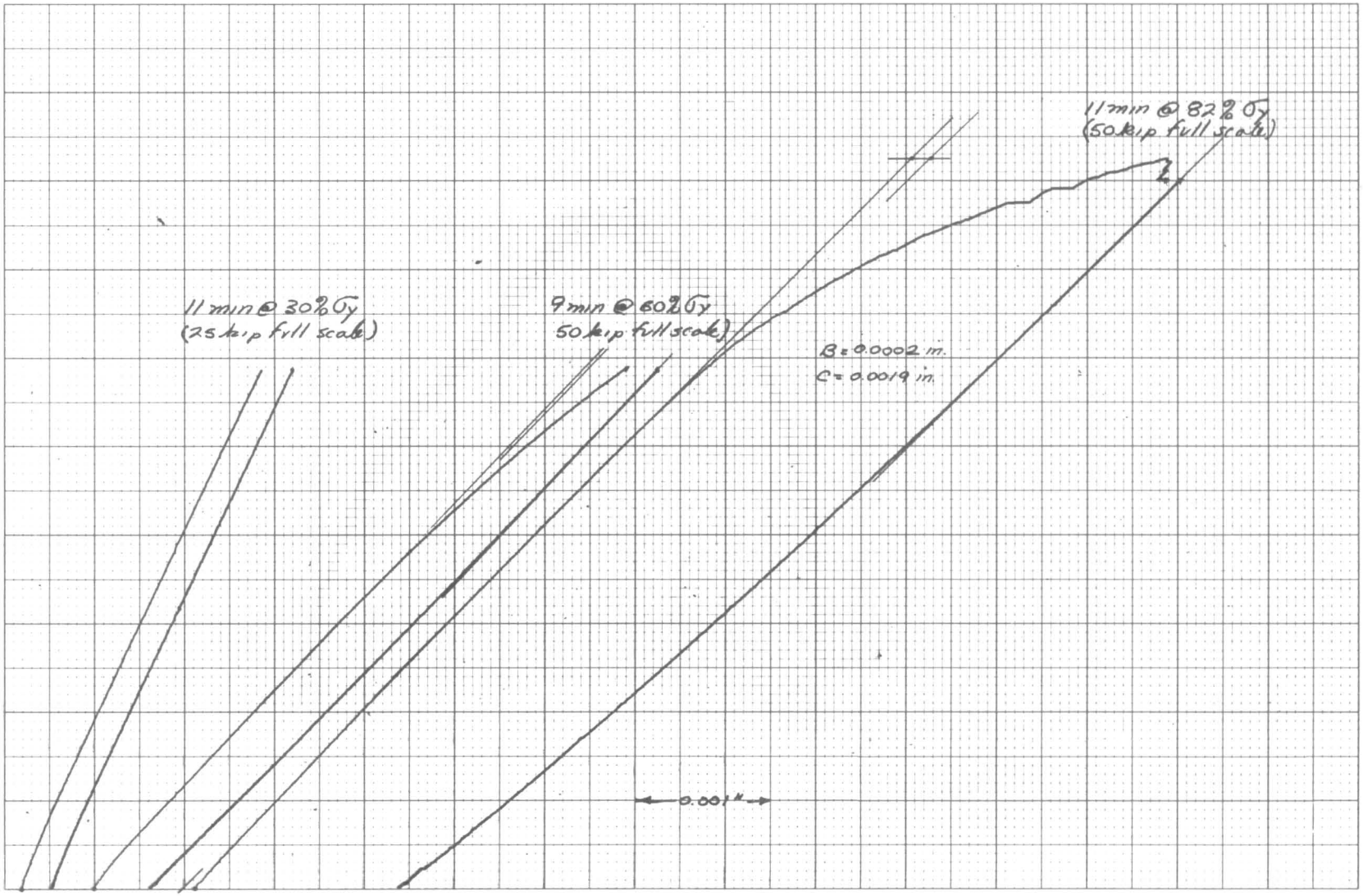

Figure 30. - Crack-opening displacement curves for aluminum-alloy specimen AOL-3.

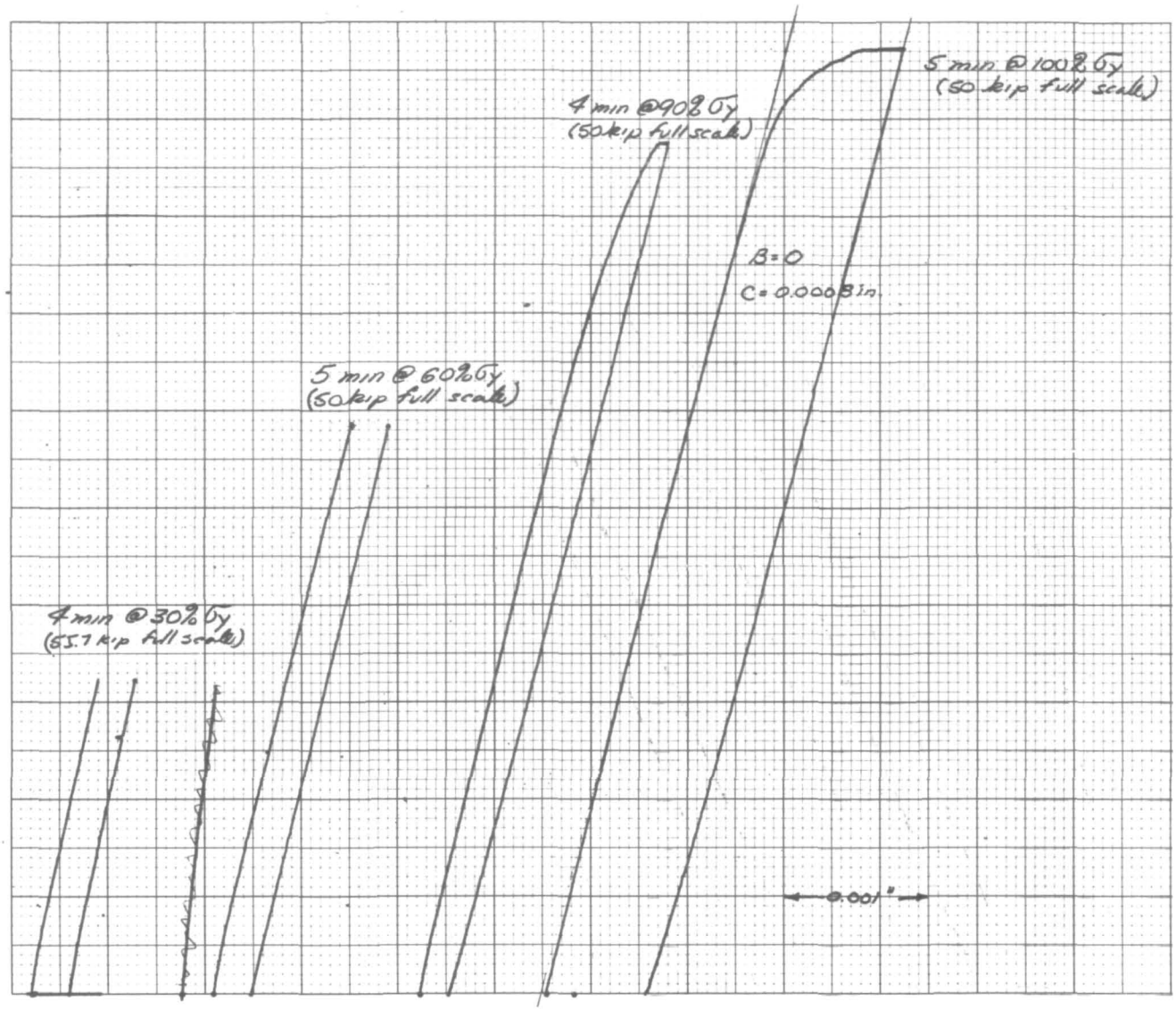

Figure 31. - Crack-opening displacement curves for aluminum-alloy specimen AOL-4.

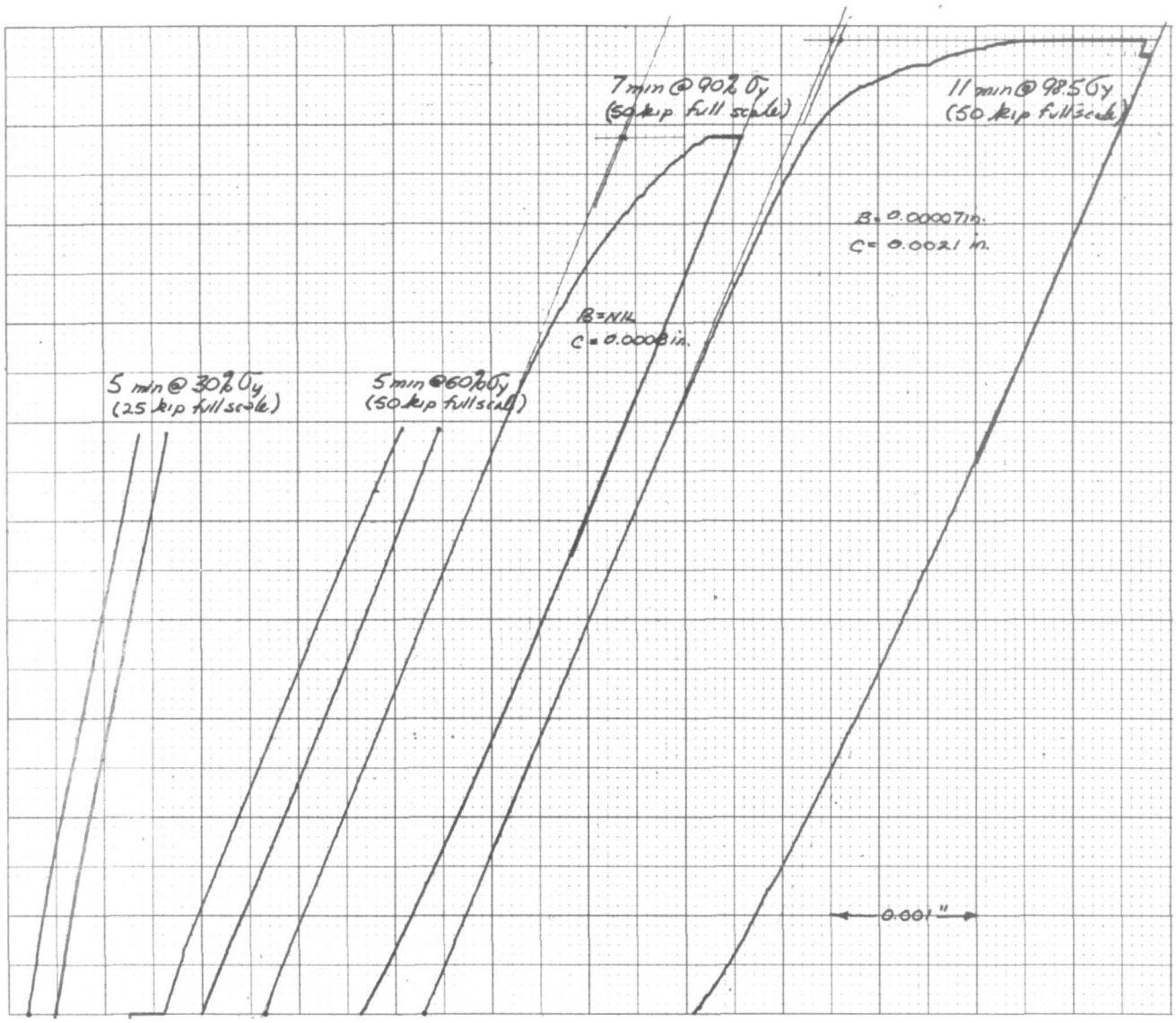

Figure 32. - Crack-opening displacement curves for aluminum-alloy specimen AOL-5.

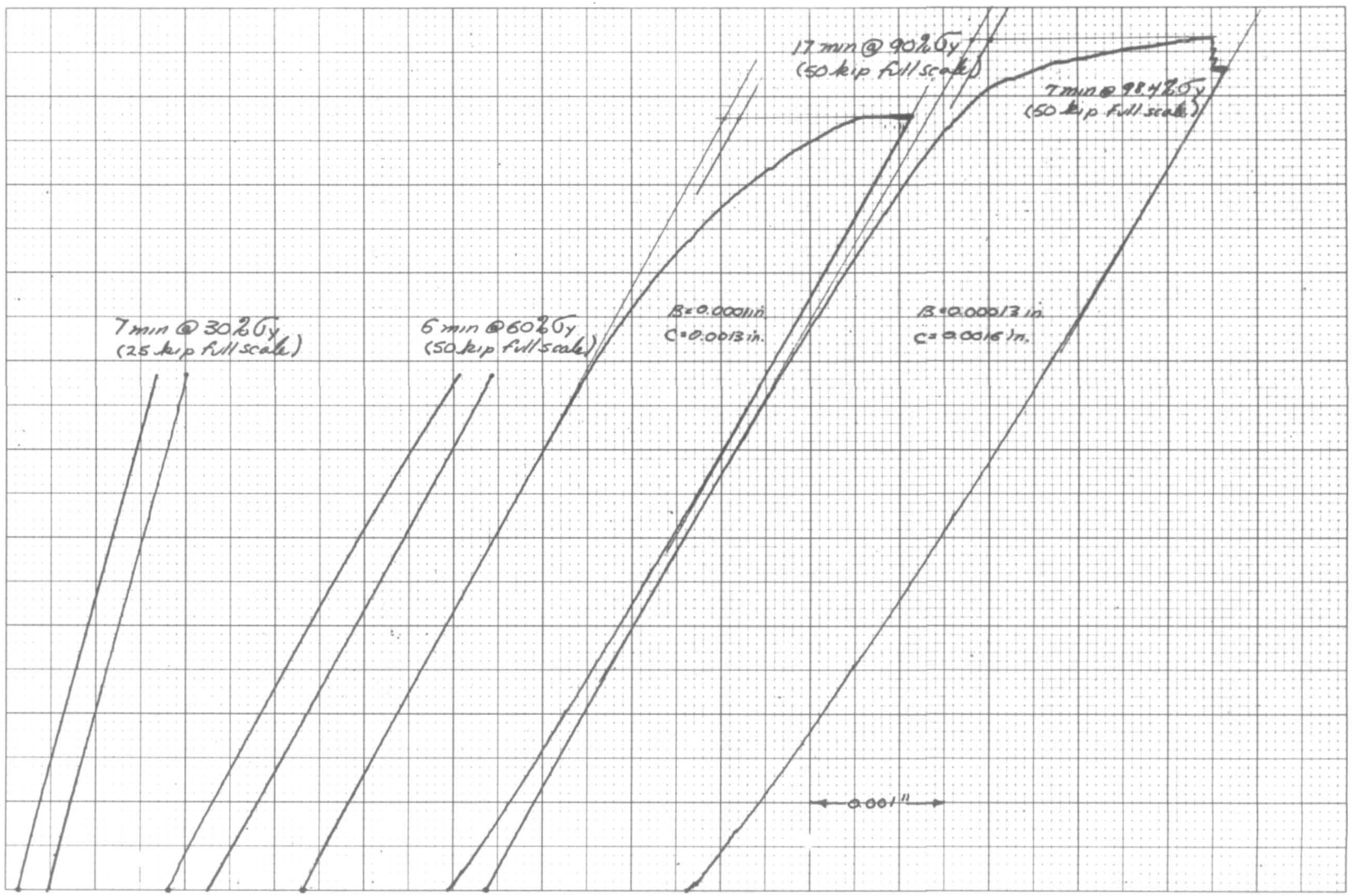

Figure 33. - Crack-opening displacement curves for aluminum-alloy specimen AOL-6.

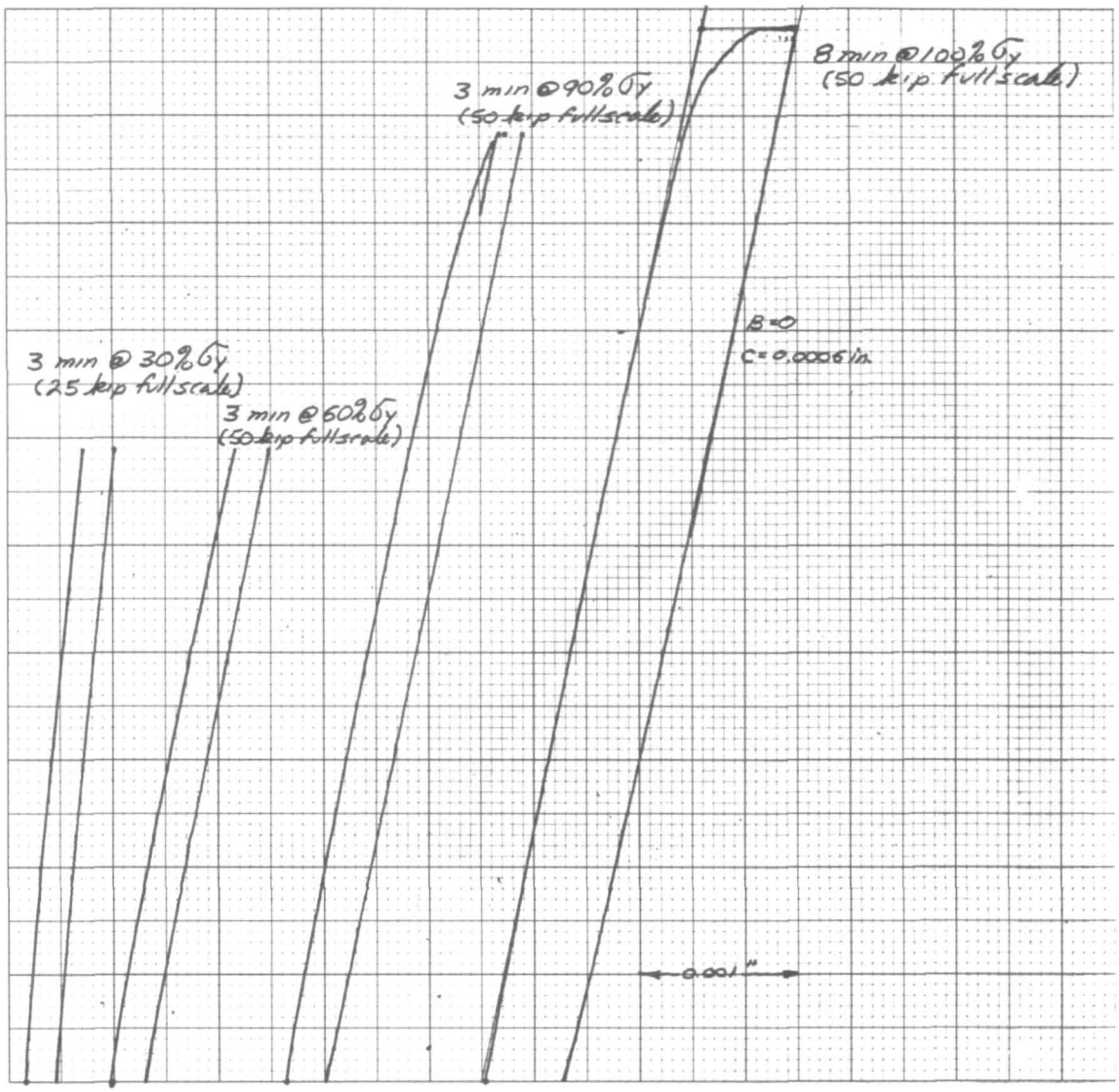

Figure 34. - Crack-opening displacement curves for aluminum-alloy specimen AOL-7.

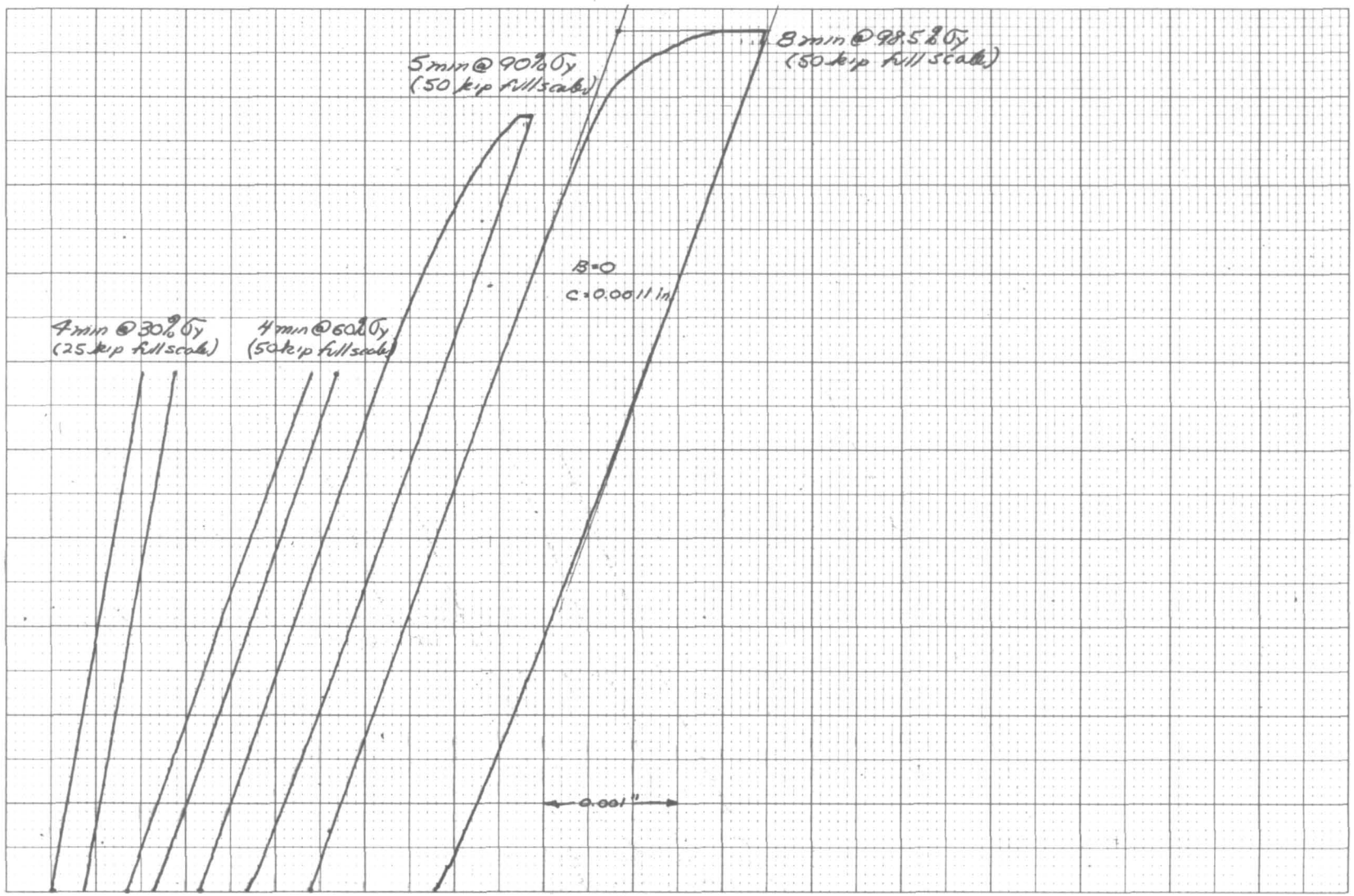

Figure 35. - Crack-opening displacement curves for aluminum-alloy specimen AOL-8.

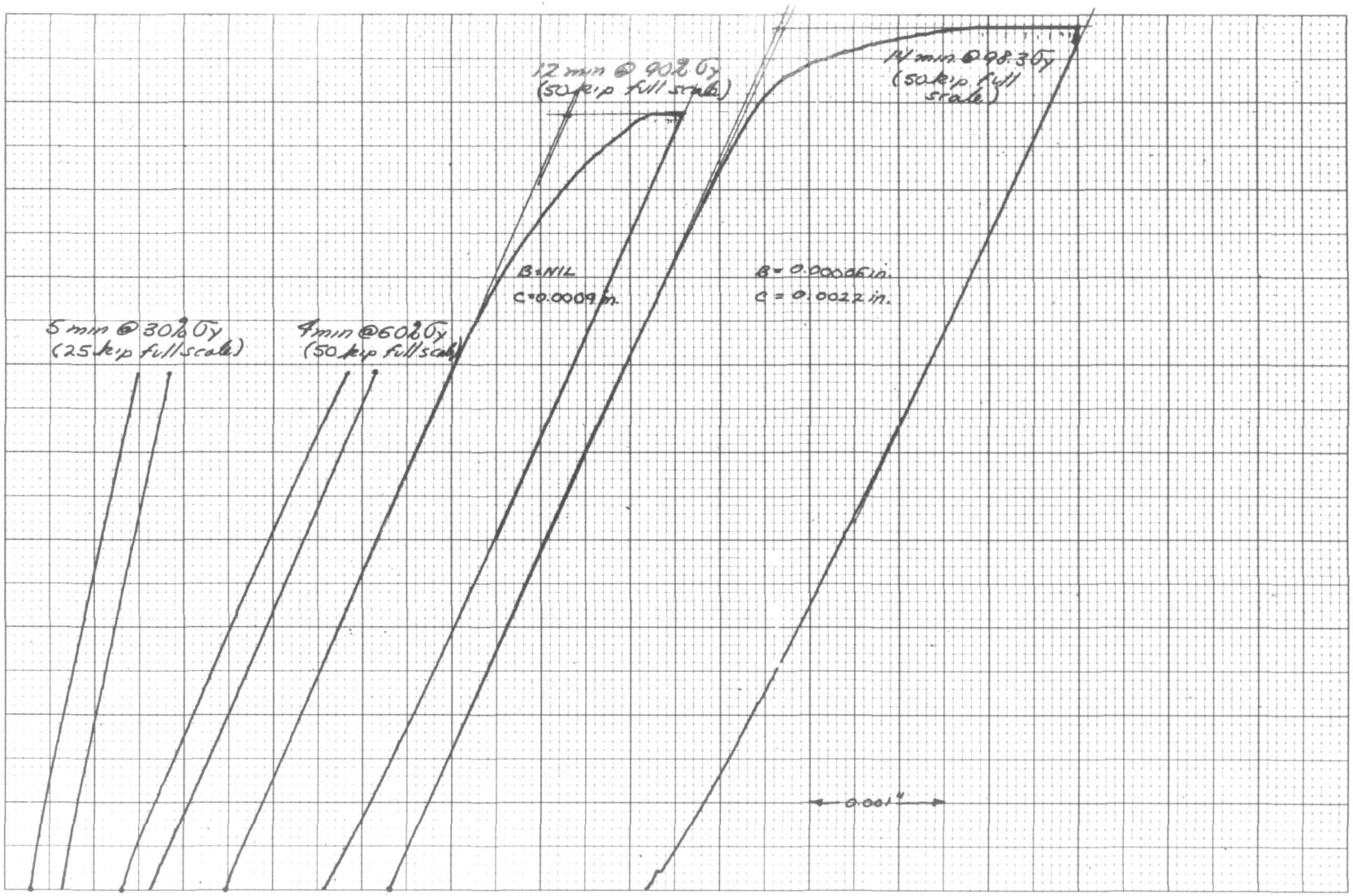

Figure 36. - Crack-opening displacement curves for aluminum-alloy specimen AOL-9.

Using these data, stress versus crack size was plotted to determine whether the subcritical growth threshold was well defined. As shown in figure 37, a well-defined boundary was obtained.

The ultrasonic system was found to be extremely sensitive to subtleties of crack behavior. The data records clearly show the effects of crack opening and closing. These data will be discussed in the next chapter. The ultrasonic method was particularly good at showing changes in flaw shape--particularly the tunneling growth commonly associated with proof testing of thin-gage materials.

Table XII compares flaw depth and crack growth data determined by the ultrasonic and crack-opening displacement techniques. The results show that both techniques give similar accuracy in measuring flaw depth. For the nine specimens evaluated, average measurement accuracy was within 4%. Both techniques demonstrated comparable accuracy in determining the change in crack depth (Δa). The principle difference between the two methods was the ability of the ultrasonic technique to map the entire flaw front and show areas of local growth, such as tunneling, whereas the crack opening displacement technique might fail to show local growth or average it into the value representing growth in the depth (a) direction.

Figures 38 through 42 are flaw maps drawn from the raw data for the five specimens that exhibited tunneling, and fractographs of the surface. As shown by the comparison of maximum growth in table XII, correspondence between the ultrasonic method and visual inspection is reasonably good.

Titanium Data

Table XIII summarizes test results for the ultrasonic calibration. These specimens contained electrodischarged machined flaws. A calibration curve of ultrasonic span width versus crack depth was prepared using these data points and those obtained from fatigue-sharpened defects after loading to 30 and 60% of yield strength. The resultant curve (fig. 43) gives an angle (66°) that agreed well with the shear angle (62.3°) resulting from the approximate incident-angle setting of 25°.

Crack-opening displacement compliance calibration curves were prepared from data obtained by loading to 30 and 60% of the yield strength. Although based on a limited number of data points, the compliance curves presented are relatively well defined (fig. 44).

Behavior similar to that exhibited by the aluminum alloy was found. Crack-opening displacement curves show plasticity, but show less evidence of subcritical growth than aluminum. Treatment of the data in a manner similar to that for aluminum showed a maximum deformation due to plasticity of 25.4 μm (0.001 in.).

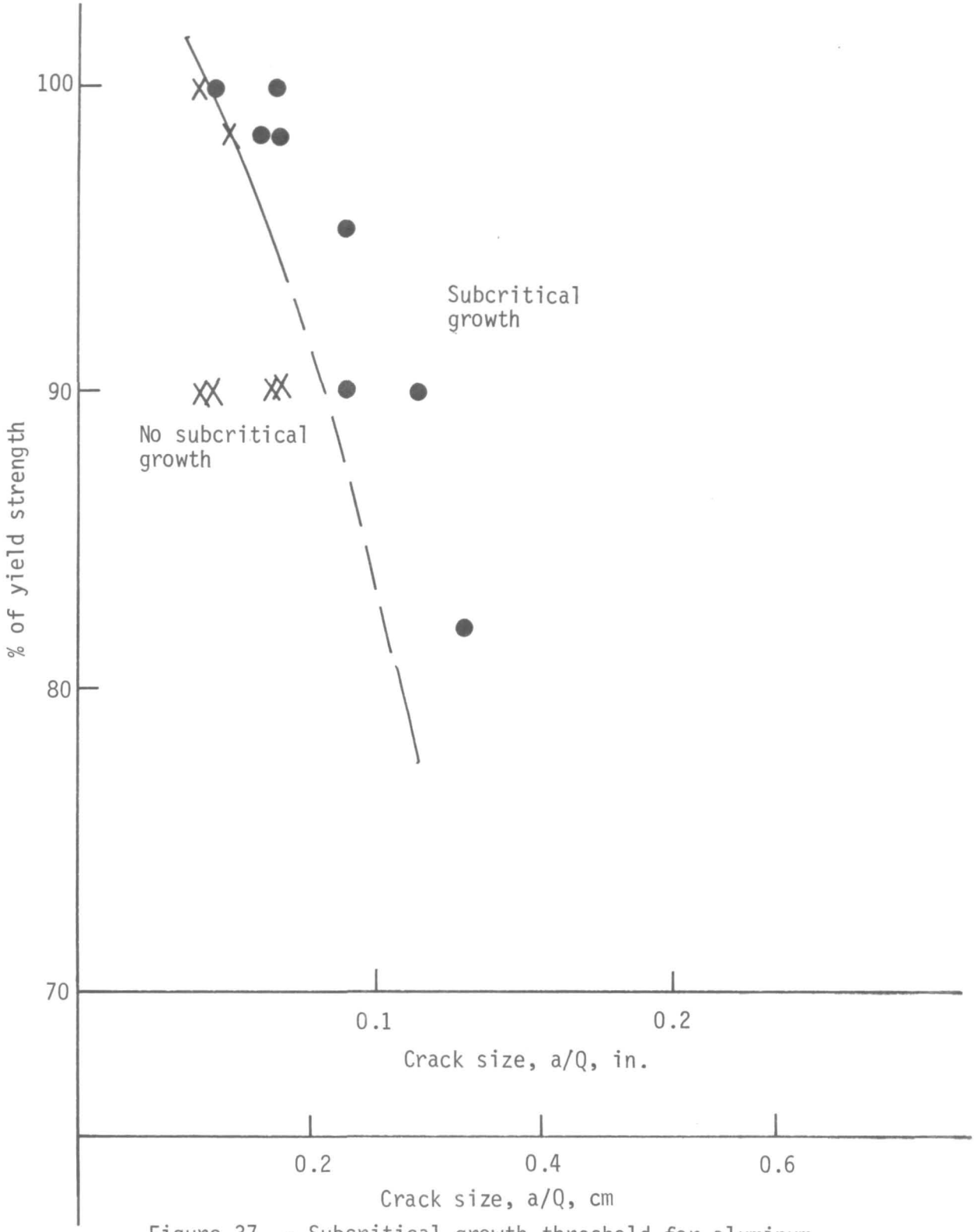

Figure 37. - Subcritical growth threshold for aluminum.

TABLE XII. - COMPARISON OF MEASUREMENT TECHNIQUES FOR ALUMINUM

Specimen no.	Condition	Flaw depth, a						Crack growth, Δa						Maximum growth, Δr				ϕ,* deg
		Visual		UT		COD		Visual		UT		COD		Visual		UT		
		mm	(in.)	mm	(in.)	mm	(in.)	mm	(in.)	mm	(in.)	mm	(in.)	mm	(in.)	mm	(in.)	
AOL-1	Initial	2.49	(0.098)	2.54	(0.100)	2.44	(0.092)	--	--	--	--	--	--	--	--	--	--	--
	Final	2.62	(0.103)	2.62	(0.103)	2.54	(0.100)	0.13	(0.005)	0.05	(0.002)	0.10	(0.004)	0.13	(0.005)	--	--	90
AOL-2	Initial	5.44	(0.214)	5.21	(0.205)	5.28	(0.208)	--	--	--	--	--	--	--	--	--	--	--
	Final	5.60	(0.224)	5.46	(0.215)	5.84	(0.230)	0.15	(0.010)	0.25	(0.010)	0.56	(0.022)	1.22	(0.048)	1.02	(0.040)	10
AOL-3	Initial	4.72	(0.186)	4.24	(0.167)	4.55	(0.179)	--	--	--	--	--	--	--	--	--	--	--
	Final	5.25	(0.207)	4.39	(0.173)	4.85	(0.191)	0.53	(0.021)	0.15	(0.006)	0.30	(0.012)	1.42	(0.056)	0.89	(0.035)	10
AOL-4	Initial	2.39	(0.094)	2.26	(0.089)	2.51	(0.099)	--	--	--	--	--	--	--	--	--	--	--
	Final	2.48	(0.098)	2.29	(0.090)	2.51	(0.099)	0.10	(0.004)	0.025	(0.001)	0	(0)	0.10	(0.004)	--	--	90
AOL-5	Initial	3.78	(0.149)	3.73	(0.147)	3.78	(0.149)	--	--	--	--	--	--	--	--	--	--	--
	Final	3.86	(0.152)	3.89	(0.153)	3.84	(0.151)	0.076	(0.003)	0.15	(0.006)	0.51	(0.012)	1.70	(0.067)	0.38	(0.015)	15
AOL-6	Initial	4.19	(0.165)	4.22	(0.166)	4.14	(0.163)	--	--	--	--	--	--	--	--	--	--	--
	Final	4.45	(0.175)	4.37	(0.172)	4.29	(0.169)	0.25	(0.010)	0.15	(0.006)	0.15	(0.006)	0.99	(0.039)	0.64	(0.025)	10
AOL-7	Initial	2.59	(0.102)	2.64	(0.104)	2.29	(0.080)	--	--	--	--	--	--	--	--	--	--	--
	Final	2.59	(0.102)	2.67	(0.105)	2.41	(0.095)	0	(0)	0.025	(0.001)	0.13	(0.005)	0	(0)	--	--	90
AOL-8	Initial	3.35	(0.132)	3.45	(0.136)	3.20	(0.126)	--	--	--	--	--	--	--	--	--	--	--
	Final	3.43	(0.135)	3.38	(0.133)	3.32	(0.131)	0.076	(0.003)	-0.076	(-0.003)	0.13	(0.005)	0.076	(0.003)	--	--	90
AOL-9	Initial	3.99	(0.157)	4.17	(0.164)	3.78	(0.149)	--	--	--	--	--	--	--	--	--	--	--
	Final	4.09	(0.161)	4.34	(0.171)	4.14	(0.163)	0.10	(0.004)	0.18	(0.007)	0.36	(0.014)	0.66	(0.026)	0.38	(0.015)	20

* ϕ = Angle measured from front surface at which maximum crack growth occurred.

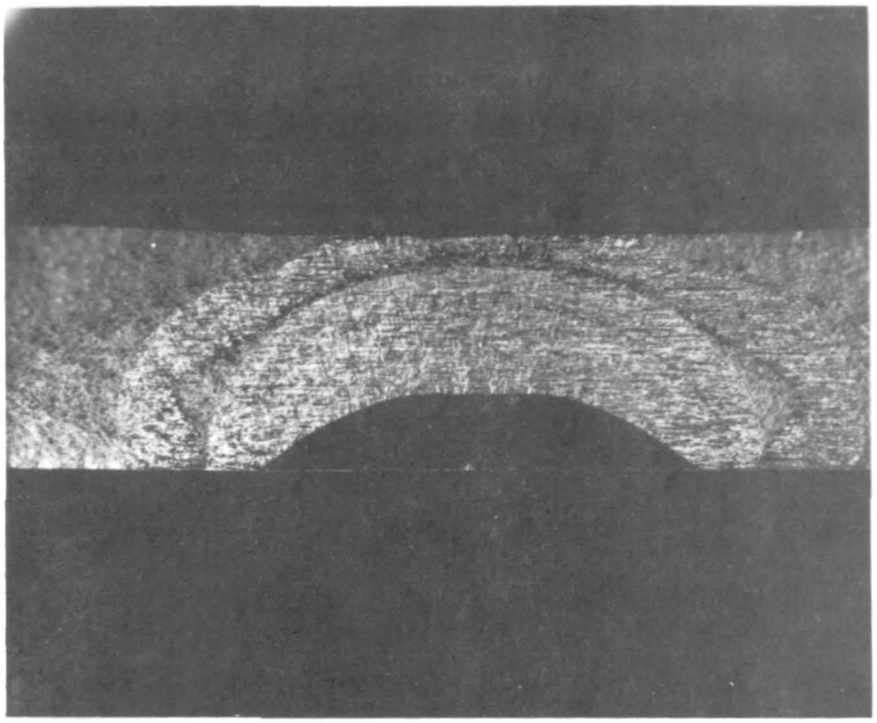

5X

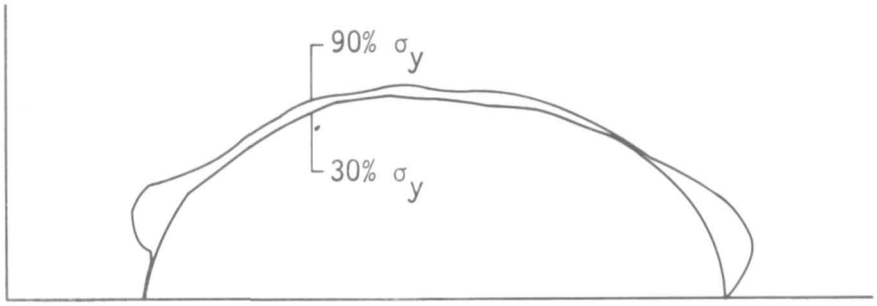

5X

Figure 38. - Fractograph and flaw map of specimen AOL-2.

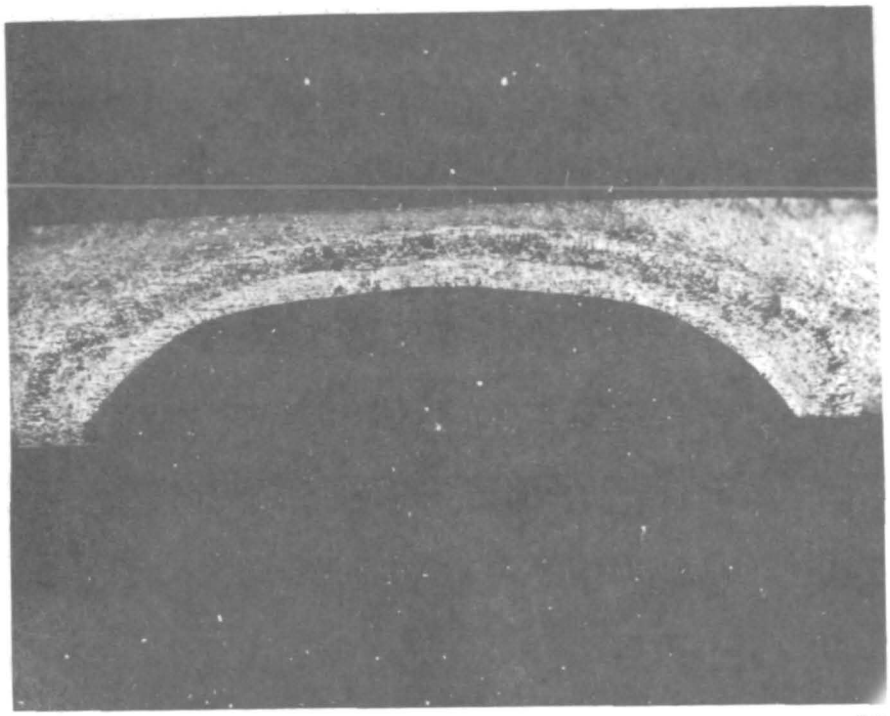

5X

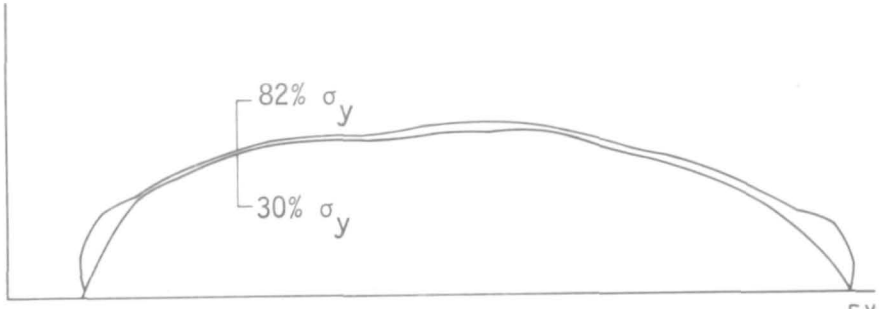

5X

Figure 39. - Fractograph and flaw map of specimen AOL-3.

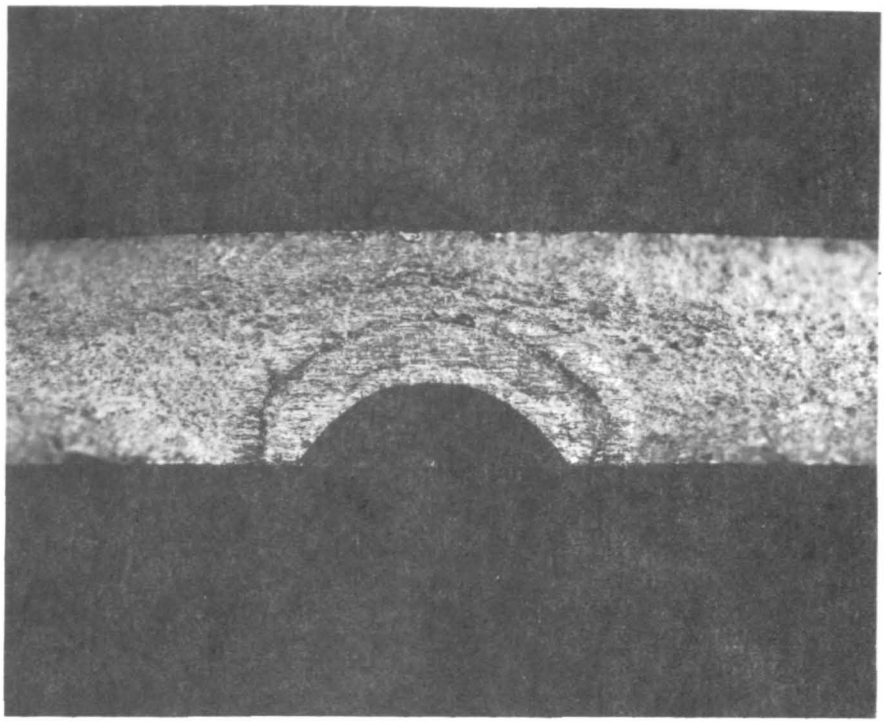

5X

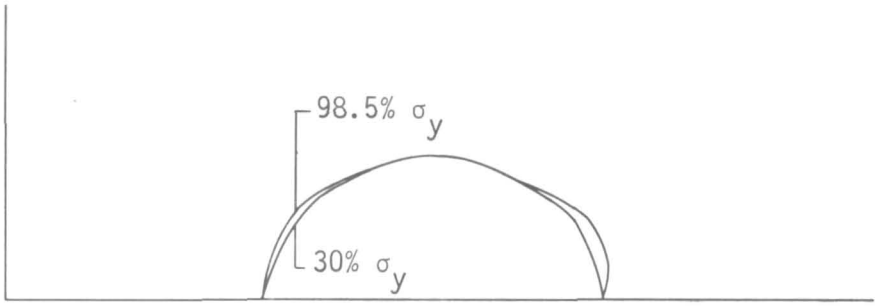

5X

Figure 40. - Fractograph and flaw map of specimen AOL-5.

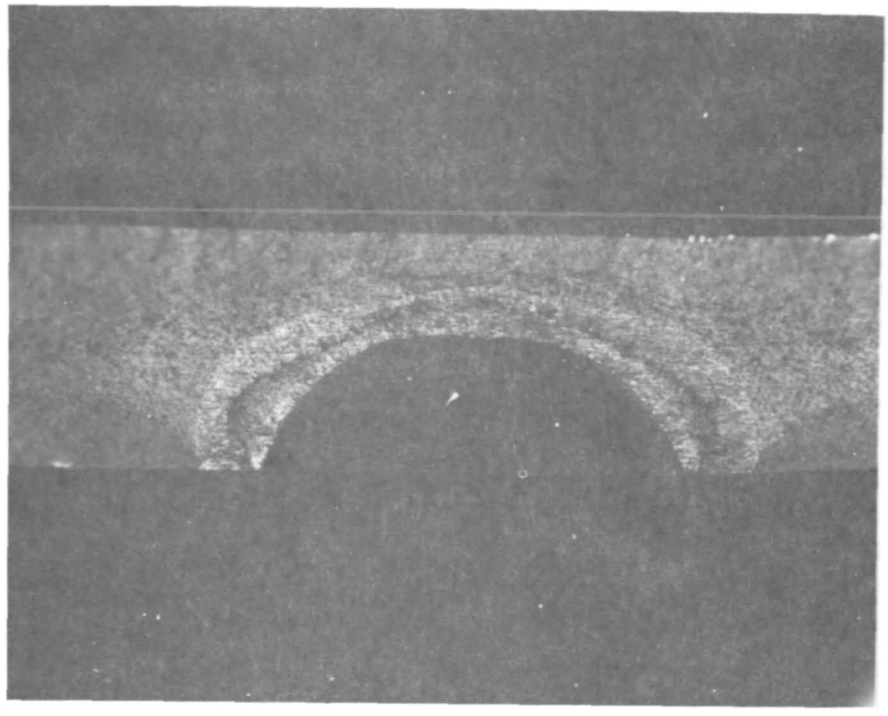

5X

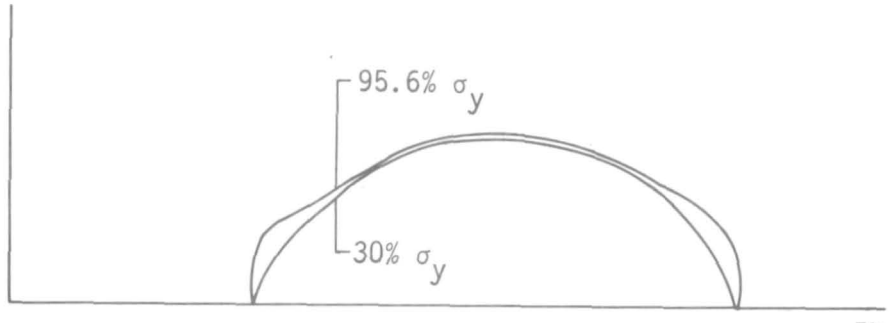

5X

Figure 41. - Fractograph and flaw map of specimen AOL-6.

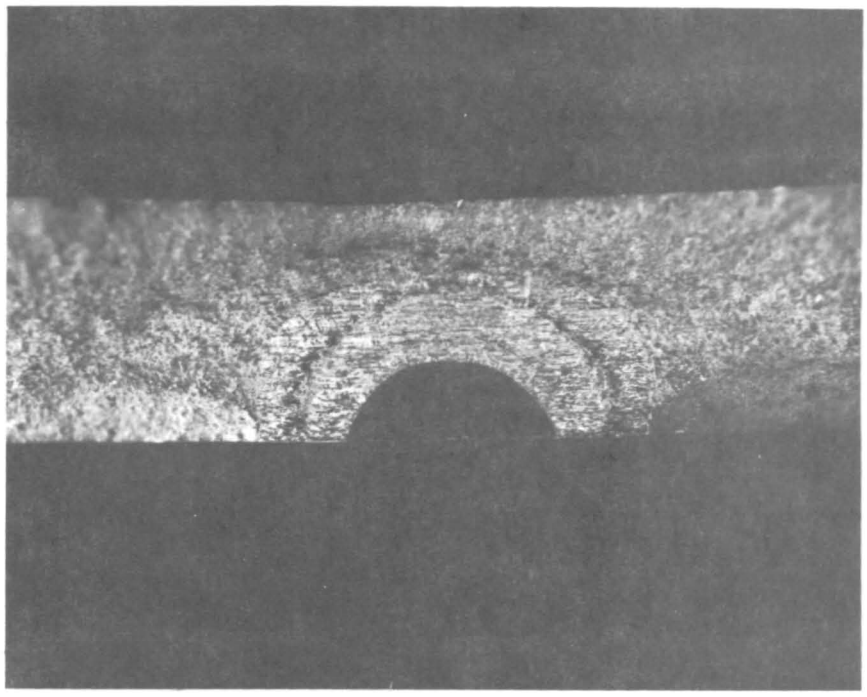

5X

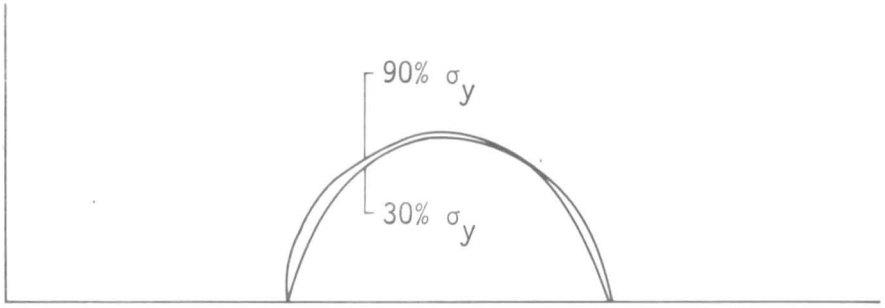

5X

Figure 42. - Fractograph and flaw map of specimen AOL-9.

TABLE XIII. - TITANIUM CALIBRATION DATA

Specimen no.*	Flaw geometry							Test condition	Stress level,	Ultrasonic scan width,	
	Depth, a,		Width, 2C,		a/2C	a/t	a/Q				
	cm	(in.)	cm	(in.)					% σ_{ys}	cm	(in.)
TE-1	0.089	(0.035)	0.384	(0.151)	0.23	0.28	0.025	Static	0	2.54	(1.00)
TE-2	0.066	(0.026)	0.630	(0.248)	0.10	0.21	0.024	Static	0	2.54	(1.00)
TE-3	0.107	(0.042)	0.874	(0.344)	0.12	0.33	0.037	Static	0	3.61	(1.42)
TE-4	0.076	(0.030)	0.196	(0.077)	0.39	0.24	0.015	Static	0	2.29	(0.90)
TE-5	0.114	(0.045)	0.297	(0.117)	0.38	0.35	0.023	Static	0	3.81	(1.50)
TE-6	0.155	(0.061)	0.447	(0.176)	0.35	0.48	0.034	Static	0	4.55	(1.79)
TE-7	0.074	(0.029)	0.112	(0.044)	0.66	0.23	0.012	Static	0	3.00	(1.18)
TE-8	0.109	(0.043)	0.201	(0.079)	0.54	0.34	0.018	Static	0	3.30	(1.30)
TE-9	0.142	(0.056)	0.216	(0.085)	0.66	0.43	0.024	Static	0	3.89	(1.53)
TE-10	0.130	(0.051)	0.193	(0.076)	0.67	0.40	0.022	Static	0	3.94	(1.55)

* TE = electrodischarge machined defect.

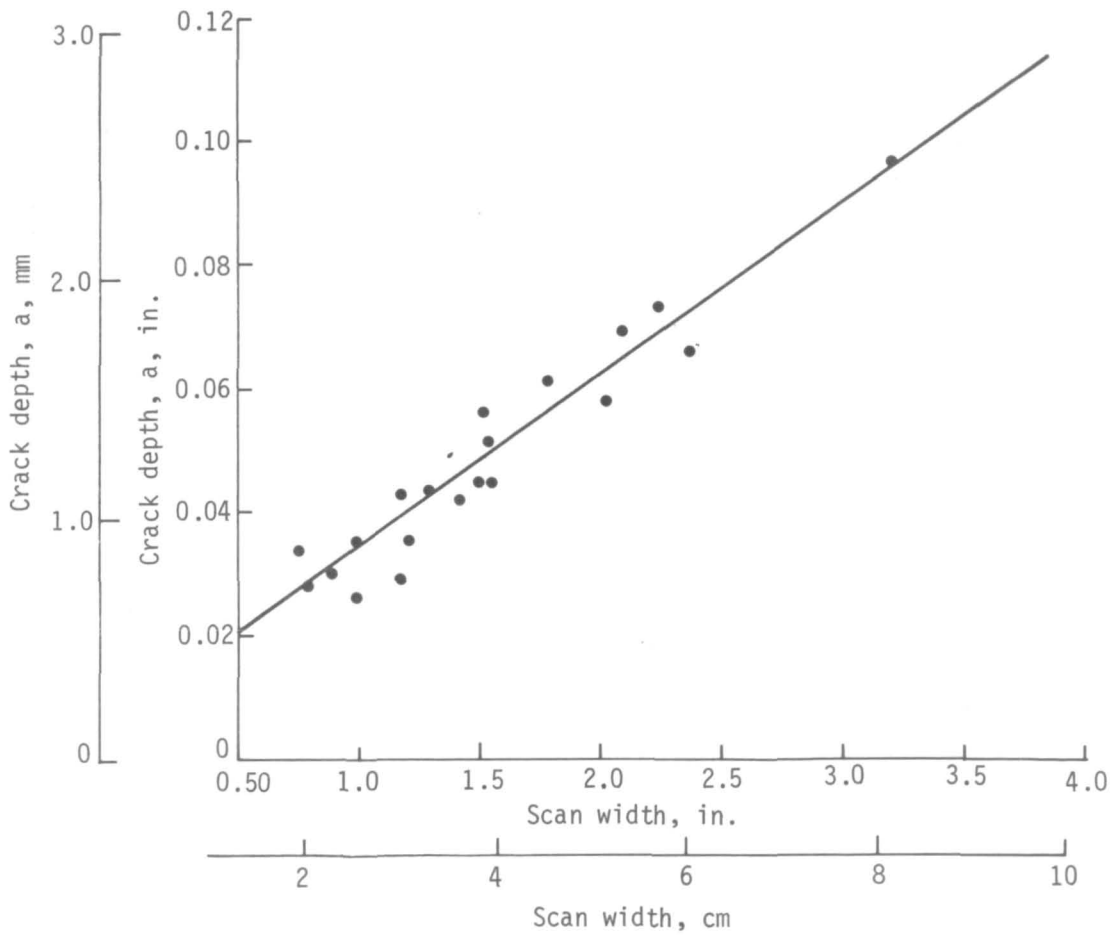

Figure 43. - Ultrasonic calibration curve for titanium.

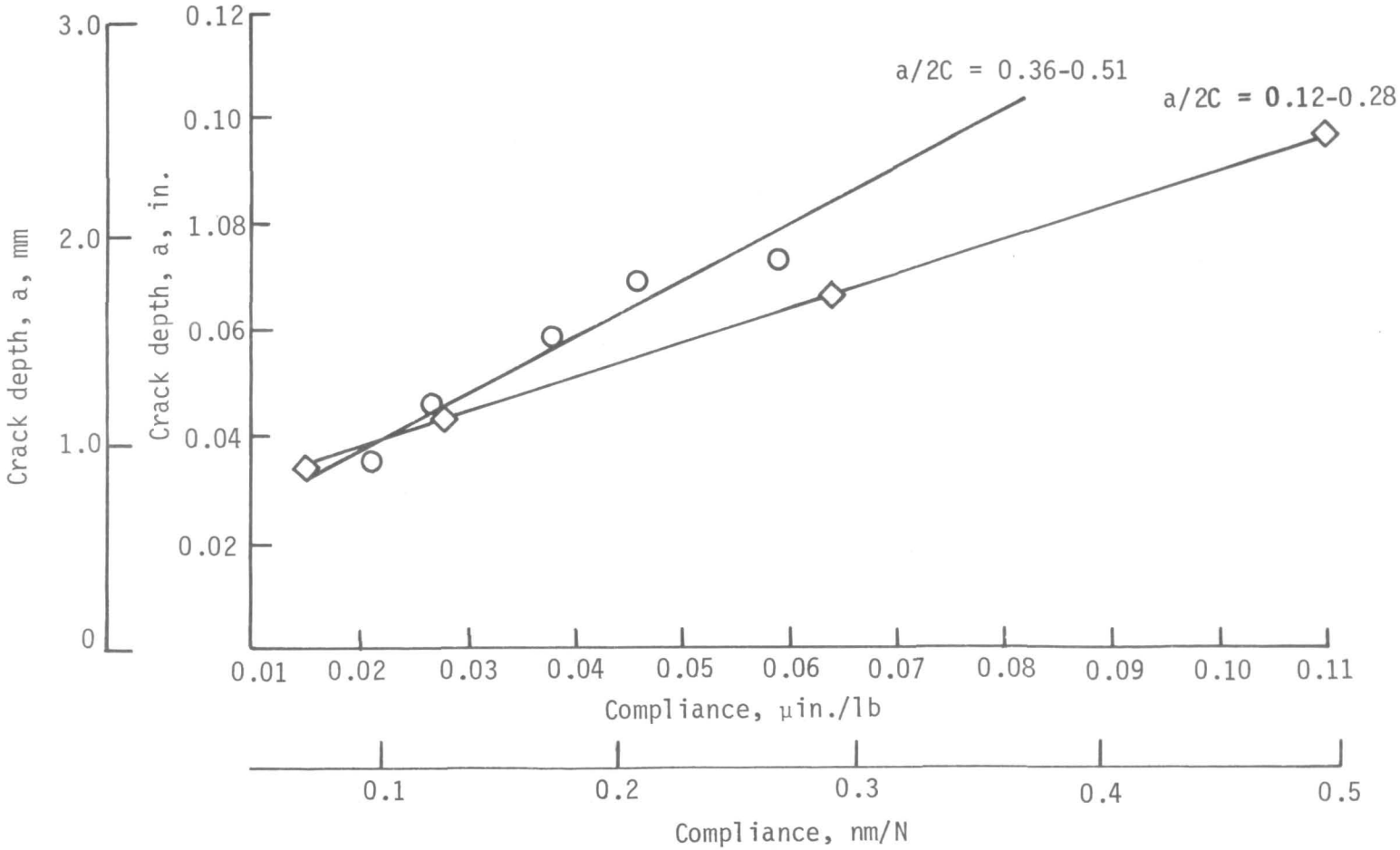

Figure 44. - Compliance calibration curve for titanium.

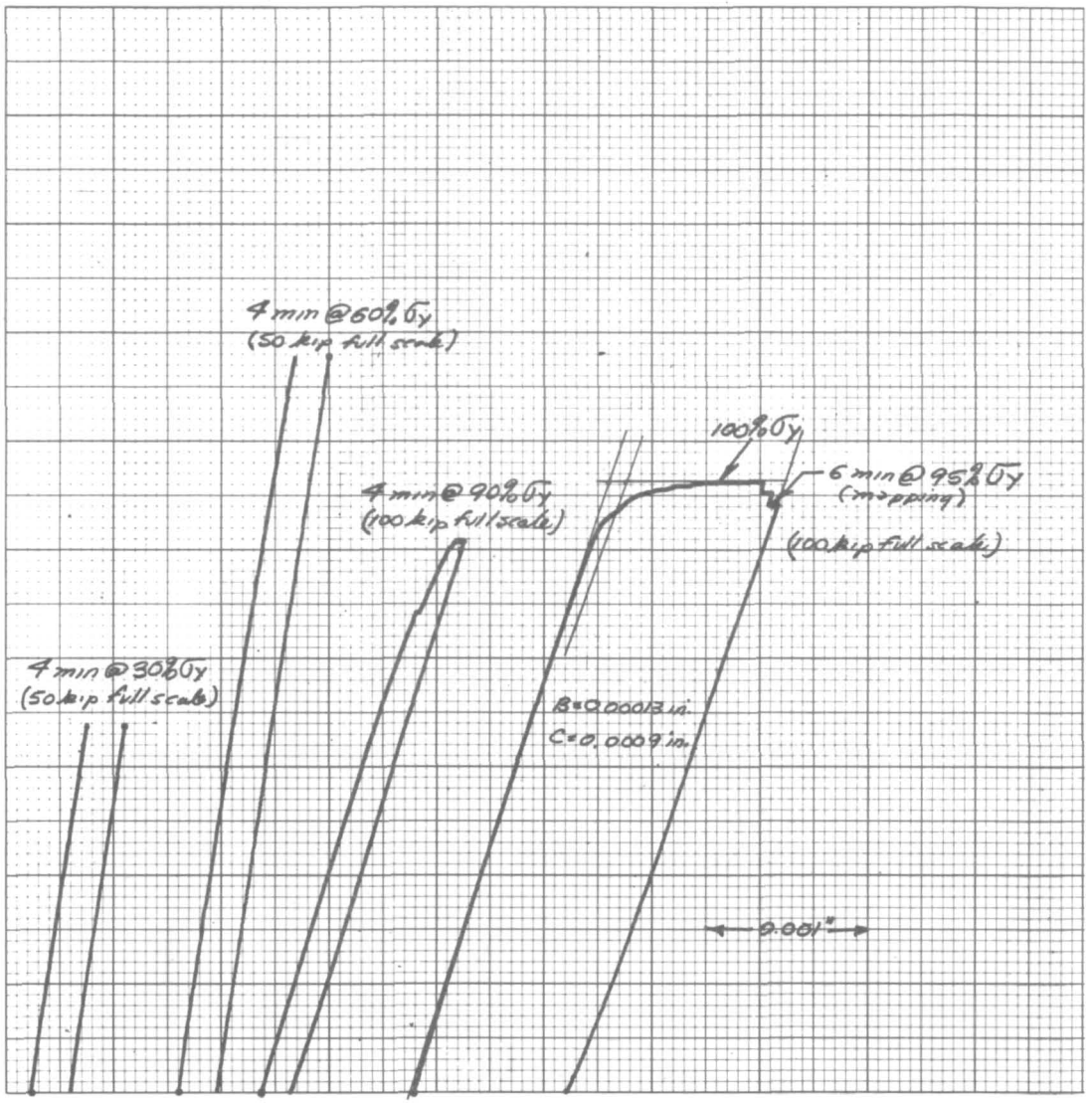

Figure 45. - Crack-opening displacement curves for titanium-alloy specimen TOL-4.

The portion of the deformation that could be attributed to subcritical growth for plasticity levels of approximately 25.4 μm (0.001 in.) were relatively small, typically 200 to 500 nm (70 to 200 μin.). We concluded that little subcritical growth occurred at a plastic deformation level of 25.4 μm (0.001 in.). No tests were performed at higher plasticity levels. Figures 45 through 47 present several typical crack-opening displacement curves. Examination of the fracture faces confirmed that very little subcritical growth had occurred in the depth direction. Maximum depth growth was 50.8 μm (0.002 in.). However, tunneling growth had occurred. Although of significant magnitude compared

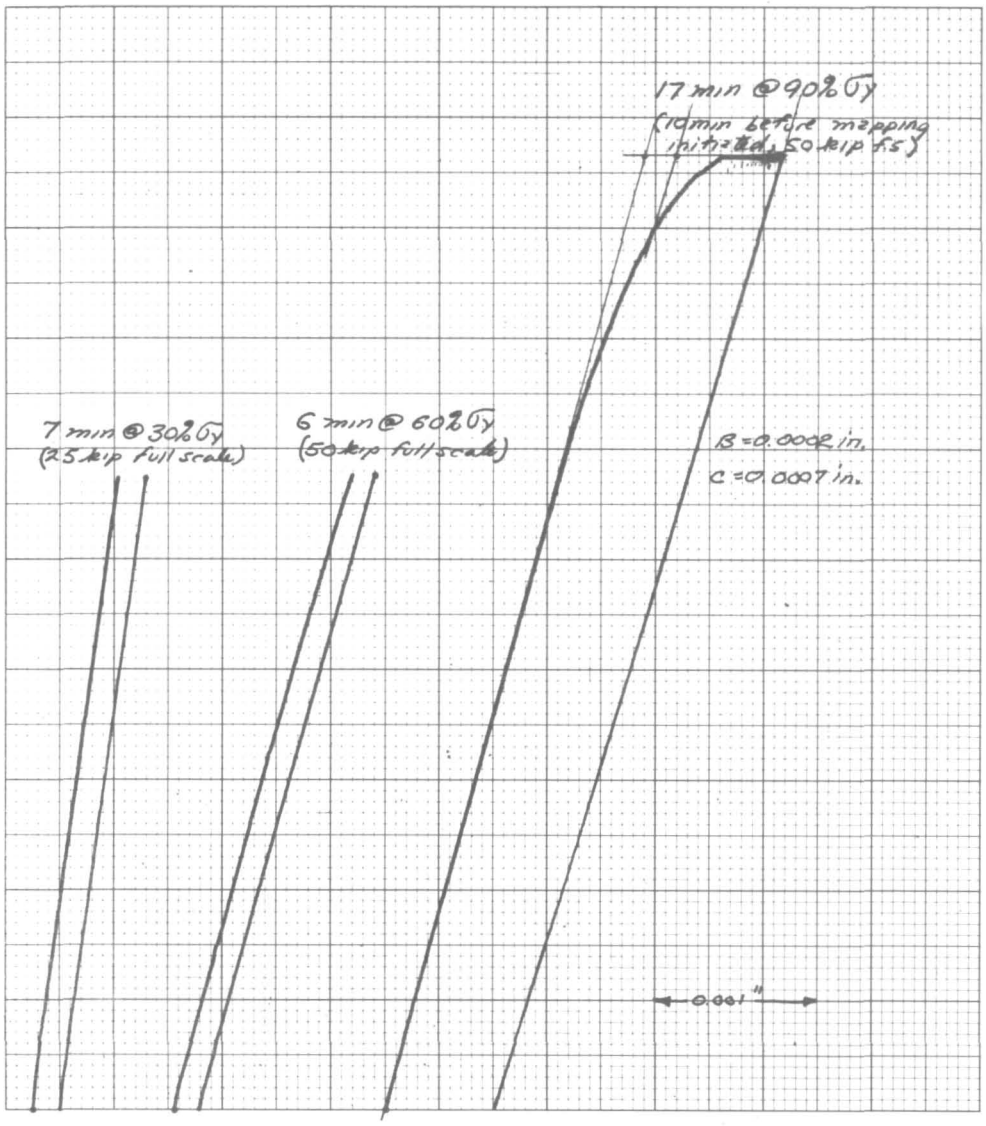

Figure 46. - Crack-opening displacement curves for titanium-alloy specimen TOL-5.

to aluminum, in some cases this growth was more localized than in aluminum. It would therefore be expected to provide less contribution to crack-opening displacement. Table XIV summarizes data for the nine specimens tested.

Comparison of flaw size and growth data obtained using the two evaluation techniques showed that both satisfactorily characterized behavior (table XV). Figure 48 is plot of the threshold for subcritical growth.

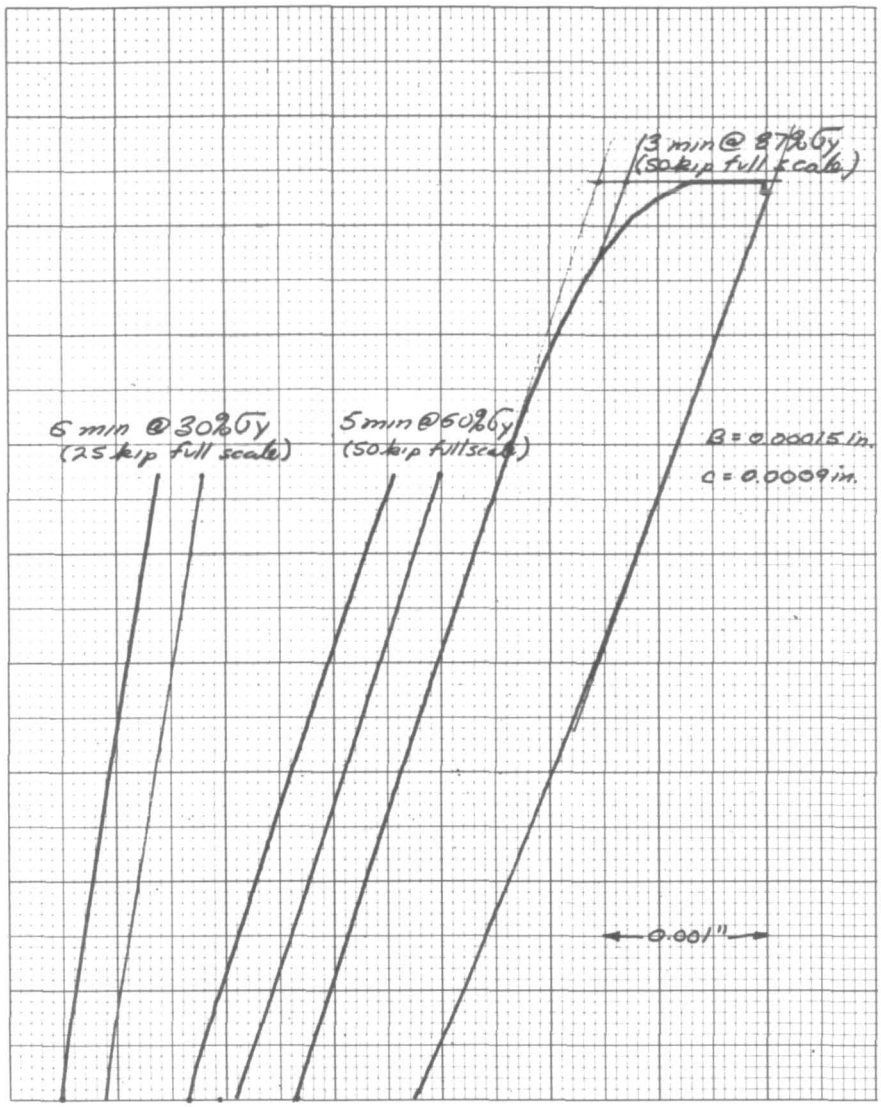

Figure 47. - Crack-opening displacement curves for titanium-alloy specimen TOL-9.

Figures 49 through 53 show flaw maps and fractographs of five specimens that exhibited localized growth. Agreement between ultrasonic predictions and actual results is quite good.

TABLE XIV. - SUMMARIZED DATA FOR OVERLOADED TITANIUM SPECIMENS

Specimen no.	Flaw geometry							Test condition	Stress level,	Ultrasonic scan width,		Compliance,	
	Depth, a,		Width, 2C,		a/2C	a/t	a/Q					nm/N	(μin./lb)
	cm	(in.)	cm	(in.)					% σ_{ys}	cm	(in.)		
TOL-1	0.109	(0.43)	0.396	(0.156)	0.28	0.34	0.028	Static	0	2.41	(0.95)		
								Loading	0-30			0.160	(0.028)
								Static	30	3.02	(1.19)		
								Unloading	30-0			0.160	(0.028)
								Static	0	2.46	(0.97)		
								Loading	0-60			0.160	(0.028)
								Static	60	3.02	(1.19)		
								Unloading	60-0			0.160	(0.028)
								Static	0	3.30	(1.30)		
								Loading	0-90			0.166	(0.029)
								Static	90	3.02	(1.19)		
								Unloading	90-0			0.177	(0.031)
								Static	0	3.68	(1.45)		
								Loading	0-92	Fractured		0.183	(0.032)
TOL-2	0.168	(0.066)	0.668	(0.263)	0.25	0.52	0.045	Static	0	4.06	(1.60)		
								Loading	0-30			0.365	(0.064)
								Static	30	5.89	(2.32)		
								Unloading	30-0			0.365	(0.064)
								Static	0	5.05	(1.99)		
								Loading	0-60			0.360	(0.063)
								Static	60	6.17	(2.43)		
								Unloading	60-0			0.377	(0.066)
								Static	0	5.92	(2.33)		
								Loading	0-75	Fractured		0.383	(0.067)
TOL-3	0.244	(0.096)	0.907	(0.357)	0.12	0.33	0.084	Static	0	6.60	(2.60)		
								Loading	0-30			0.628	(0.110)
								Static	30	8.10	(3.19)		
								Unloading	30-0			0.611	(0.107)
								Static	0	6.83	(2.69)		
								Loading	0-52			0.622	(0.109)
								Static	52	8.18	(3.22)		
								Unloading	52-0			0.634	(0.111)
	0.246	(0.097)	0.907	(0.357)	0.27	0.78	0.063	Static	0	8.31	(3.27)		
TOL-4	0.088	(0.0345)	0.226	(0.089)	0.39	0.27	0.018	Static	0	2.01	(0.79)		
								Loading	0-30			0.120	(0.021)
								Static	30	3.02	(1.19)		
								Unloading	30-0			0.120	(0.021)
								Static	0	2.29	(0.90)		
								Loading	0-60			0.120	(0.021)
								Static	60	3.18	(1.25)		
								Unloading	60-0			0.120	(0.021)
								Static	0	2.62	(1.03)		
								Loading	0-90			0.120	(0.021)
								Static	90	3.15	(1.24)		
								Unloading	90-0			0.120	(0.021)
								Static	0	3.02	(1.19)		
								Loading	0-95			0.120	(0.021)
								Static	95	3.35	(1.32)		
								Unloading	95-0			0.131	(0.023)
	0.090	(0.0355)	0.226	(0.089)	0.40	0.28	0.018	Static	0	3.30	(1.30)		

TABLE XIV. - Continued.

Specimen no.	Flaw geometry							Test condition	Stress level,	Ultrasonic scan width,		Compliance,	
	Depth, a,		Width, 2C,		a/2C	a/t	a/Q					nm/N	(μin./lb)
	cm	(in.)	cm	(in.)					% σ_{ys}	cm	(in.)		
TOL-5	0.147	(0.058)	0.343	(0.135)	0.43	0.45	0.027	Static	0	3.81	(1.50)		
								Loading	0-30			0.217	(0.038)
								Static	30	4.88	(1.92)		
								Unloading	30-0			0.217	(0.038)
								Static	0	4.50	(1.77)		
								Loading	0-60			0.217	(0.038)
								Static	60	5.38*	(2.12)*		
								Unloading	60-0			0.217	(0.038)
								Static	0	5.38*	(2.12)*		
								Loading	0-90			0.217	(0.038)
								Static	90	6.12*	(2.41)*		
								Unloading	90-0			0.228	(0.040)
	0.152	(0.060)	0.343	(0.135)	0.44	0.46	0.027	Static	0	4.32	(1.70)		
TOL-6	0.185	(0.073)	0.518	(0.204)	0.36	0.57	0.039	Static	0	4.65	(1.83)		
								Loading	0-30			0.337	(0.059)
								Static	30	5.59	(2.20)		
								Unloading	30-0			0.337	(0.059)
								Static	0	4.80	(1.89)		
								Loading	0-60			0.331	(0.058)
								Static	60	5.84	(2.30)		
								Unloading	60-0			0.331	(0.058)
								Static	0	5.49	(2.16)		
								Loading	0-79			0.331	(0.058)
								Static	79	6.17	(2.43)		
								Unloading	79-0			0.354	(0.062)
	0.191	(0.075)	0.518	(0.204)	0.37	0.59	0.040	Static	0	5.82	(2.29)		
TOL-7	0.086	(0.034)	0.175	(0.069)	0.49	0.27	0.014	Static	0	1.85	(0.73)		
								Loading	0-30			0.086	(0.015)
								Static	30	1.98	(0.78)		
								Unloading	30-0			0.086	(0.015)
								Static	0	1.75	(0.69)		
								Loading	0-60			0.086	(0.015)
								Static	60	1.85	(0.73)		
								Unloading	60-0			0.086	(0.015)
								Static	0	1.85	(0.73)		
								Loading	0-Fracture				
TOL-8	0.114	(0.045)	0.259	(0.102)	0.44	0.35	0.021	Static	0	3.35	(1.32)		
								Loading	0-30			0.154	(0.027)
								Static	30	3.89	(1.53)		
								Unloading	30-0			0.154	(0.027)
								Static	0	3.38	(1.33)		
								Loading	0-60			0.160	(0.028)
								Static	60	4.01	(1.58)		
								Unloading	60-0			0.177	(0.031)
								Static	0	3.63	(1.43)		
								Loading	0-92			0.154	(0.027)
								Static	92	4.47	(1.76)		
								Unloading	92-0			0.206	(0.036)
	0.117	(0.046)	0.259	(0.102)	0.45	0.36	0.021	Static	0	4.37	(1.72)		

* Air in transducer housing

TABLE XIV. - Concluded.

Specimen no.	Flaw geometry							Test condition	Stress level,	Ultrasonic scan width,		Compliance,	
	Depth, a,		Width, 2C,		a/2C	a/t	a/Q					nm/N	(μin./lb)
	cm	(in.)	cm	(in.)					% σ_{ys}	cm	(in.)		
TOL-9	0.175	(0.069)	0.356	(0.140)	0.49	0.53	0.029	Static	0	3.78	(1.49)		
								Loading	0-30			0.263	(0.046)
								Static	30	5.33	(2.10)		
								Unloading	30-0			0.263	(0.046)
								Static	0	3.73	(1.47)		
								Loading	0-60			0.251	(0.044)
								Static	60	5.33	(2.10)		
								Unloading	60-0			0.251	(0.044)
								Static	0	5.11	(2.01)		
								Loading	0-87			0.251	(0.044)
								Static	87	5.64	(2.22)		
								Unloading	87-0			0.286	(0.050)
	0.180	(0.071)	0.356	(0.140)	0.51	0.55	0.030	Static	0	5.46	(2.15)		

TABLE XV. - COMPARISON OF MEASUREMENT TECHNIQUES FOR TITANIUM

Specimen no.	Condition	Flaw depth, a						Crack growth, Δa						Maximum growth, Δr				ϕ, deg
		Visual		UT		COD		Visual		UT		COD		Visual		UT		
		cm	(in.)	cm	(in.)	cm	(in.)	cm	(in.)	cm	(in.)	cm	(in.)	cm	(in.)	cm	(in.)	
TOL-1	Initial	0.109	(0.043)	0.099	(0.039)	0.109	(0.043)	--	--	--	--	--	--	--	--	--	--	--
	Final	*	*	--	--	--	--	--	--	--	--	--	--	--	--	--	--	--
TOL-2	Initial	0.168	(0.066)	0.180	(0.071)	0.168	(0.066)	--	--	--	--	--	--	--	--	--	--	--
	Final	*	*	--	--	--	--	--	--	--	--	--	--	--	--	--	--	--
TOL-3	Initial	0.244	(0.096)	0.241	(0.095)	0.244	(0.096)	--	--	--	--	--	--	--	--	--	--	--
	Final	0.246	(0.097)	0.246	(0.097)	0.246	(0.097)	0.0025	(0.001)	0.005	(0.002)	0.0025	(0.001)	0.066	(0.026)	0.048	(0.19)	15
TOL-4	Initial	0.087	(0.0345)	0.099	(0.039)	0.097	(0.038)	--	--	--	--	--	--	--	--	--	--	--
	Final	0.090	(0.0355)	0.107	(0.042)	0.102	(0.040)	0.0025	(0.001)	0.008	(0.003)	0.005	(0.002)	0.043	(0.017)	0.020	(0.008)	30
TOL-5	Initial	0.147	(0.058)	0.150	(0.059)	0.142	(0.056)	--	--	--	--	--	--	--	--	--	--	--
	Final	0.152	(0.060)	†	†	0.147	(0.058)	0.005	(0.002)	†	†	0.005	(0.002)	0.025	(0.010)	--	--	30
TOL-6	Initial	0.185	(0.073)	0.170	(0.067)	0.198	(0.078)	--	--	--	--	--	--	--	--	--	--	
	Final	0.191	(0.075)	0.178	(0.070)	0.208	(0.082)	0.005	(0.002)	0.008	(0.003)	0.010	(0.004)	0.099	(0.039)	0.084	(0.033)	25
TOL-7	Initial	0.086	(0.034)	0.071	(0.028)	0.081	(0.032)	--	--	--	--	--	--	--	--	--	--	
	Final	*	*	--	--	--	--	--	--	--	--	--	--	--	--	--	--	
TOL-8	Initial	0.114	(0.045)	0.124	(0.049)	0.114	(0.045)	--	--	--	--	--	--	--	--	--	--	
	Final	0.117	(0.046)	0.137	(0.054)	0.137	(0.054)	0.0025	(0.001)	0.013	(0.005)	0.023	(0.009)	0.056	(0.022)	0.033	(0.013)	30
TOL-9	Initial	0.175	(0.069)	0.165	(0.065)	0.165	(0.065)	--	--	--	--	--	--	--	--	--	--	
	Final	0.180	(0.071)	0.168	(0.066)	0.175	(0.069)	0.005	(0.002)	0.0025	(0.001)	0.010	(0.004)	0.076	(0.030)	0.041	(0.016)	30

* Fractured in test
† Air in transducer housing.

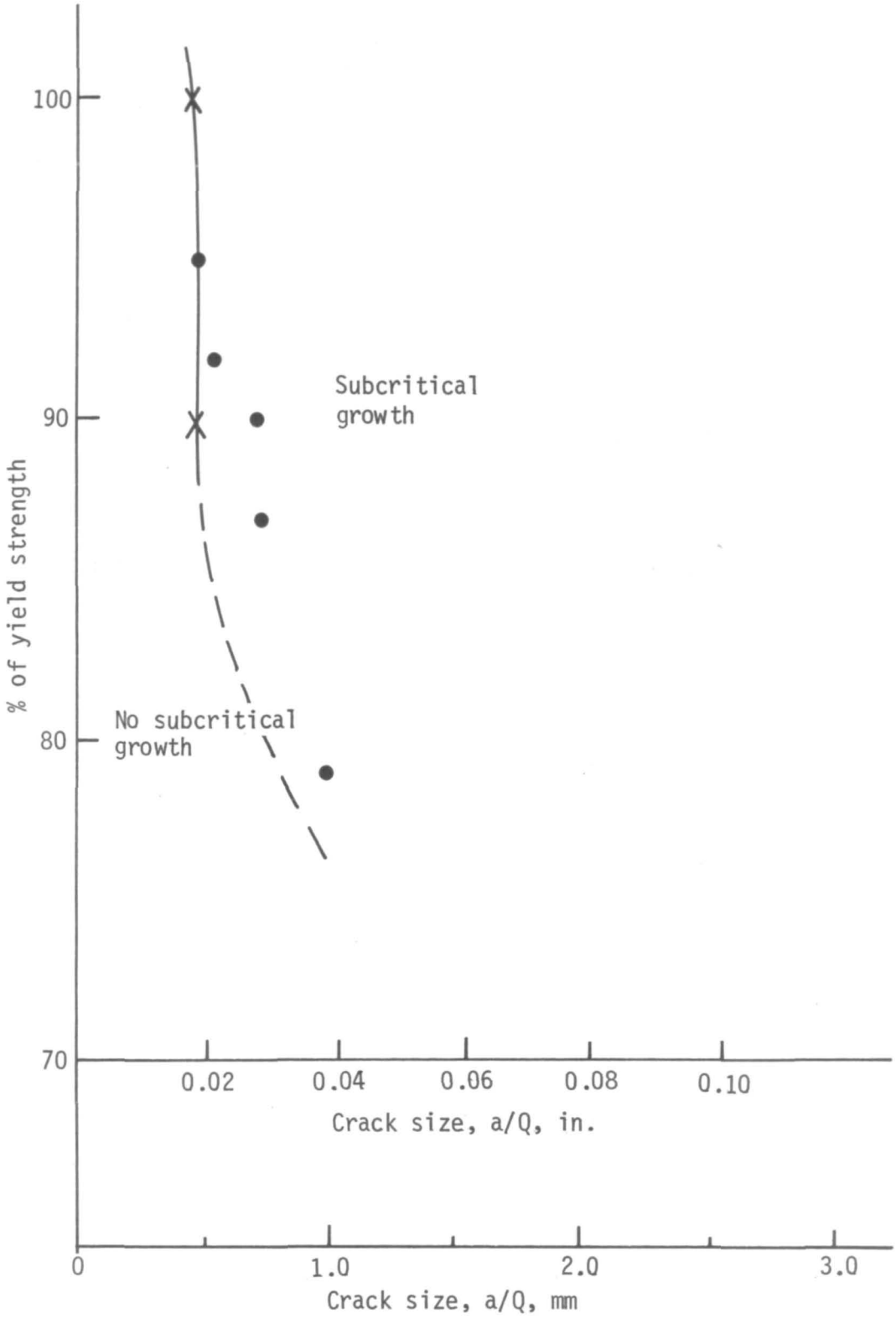

Figure 48. - Subcritical growth threshold for titinium.

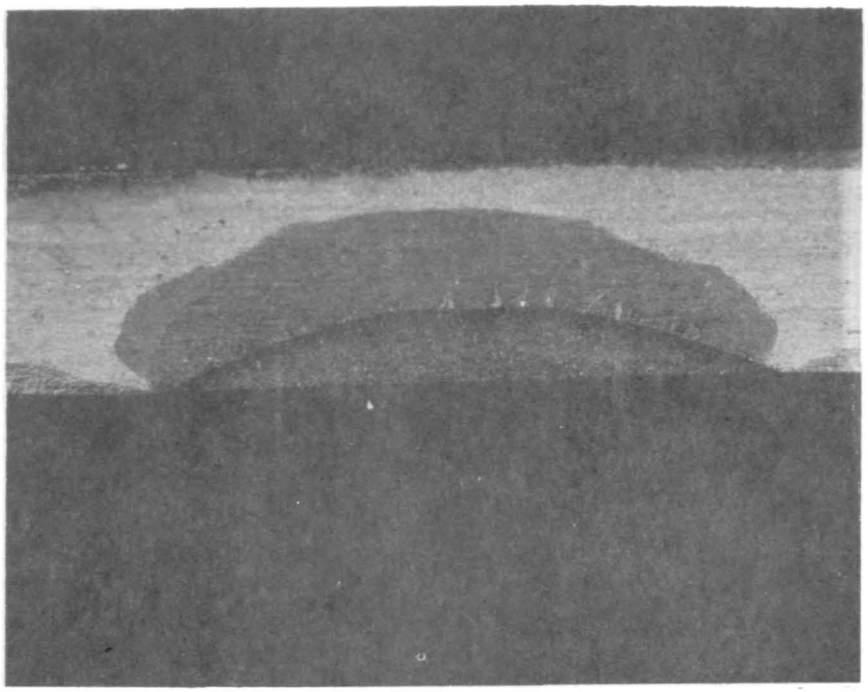

10X

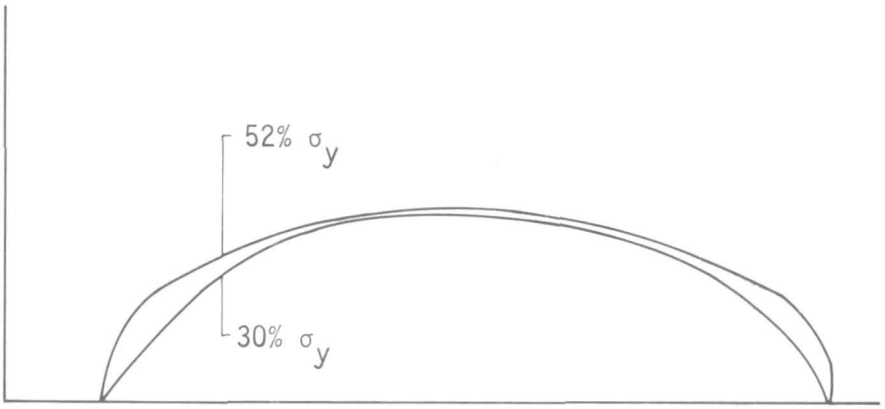

10X

Figure 49. - Fractograph and flaw map of specimen TOL-3.

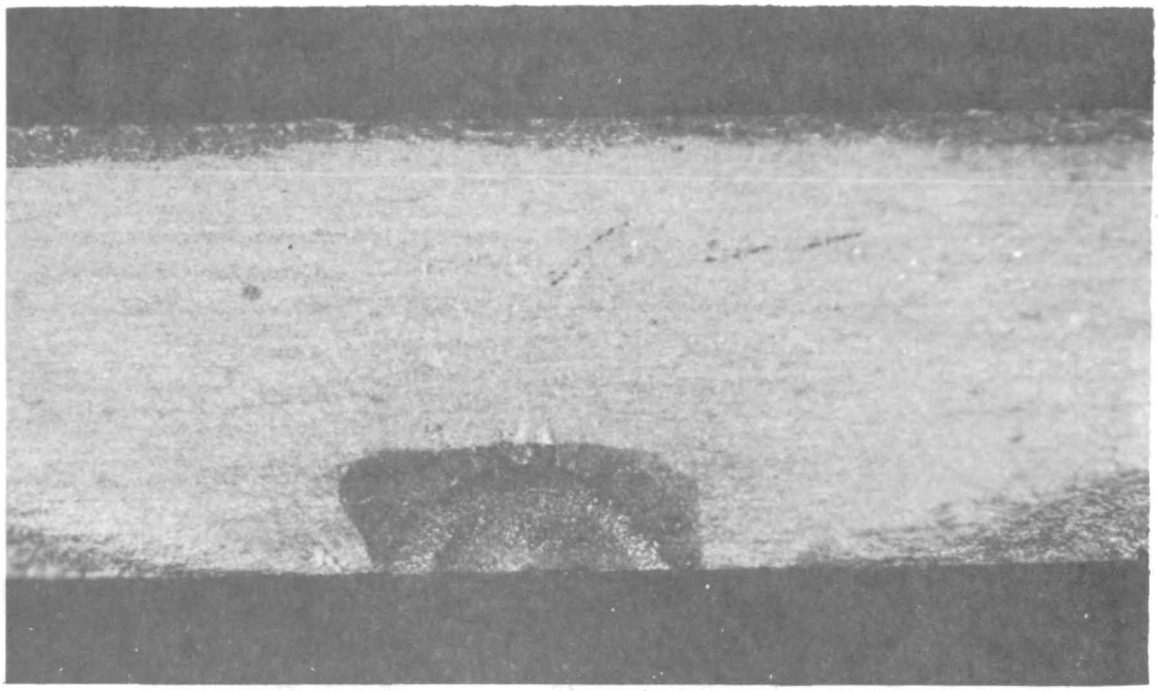

20X

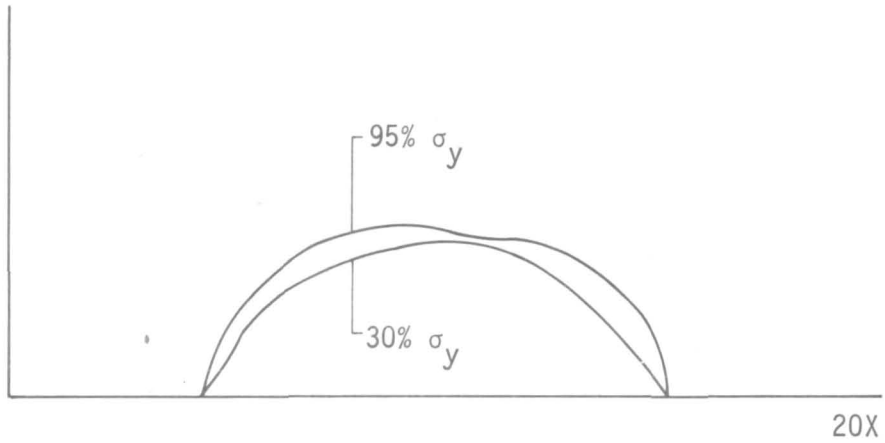

Figure 50. - Fractograph and flaw map of specimen TOL-4.

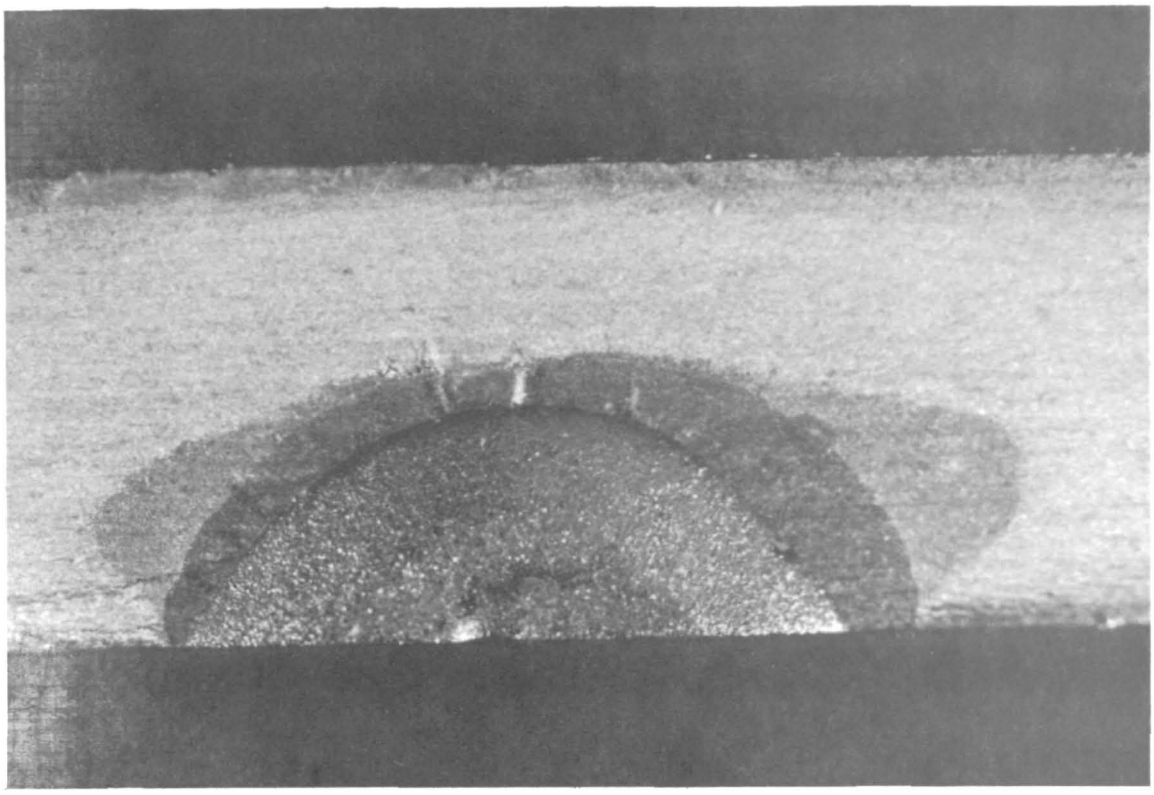

20X

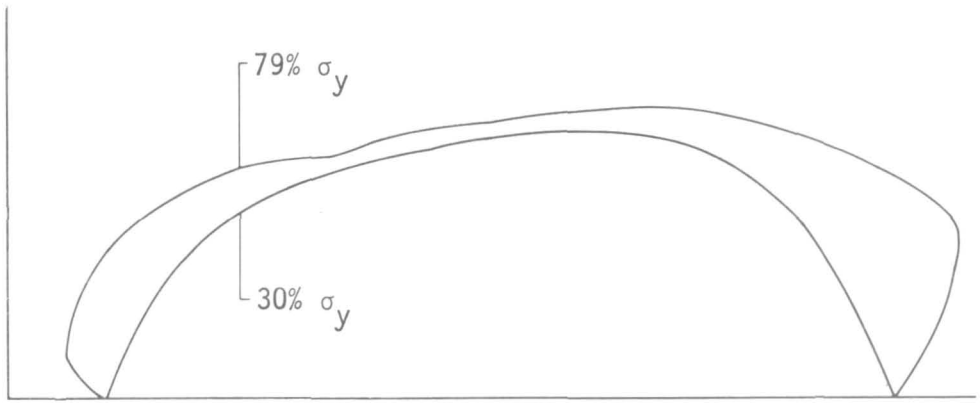

20X

Figure 51. - Fractograph and flaw map of specimen TOL-6.

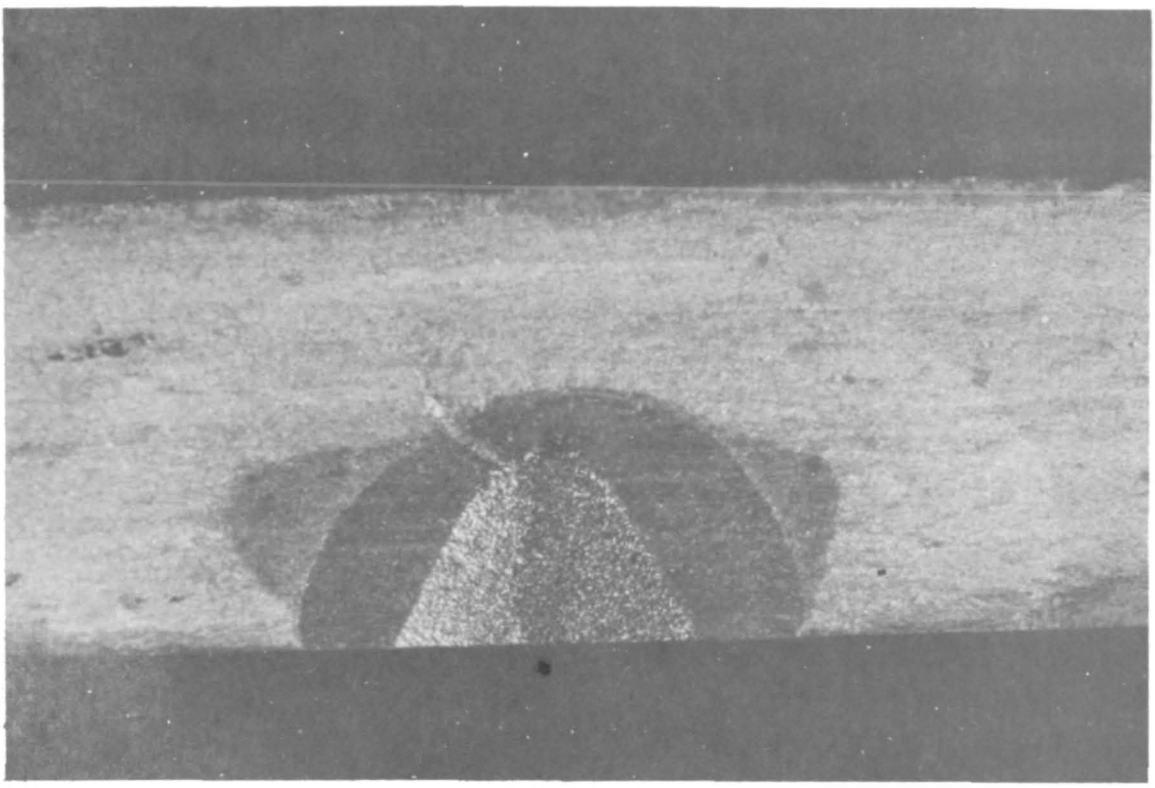

20X

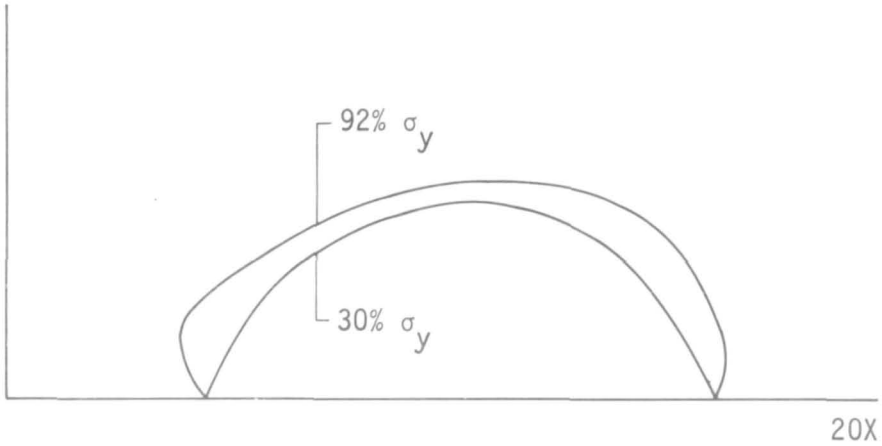

Figure 52. - Fractograph and flaw map of specimen TOL-8.

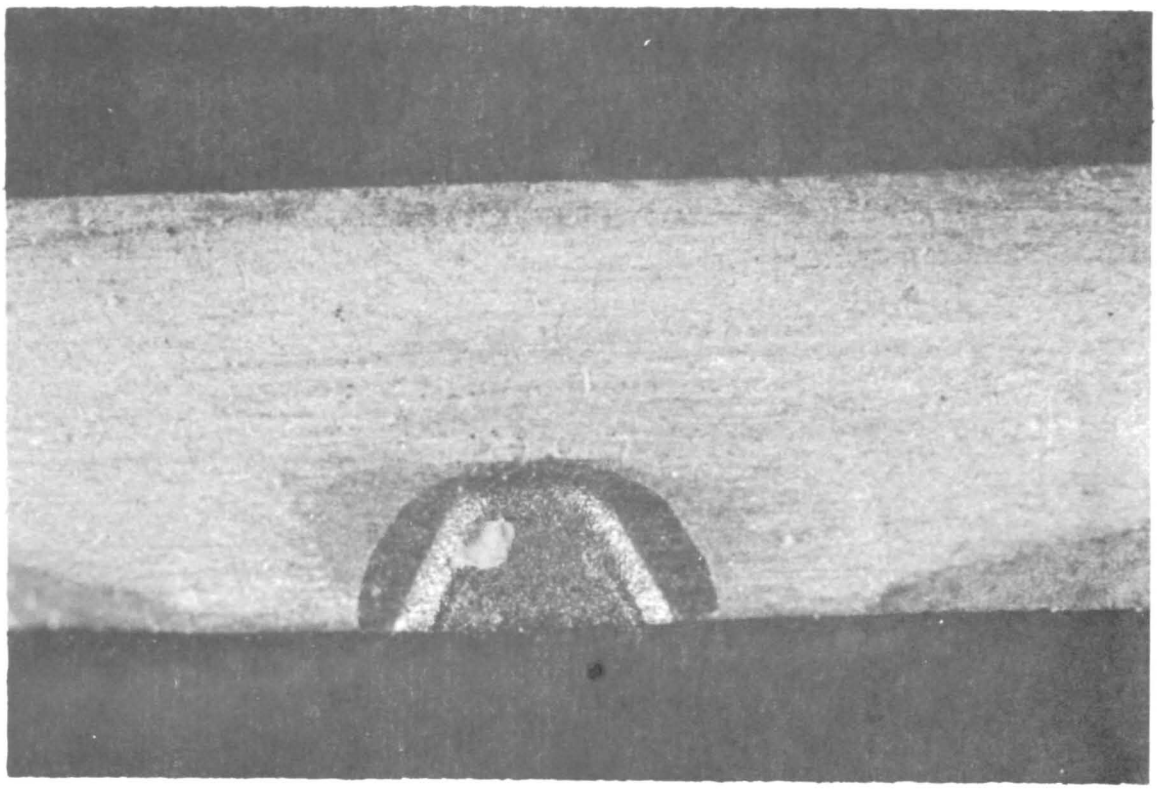

20X

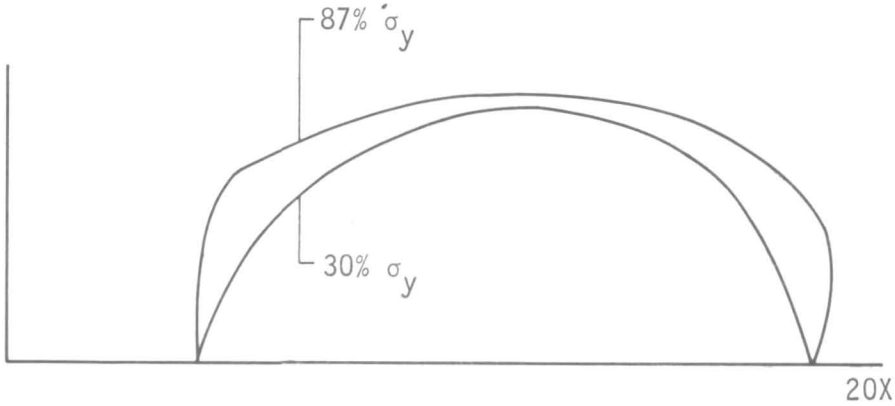

Figure 53. - Fractograph and flaw map of specimen TOL-9.

Steel Data

Table XVI summarizes test results for steel calibration specimens, which contained electromachined defects. A calibration curve of ultrasonic span width versus crack depth was prepared using these data points and those obtained from fatigue-sharpened defects after loading to 30 and 60% of yield strength (fig. 54). Crack-opening displacement compliance curves were prepared from data obtained by loading at 30 and 60% of the yield strength (fig 55).

Behavior similar to that of the other two alloys was exhibited. Subcritical growth occurred at plastic deformation levels exceeding 0.025 mm (0.001 in.). Figures 56 through 58 present typical crack-opening displacement curves. Fracture-face examination confirmed the subcritical growth. Maximum depth of growth was 0.005 mm (0.002 in.). No tunneling was noted. Table XVII summarizes data for the nine specimens tested.

A comparison of flaw size and growth data obtained using the ultrasonic and crack-opening displacement techniques showed that the two techniques provided fair measurements of defect size--but not as satisfactory as for aluminum or titanium. Table XVIII presents comparison data.

Figure 59 is a graphic presentation of the threshold for subcritical growth.

TABLE XVI. - STEEL CALIBRATION DATA

Specimen no.	Flaw geometry							Test condition	Stress level,	Ultrasonic scan width,	
	Depth, a,		Width, 2C,		a/2C	a/t	a/Q				
	cm	(in.)	cm	(in.)					% σ_{ys}	cm	(in.)
SE-1	0.048	(0.019)	0.330	(0.130)	0.15	0.16	0.016	Static	0	2.08	(0.82)
SE-2	0.119	(0.047)	0.561	(0.221)	0.21	0.39	0.035	Static	0	3.28	(1.29)
SE-3	0.132	(0.052)	0.820	(0.323)	0.16	0.43	0.042	Static	0	3.61	(1.42)
SE-4	0.064	(0.025)	0.211	(0.083)	0.30	0.22	0.015	Static	0	1.70	(0.67)
SE-5	0.091	(0.036)	0.312	(0.123)	0.29	0.30	0.023	Static	0	2.29	(0.90)
SE-6	0.150	(0.059)	0.452	(0.178)	0.33	0.49	0.034	Static	0	3.86	(1.52)
SE-7	0.064	(0.025)	0.102	(0.040)	0.63	0.21	0.011	Static	0	1.83	(0.72)
SE-8	0.117	(0.046)	0.203	(0.080)	0.58	0.38	0.020	Static	0	2.79	(1.10)
SE-9	0.168	(0.066)	0.305	(0.120)	0.55	0.57	0.028	Static	0	4.50	(1.77)

SE = electrodischarge machined defect

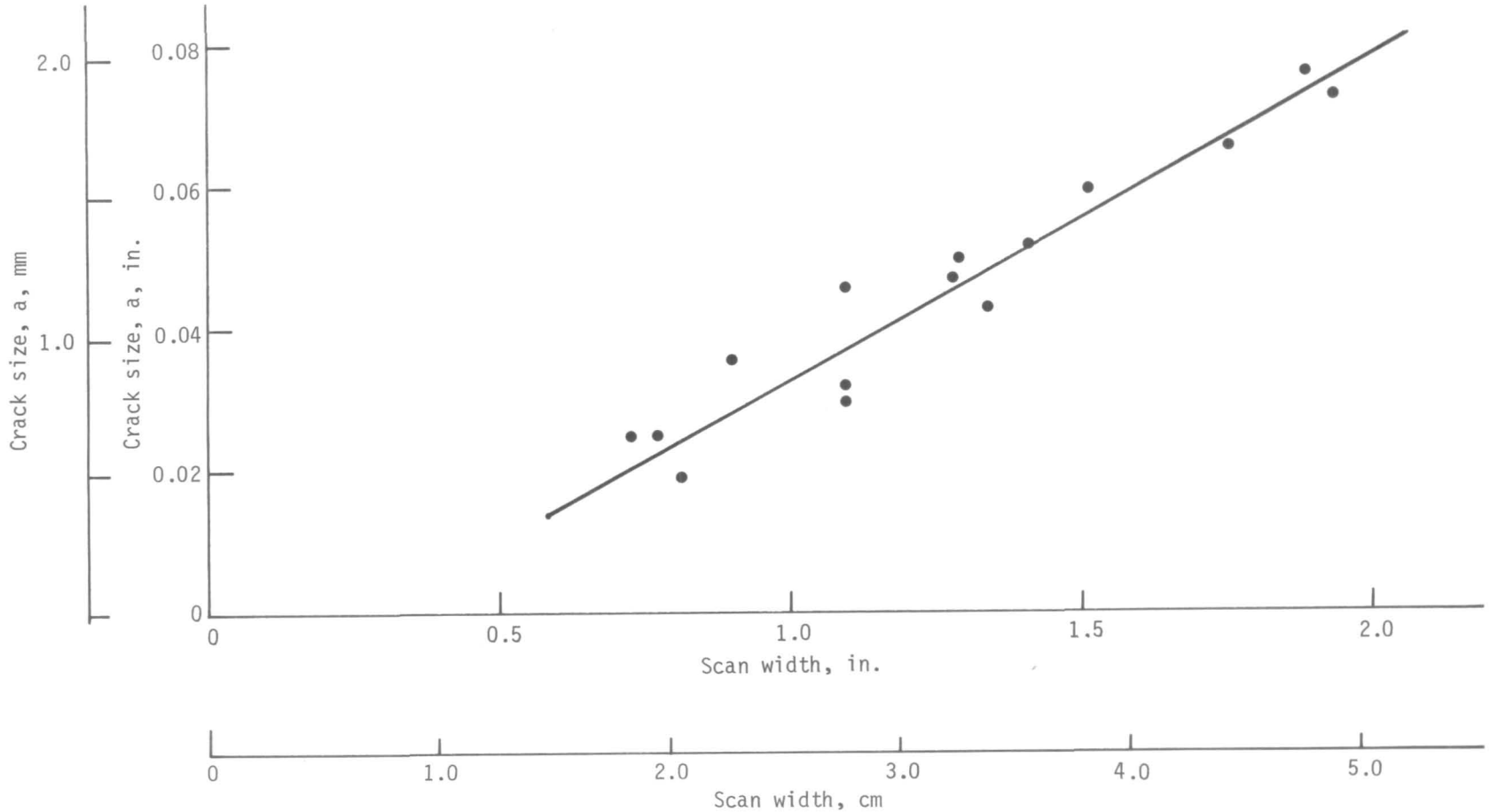

Figure 54. - Ultrasonic calibration curve for steel.

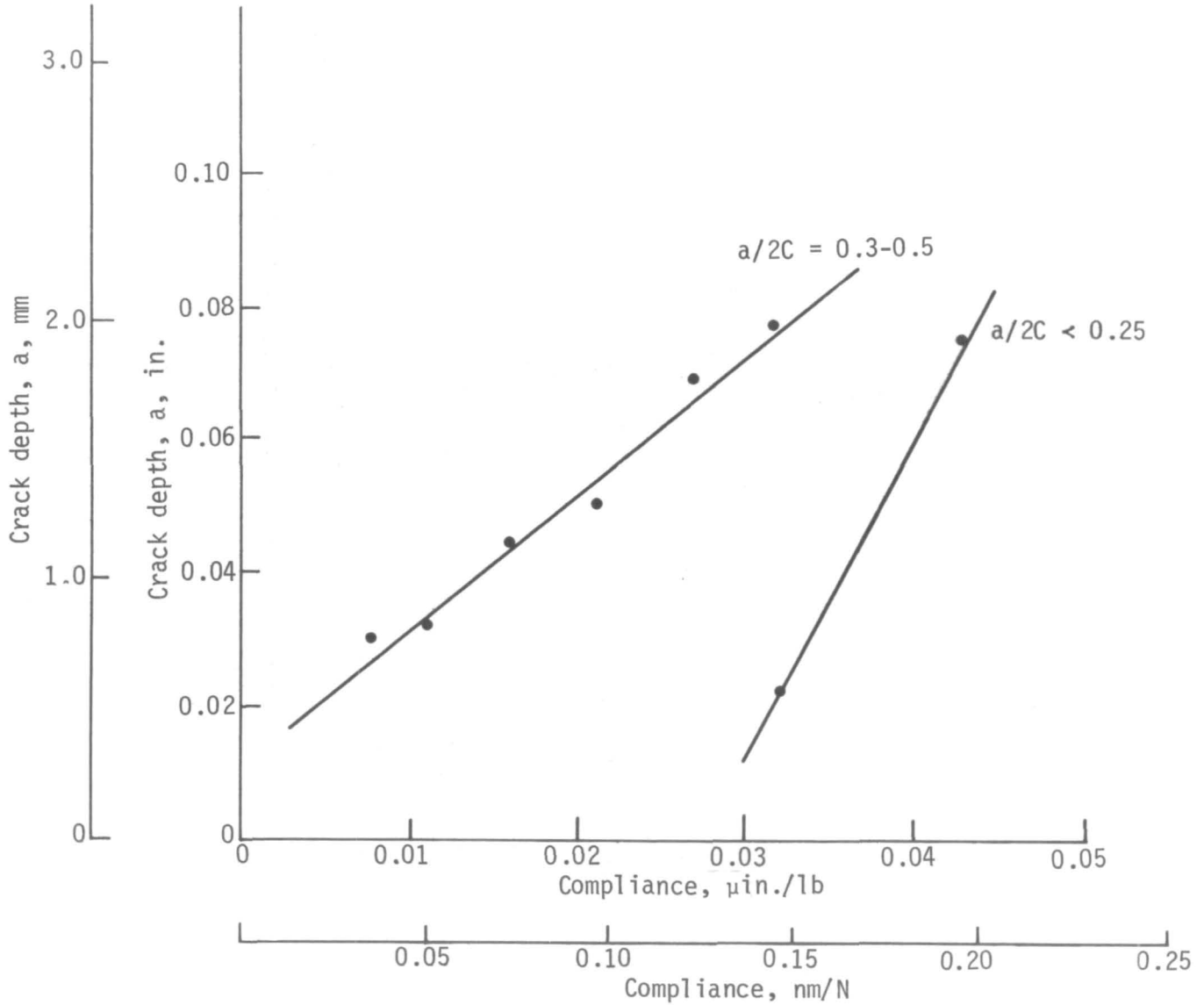

Figure 55. - Compliance calibration curves for steel.

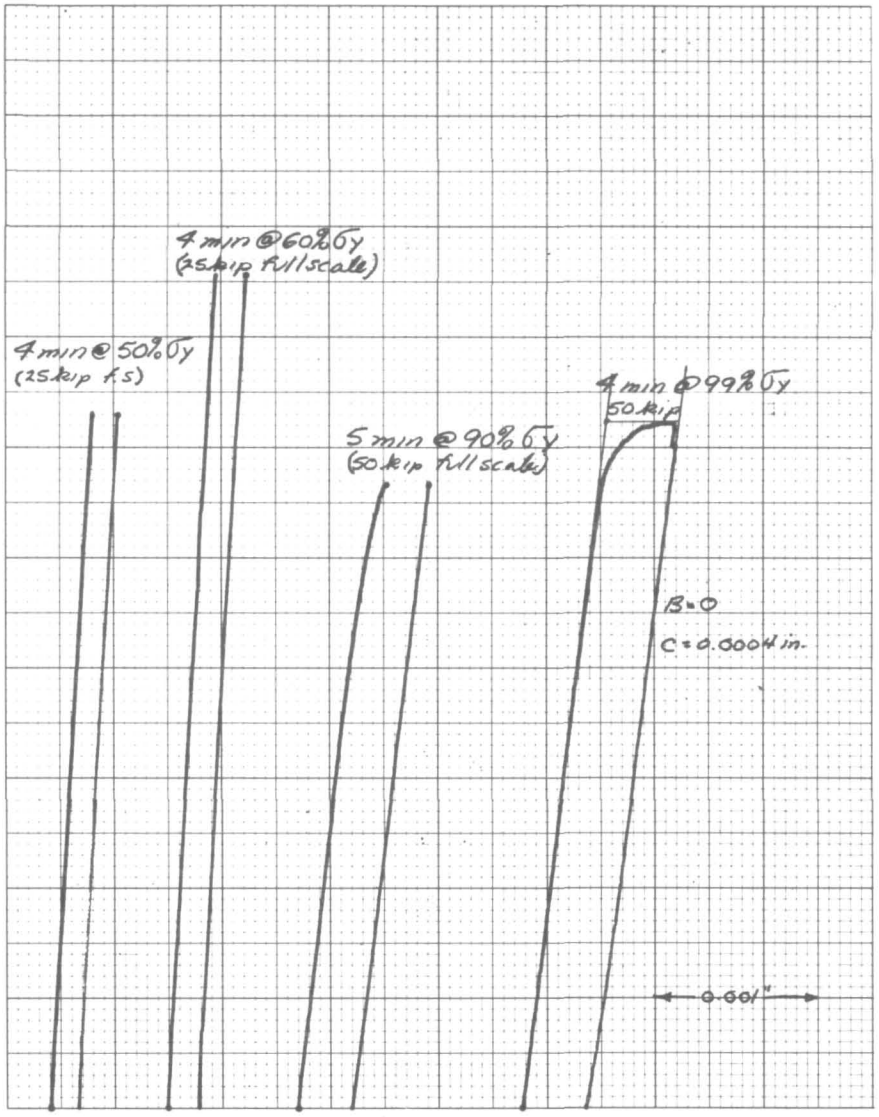

Figure 56. - Crack-opening displacement curves for steel specimen SOL-1.

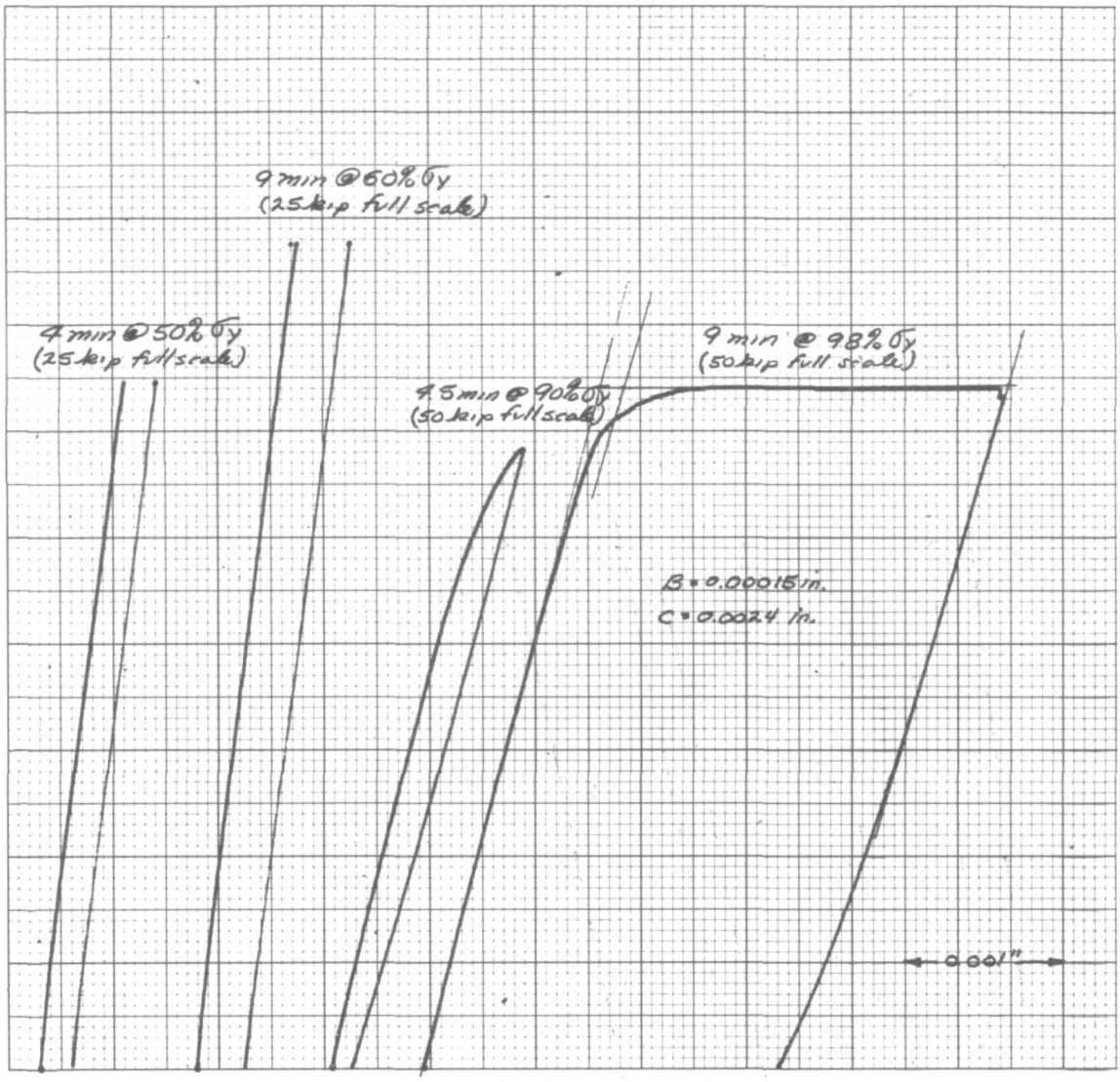

Figure 57. - Crack-opening displacement curves for steel specimen SOL-6.

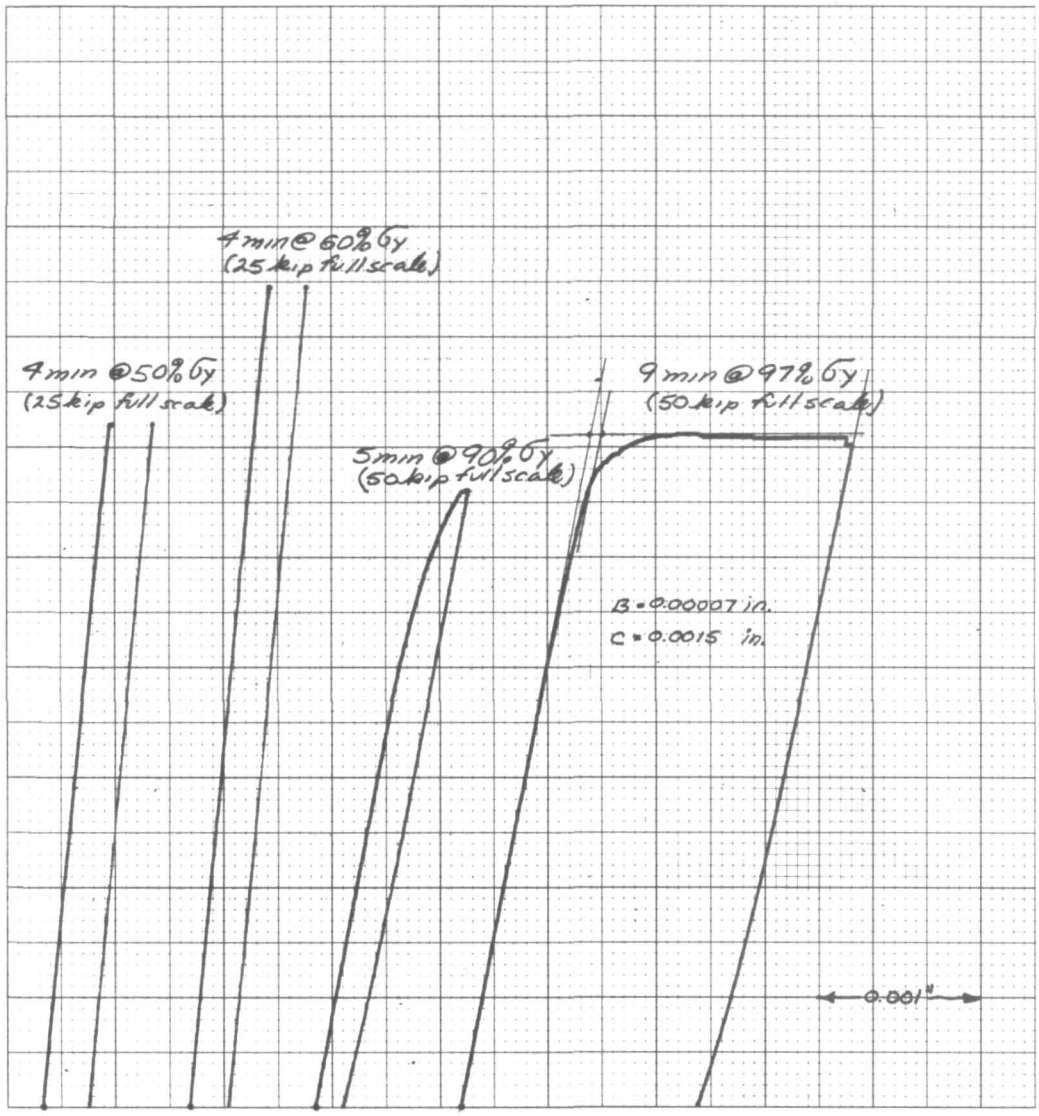

Figure 58. - Crack-opening displacement curves for steel specimen SOL-9.

TABLE XVII. - SUMMARIZED DATA FOR OVERLOADED STEEL SPECIMENS

Specimen no.	Flaw geometry							Test condition	Stress level, % σ_{ys}	Ultrasonic scan width,		Compliance,	
	Depth, a,		Width, 2C,		a/2C	a/t	a/Q					nm/N	(μin./lb)
	cm	(in.)	cm	(in.)						cm	(in.)		
SOL-1	0.109	(0.043)	0.343	(0.135)	0.32	0.36	0.025	Static	0	2.29	(0.90)		
								Loading	0-50			0.091	(0.016)
								Static	50	3.43	(1.35)		
								Unloading	50-0			0.091	(0.016)
								Static	0	2.31	(0.91)		
								Loading	0-60			0.091	(0.016)
								Static	60	3.40	(1.34)		
								Unloading	60-0			0.091	(0.016)
								Static	0	2.59	(1.02)		
								Loading	0-90			0.091	(0.016)
								Static	90	3.33	(1.31)		
								Unloading	90-0			0.091	(0.016)
								Static	0	3.10	(1.22)		
								Loading	0-99			0.091	(0.016)
								Static	99	3.10	(1.22)		
								Unloading	99-0			0.091	(0.016)
	0.109	(0.043)	0.343	(0.135)	0.32	0.36	0.025	Static	0	3.07	(1.21)		
SOL-2	0.052	(0.0205)	0.589	(0.232)	0.08	0.17	0.019	Static	0	3.35	(1.32)		
								Loading	0-50			0.183	(0.032)
								Static	50	4.57	(1.80)		
								Unloading	50-0			0.183	(0.032)
								Static	0	3.25	(1.28)		
								Loading	0-60			0.183	(0.032)
								Static	60	4.42	(1.74)		
								Unloading	60-0			0.183	(0.032)
								Static	0	3.25	(1.28)		
								Loading	0-90			0.166	(0.029)
								Static	90	4.39	(1.73)		
								Unloading	90-0			0.166	(0.029)
								Static	0	4.19	(1.65)		
								Loading	0-94			0.183	(0.032)
								Static	94	4.57	(1.80)		
								Unloading	94-0			*	*
	0.053	(0.0207)	0.589	(0.232)	0.09	0.17	0.019	Static	0	4.37	(1.72)		
SOL-3	0.185	(0.073)	0.820	(0.323)	0.23	0.60	0.052	Static	0	4.32	(1.70)		
								Loading	0-50			0.263	(0.046)
								Static	50	5.03	(1.98)		
								Unloading	50-0			0.263	(0.046)
								Static	0	4.39	(1.73)		
								Loading	0-60			0.246	(0.043)
								Static	60	4.83	(1.90)		
								Unloading	60-0			0.246	(0.043)
								Static	0	4.65	(1.83)		
								Loading	0-90			0.240	(0.042)
								Static	90	4.80	(1.89)		
								Unloading	90-0			0.263	(0.046)
								Static	0	4.67	(1.84)		
								Loading	0-95			0.240	(0.042)
								Static	95	4.67	(1.84)		
								Unloading	95-0			0.251	(0.044)
	0.188	(0.074)	0.820	(0.323)	0.23	0.61	0.052	Static	0	4.62	(1.82)		

* COD gage failed.

TABLE XVII. - Continued.

Specimen no.	Flaw geometry							Test condition	Stress level,	Ultrasonic scan width,		Compliance,	
	Depth, a,		Width, 2C,		a/2C	a/t	a/Q					nm/N	(μin./lb)
	cm	(in.)	cm	(in.)					% σ_{ys}	cm	(in.)		
SOL-4	0.081	(0.032)	0.224	(0.088)	0.36	0.28	0.017	Static	0	1.80	(0.71)		
								Loading	0-50			0.063	(0.011)
								Static	50	2.77	(1.09)		
								Unloading	50-0			0.063	(0.011)
								Static	0	1.80	(0.71)		
								Loading	0-60			0.063	(0.011)
								Static	60	2.79	(1.10)		
								Unloading	60-0			0.063	(0.011)
								Static	0	1.96	(0.77)		
								Loading	0-90			0.074	(0.013)
								Static	90	2.92	(1.15)		
								Unloading	90-0			0.074	(0.013)
								Static	0	2.11	(0.83)		
								Loading	0-100			0.074	(0.013)
								Static	100	3.05	(1.20)		
								Unloading	100-0			0.074	(0.013)
	0.081	(0.032)	0.224	(0.088)	0.36	0.28	0.017	Static	0	2.51	(0.99)		
SOL-5	0.127	(0.050)	0.356	(0.140)	0.36	0.42	0.027	Static	0	2.72	(1.07)		
								Loading	0-50			0.120	(0.021)
								Static	50	3.40	(1.34)		
								Unloading	50-0			0.120	(0.021)
								Static	0	2.54	(1.00)		
								Loading	0-60			0.120	(0.021)
								Static	60	3.30	(1.30)		
								Unloading	60-0			0.120	(0.021)
								Static	0	2.36	(0.93)		
								Loading	0-90			0.114	(0.020)
								Static	90	3.18	(1.25)		
								Unloading	90-0			0.114	(0.020)
								Static	0	3.00	(1.18)		
								Loading	0-98			0.120	(0.021)
								Static	98	3.02	(1.19)		
								Unloading	98-0			0.120	(0.021)
	0.132	(0.052)	0.356	(0.140)	0.37	0.43	0.028	Static	0	2.82	(1.11)		
SOL-6	0.193	(0.076)	0.508	(0.200)	0.38	0.63	0.039	Static	0	4.24	(1.67)		
								Loading	0-50			0.183	(0.032)
								Static	50	4.85	(1.91)		
								Unloading	50-0			0.183	(0.032)
								Static	0	4.29	(1.69)		
								Loading	0-60			0.183	(0.032)
								Static	60	4.78	(1.88)		
								Unloading	60-0			0.183	(0.032)
								Static	0	4.34	(1.71)		
								Loading	0-90			0.183	(0.032)
								Static	90	4.80	(1.89)		
								Unloading	90-0			0.206	(0.036)
								Static	0	4.75	(1.87)		
								Loading	0-98			0.206	(0.036)
								Static	98	4.65	(1.83)		
								Unloading	98-0			0.228	(0.040)
	0.198	(0.078)	0.508	(0.200)	0.39	0.64	0.040	Static	0	4.83	(1.90)		

TABLE XVII. - Concluded

Specimen no.	Flaw geometry							Test condition	Stress level,	Ultrasonic scan width,		Compliance,	
	Depth, a,		Width, 2C,		a/2C	a/t	a/Q					nm/N	(μin./lb)
	cm	(in.)	cm	(in.)					% σ_{ys}	cm	(in.)		
SOL-7	0.076	(0.030)	0.150	(0.059)	0.51	0.25	0.013	Static	0	2.16	(0.85)		
								Loading	0-50			0.046	(0.008)
								Static	50	3.07	(1.21)		
								Unloading	50-0			0.046	(0.008)
								Static	0	2.16	(0.85)		
								Loading	0-60			0.046	(0.008)
								Static	60	2.59	(1.02)		
								Unloading	60-0			0.046	(0.008)
								Static	0	1.75	(0.69)		
								Loading	0-90			0.051	(0.009)
								Static	90	2.29	(0.90)		
								Unloading	90-0			0.051	(0.009)
								Static	0	1.80	(0.71)		
								Loading	0-100			0.051	(0.009)
								Static	100	2.08	(0.82)		
								Unloading	100-0			0.051	(0.009)
	0.076	(0.030)	0.150	(0.059)	0.51	0.25	0.013	Static	0	2.08	(0.82)		
SOL-8	0.124	(0.049)	0.251	(0.099)	0.49	0.40	0.021	Static	0	3.15	(1.24)		
								Loading	0-50			0.108	(0.019)
								Static	50	3.51	(1.38)		
								Unloading	50-0			0.108	(0.019)
								Static	0	3.28	(1.29)		
								Loading	0-60			0.108	(0.019)
								Static	60	3.56	(1.40)		
								Unloading	60-0			0.108	(0.019)
								Static	0	3.12	(1.23)		
								Loading	0-90			0.091	(0.016)
								Static	90	3.51	(1.38)		
								Unloading	90-0			0.091	(0.016)
								Static	0	3.35	(1.32)		
								Loading	0-100			0.091	(0.016)
								Static	100	3.35	(1.32)		
								Unloading	100-0			0.091	(0.016)
	0.124	(0.049)	0.251	(0.099)	0.49	0.40	0.021	Static	0	3.30	(1.30)		
SOL-9	0.175	(0.069)	0.358	(0.141)	0.49	0.59	0.029	Static	0	4.62	(1.82)		
								Loading	0-50			0.154	(0.027)
								Static	50	5.89	(2.32)		
								Unloading	50-0			0.154	(0.027)
								Static	0	4.65	(1.83)		
								Loading	0-60			0.154	(0.027)
								Static	60	5.84	(2.30)		
								Unloading	60-0			0.154	(0.027)
								Static	0	4.80	(1.89)		
								Loading	0-90			0.154	(0.027)
								Static	90	5.89	(2.32)		
								Unloading	90-0			0.154	(0.027)
								Static	0	5.23	(2.06)		
								Loading	0-97			0.154	(0.027)
								Static	97	6.30	(2.48)		
								Unloading	97-0			0.160	(0.028)
	0.177	(0.0695)	0.358	(0.141)	0.49	0.60	0.030	Static	0	5.66	(2.23)		

TABLE XVIII. - COMPARISON OF MEASUREMENT TECHNIQUES FOR STEEL

Specimen no.	Condition	Flaw depth, a						Crack growth, Δa						Maximum growth, visual
		Visual		UT		COD		Visual		UT		COD		
		cm	(in.)	cm	(in.)	cm	(in.)	cm	(in.)	cm	(in.)	cm	(in.)	
SOL-1	Initial	0.109	(0.043)	0.124	(0.049)	0.107	(0.042)	--	--	--	--	--	--	
	Final	0.109	(0.043)	0.114	(0.045)	0.107	(0.042)	0.000	(0.000)	-0.010	(-0.004)	0.000	(0.000)	Δr = Δa
SOL-2	Initial	0.052	(0.0205)	0.165	(0.065)	0.051	(0.020)	--	--	--	--	--	--	
	Final	0.053	(0.0207)	0.165	(0.065)	0.030	(0.012)	0.001	(0.002)	0.000	(0.000)	-0.021	(-0.008)	
SOL-3	Initial	0.185	(0.073)	0.180	(0.071)	0.218	(0.086)	--	--	--	--	--	--	
	Final	0.188	(0.074)	0.168	(0.066)	0.198	(0.078)	0.003	(0.001)	-0.012	(-0.005)	-0.020	(-0.008)	
SOL-4	Initial	0.081	(0.032)	0.102	(0.040)	0.081	(0.032)	--	--	--	--	--	--	
	Final	0.081	(0.032)	0.112	(0.044)	0.091	(0.036)	0.000	(0.000)	0.010	(0.004)	0.010	(0.004)	
SOL-5	Initial	0.127	(0.050)	0.124	(0.049)	0.127	(0.050)	--	--	--	--	--	--	
	Final	0.132	(0.052)	0.112	(0.044)	0.127	(0.050)	0.005	(0.002)	-0.012	(-0.005)	0.000	(0.000)	
SOL-6	Initial	0.193	(0.076)	0.175	(0.069)	0.193	(0.076)	--	--	--	--	--	--	
	Final	0.198	(0.078)	0.168	(0.066)	0.224	(0.088)	0.005	(0.002)	-0.007	(-0.003)	0.031	(0.012)	
SOL-7	Initial	0.076	(0.030)	0.112	(0.044)	0.066	(0.026)	--	--	--	--	--	--	
	Final	0.076	(0.030)	0.076	(0.030)	0.071	(0.028)	0.000	(0.000)	-0.036	(-0.014)	0.005	(0.002)	
SOL-8	Initial	0.124	(0.049)	0.127	(0.050)	0.122	(0.048)	--	--	--	--	--	--	
	Final	0.124	(0.049)	0.122	(0.048)	0.107	(0.042)	0.000	(0.000)	-0.005	(-0.002)	-0.015	(-0.006)	
SOL-9	Initial	0.175	(0.069)	0.211	(0.083)	0.163	(0.064)	--	--	--	--	--	--	
	Final	0.177	(0.0695)	0.226	(0.089)	0.168	(0.066)	0.002	(0.0005)	0.015	(0.006)	-0.005	(0.002)	

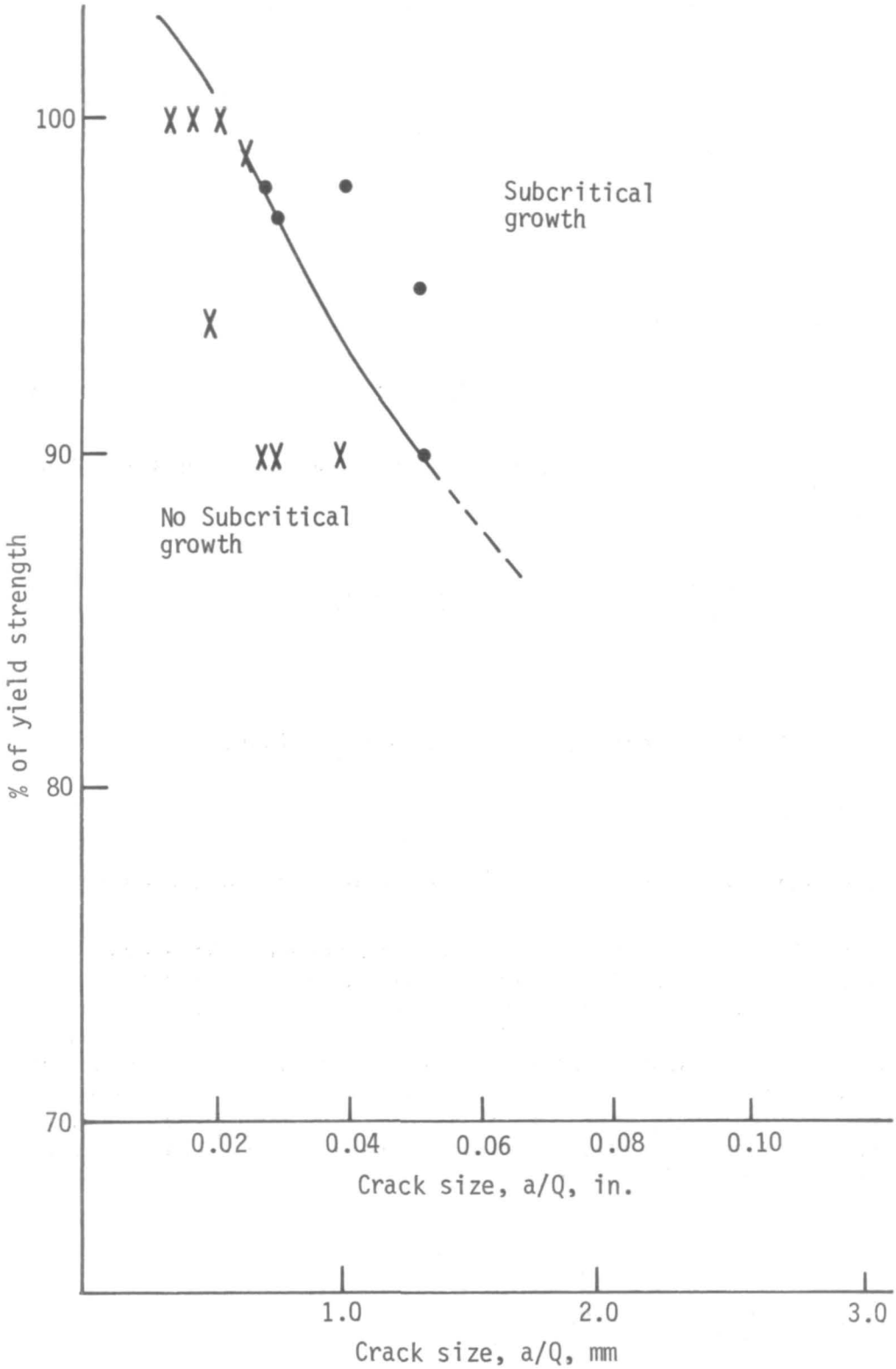

Figure 59. - Subcritical growth threshold for steel.

CRACK CLOSURE CHARACTERISTICS OF SURFACE-FLAWED SPECIMENS UNDER CYCLIC LOADING CONDITIONS

The objective of this effort was to characterize the crack opening and closing behavior of surface-flawed defects using the ultrasonic collimated flaw measuring system for both constant-amplitude and periodic overload cycling conditions.

Background

Much conventional analysis of the growth of cracks subjected to variable loading has been characterized by the crack-growth equations of the form

$$\frac{da}{dN} = f(\Delta K) \tag{3}$$

If the dependence of ΔK on a is neglected, the equation can be written as

$$a_n = a_o + \sum_{i=1}^{n} f\left(\Delta K_i\right) \tag{4}$$

where

a_n = total crack length after n load applications,

a_o = initial crack length,

ΔK_i = range of the stress intensity factor for loading cycle i.

Wheeler (ref. 3) noted discrepancies between these crack growth laws and experimentally obtained data. He therefore proposed a crack retardation model that would empirically account for what happens at the tip of the crack when a high overload is applied to a constant-amplitude load spectrum. He believed that this overload would create a large plastic zone ahead of the crack tip, and this zone would retard growth while the crack was growing through it. He proposed an empirical relation that provides a modified form of equation 4 as

$$a_n = a_o + \sum_{i=1}^{n} C_{pi}\, f\left(\Delta K_i\right) \tag{5}$$

where C_{pi} is the retardation parameter. This factor should have a magnitude that would delay crack growth after application of a high load. To do this, it should have a minimum value near zero immediately after a high-load application, and should later increase to a value of one. The retardation parameter could then be defined as

$$C_p = \left(\frac{R_y}{a_p - a}\right)^m$$

where (fig. 60):

R_y = size of current plastic zone,

$a_p - a$ = distance from crack tip to elastic-plastic interface,

m = shaping parameter, and provides the ability to shape the retardation parameter to the test data.

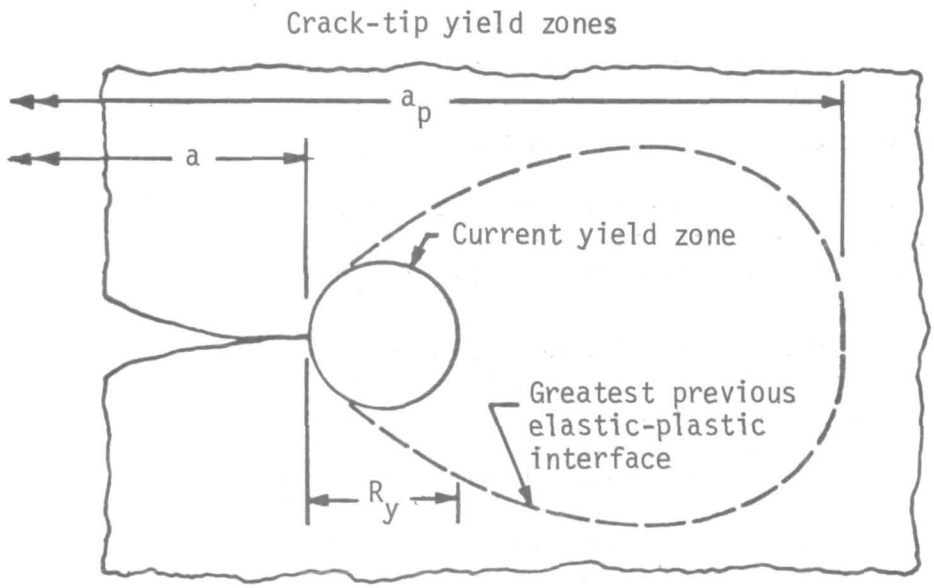

Figure 60. - Basic principle of Wheeler crack-growth retardation model.

Willenborg, Engle, and Wood (ref. 4) suggested a retardation model based on an "effective stress." This concept retards crack growth by effectively reducing the level of applied loading after an overload, and may be shown as

$$\sigma_{eff} = \sigma_a - \sigma_{red} \tag{7}$$

where:

σ_a = applied stress,

σ_{red} = reducing stress.

The reducing stress is defined as

$$\sigma_{red} = \sigma_{a_p} - \sigma_{max} \tag{8}$$

where:

σ_{a_p} = no-retardation stress,

σ_{max} = maximum applied cyclic stress.

The magnitude of no-retardation stress, σ_{a_p}, is the stress required to make the current plastic zone coincident with the elastic-plastic interface. Equation 8 shows that steady-state crack growth prevails if σ_{a_p} equals σ_{max}.

Gallagher (ref. 5) generalized crack-growth retardation models of both Wheeler and Willenborg by reformulating them in a stress-intensity-factor format. He also presented the concept of a load interaction zone, z, that defines the zone of influence of any load on subsequent crack growth behavior.

By assuming that the load interaction zone was a function of the crack-tip plastic-zone radius, the maximum stress intensity factor, K^{∞}_{max}, and the material yield strength, σ_{ys}, Gallagher developed the following relationship

$$K^{*}_{max} = K^{OL}_{max} \sqrt{1 - \frac{\Delta a}{z_{OL}}} \tag{9}$$

where:

K^*_{max} = no-retardation stress intensity factor,

$K^{OL}_{max} = K_{max}$ for application of overload,

Δ_a = crack movement following overload application,

z_{OL} = load interaction zone created by overload.

Wheeler's retardation model of equation 5 was generalized by Gallagher is terms of the stress intensity factors as

$$\frac{da}{dN} = C \left[\left(\frac{K_{max}}{K^*_{max}} \right)^{\frac{2m}{p}} \cdot \Delta K \right]^p \tag{10}$$

where:

K^{∞}_{max} = maximum remote stress intensity factor.

Gallagher generalized Willenborg's model and equations 7 and 8 to yield

$$K_{eff} = K^{\infty} - K_{red} \tag{11}$$

and

$$K_{red} = K^*_{max} - K^{\infty}_{max} \tag{12}$$

From equation 12, it is obvious that if $K^*_{max} = K^{\infty}_{max}$, steady-state crack growth will be present.

Reformulation of Willenborg's model has eliminated the restriction of the original model in which stresses applied after an overload were required to be more than one-half the magnitude of the overload stresses.

The fundamental idea expressed by Elber (ref. 6 and 7) regarding prediction of crack-growth retardation effects is that crack closure occurs because of the presence of the plastic zone at the crack tip. The plastic deformations render the crack

surfaces incompatible so they interfere on unloading and effectively hold the crack open. This means that, in cyclic loading situations, the $\Delta\sigma$ used to calculate ΔK crack growth equations of the form

$$\frac{da}{dN} = f(\Delta K)$$

should not be

$$\Delta\sigma = \sigma_{max} - \sigma_{min}$$

but

$$\Delta\sigma = \sigma_{max} - \sigma_c$$

where σ_c is the stress at which closure occurs.

This concept permits description of crack-growth retardation effects in the following way. When the crack propagates under constant-amplitude conditions, a certain level of σ_c is established. When an overload occurs, this value increases markedly because the plasticity effects are increased. This decreases $\Delta\sigma$ and thus da/dN, causing the retardation effect. As cycling continues, the crack grows at the slower rate; but, as it grows, the overload plasticity effect becomes less important because the crack tip is deeper and eventually away from the overload plastic zone.

If a reliable crack-growth equation like equation 13 is available, this concept can provide the ability to model the retardation behavior described. The information necessary to do so is some functional relationship describing the closure stress, σ_c, in terms of steady-state cyclic loading parameters, and the position of the crack tip relative to the overload-produced plastic zone.

Approach

The equipment and ultrasonic flow monitoring and crack-opening displacemnt techniques used for this study were identical to those previously described. The principal difference between the measurements taken in this work and those reported earlier was that, rather than map the entire flaw shape for each load increment, only the crack depth, a, was monitored. By plotting a single trace for each load increment, a pattern was obtained that readily illustrated the nature of the crack opening and closing. Figure 61 is a typical data record.

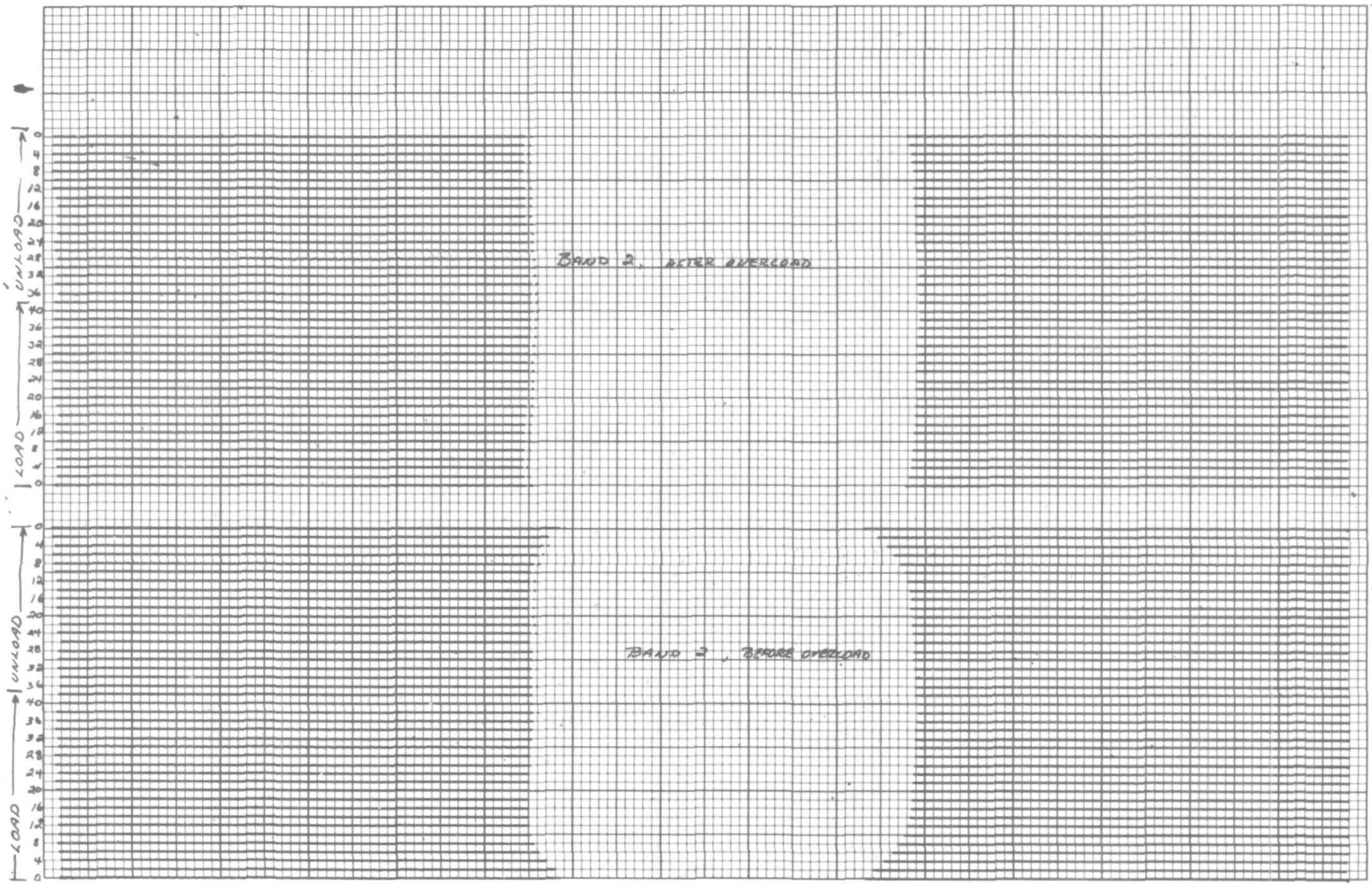

Figure 61. - Typical data record.

To demonstrate the effect of overloading, duplicate specimens of each defect configuration were prepared. One was evaluated by cycling without overloading. The second was periodically overloaded.

Results

Using 2219-T87 aluminum alloy stock, 0.64-cm (0.25-in.) thick, a series of specimens with nominal flaw shapes (a/2c) of 0.2, 0.35, and 0.5 were approximately 25 mm (0.10 in.) [a/t = 0.40]. Specimens of each shape were constant-amplitude cyclically loaded to produce crack growth at 40, 45, 50, and 55% of yield strength. Cycling was periodically interrupted and the specimen incrementally loaded to produce both ultrasonic and crack-opening displacement measurements. To give maximum reading accuracy, the latter measurement was recorded from a digital voltmeter.

Data were plotted as stress versus crack depth, as shown in figure 62 (bottom plot). Note that crack size initially increased with increasing load, then became independent of load level. The unloading curve closely matched the loading curve.

Using constant-amplitude data as a guide, the specimen containing the matching-defect configuration was cycled to give a crack depth of approximately the same value as shown by the first load-unload curve in the constant-amplitude series. At this point, cycling was halted and an incremental load-unload curve was obtained. The specimen was then loaded to 70% of yield strength and another incremental load-unload series taken. The curve obtained after the overload did not show a change in defect size as a function of load. Cycling was resumed and periodic load-unload measurements taken. The data show that, as crack growth proceeds, the opening and closing behavior begins to reappear. Cycling was continued until the change in crack opening and closing at a particular crack size was approximately the same as that shown for the constant-amplitude-cycled data. At this point, the effects of overloading were deemed to be overcome. Figure 62 (upper plot) illustrates this behavior. The overload cycle $\left(70\% \text{ of } \sigma_{ys}\right)$ was again applied and cycling reinstated. Cycling was continued until overload effects were overcome. Typically, three overloads were applied to each specimen.

Tests performed on eleven other aluminum specimens showed similar behavior. Figures 63 through 73 show data from the ultrasonic results.

Crack-opening displacement plots made from the digital data showed the same type of behavior as found by ultrasonic measurements. Figures 74 through 85 present the displacement results.

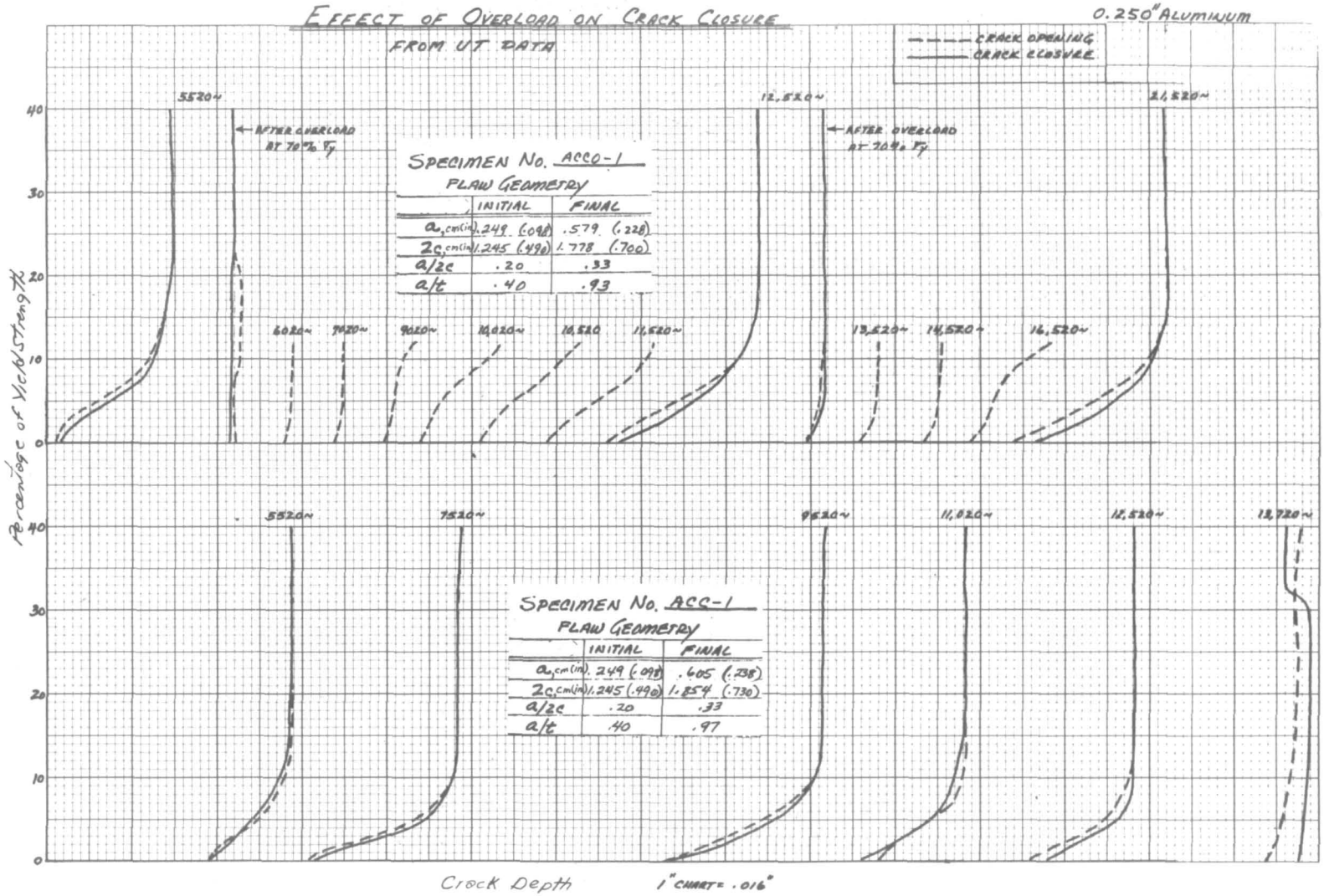

Figure 62. - Ultrasonic data illustrating effect of overload on crack closure for specimens ACC-1 and ACCO-1.

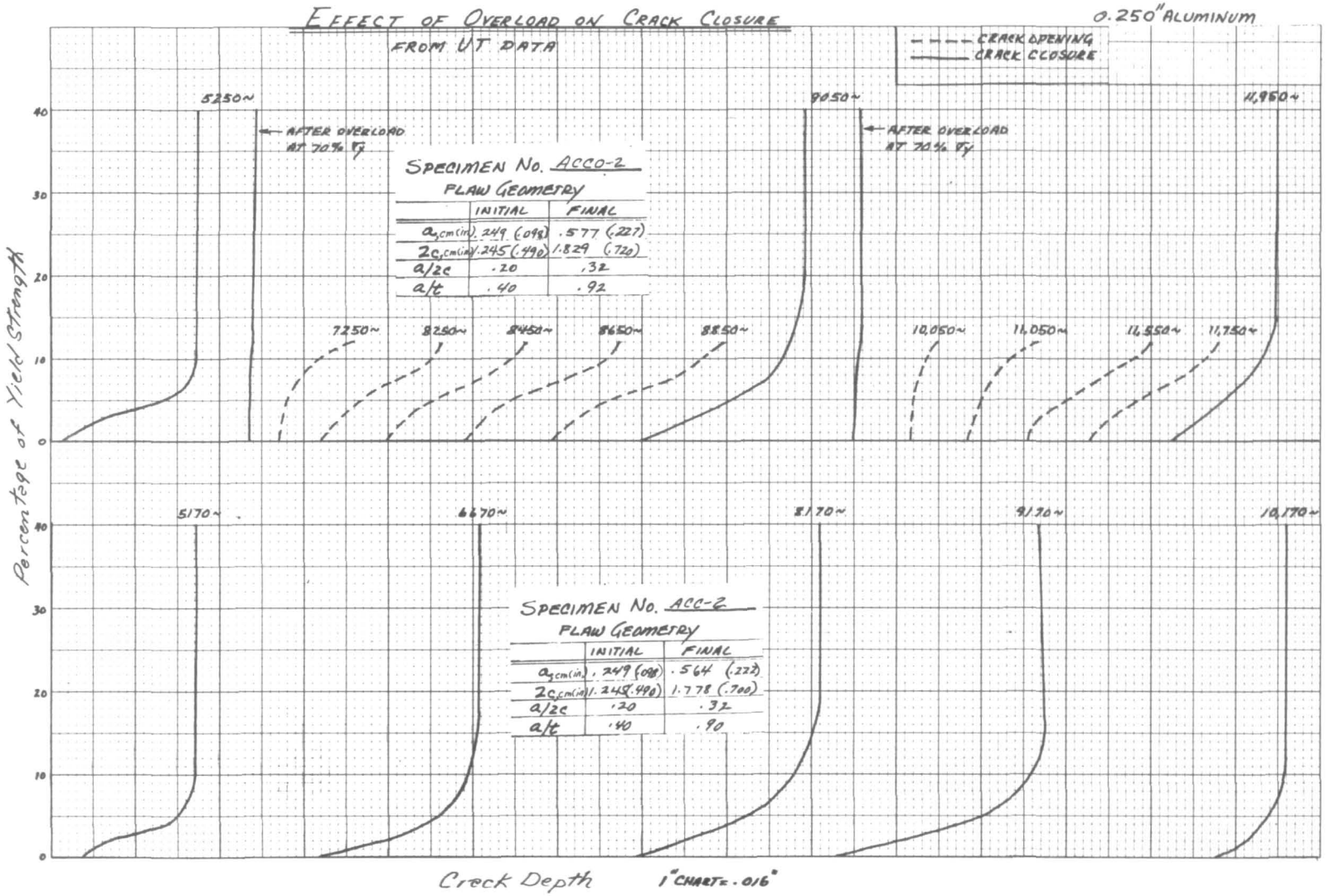

Figure 63. - Ultrasonic data illustrating effect of overload on crack closure for specimens ACC-2 and ACCO-2.

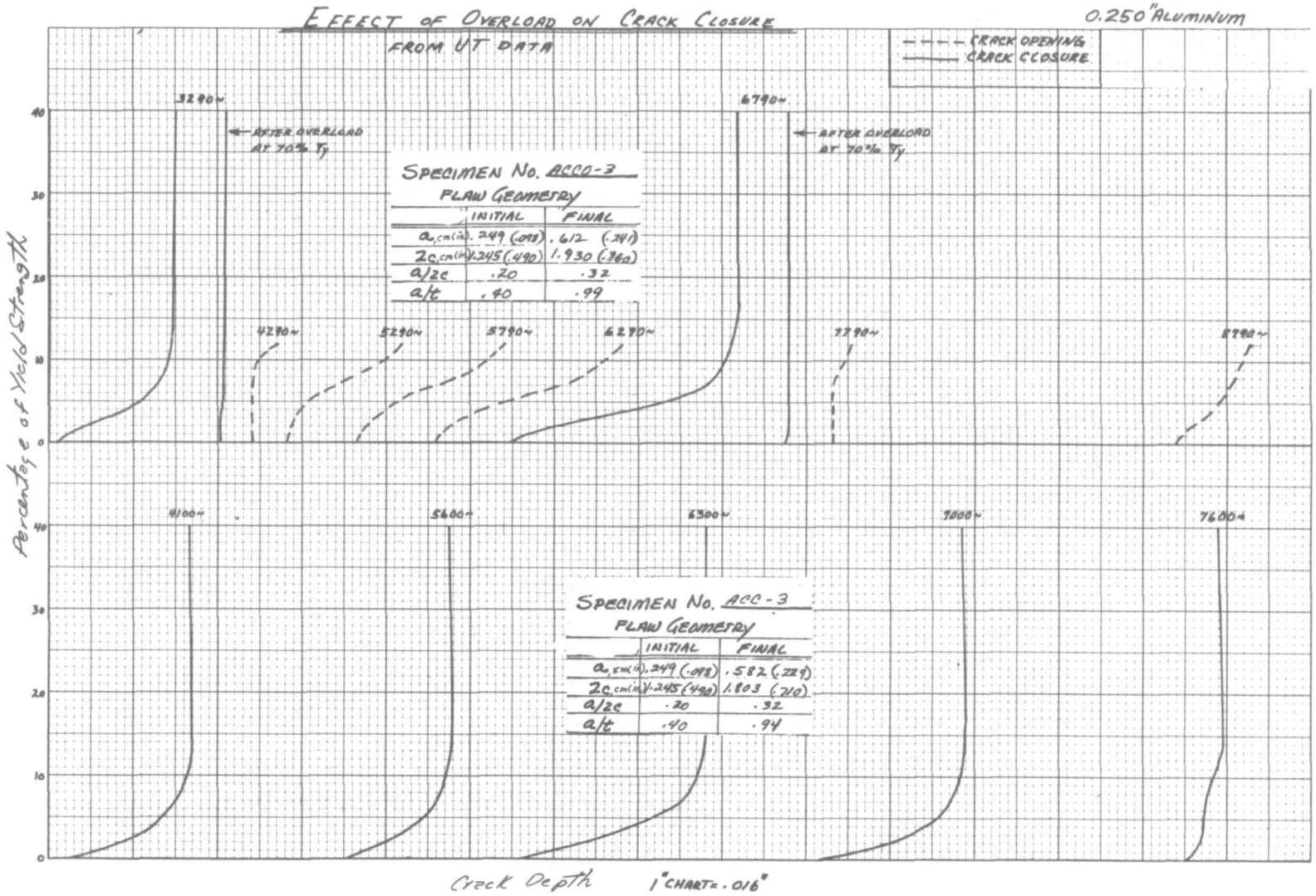

Figure 64. - Ultrasonic data illustrating effect of overload on crack closure for specimens ACC-3 and ACCO-3.

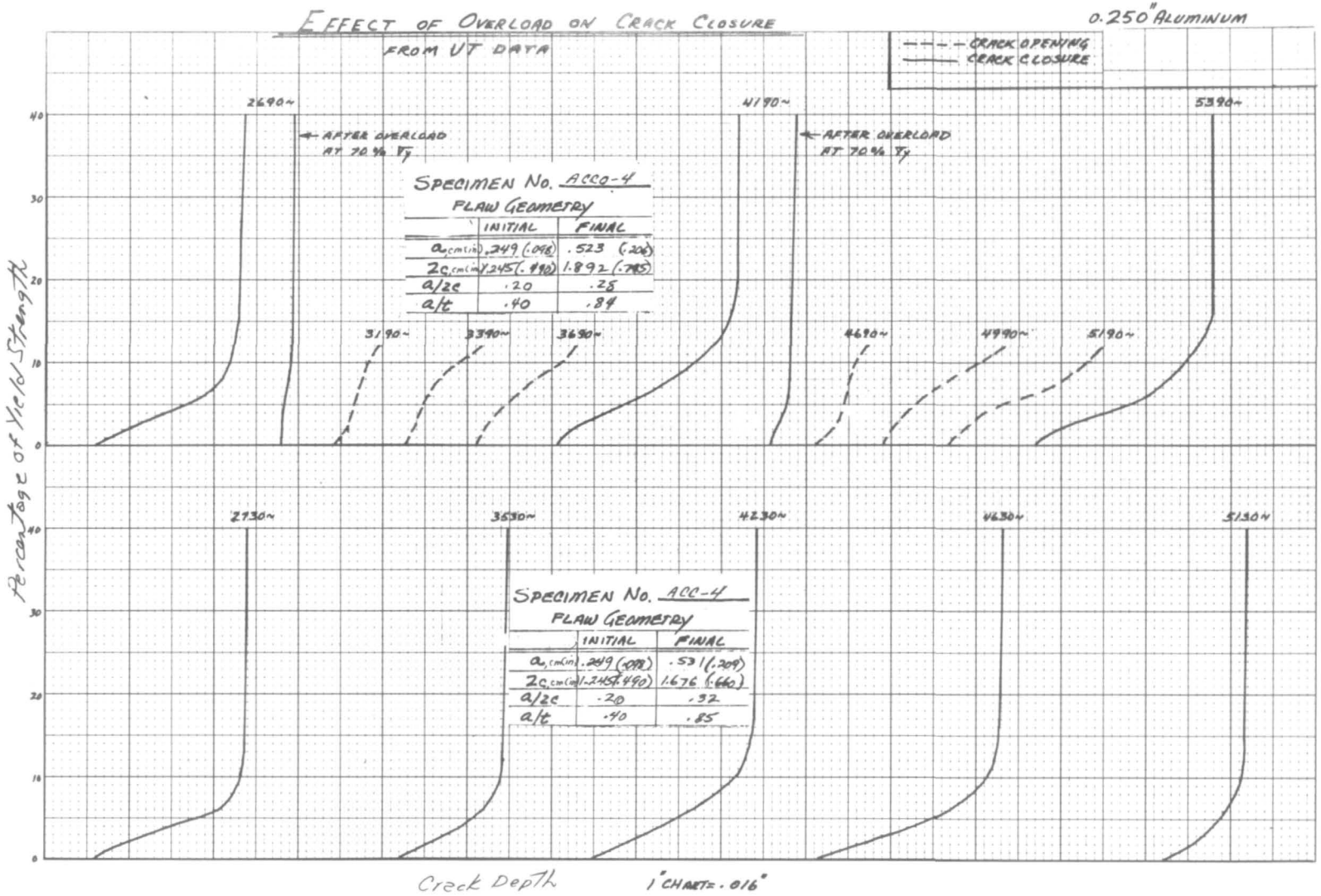

Figure 65. - Ultrasonic data illustrating effect of overload on crack closure for specimens ACC-4 and ACCO-4.

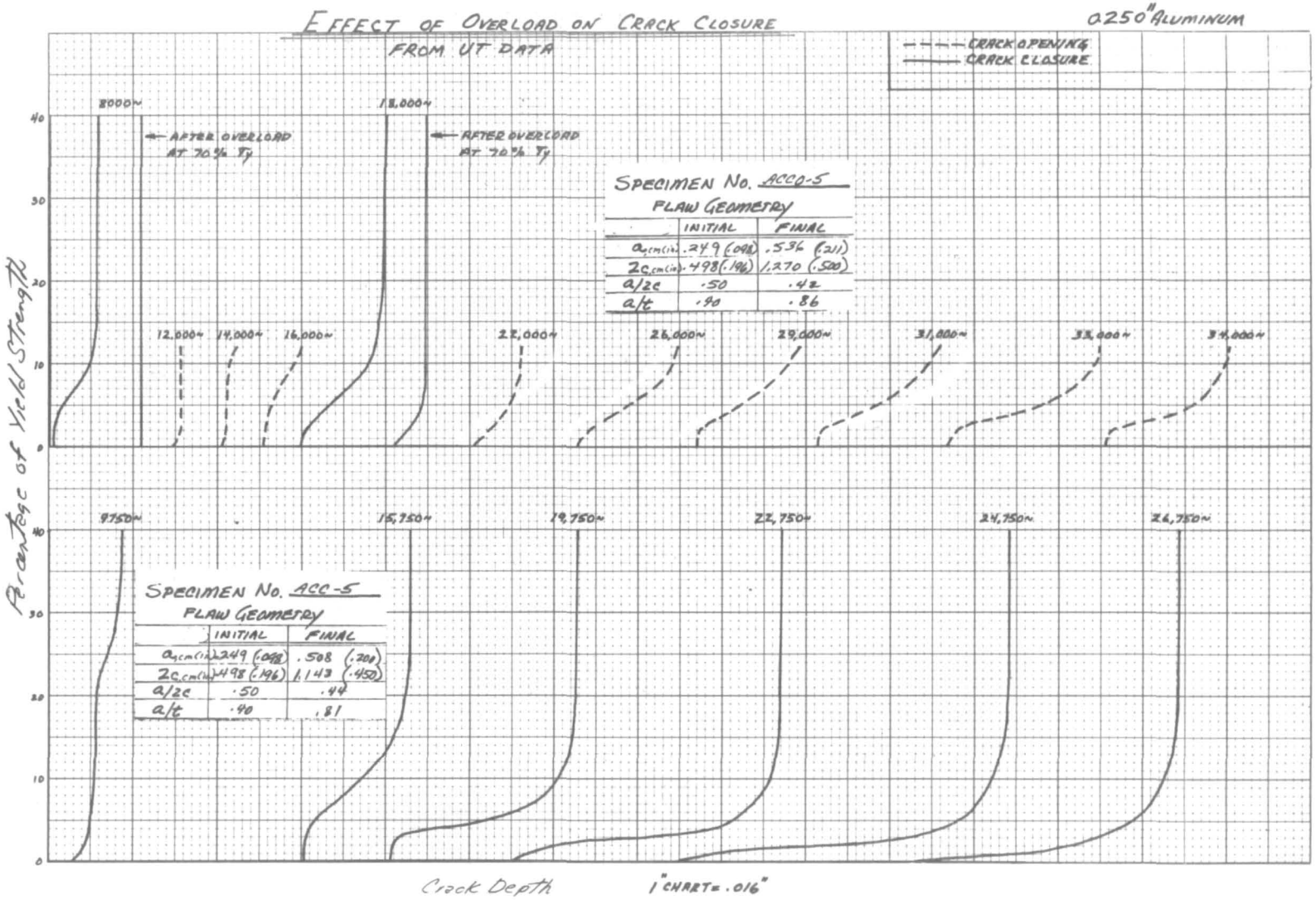

Figure 66. - Ultrasonic data illustrating effect of overload on crack closure for specimens ACC-5 and ACCO-5.

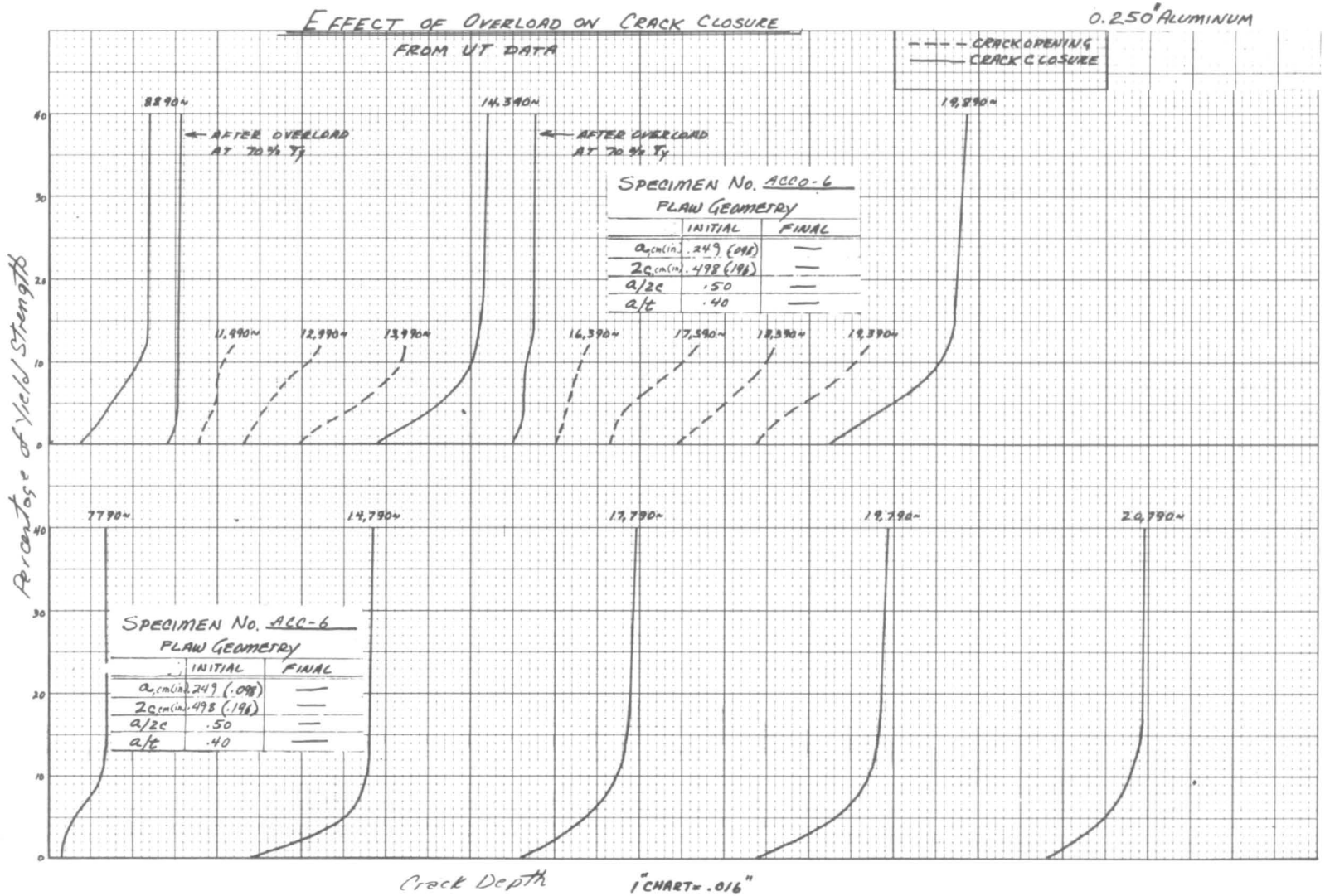

Figure 67. - Ultrasonic data illustrating effect of overload on crack closure for specimens ACC-6 and ACCO-6.

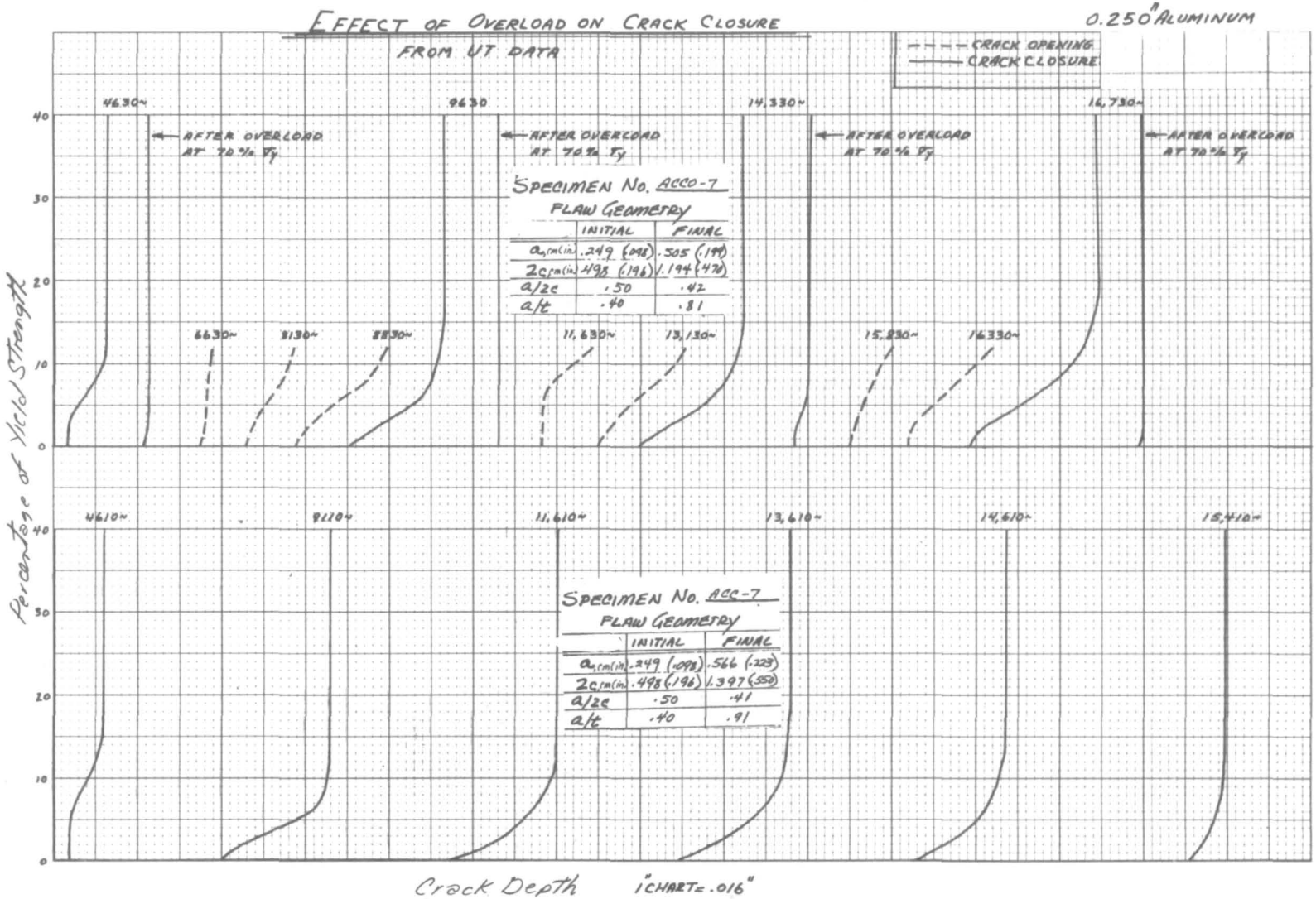

Figure 68. - Ultrasonic data illustrating effect of overload on crack closure for specimens ACC-7 and ACCO-7.

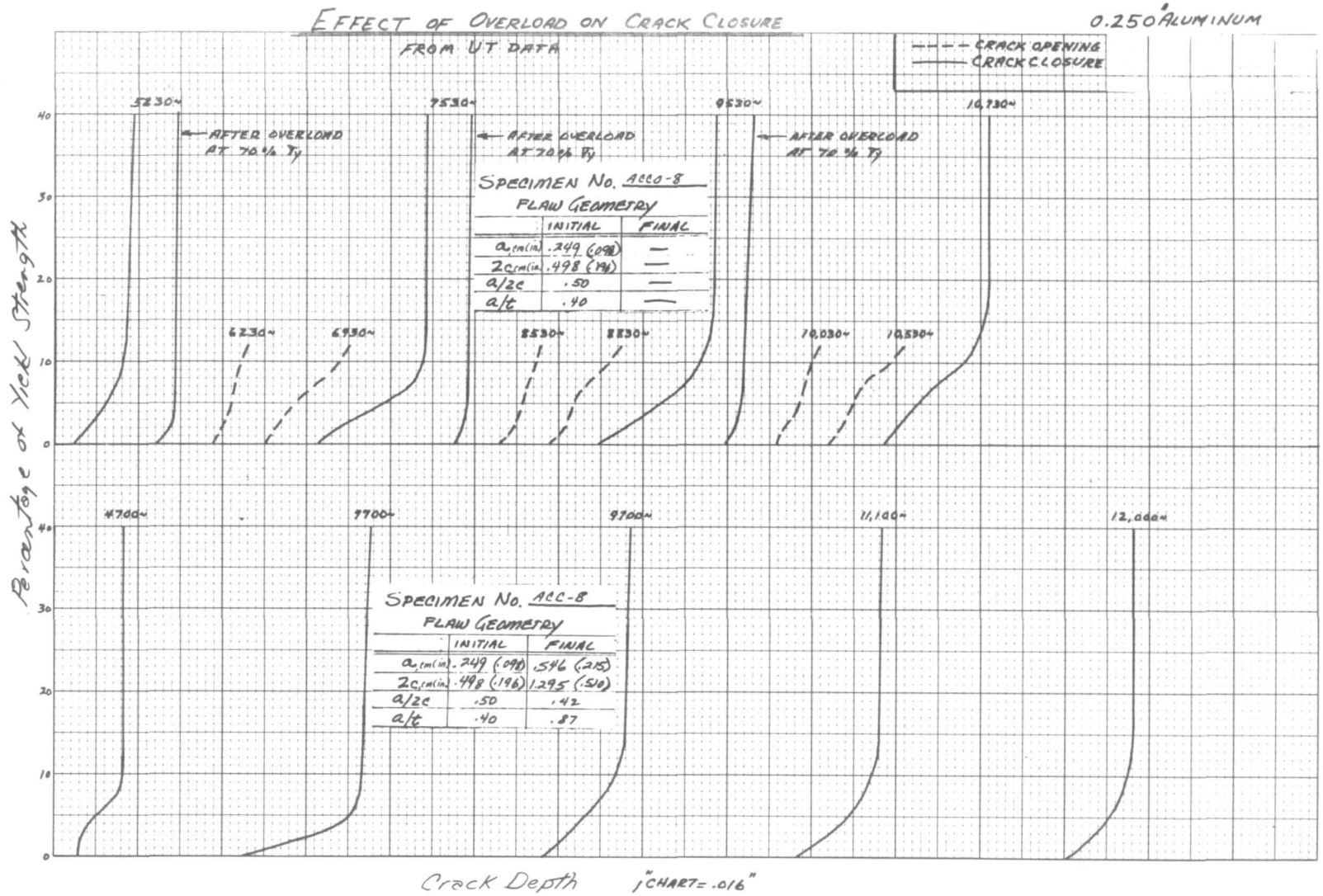

Figure 69. - Ultrasonic data illustrating effect of overload on crack closure for specimens ACC-8 and ACCO-8.

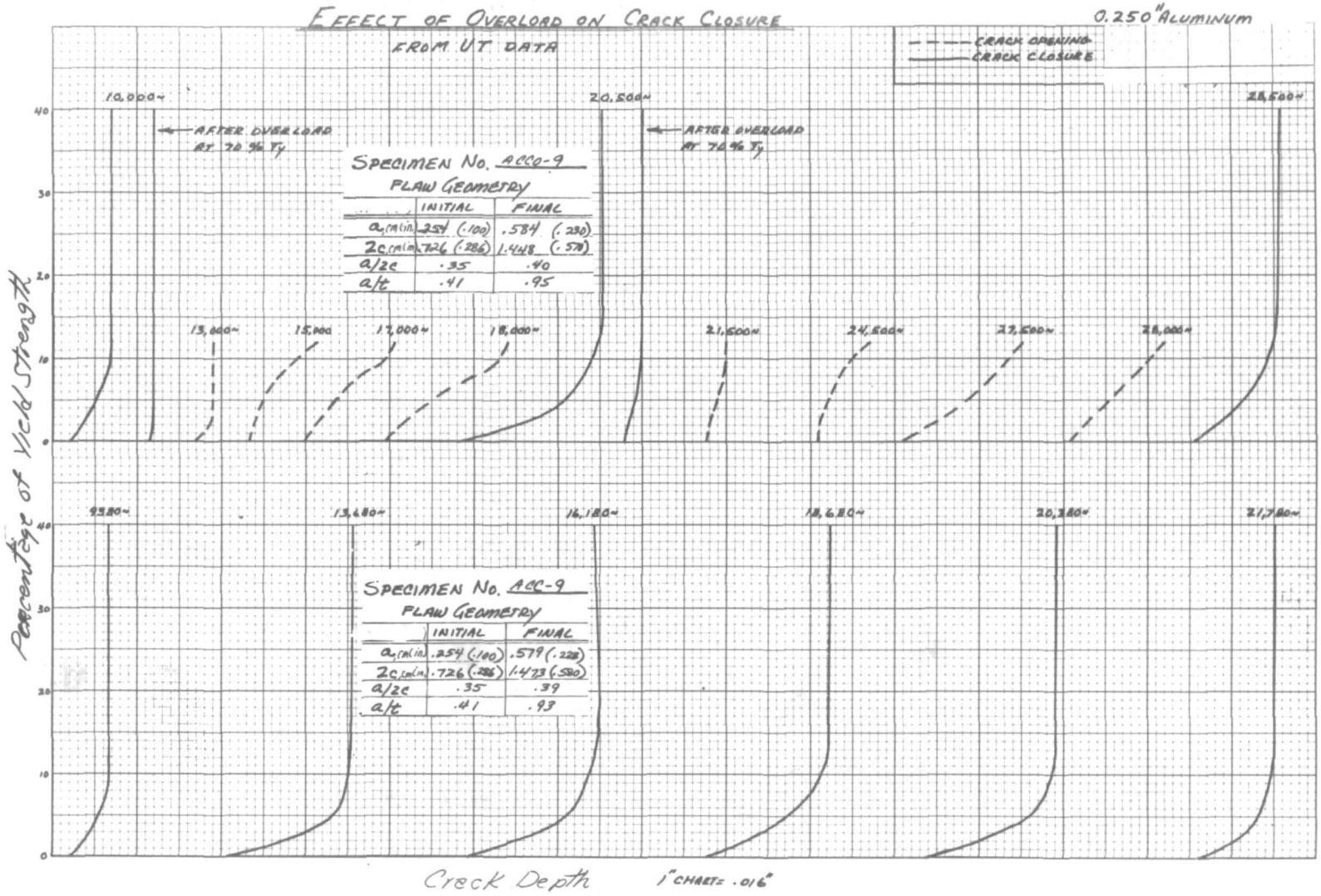

Figure 70. - Ultrasonic data illustrating effect of overload on crack closure for specimens ACC-9 and ACCO-9.

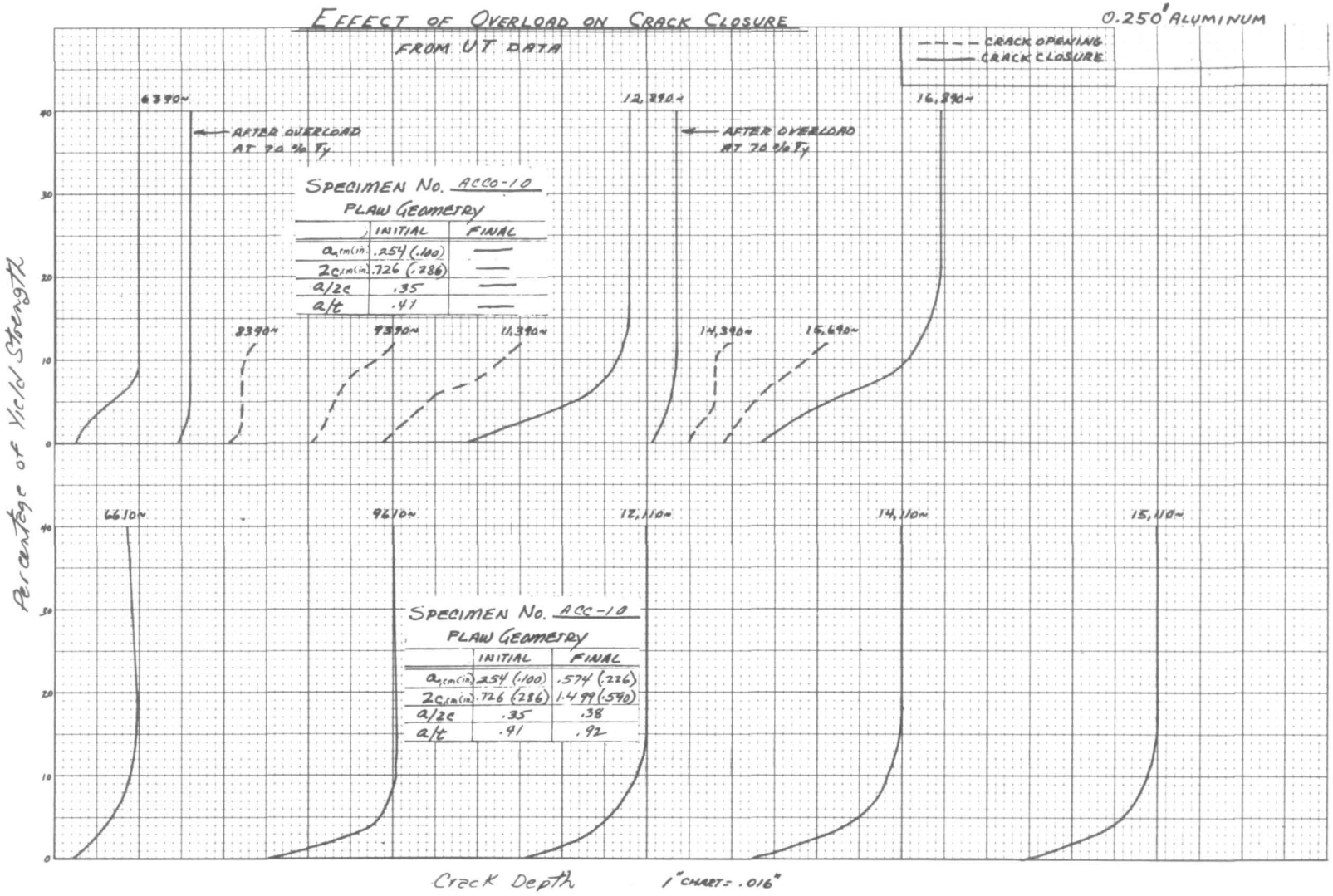

Figure 71. - Ultrasonic data illustrating effect of overload on crack closure for specimens ACC-10 and ACCO-10.

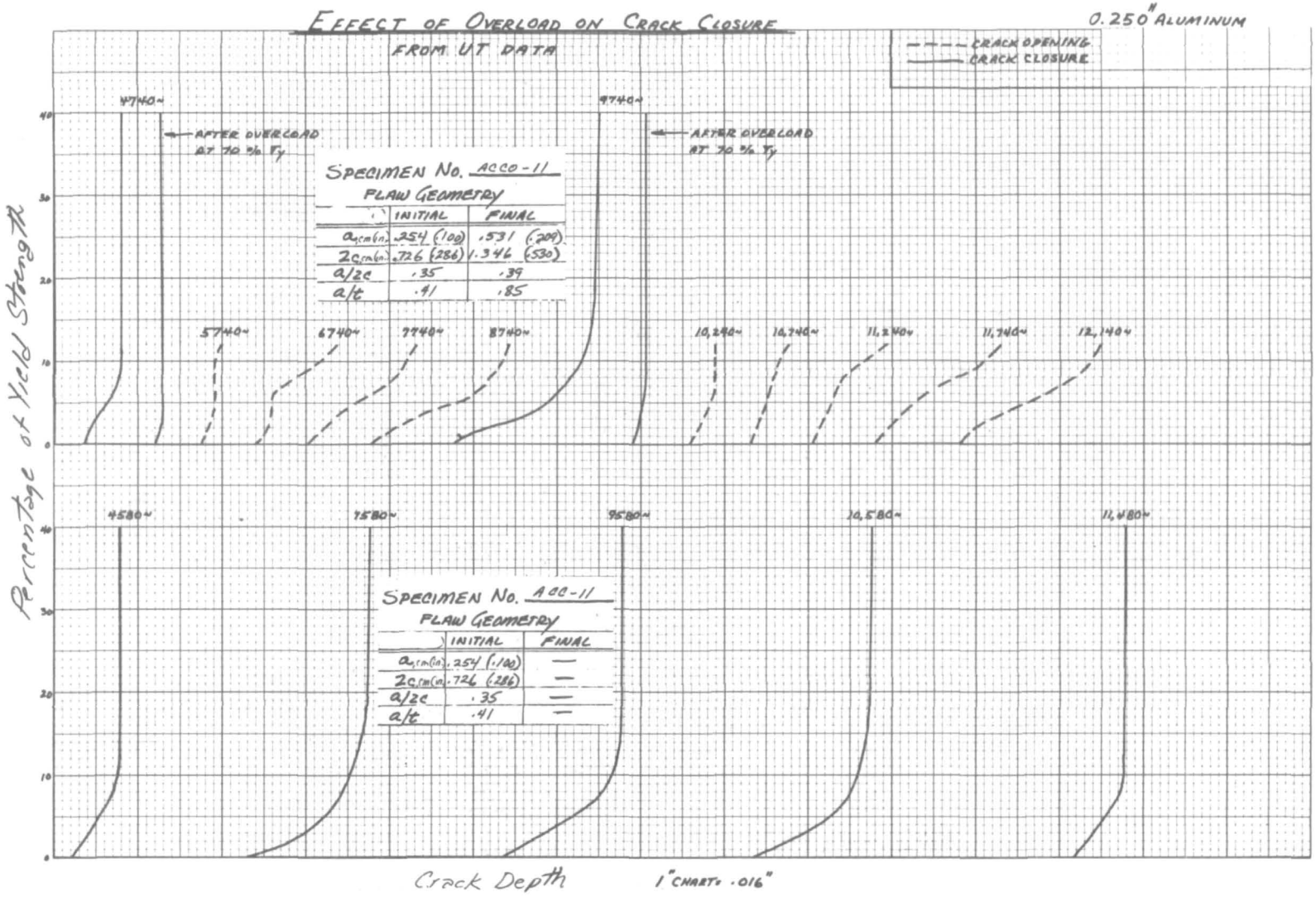

Figure 72. - Ultrasonic data illustrating effect of overload on crack closure for specimens ACC-11 and ACCO-11.

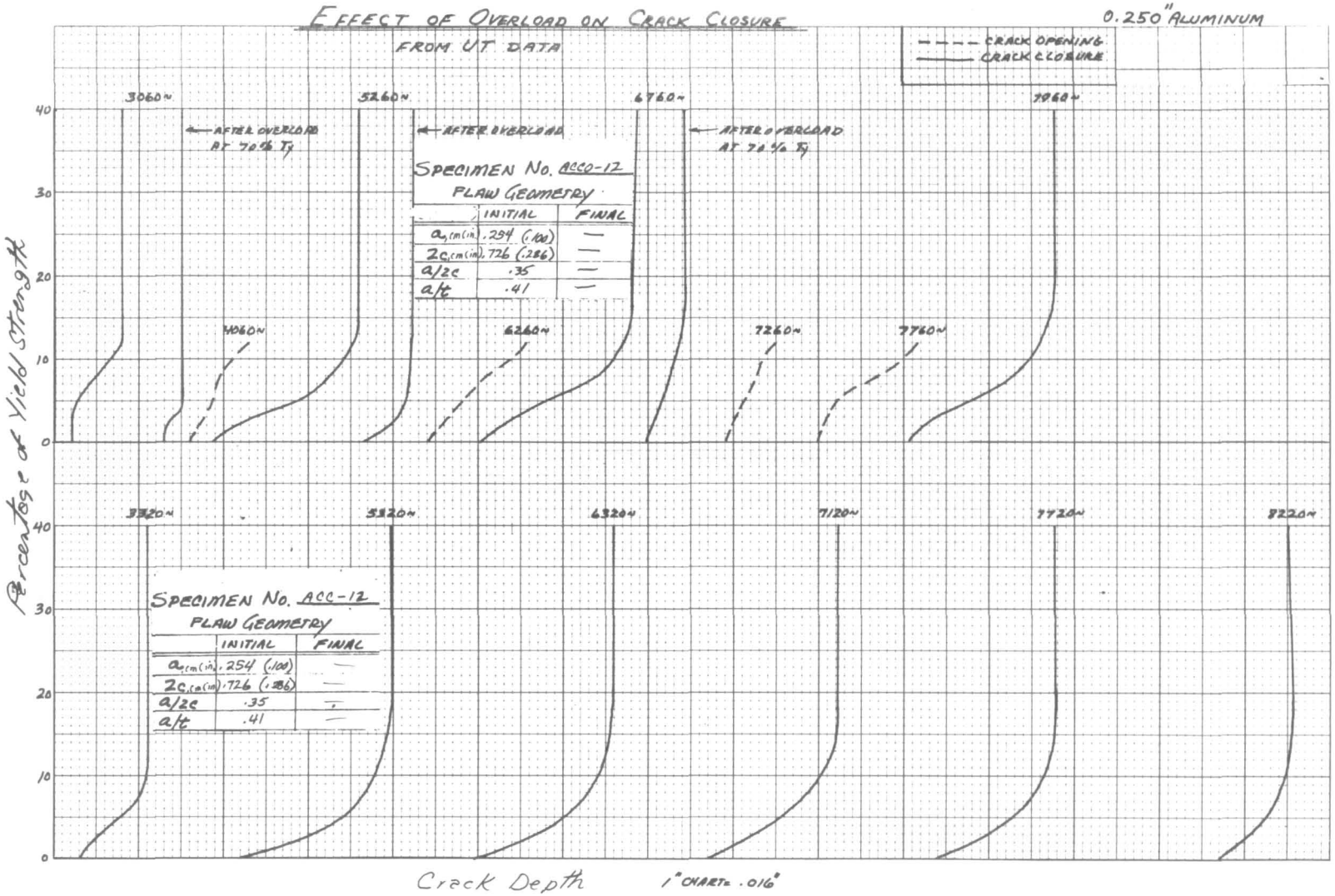

Figure 73. - Ultrasonic data illustrating effect of overload on crack closure for specimens ACC-12 and ACCO-12.

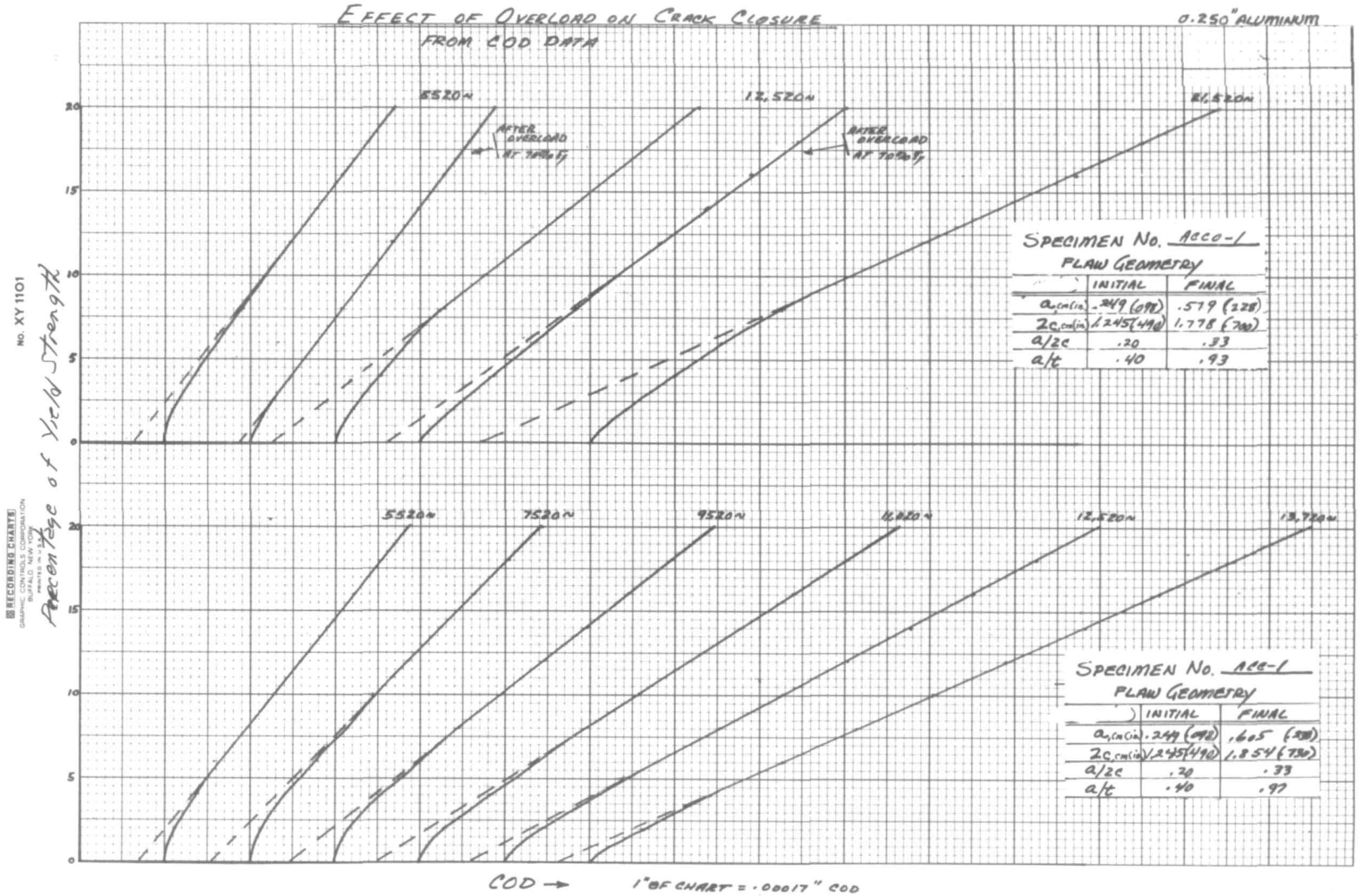

Figure 74. - COD data illustrating effect of overload on crack closure for specimens ACC-1 and ACCO-1.

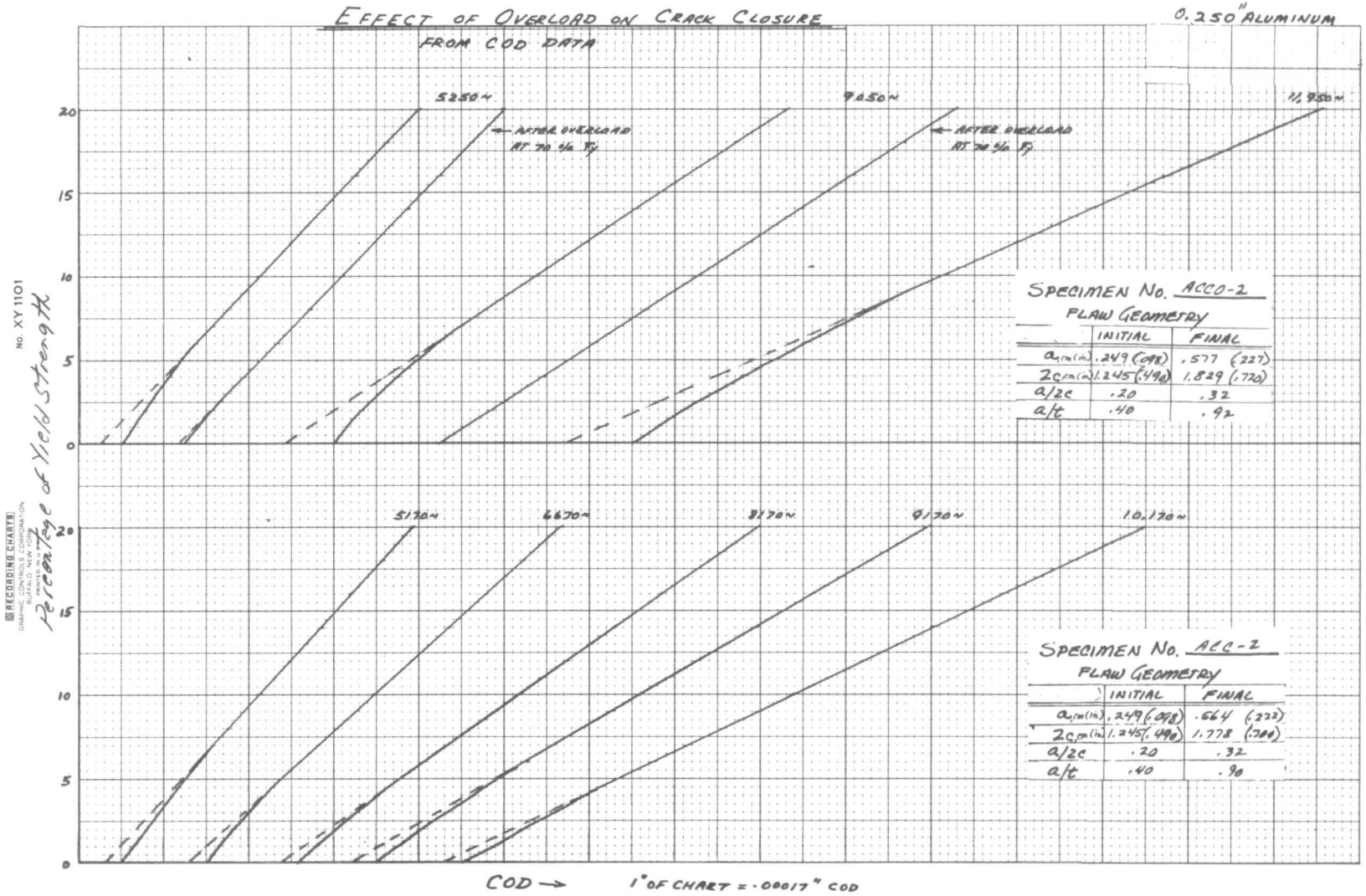

Figure 75. - COD data illustrating effect of overload on crack closure for specimens ACC-2 and ACCO-2.

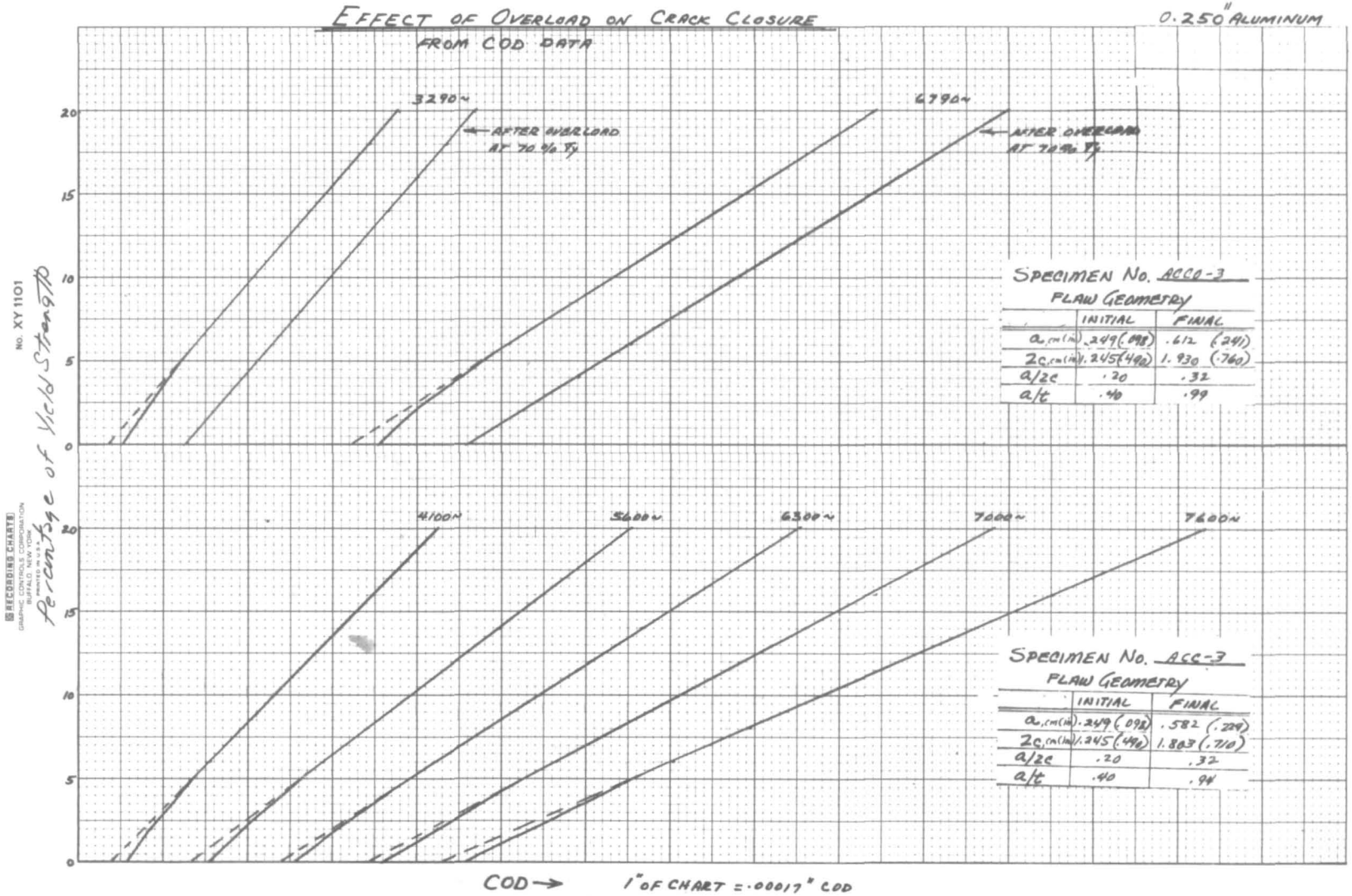

Figure 76. - COD data illustrating effect of overload on crack closure for specimens ACC-3 and ACCO-3

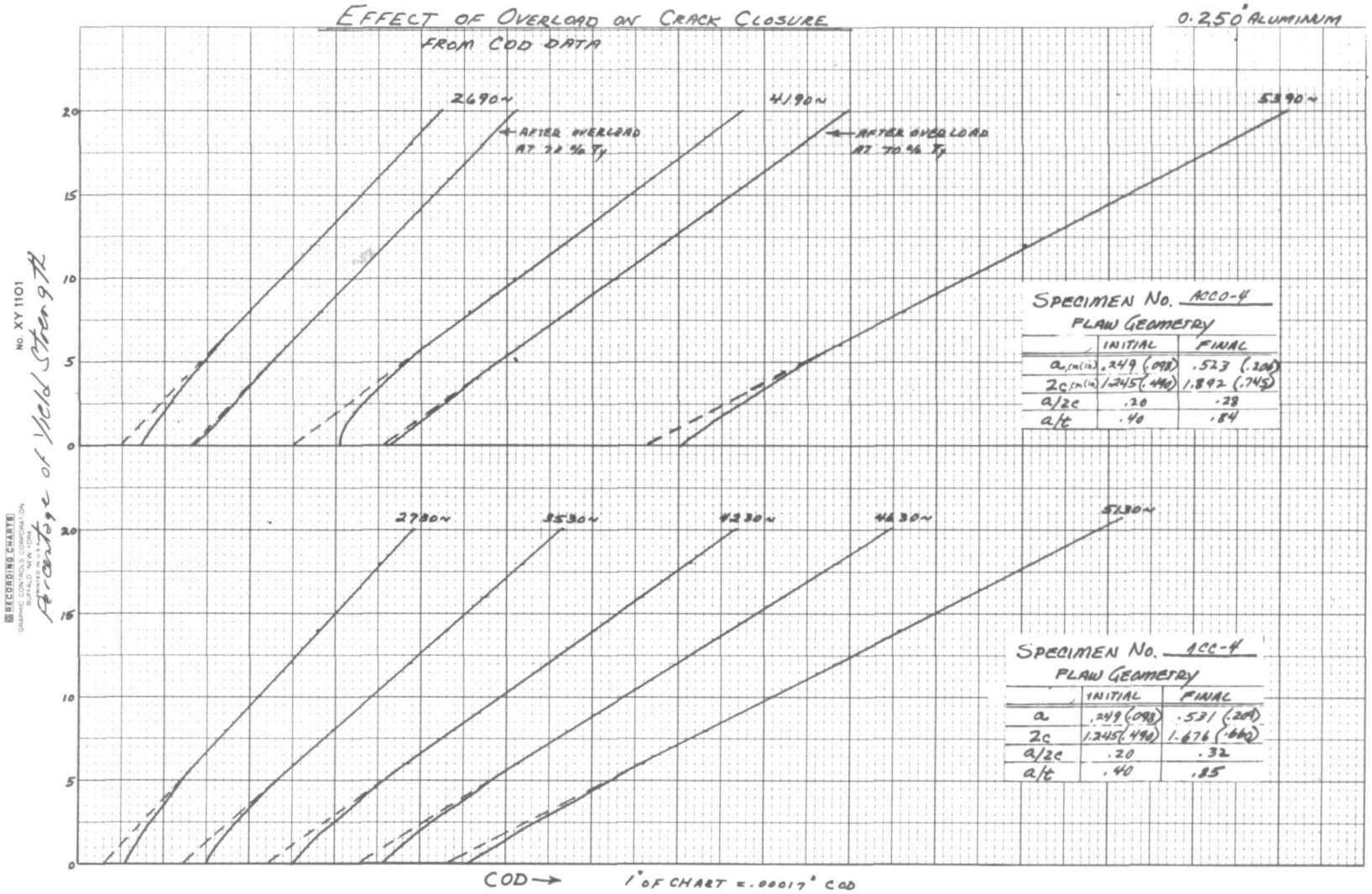

Figure 77. - COD data illustrating effect of overload on crack closure for specimens ACC-4 and ACCO-4.

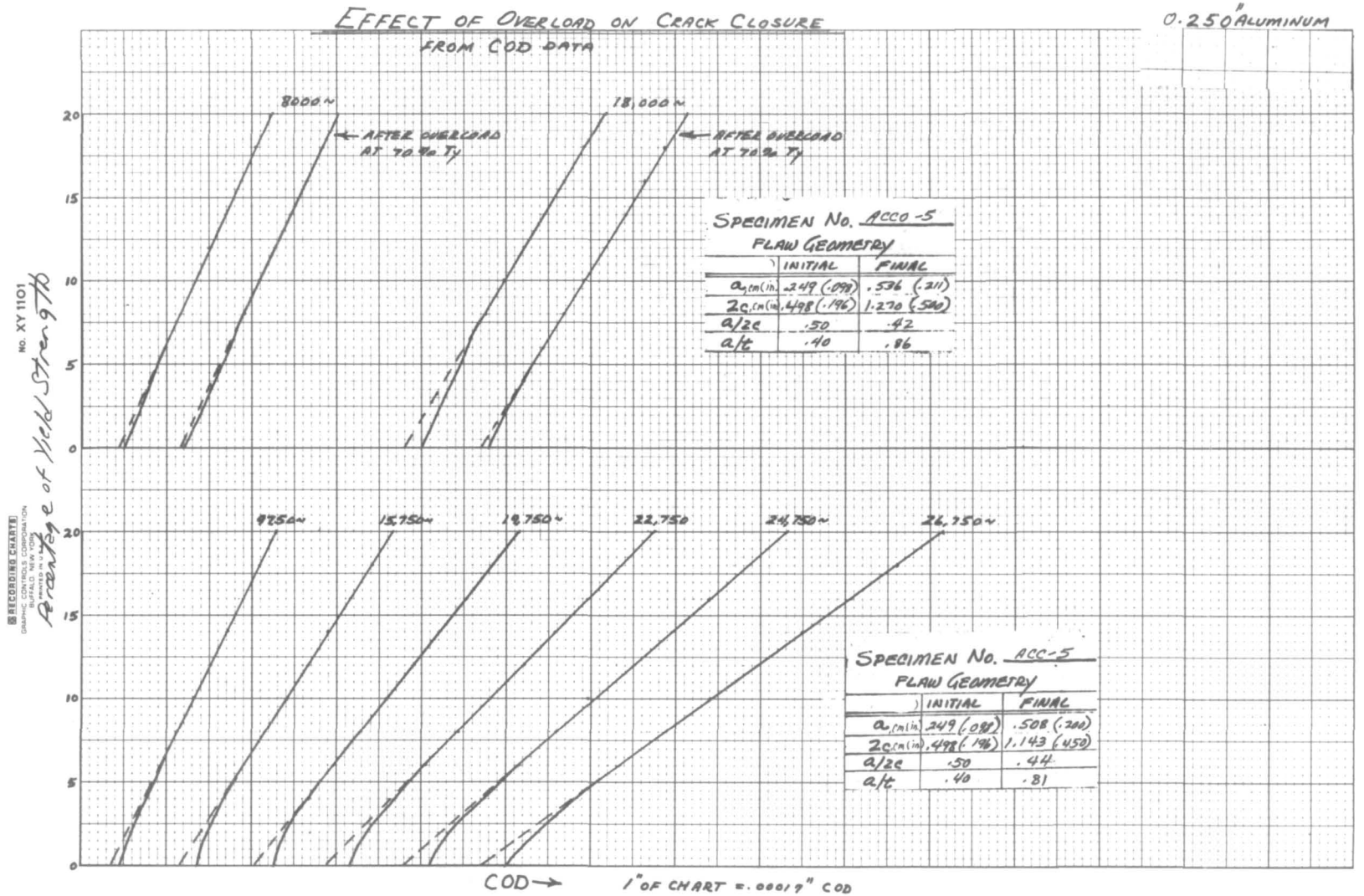

Figure 78. - COD data illustrating effect of overload on crack closure for specimens ACC-5 and ACCO-5.

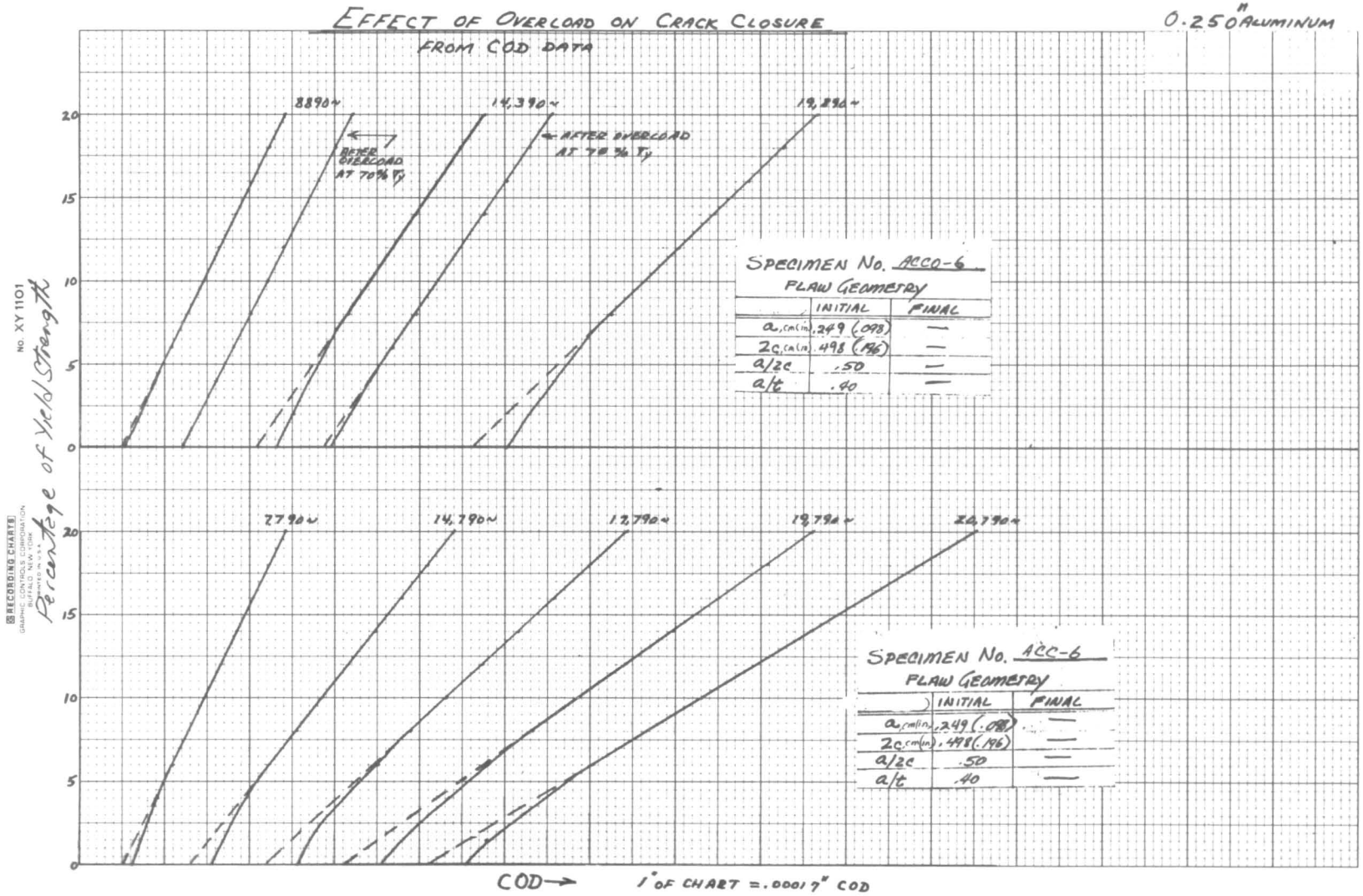

Figure 79. - COD data illustrating effect of overload on crack closure for specimens ACC-6 and ACCO-6

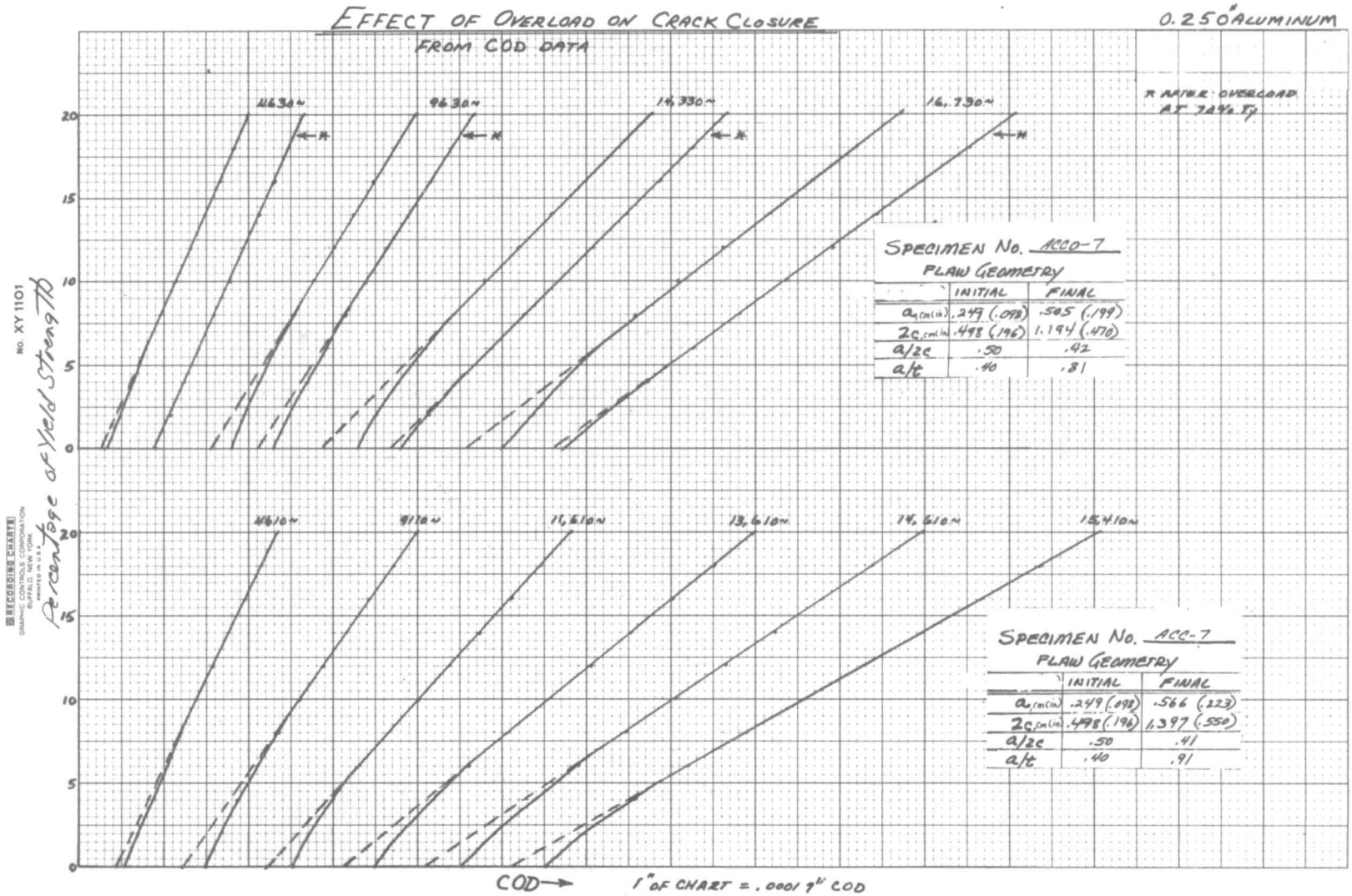

Figure 80. - COD data illustrating effect of overload on crack closure for specimens ACC-7 and ACCO-7.

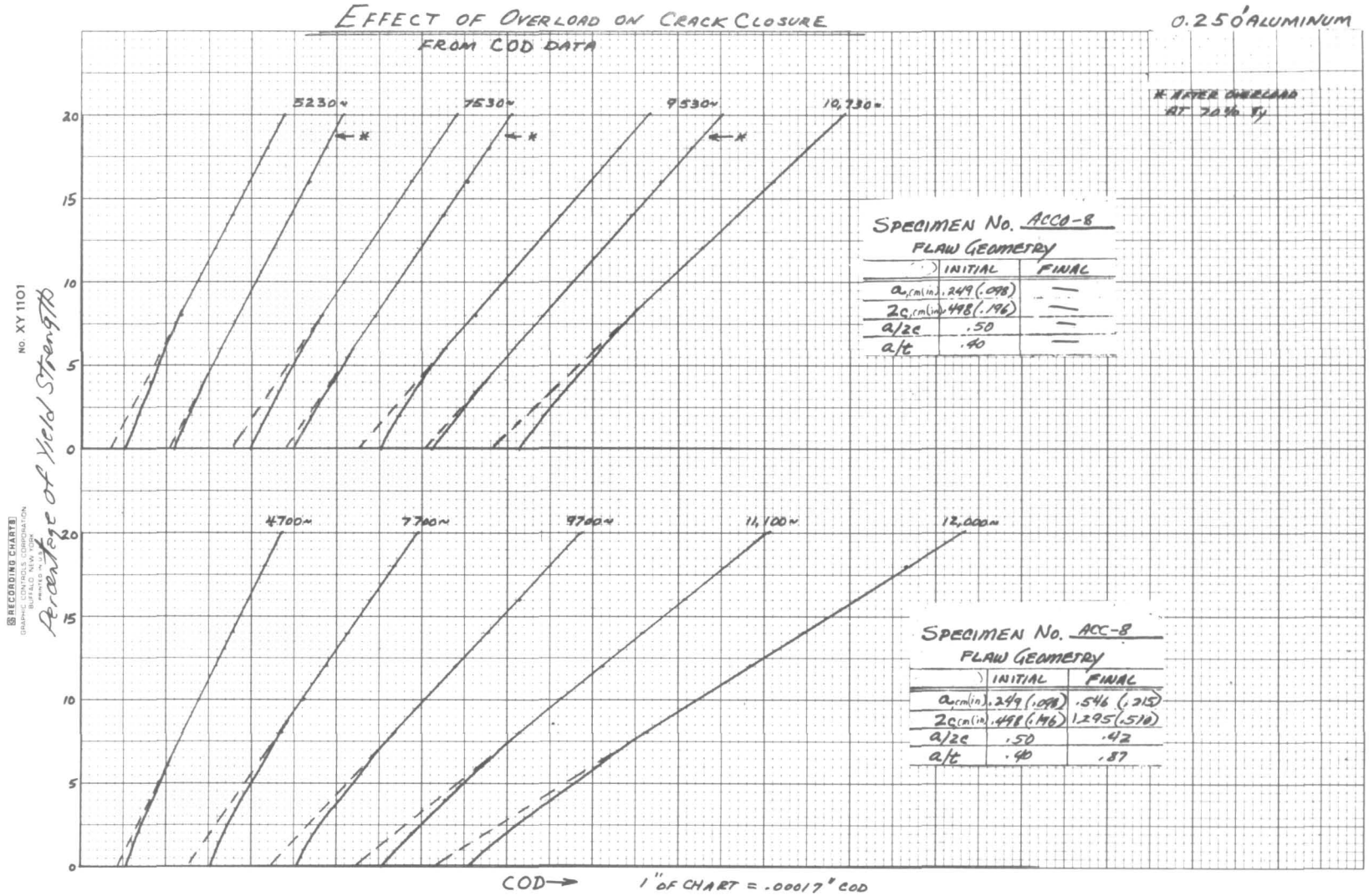

Figure 81. - COD data illustrating effect of overload on crack closure for specimens ACC-8 and ACCO-8.

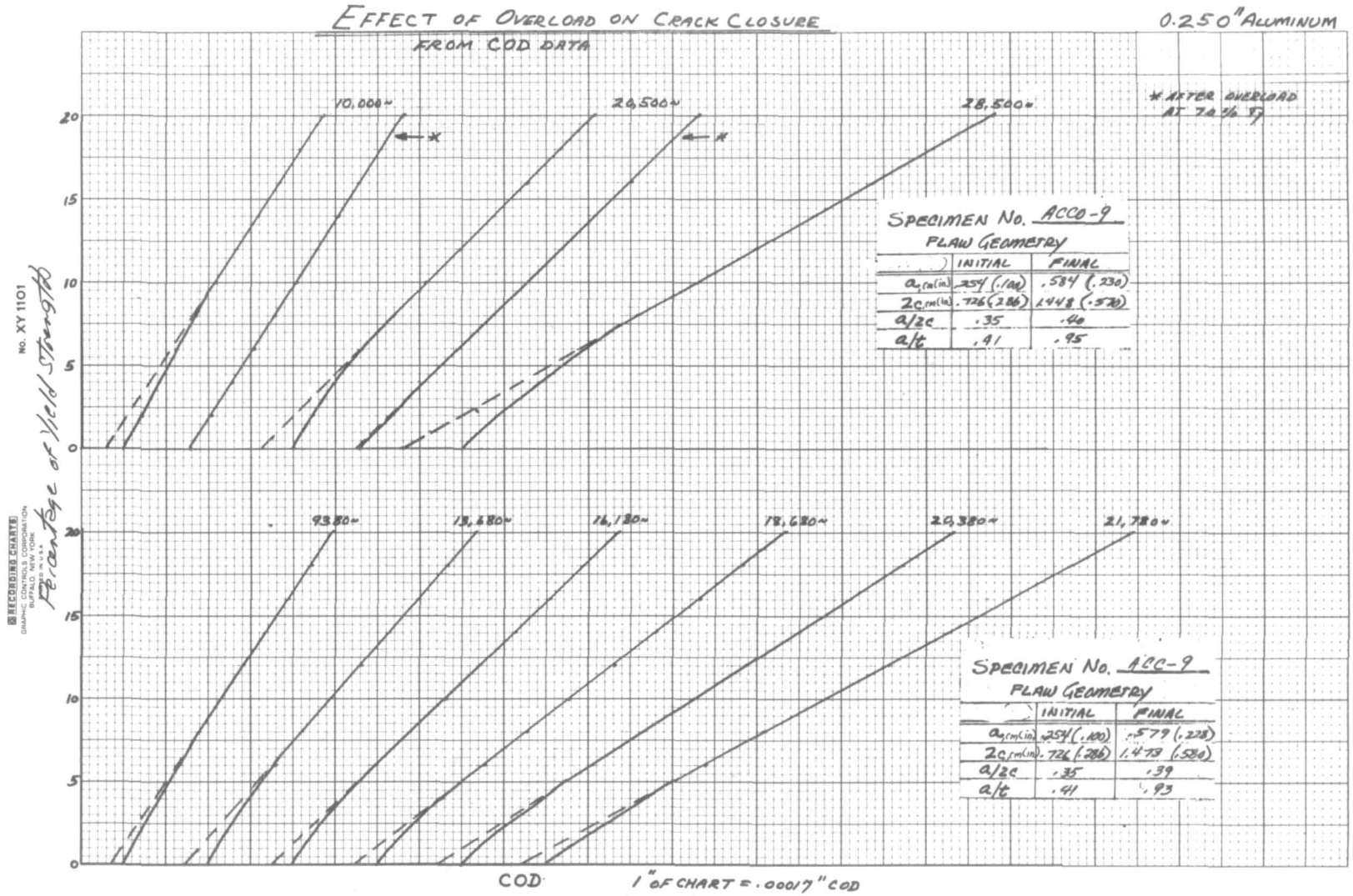

Figure 82. - COD data illustrating effect of overload on crack closure for specimens ACC-9 and ACCO-9.

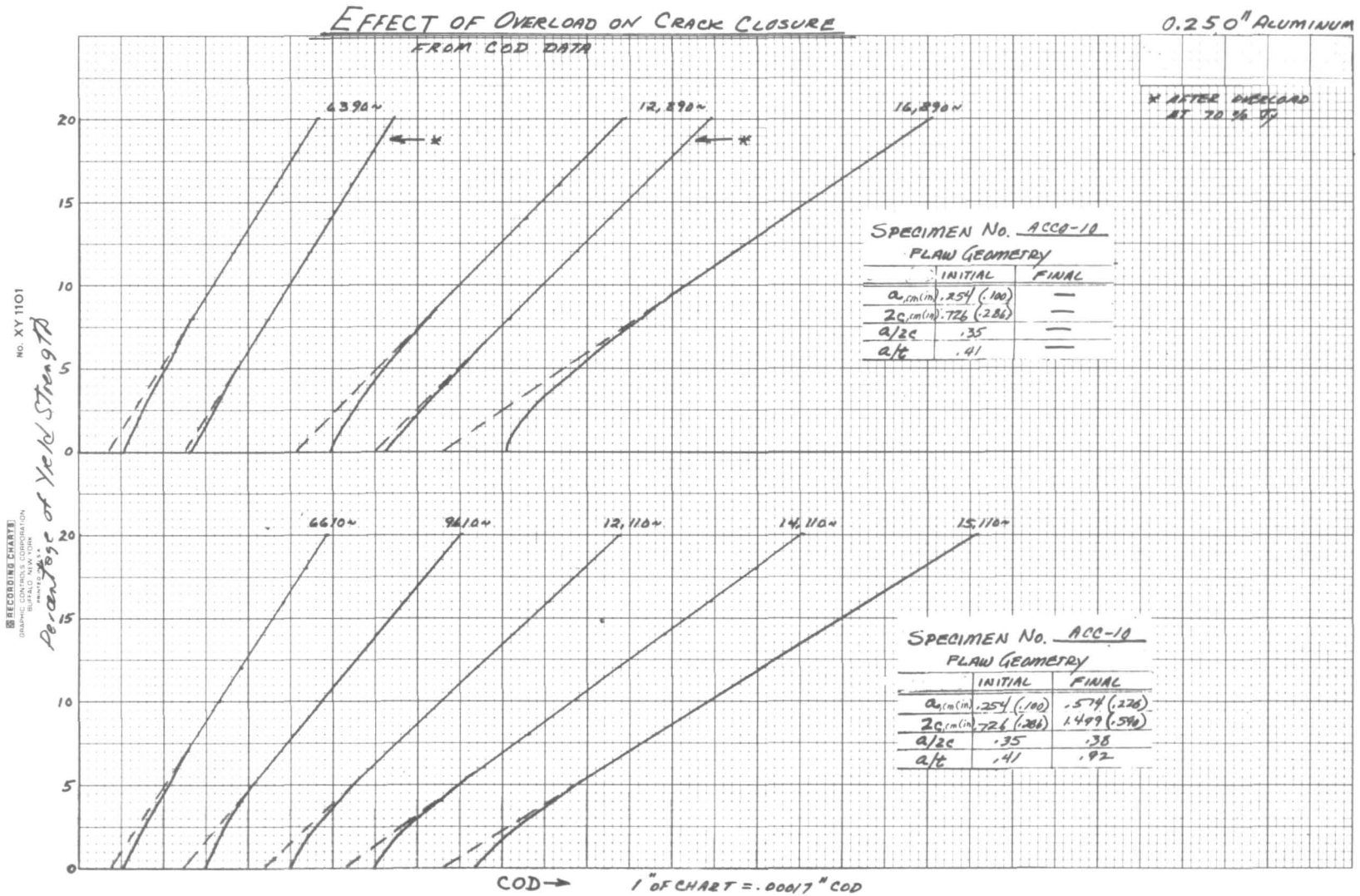

Figure 83. - COD data illustrating effect of overload on crack closure for specimens ACC-10 and ACCO-10.

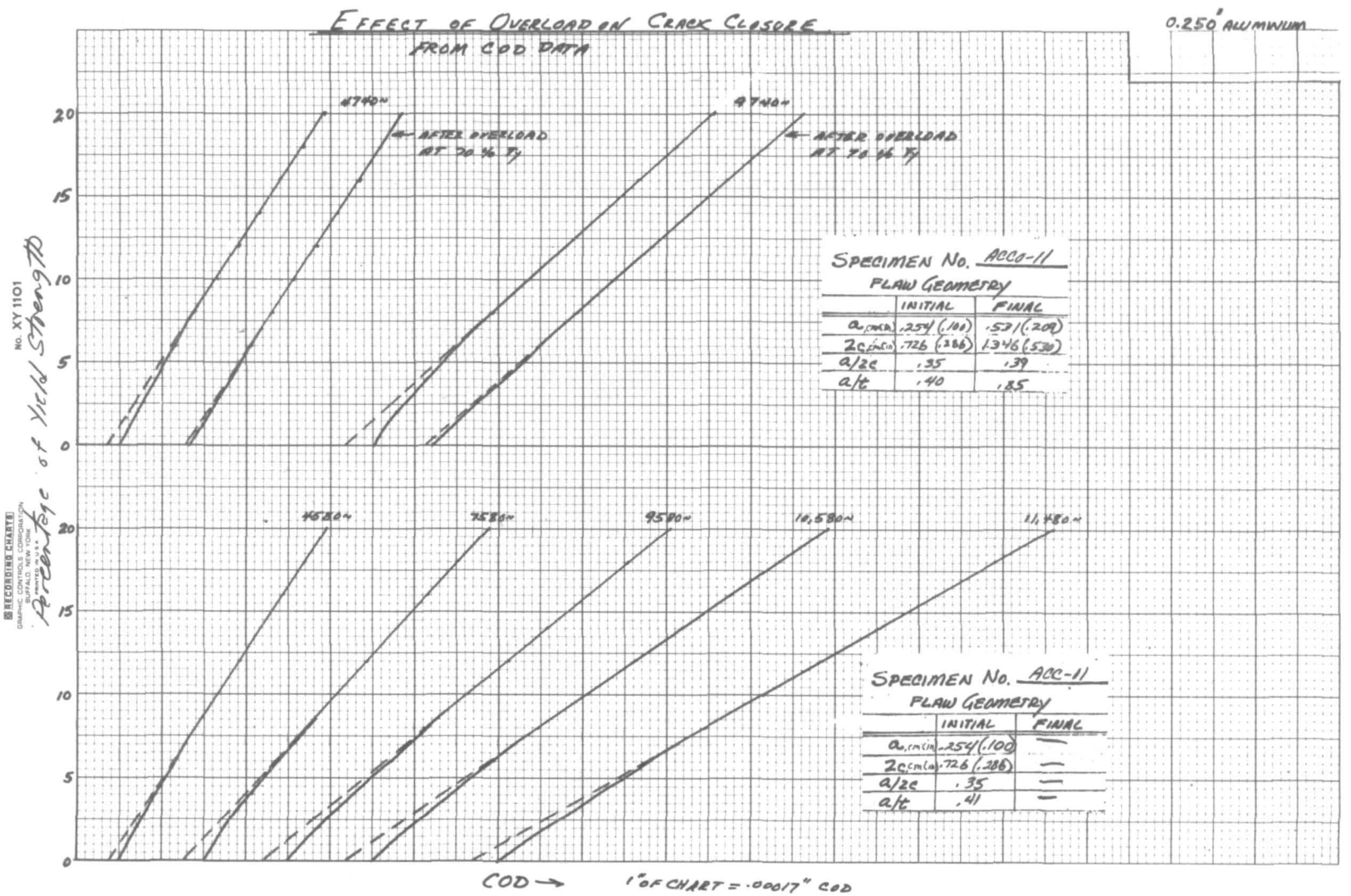

Figure 84. - COD data illustrating effect of overload on crack closure for specimens ACC-11 and ACCO-11.

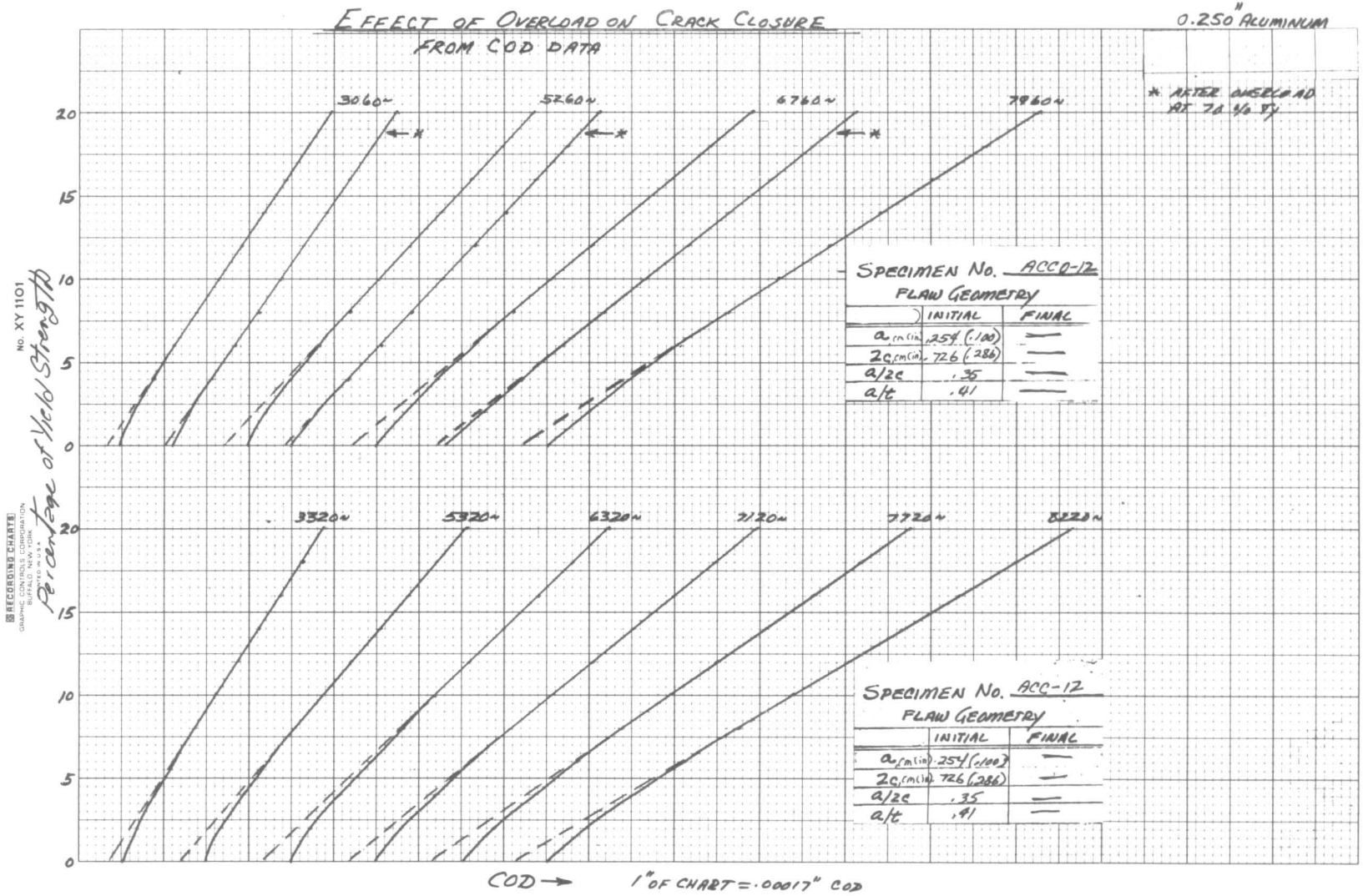

Figure 85. - COD data illustrating effect of overload on crack closure for specimens ACC-12 and ACCO-12.

Crack-opening stress can be readily selected from the plot. Note that after the overload, crack-opening stress is quite low.

Figures 86 through 97 are plots of flaw depth versus number of cycles (a vs N) for the three flaw shapes and four cyclic stress levels. Comparison of the 12 plots shows that the overload effect decreases with increasing cyclic stress. At 40% of yield strength, the effect is quite pronounced for all three shapes. Increasing the cyclic stress to 45% of σ_{ys}, produces slightly less retardation. At 50 and 55% of σ_{ys}, the retardation, although still apparent, is significantly reduced.

Plots for the overloaded specimens appear to exhibit a change in crack depth after the overload. Although this might suggest subcritical growth during the overload, the fracture faces fail to show evidence of subcritical growth. Based on previous work on the effects of overload, the level of 70% of σ_{ys} is not high enough to cause subcritical growth. This apparent increase in depth after the overload is not real and is probably attributable to a sensitivity of the ultrasonic process to a change in crack geometry such as crack sharpness or distance between faying surfaces.

The stress at which crack opening and closing occurred, as determined by the ultrasonic technique, generally varied from 5 to 15% of yield strength. Analysis of the data as a function of crack depth and crack shape revealed no clear trends of the parametric variables affecting the closure or opening stress. The change in crack size (ultrasonically determined) was typically 0.25 to 0.75 mm (0.010 to 0.030 in.). The change in crack size associated with the load-unload cycle appeared to increase as a function of crack depth, then decreased as the flaw approached the back surface.

Crack-opening displacement data showed the typical crack opening stress to be 5 to 10% of yield strength. Traces after overload generally showed linear behavior with no evidence of opening or closing.

Two series of titanium and two of steel were evaluated using the same techniques. Duplicate specimens (one overloaded, one constant-amplitude cycled) were evaluated to determine whether observations for aluminum applied to other materials. The behavior was very similar to that noted for aluminum. Figures 98 and 99 show the titanium ultrasonic data. Figures 100 and 101 give the crack opening displacement results. Figures 102 through 105 show the corresponding data for steel specimens.

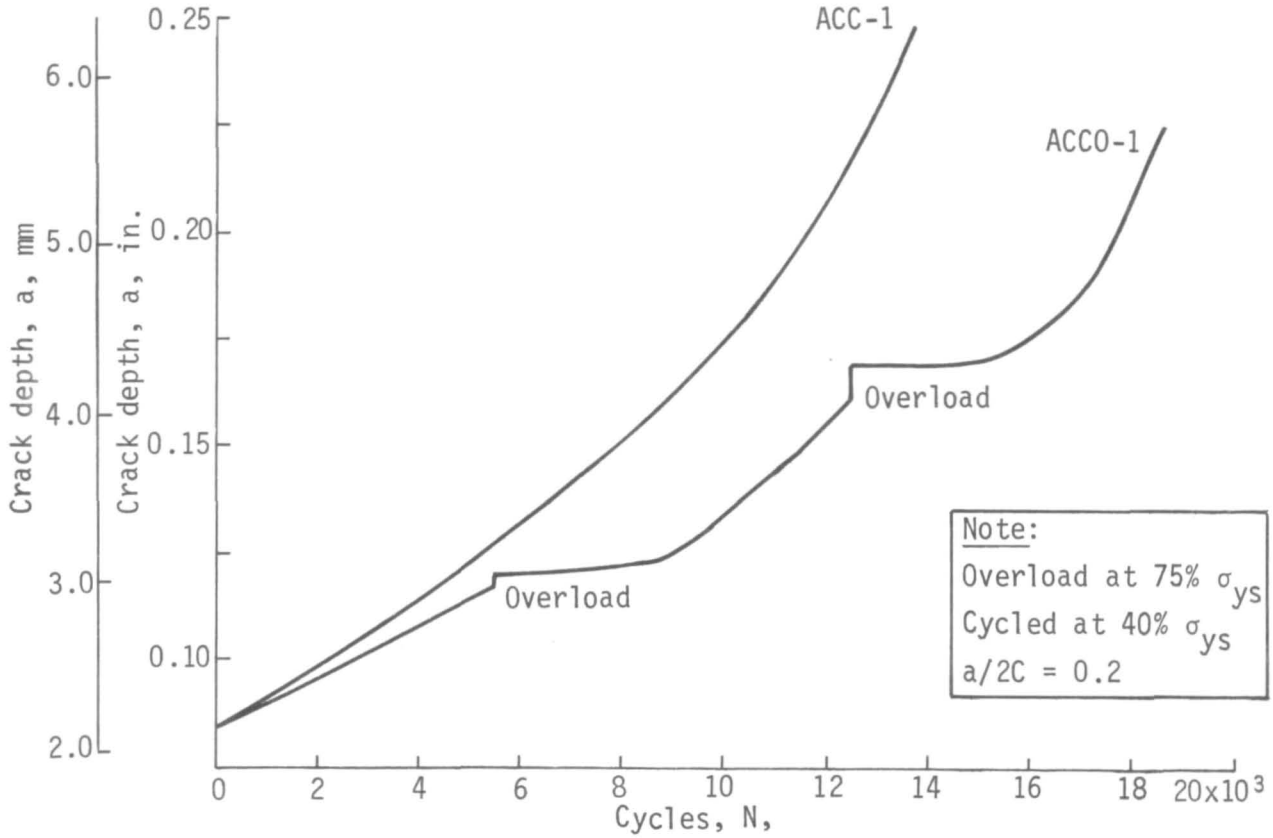

Figure 86. - Cyclic flaw growth curves for specimens ACC-1 and ACCO-1.

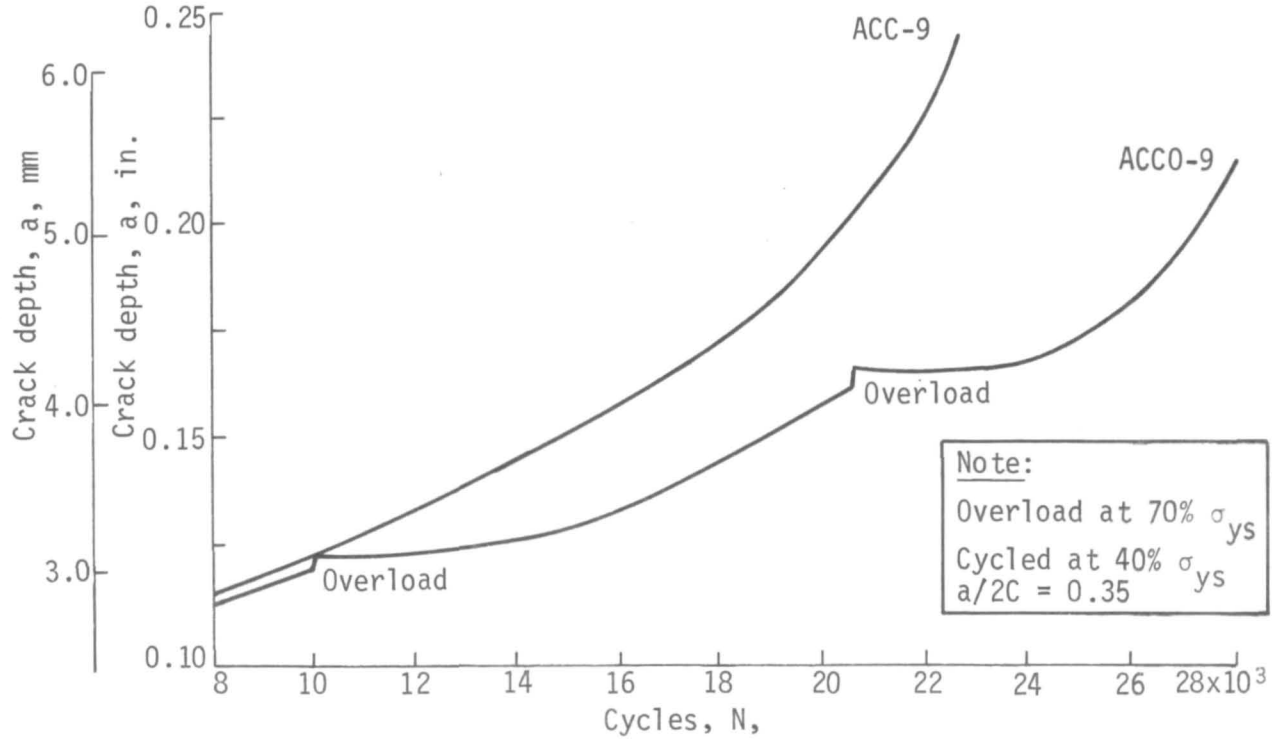

Figure 87. - Cyclic flaw growth curves for specimens ACC-9 and ACCO-9.

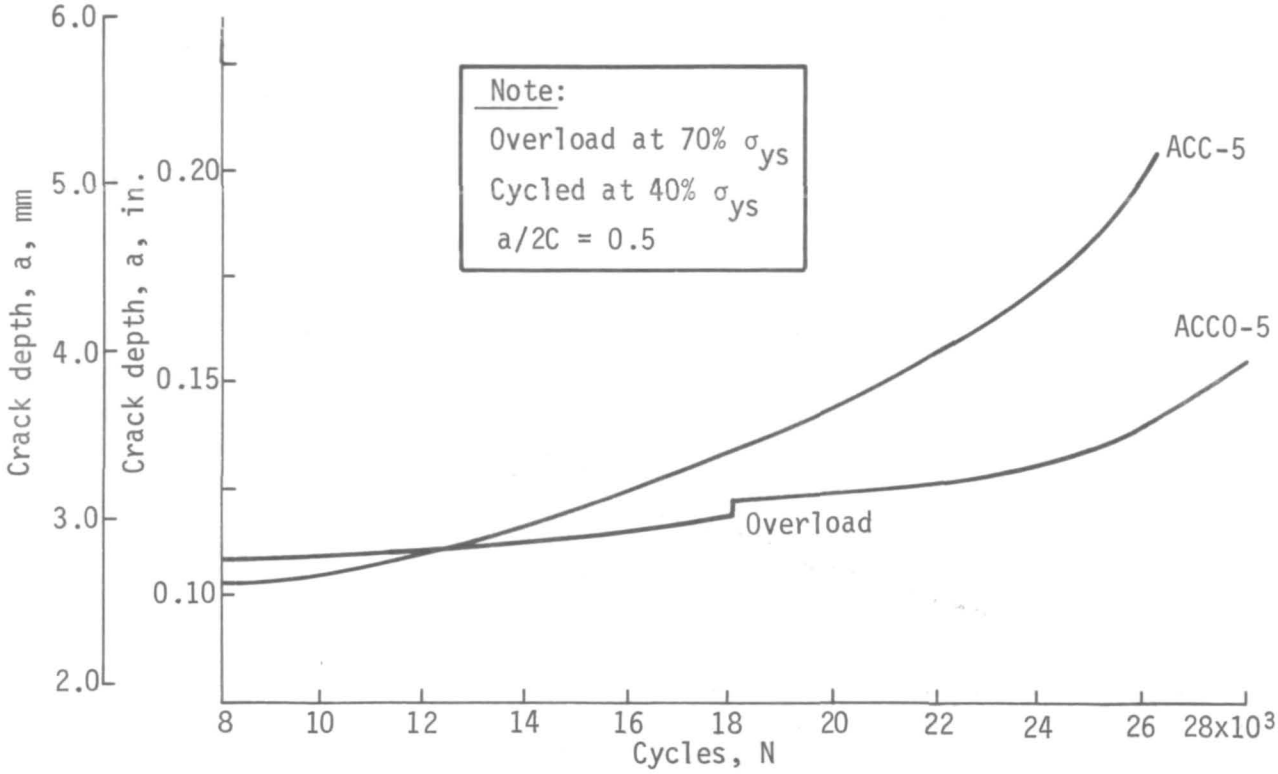

Figure 88. - Cyclic flaw growth curves for specimens ACC-5 and ACCO-5.

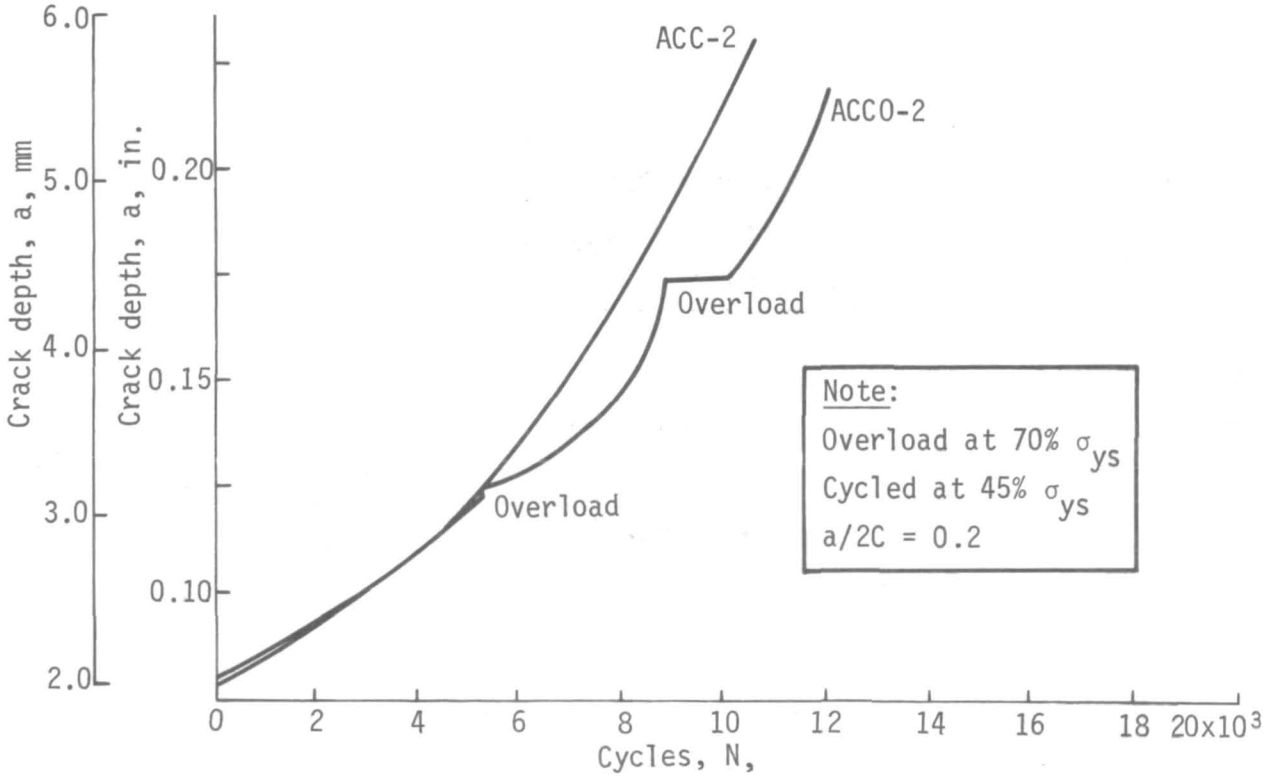

Figure 89. - Cyclic flaw growth curves for specimens ACC-2 and ACCO-2.

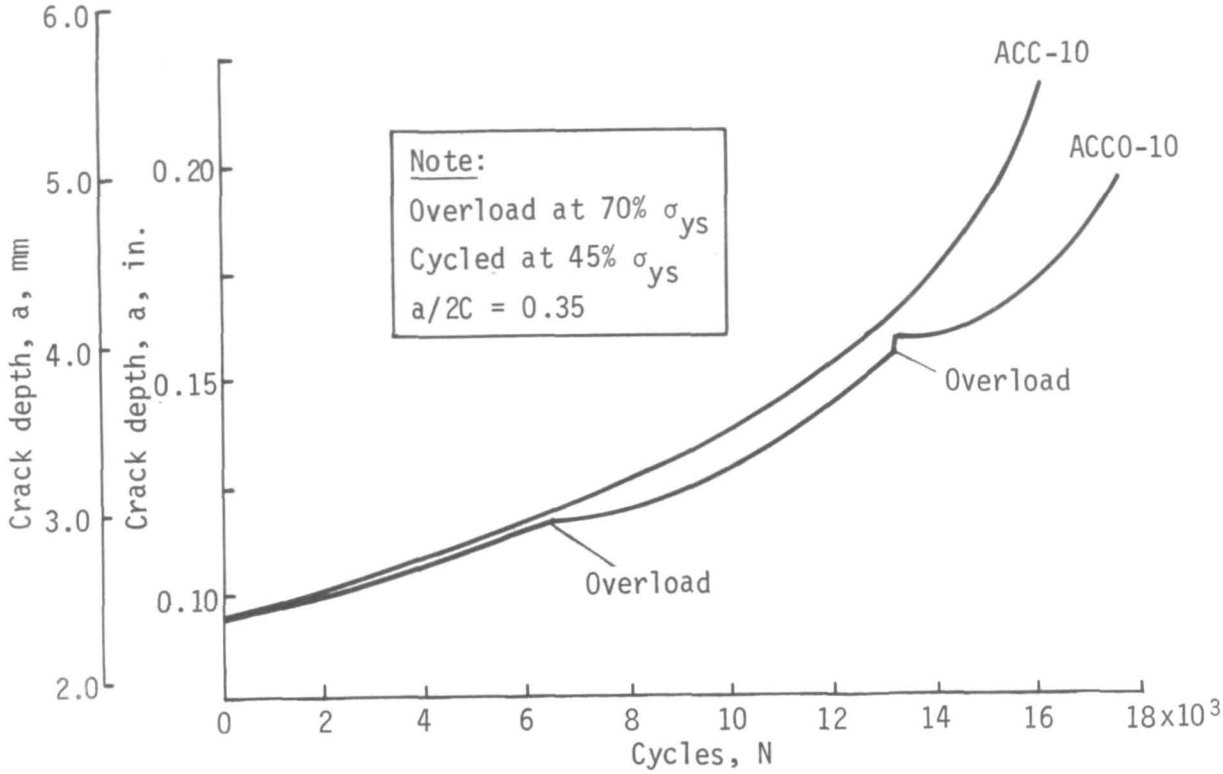

Figure 90. - Cyclic flaw growth curves for specimens ACC-10 and ACCO-10.

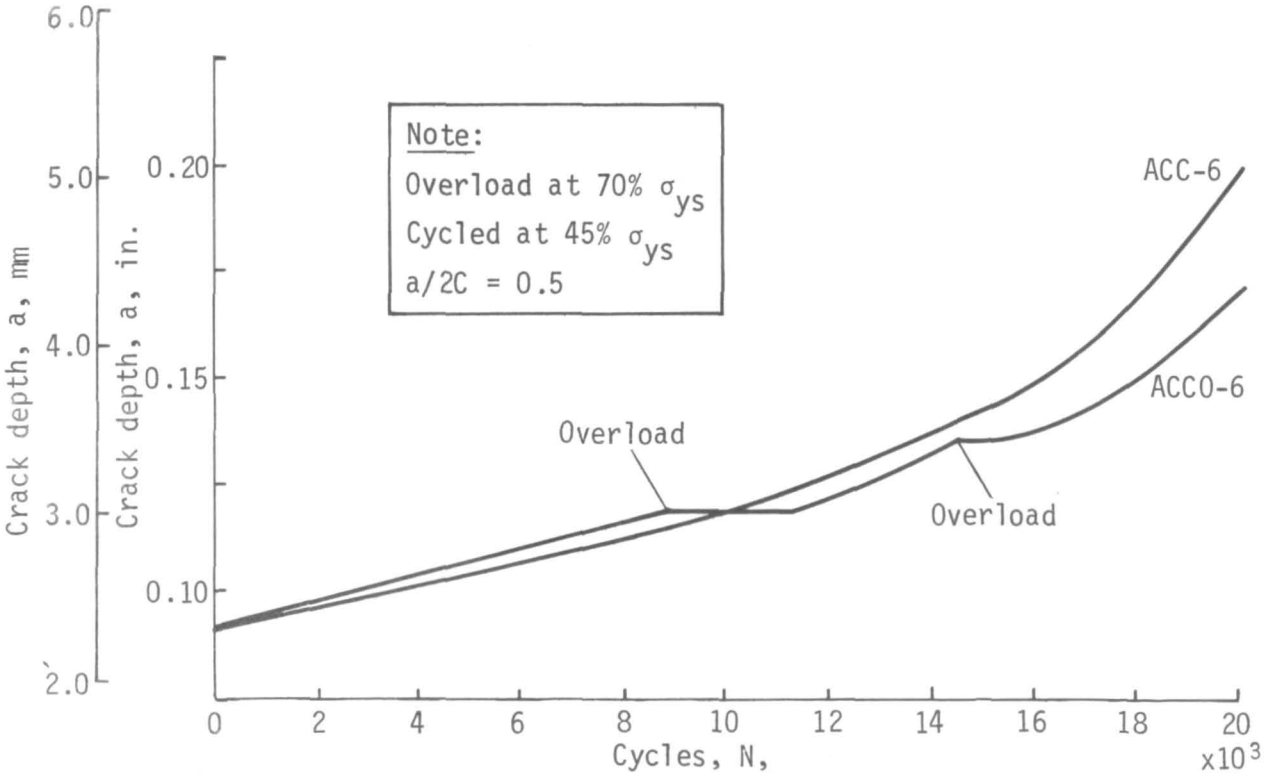

Figure 91. - Cyclic flaw growth curves for specimens ACC-6 and ACCO-6.

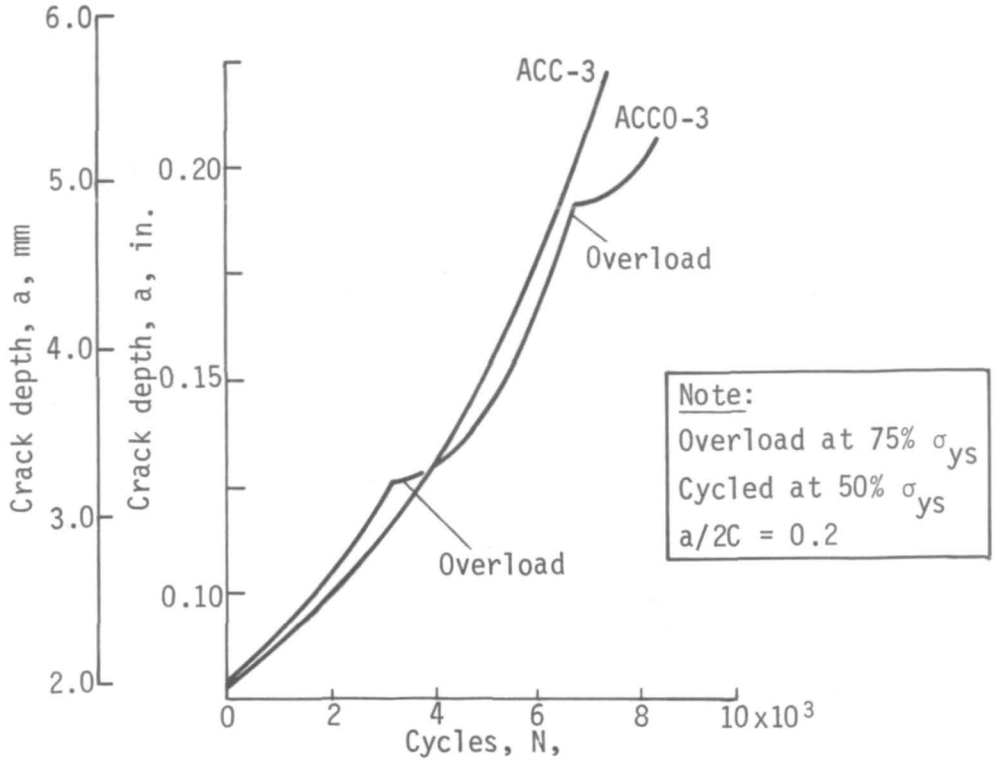

Figure 92. - Cyclic flaw growth curves for specimens ACC-3 and ACCO-3.

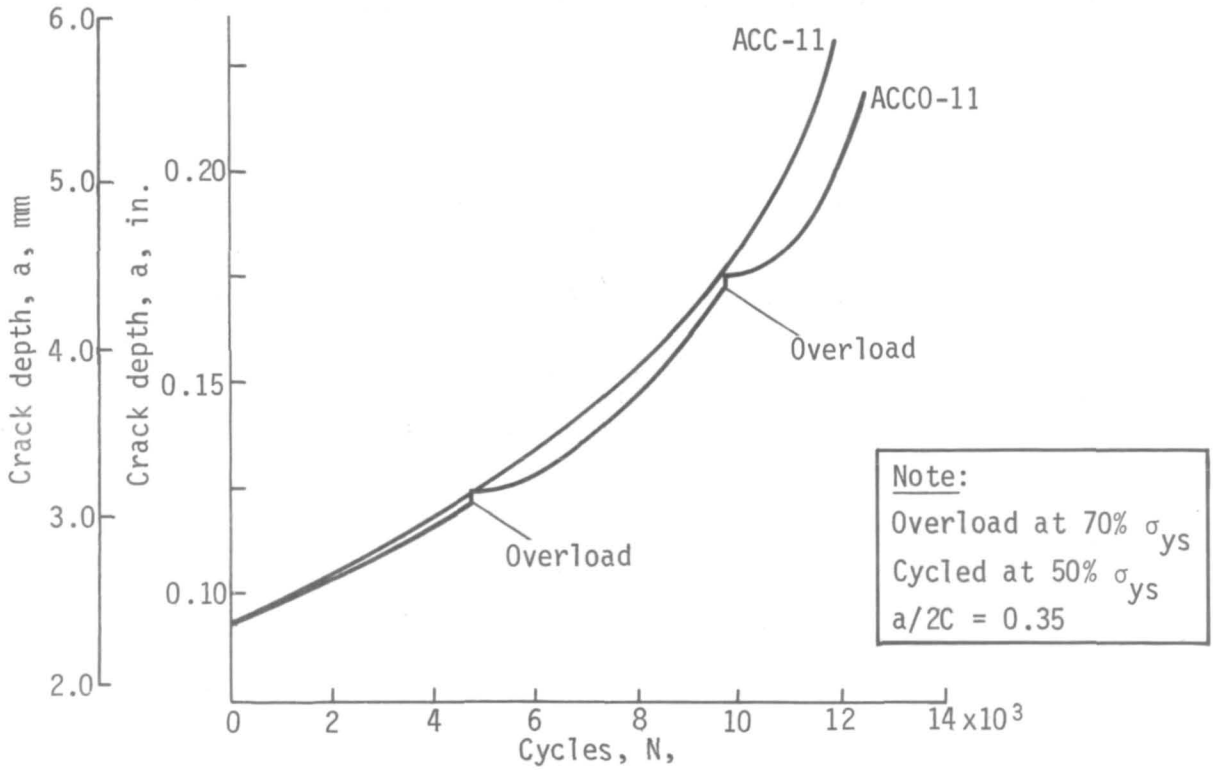

Figure 93. - Cyclic flaw growth curves for specimens ACC-11 and ACCO-11.

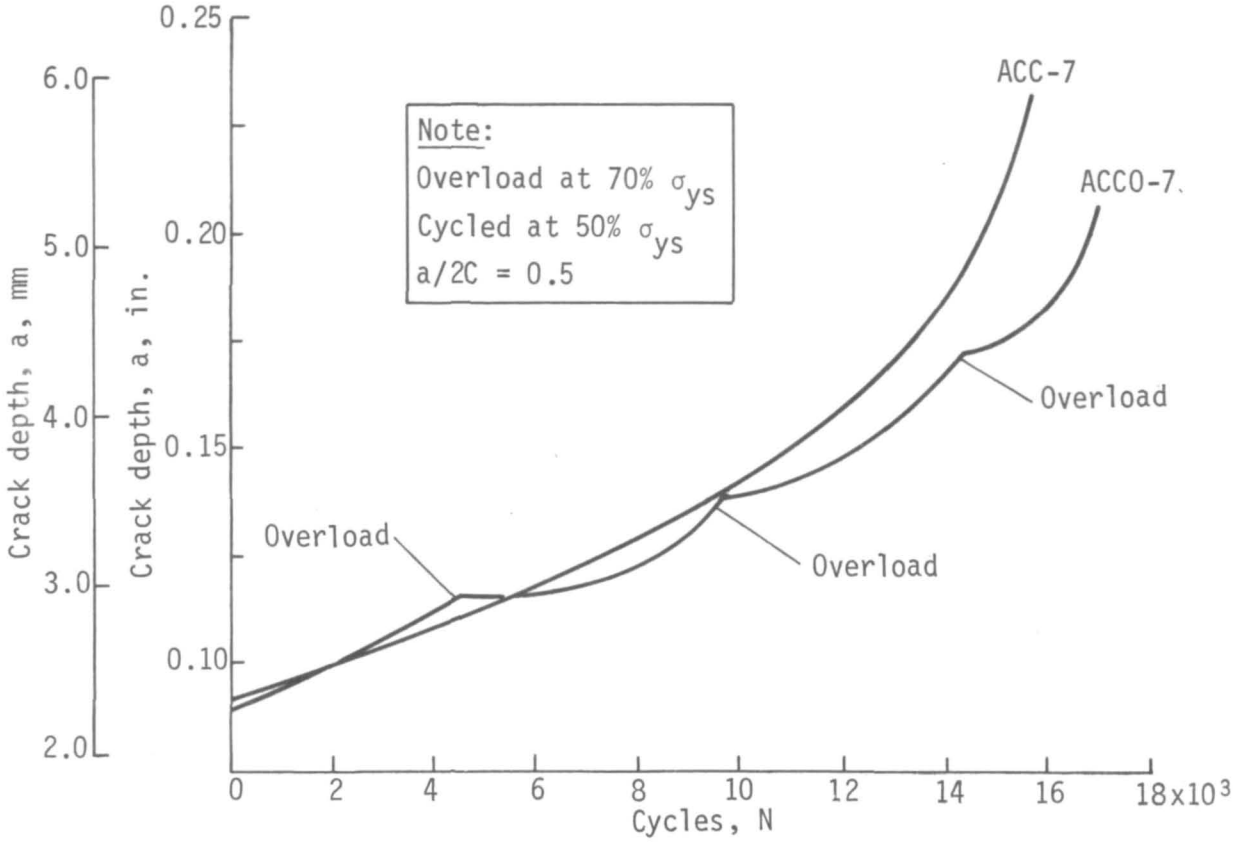

Figure 94. - Cyclic flaw growth curves for specimens ACC-7 and ACCO-7.

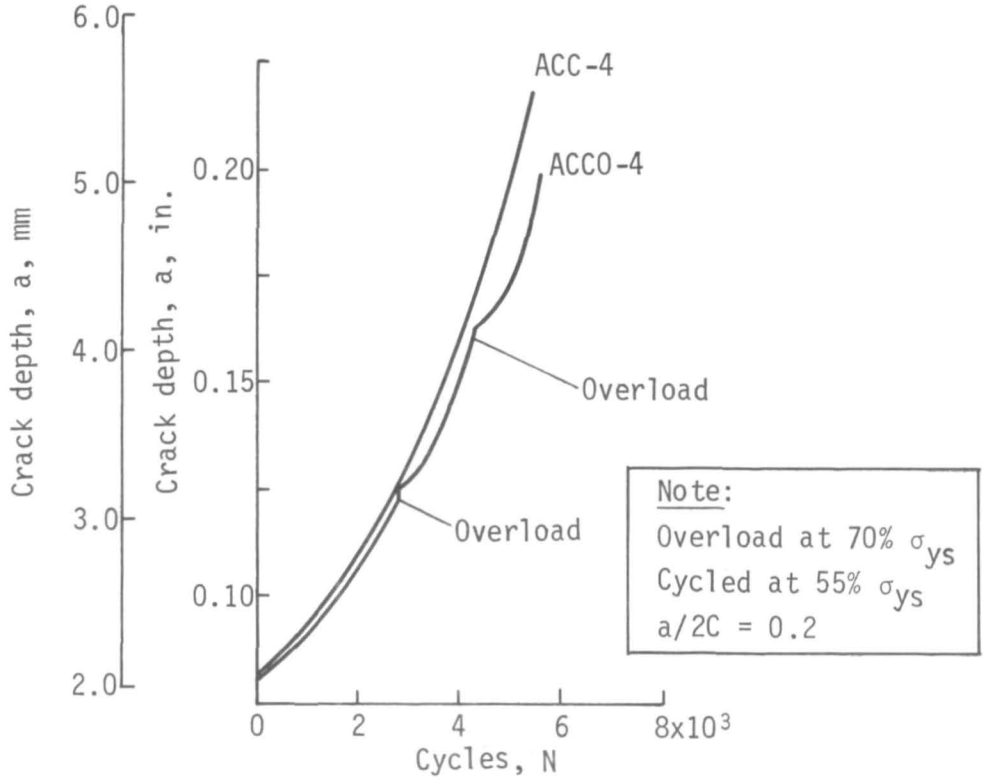

Figure 95. - Cyclic flaw growth curves for specimens ACC-4 and ACCO-4.

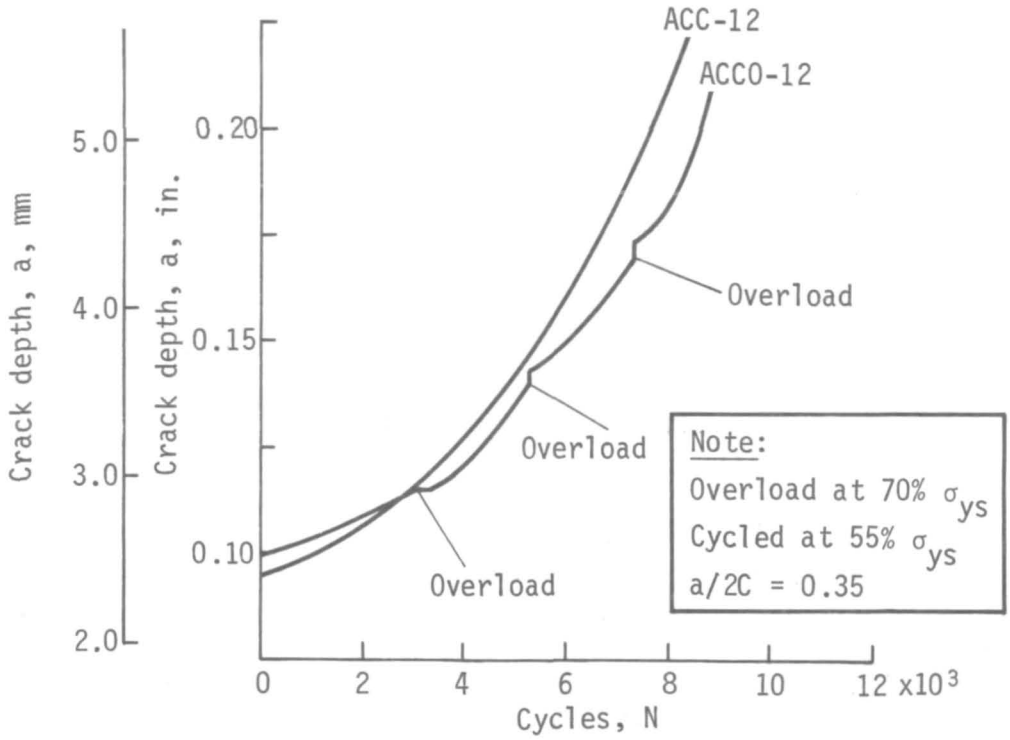

Figure 96. - Cyclic flaw growth curves for specimens ACC-12 and ACCO-12.

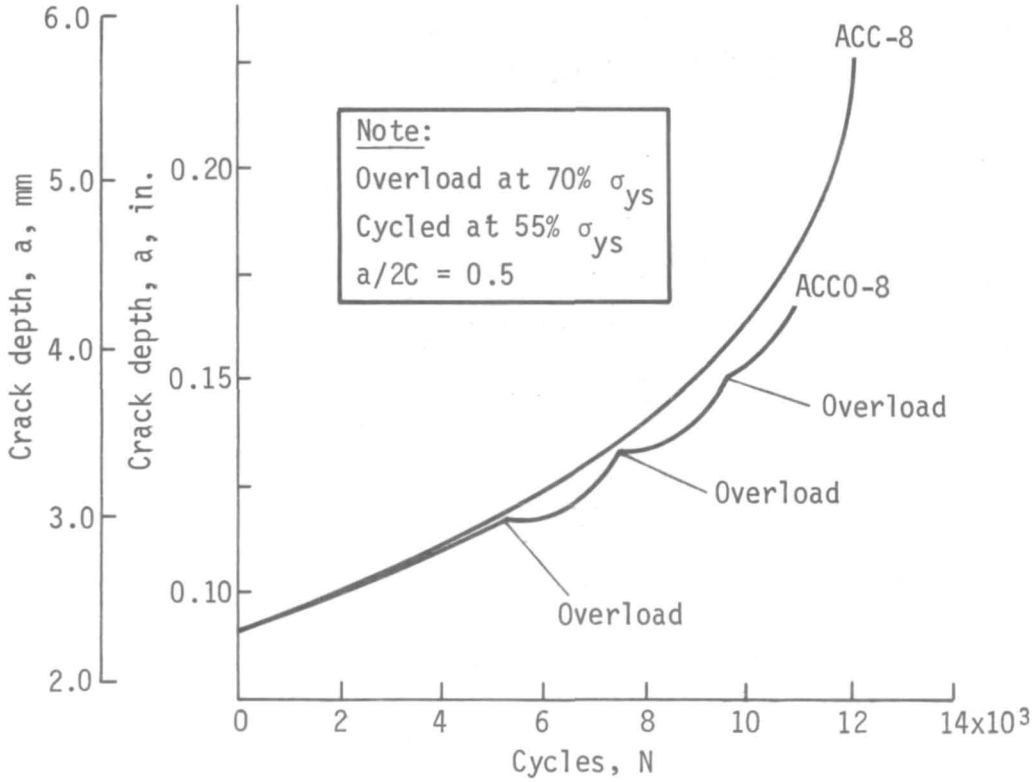

Figure 97. - Cyclic flaw growth curves for specimens ACC-8 and ACCO-8.

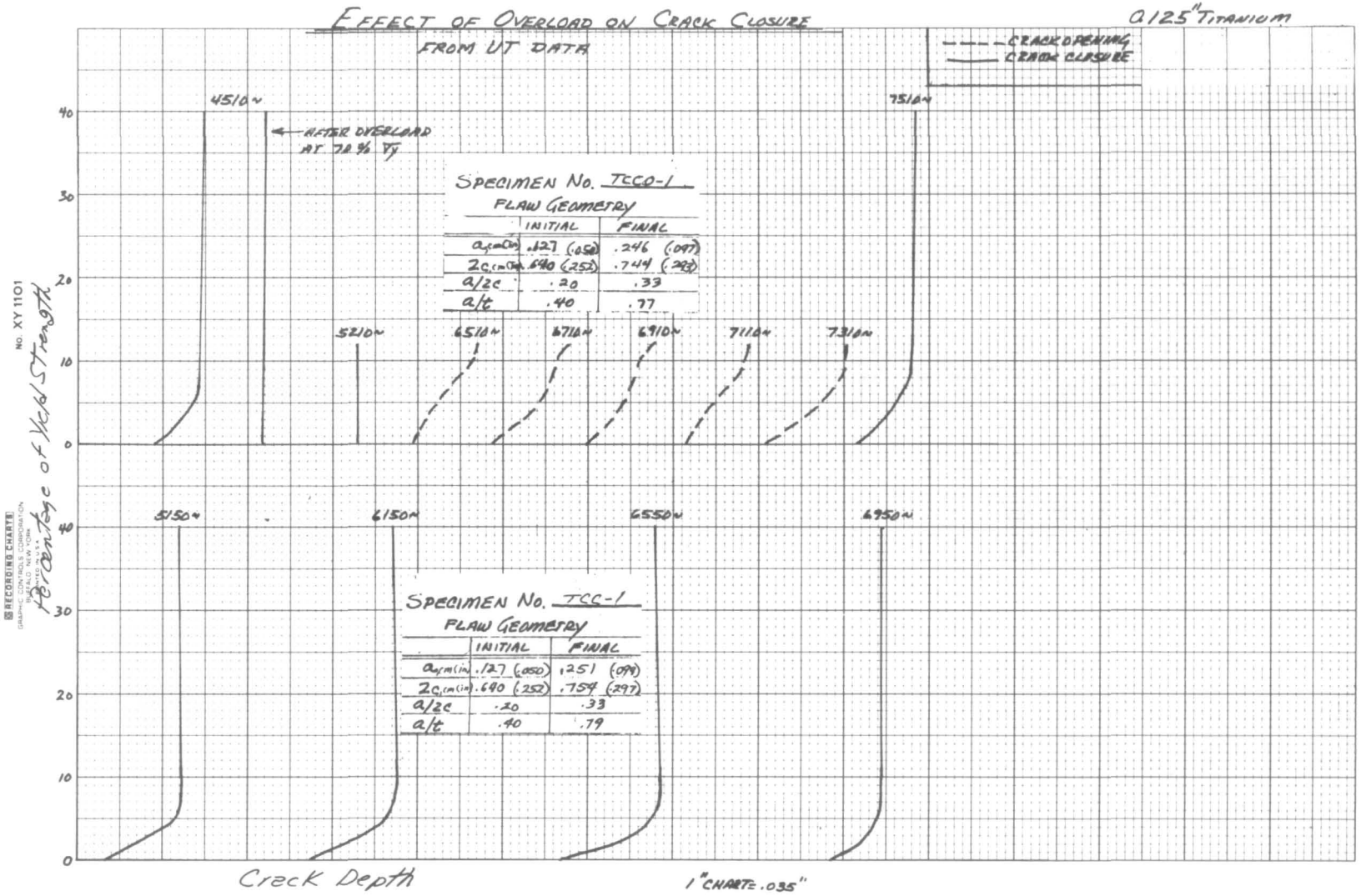

Figure 98. - Ultrasonic data illustrating effect of overload on crack closure for specimens TCC-1 and TCCO-1.

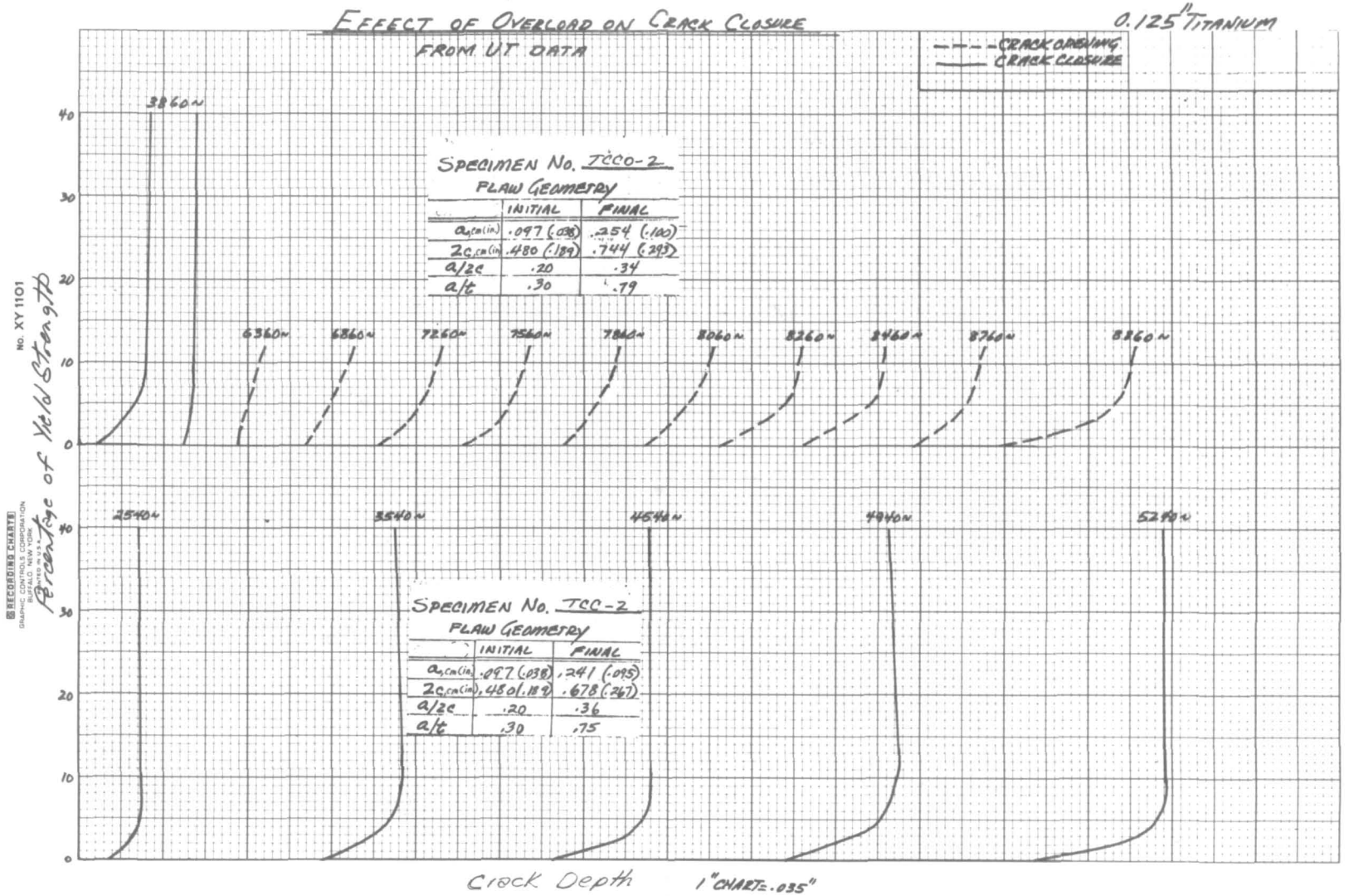

Figure 99. - Ultrasonic data illustrating effect of overload on crack closure for specimens TCC-2 and TCCO-2.

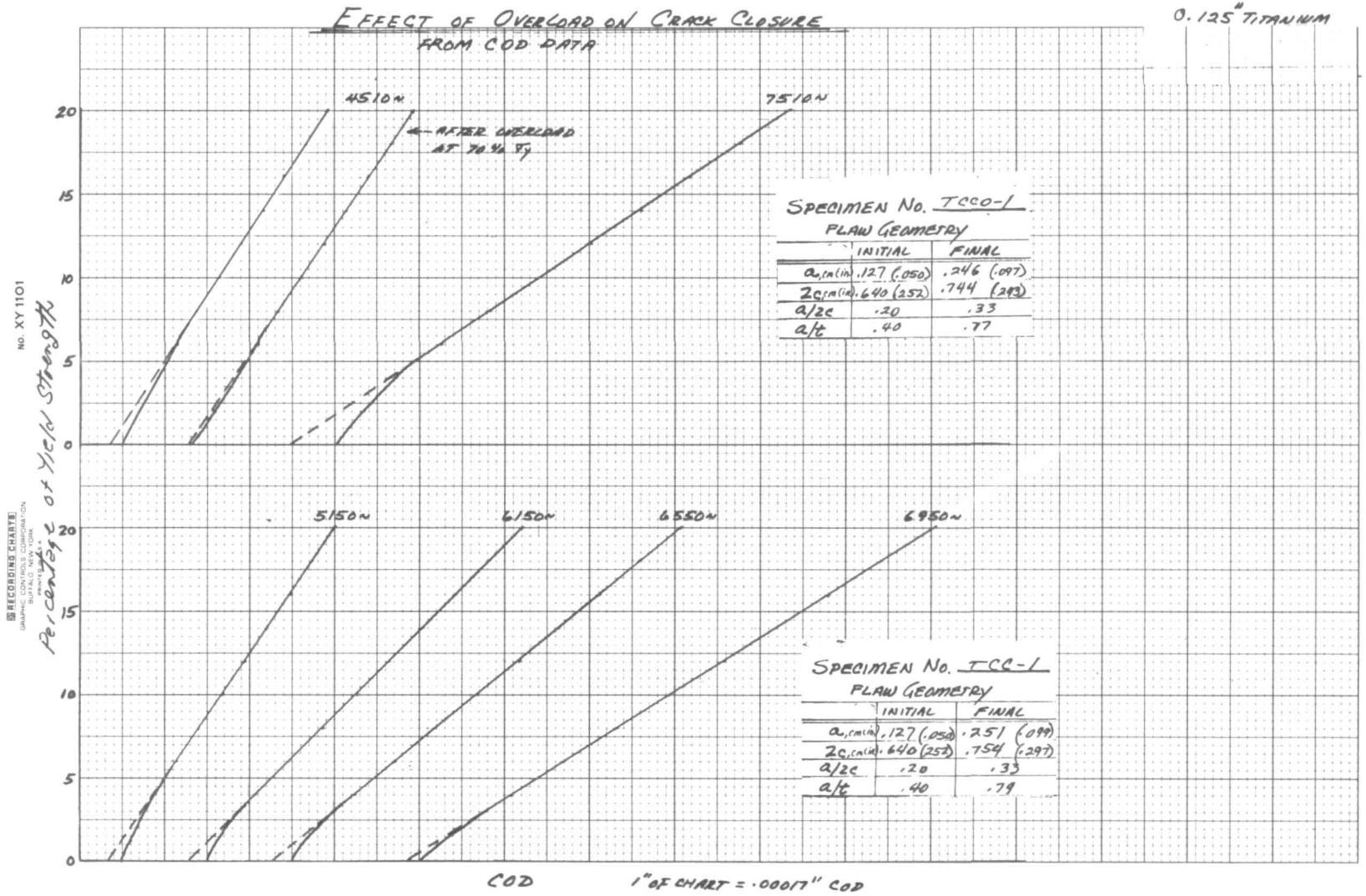

Figure 100. - COD data illustrating effect of overload on crack closure for specimens TCC-1 and TCCO-1.

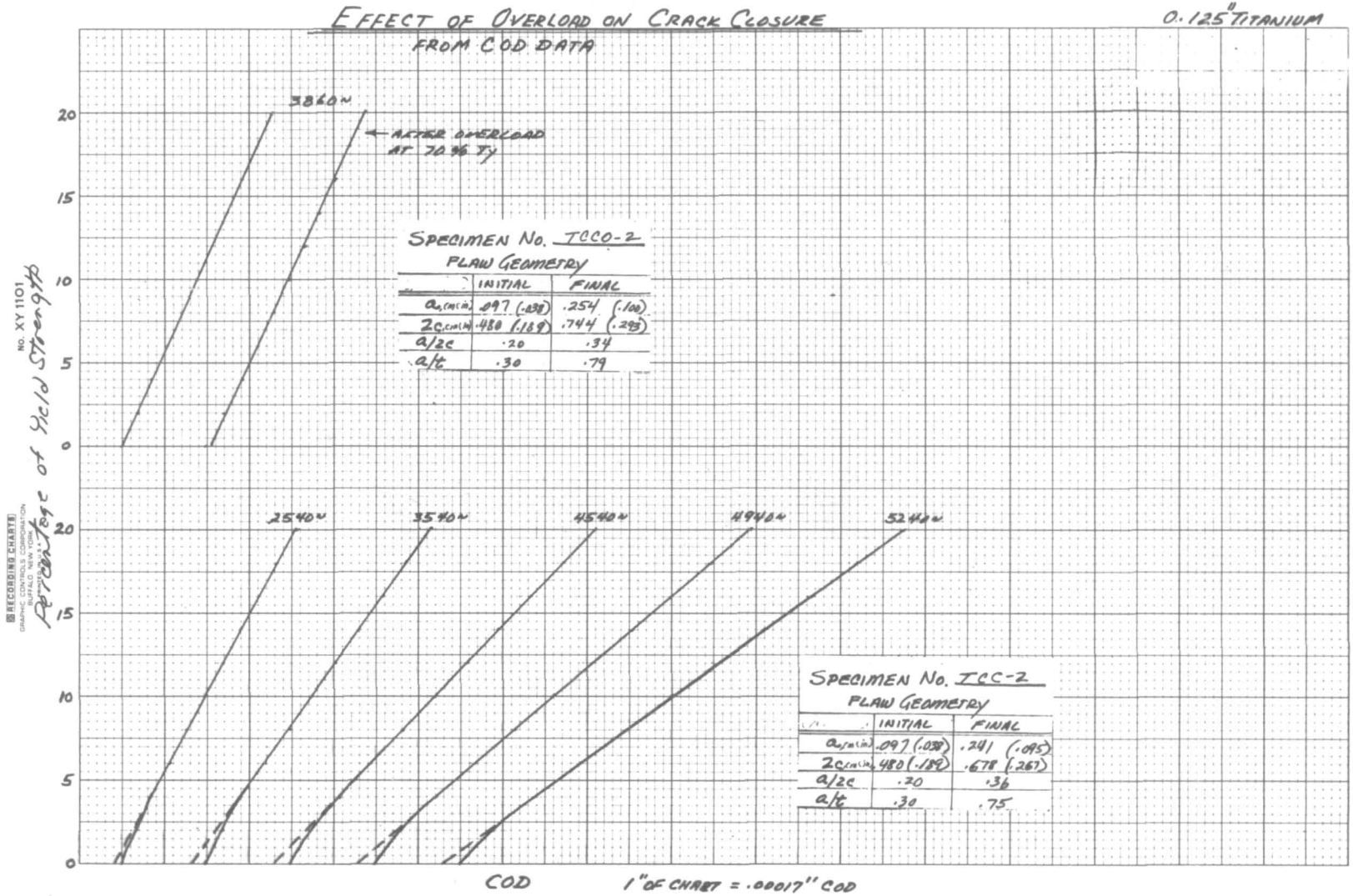

Figure 101. - COD data illustrating effect of overload on crack closure for specimens TCC-2 and TCCO-2.

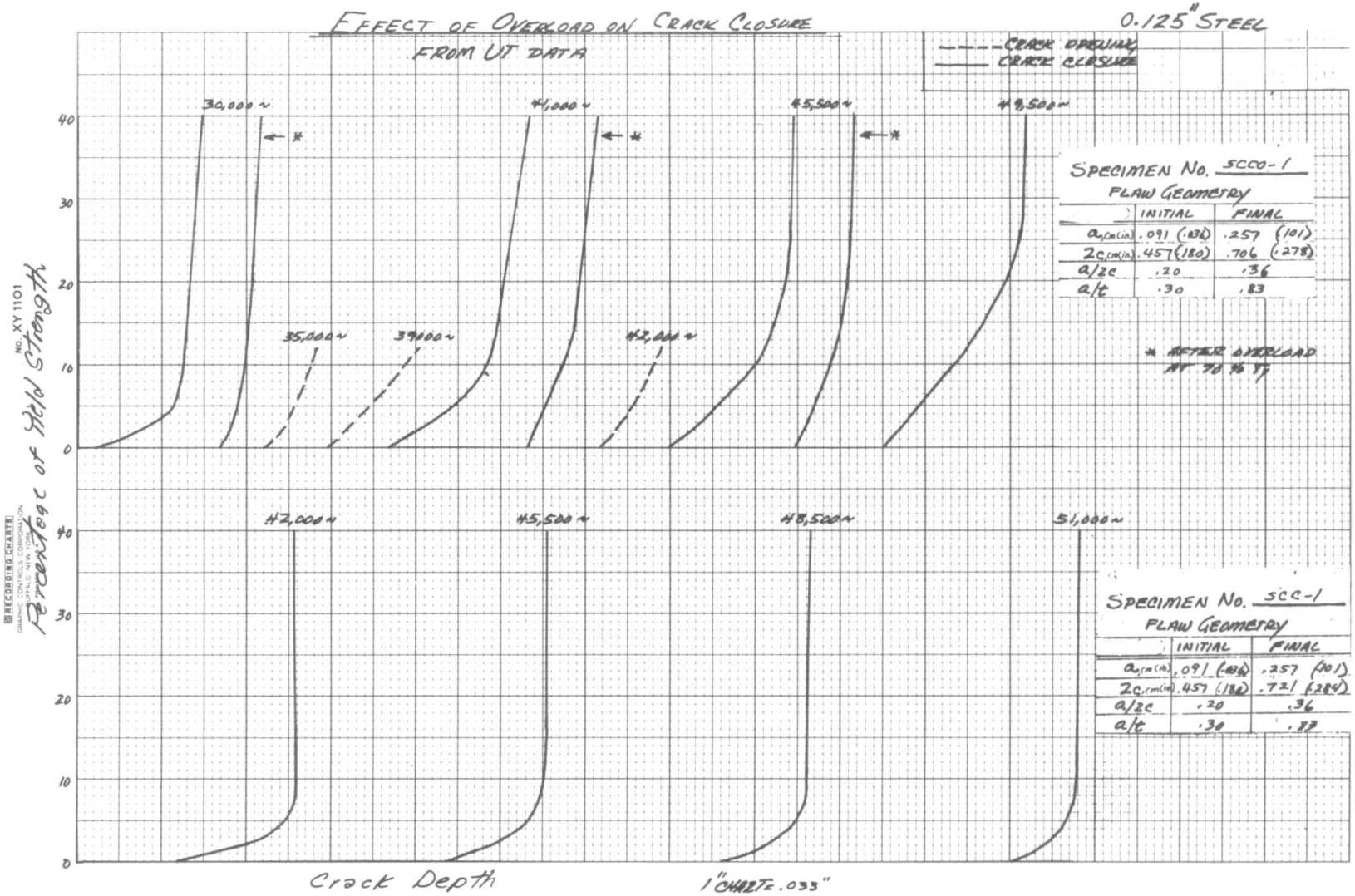

Figure 102. - Ultrasonic data illustrating effect of overload on crack closure for specimens SCC-1 and SCCO-1.

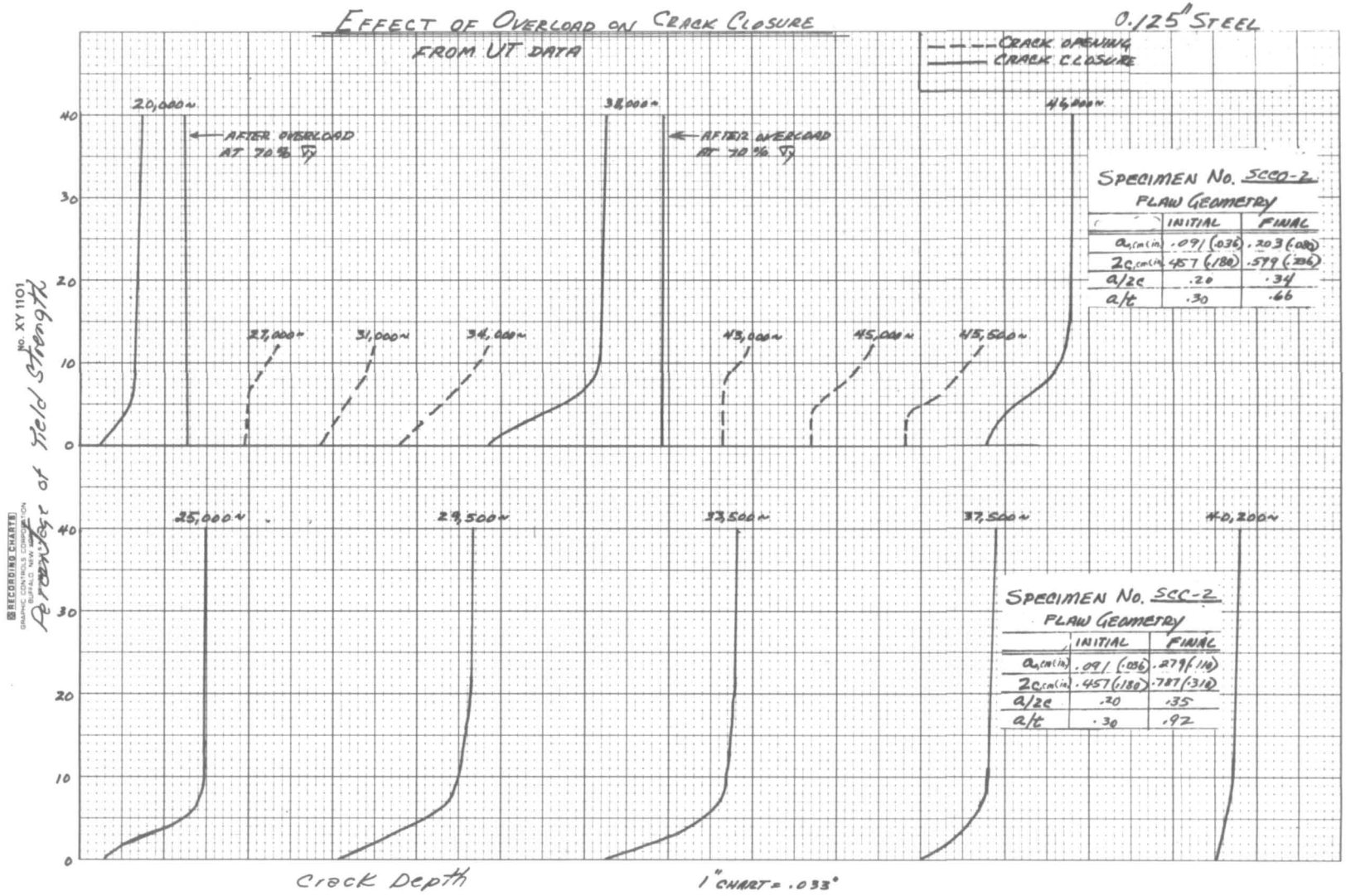

Figure 103. - Ultrasonic data illustrating effect of overload on crack closure for specimens SCC-2 and SCCO-2.

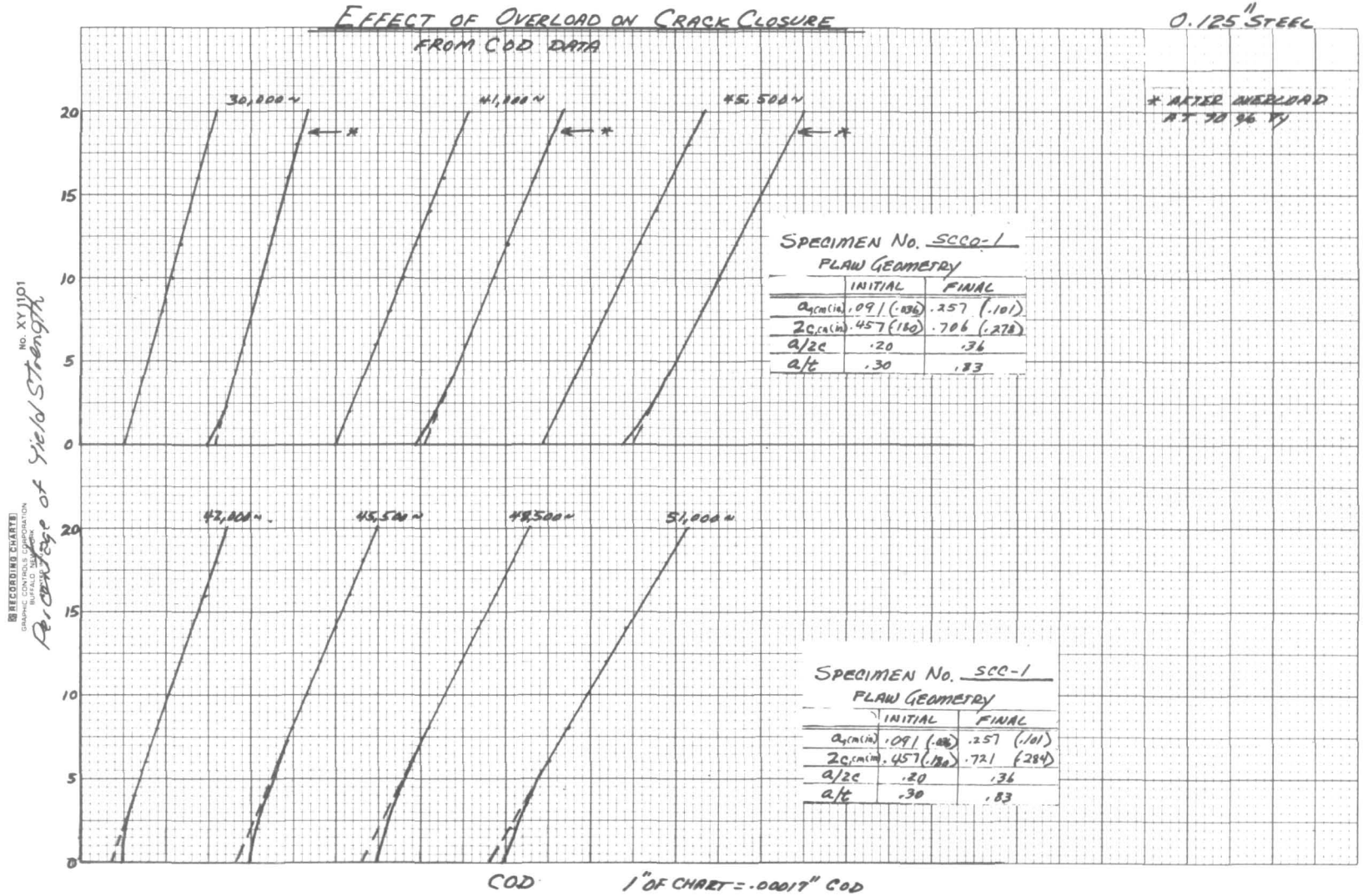

Figure 104. - COD data illustrating effect of overload on crack closure for specimens SCC-1 and SCCO-1.

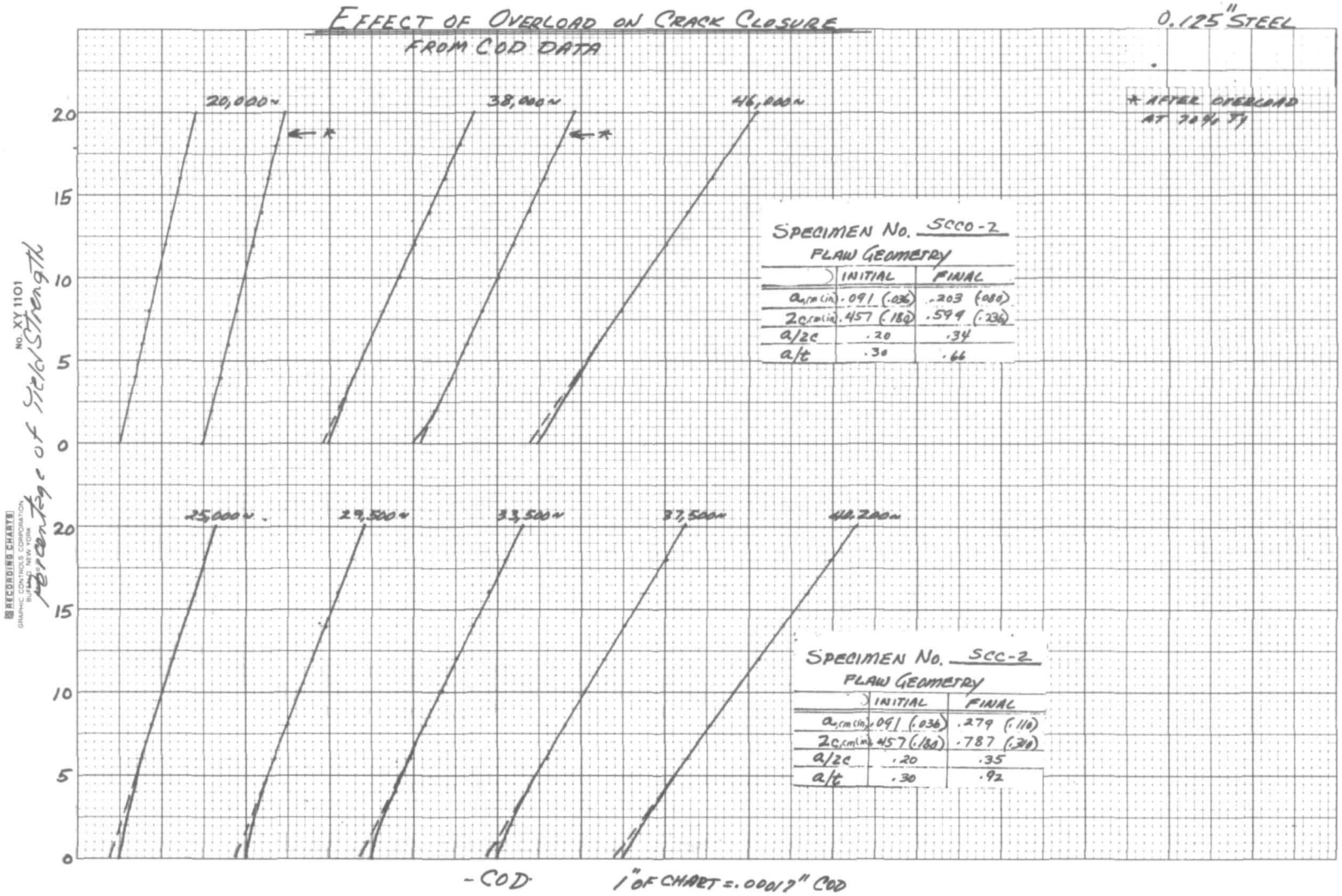

Figure 105. - COD data illustrating effect of overload on crack closure for specimens SCC-2 and SCCO-2.

Discussion

Data obtained in this study clearly illustrate an opening and closing behavior associated with load-unload curves. Both measurement techniques show an initial deviation from linearity at low load levels. Whereas crack-opening displacement measurements show the behavior as a surface compliance, the ultrasonic method clearly shows a reversible change in flaw depth.

Introduction of an overload sequence in the constant-amplitude load cycling caused the opening and closing behavior to disappear. Continued cyclic loading caused the opening-closing phenomena to recur.

Evaluation of the data shows that loading and unloading curves were nearly identical. The stresses at which opening and closing occurred were almost identical; similarly, the changes in crack depth associated with opening and closing were almost the same.

The results of this task are in general agreement with the crack closure concepts of Elber (ref. 5 and 6). Based on the data obtained, the concept of an effective stress range for establishing an effective stress intensity range $\left(\Delta K_{eff}\right)$ appears valid. Ultrasonic data show a change in crack depth associated with opening and closing. It appears that this change occurs at the crack tip. Therefore, until the tip is open, there is no stress intensity.

Evaluation of crack growth based on the Elber model cannot be performed with our data because only depth measurements were taken; no crack width data were obtained. However, based on the magnitude of the crack opening stress $\left(5 \text{ to } 15\% \text{ of } \sigma_{ys}\right)$, it is obvious that the effect on crack growth rate could be significant. Depending on the value of the exponent (n) in the crack-growth relationship, the error in rate calculation could be as great as 50%.

In his first paper, Elber (ref. 5) pointed out the need to determine crack-opening and -closing stress values and speculated that closing stress values would exceed opening stress values. The data reported here indicate no difference between the two values.

Elber's paper (ref. 6) that includes data on 2024-T3 shows a decrease in crack-opening stress immediately after the overload cycle and an increase in opening stress after postoverload cycling to more than that immediately preceding overload. These data are somewhat similar to our results, but the discrepancies should be noted. Whereas Elber showed a decrease in opening stress after

the overload, the data presented in this report show the crack to be fully open after the overload. After cycling, Elber shows the opening stress to rise to a higher level than that immediately before the overload. The results presented here show that the opening stress was gradually restored with cycling, but did not appear to be greater than the preoverload value.

Differences between these results and those of Elber could be attributed to differing behavior of surface-flawed specimens compared to through-cracked specimens.

Metallographic studies of crack closure behavior performed in independent research provide interesting physical evidence to supplement the findings of this research. Selected information from this study is presented in the following paragraphs.

Eleven specimens, 9.9 cm (3.90 in.) wide, 0.95 cm (0.375 in.) thick, and of varying lengths, were tested. The first seven specimens contained transverse repair welds approximately 1 cm (0.5 in.) wide. In each specimen, a surface flaw was machined in the weld, as shown in Figure 106. Table XIX summarizes test data for these specimens.

Surface-flawed base-metal and weldment specimens were subjected to cyclic fatigue overloads to progressively higher stress levels and, in selected cases, to postoverload cyclic fatigue.

After testing, specimens were sectioned as shown in figure 107. Each section thus obtained was mounted, polished, etched, and photographed at 50X, 100X, 200X, and 400X.

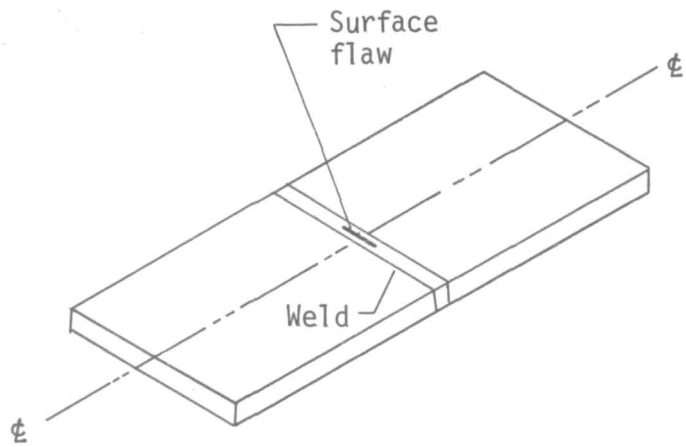

Figure 106. - Location of flaw in welded specimen.

TABLE XIX. - SUMMARY OF TEST DATA

Specimen no.*	Depth of saw cut,		Initial fatigue							Overload stress,		Postoverload fatigue						
			Stress,		Cycles	Crack length,		Average crack growth rate,				Stress,		Cycles	Crack length,		Average crack growth rate,	
	nm	(in.)	MN/m^2	(ksi)		nm	(in.)	nm/cycle	(μin./cycle)	MN/m^2	(ksi)	MN/m^2	(ksi)		nm	(in.)	nm/cycle	(μin./cycle)
W-1	4.27	(0.168)	76	(11)	12 190	1.88	(0.074)	154	(6.07)									
W-2	4.24	(0.167)	76	(11)	8 060	1.68	(0.066)	208	(8.19)									
W-3	4.32	(0.170)	76	(11)	12 250	0.99	(0.039)	80.8	(3.18)	90	(13)							
W-4	4.29	(0.169)	76	(11)	9 310	1.27	(0.050)	140	(5.51)	117	(17)							
W-5	4.22	(0.166)	76	(11)	12 380	1.63	(0.064)	131	(5.17)	145	(21)							
W-6	4.09	(0.161)	76	(11)	19 430	1.12	(0.044)	57.4	(2.26)	117	(17)†							
W-7	4.22	(0.166)	76	(11)	20 360	1.27	(0.064)	79.8	(3.14)	117	(17)	76	(11)	16 290	0.43	(0.017)	26.4	(1.04)
BM-1			110	(16)	8 390							110	(16)					
BM-2	4.60	(0.181)	110	(16)	8 710	2.16	(0.085)	248	(9.76)	206	(30)	110	(16)	10 060	0.71	(0.028)	70.6	(2.78)
BM-3	4.62	(0.182)	110	(16)	6 300	1.60	(0.063)	254	(10.00)	241	(35)	110	(16)	9 240	0.51	(0.020)	54.9	(2.16)
BM-4	4.52	(0.178)	110	(16)	10 300	2.03	(0.080)	197	(7.77)	276	(40)	110	(16)	15 220	0.30	(0.012)	20.1	(0.79)§

* BM - base metal, W - welded.
† After overload, this specimen was subjected to a compressive stress of 62 MN/m^2 (9 ksi).
§ Under this high overload stress, severe delamination resulted in a very low apparent average crack growth rate.

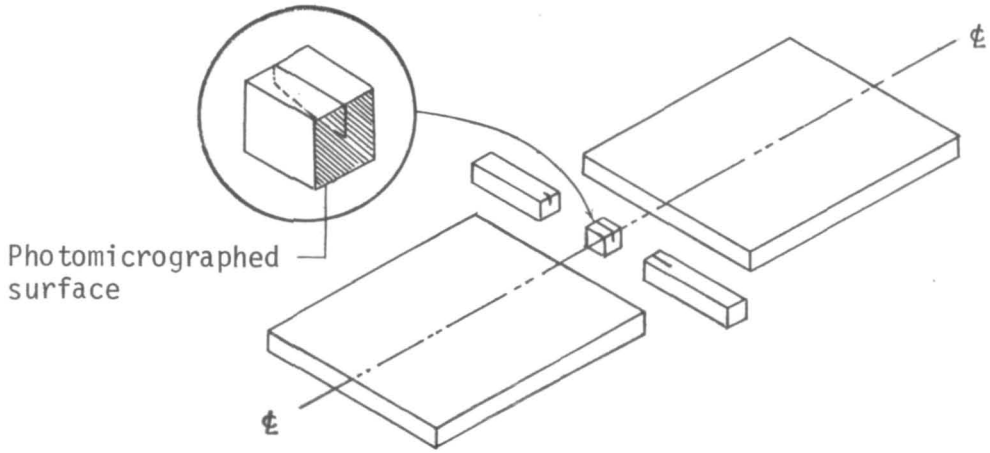

Figure 107. - Sectioning of specimens.

Photomicrographs of specimen W-2 show a fatigue crack in welded material not subjected to an overload (fig. 108). Although the crack front was extremely tight, examination at a higher magnification revealed that the crack appeared open along its entire length. The effect of increasing overloads can be seen in the photomicrographs of specimens W-3, W-4, and W-5 (fig. 109 through 111). As the overload stress was increased, plastic deformation and tearing were evident at the crack front in specimen W-5, which was subjected to a 145-MN/m^2 (21-ksi) overload. Even at the lowest overload stress of 90 MN/m^2 (13 ksi) (specimen W-3), the crack showed evidence of blunting, and its width became much more uniform along its length.

Note that, after the application of an overload, average crack growth rate was reduced by a factor of three to four. Compression of a fatigue crack at just over half its overload stress (specimen W-6) caused no appreciable closing of the crack front (fig. 112).

The four parent specimens were similarly tested. Photomicrographs of specimen BM-1 (fig 113) show a fatigue crack that was not subjected to an overload. Comparing this fatigue crack with the original fatigue crack in specimen W-2 revealed that the fatigue crack in the welded material was three to four times tighter than the comparable fatigue crack in the parent material. As in the case of the welded material, increasing levels of overload caused widening of the fatigue cracks and blunting of the crack fronts (fig. 114, 115, and 116). In addition, the parent material suffered varying degrees of delimination--in one case quite severe (specimen BM-4), fig. 116. Fatigue cracks that grew into the previous overload yield zone remained open along their entire lengths, and compared quite closely with the original fatigue crack (specimen BM-1) in terms of width for all levels of overload stress used.

Based on the results of Elber's papers (ref. 6 and 7), the ultrasonic information reported here, and the metallographic information, a picture of the crack closure phenomenon can be created.

The initial fatigue crack is relatively tight. A monotonic loading cycle causes the tip to open and close. No growth can occur unless the applied stress exceeds the opening stress level. An overload results in extensive plastic deformation ahead of the crack, significant blunting of the tip, and permanent separation of the faying surfaces. Cycling eventually causes growth to occur. The newly formed crack segment is tight and similar in appearance to the preoverload condition. As the crack grows through the plastic zone, the opening behavior (as measured by opening stress and amount of change in crack length) increases until it is similar to that before the overload.

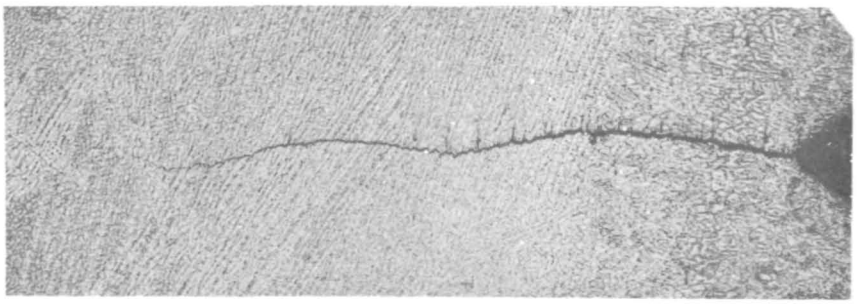

50X

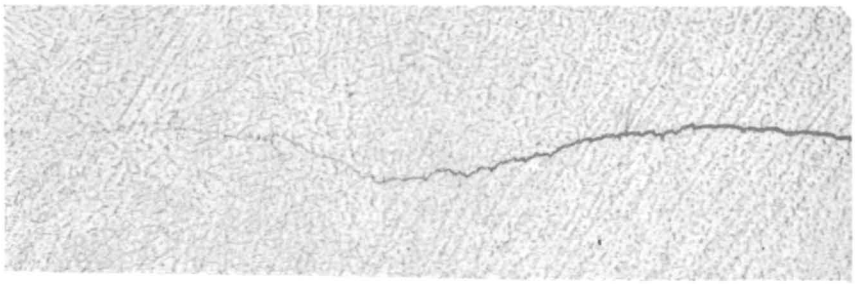

100X

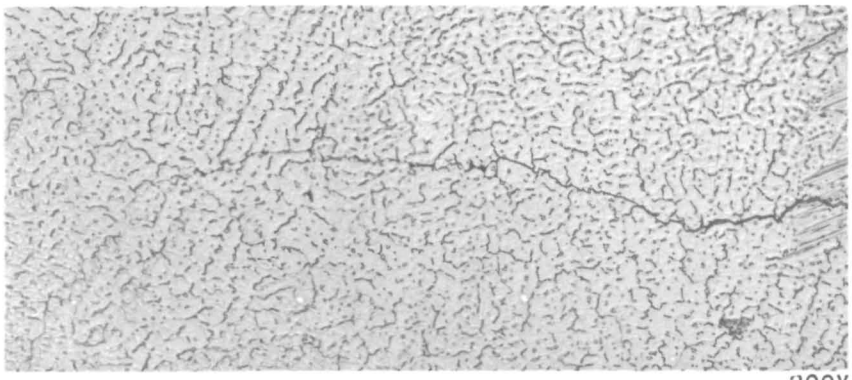

200X

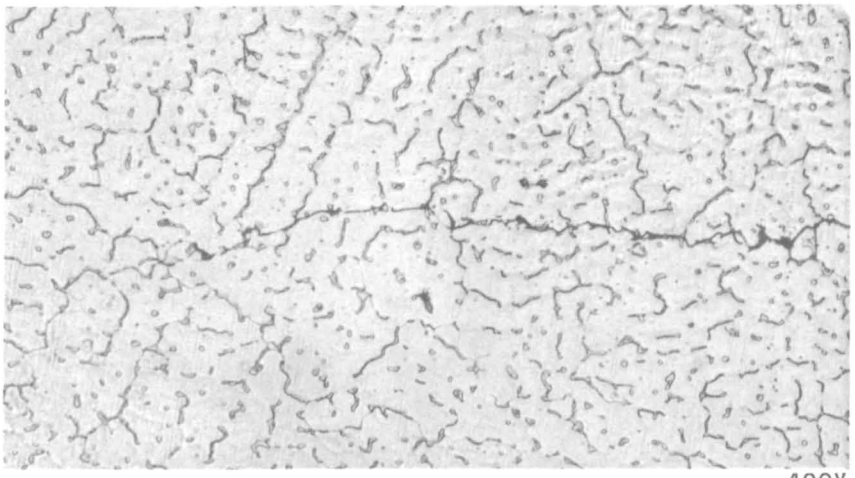

400X

Figure 108. - Welded 2219-T87 after original fatigue extension (W-2).

50X

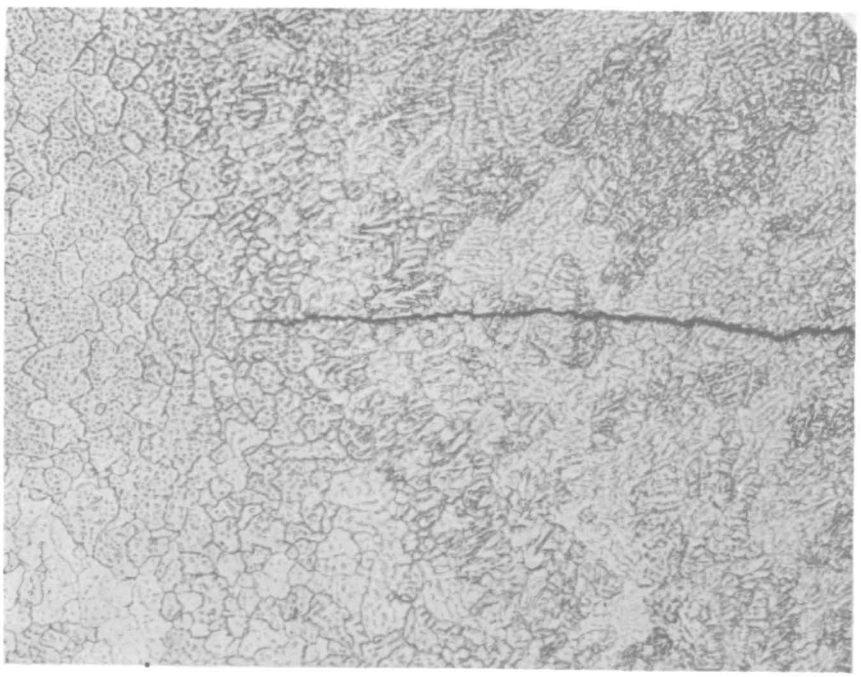

100X

Figure 109. - Welded 2219-T87 after 90-MN/m^2 (13-ksi) overload (W-3).

50X

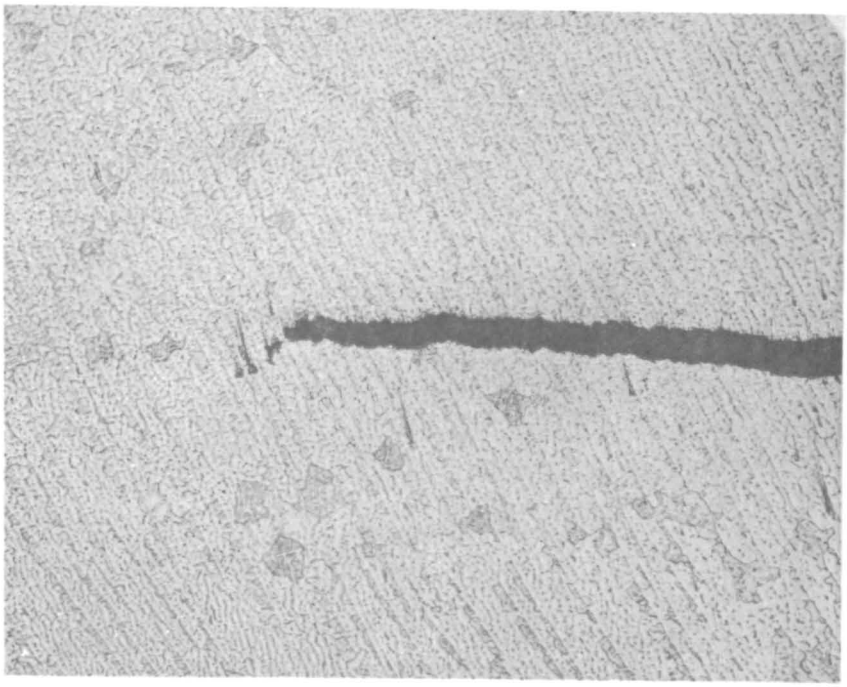

100X

Figure 110. - Welded 2219-T87 after 145-MN/m^2 (17-ksi) overload (W-4).

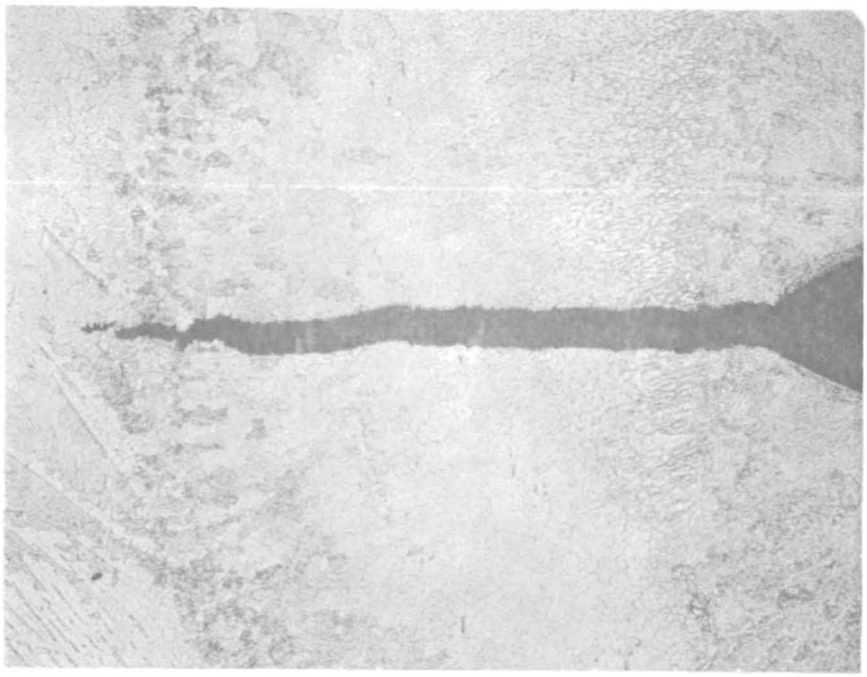

50X

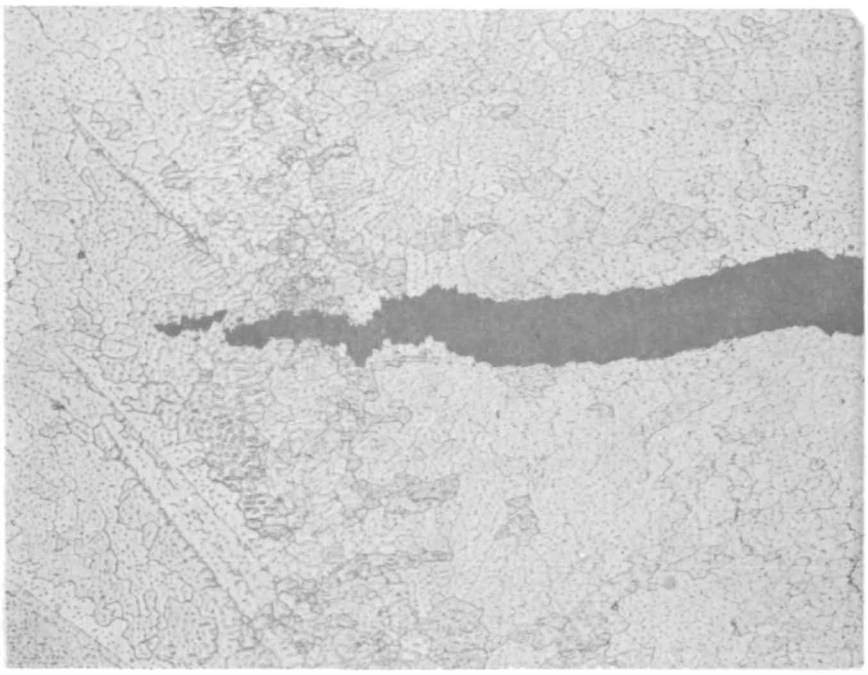

100X

Figure 111. - Welded 2210-T87 after 145-MN/m^2 (21-ksi) overload (W-5).

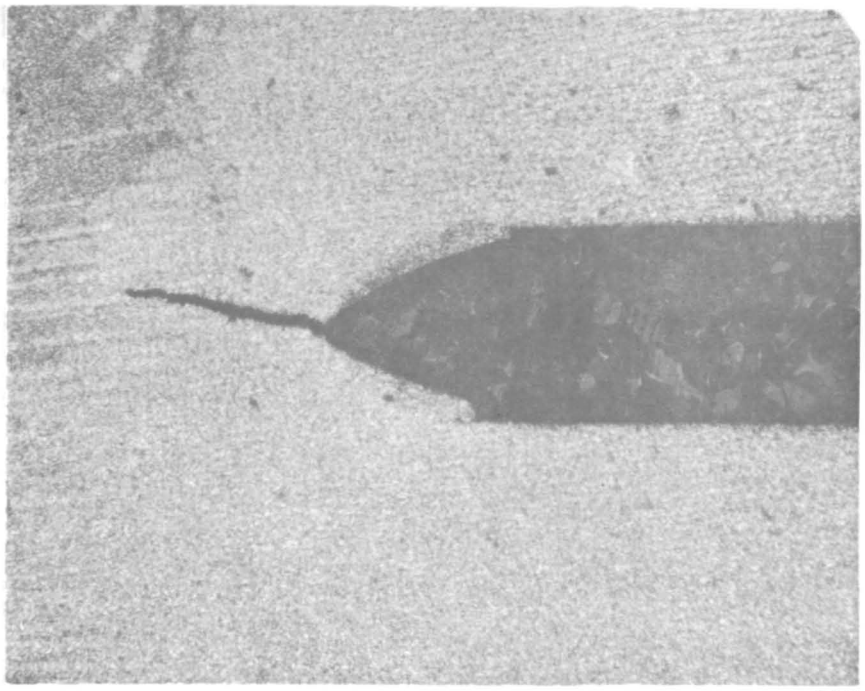

50X

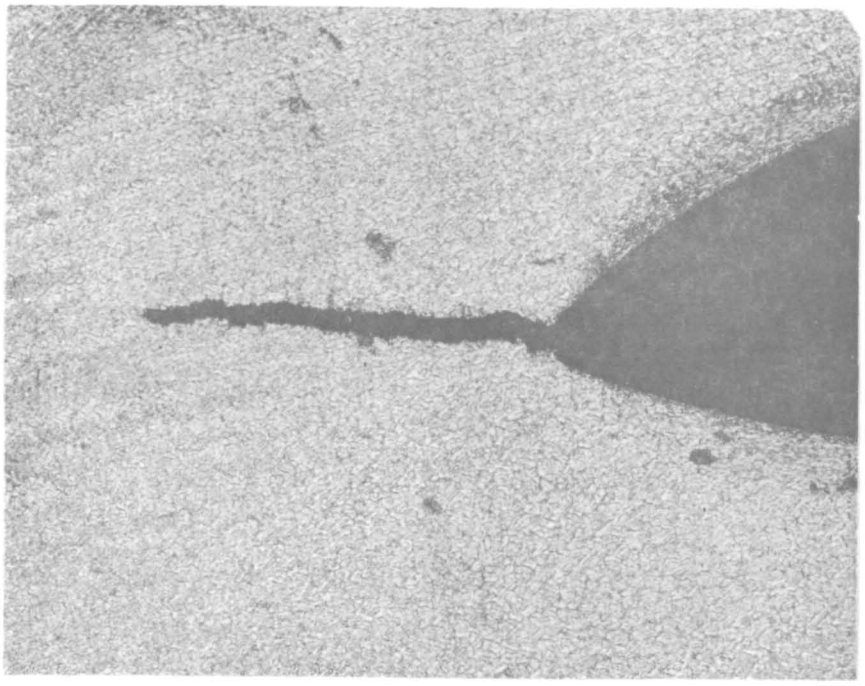

100X

Figure 112. - Welded 2219-T87 after 118-MN/m^2 (17-ksi) overload followed by 62-MN/m^2 (9-ksi) compressive load (W-6).

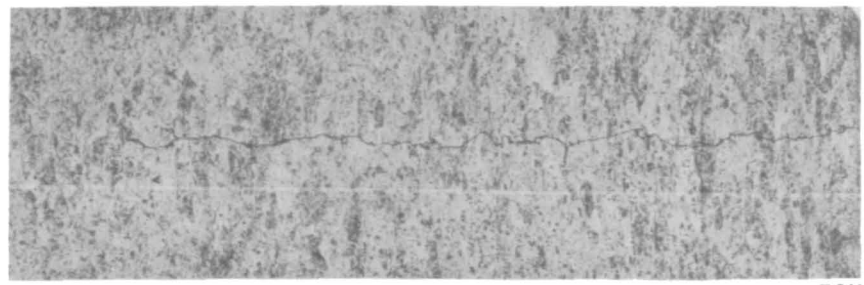

50X

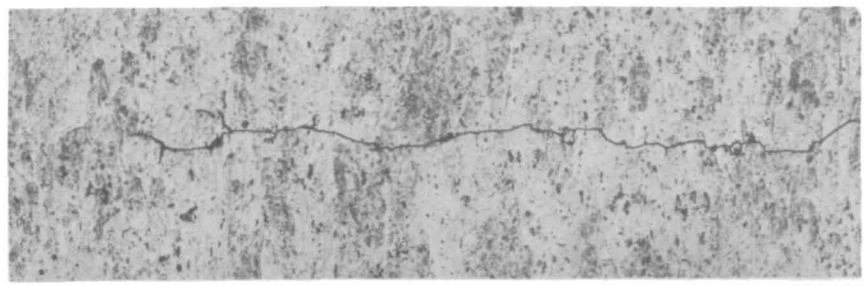

100X

200X

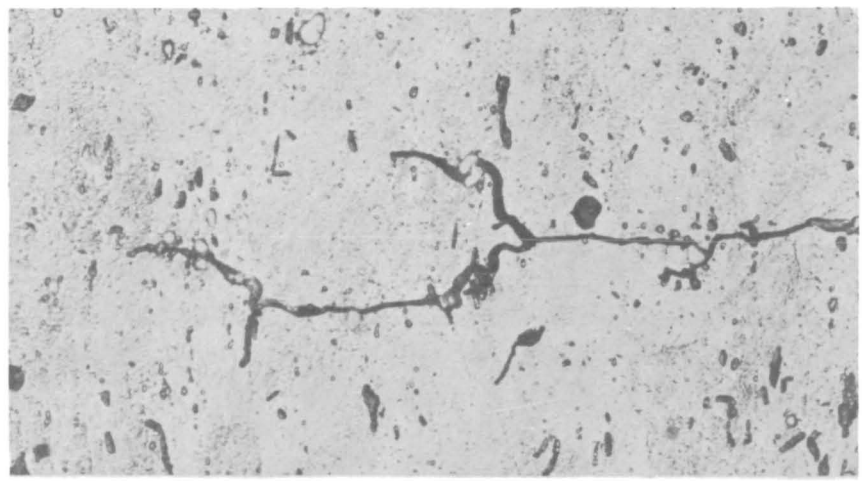

400X

Figure 113. - Base-metal 2219-T87 after original fatigue extension (BM-1).

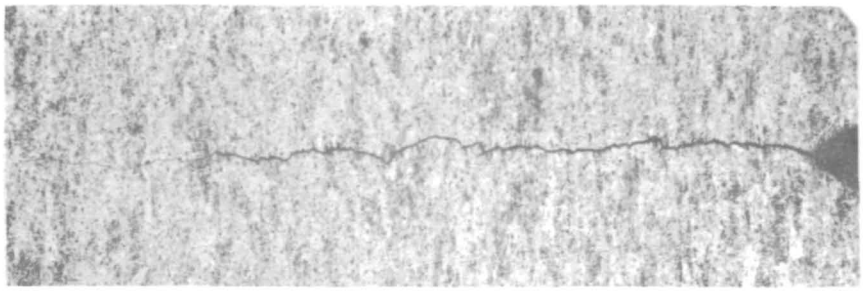

50X

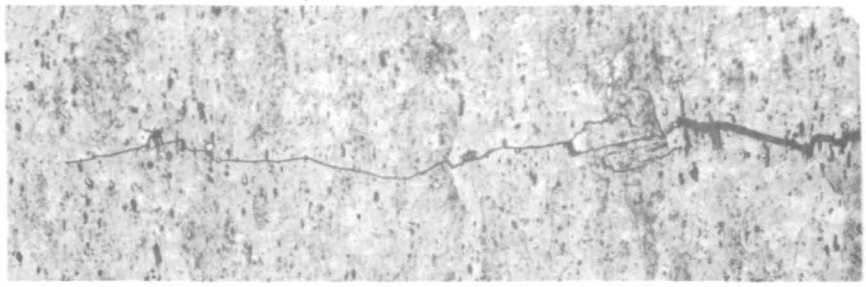

100X

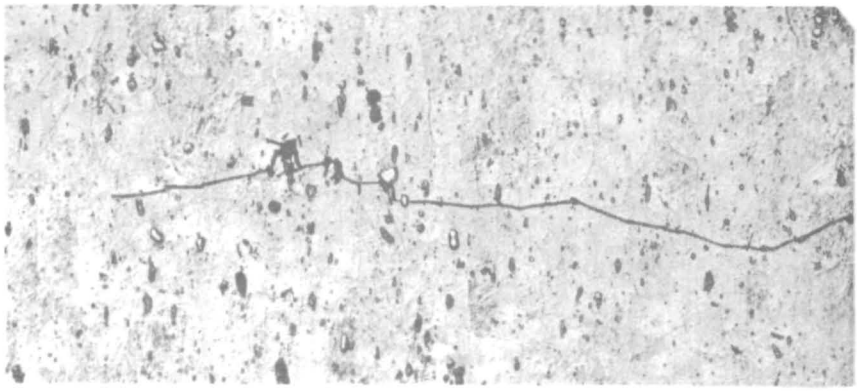

200X

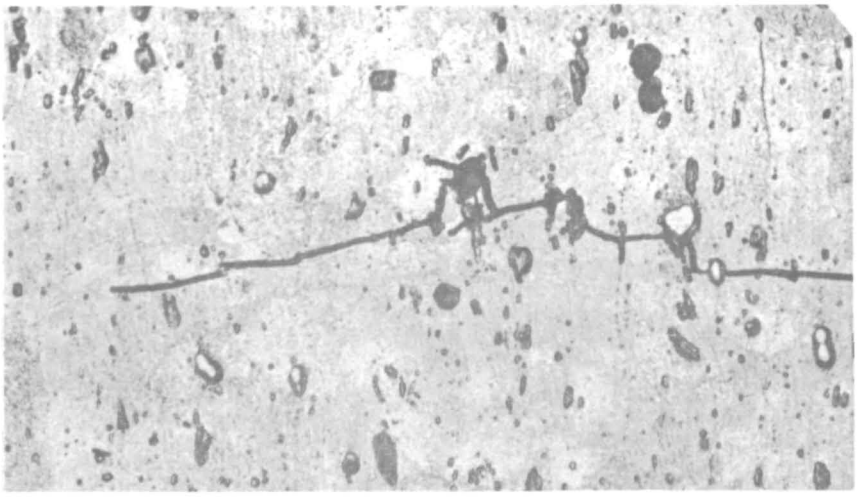

400X

Figure 114. - Base-metal 2219-T87 after 206-MN/m^2 (30-ksi) overload and postoverload fatigue extension (BM-2).

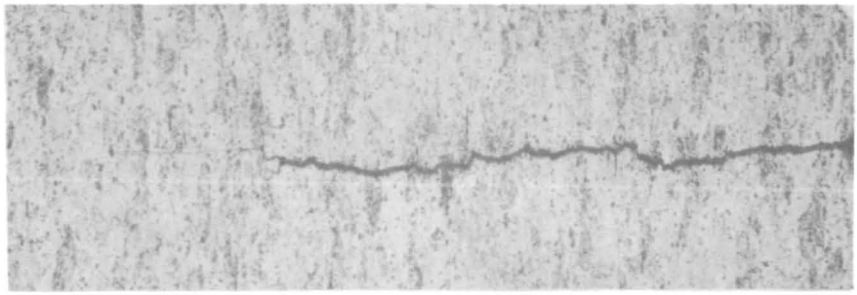

50X

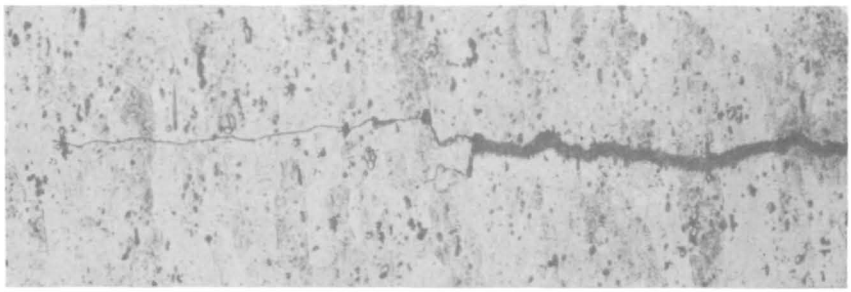

100X

200X

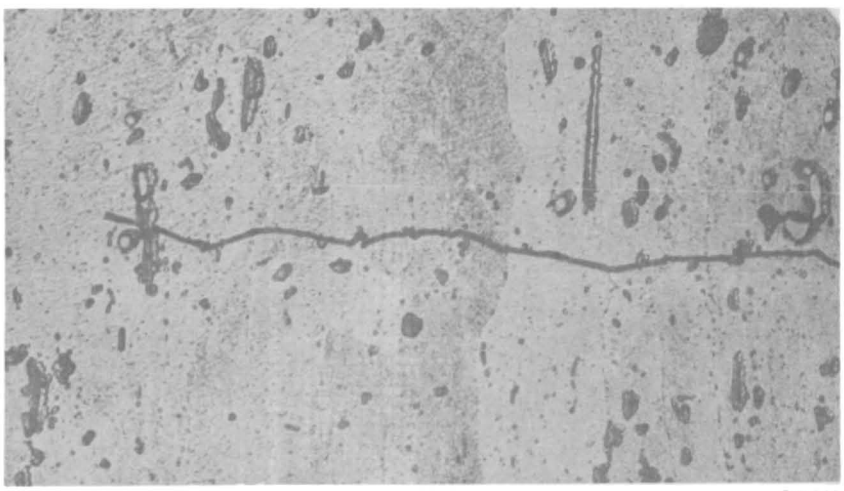

400X

Figure 115. - Base-metal 2219-T87 after 241-MN/m^2 (35-ksi) overload and postoverload fatigue extension (BM-3).

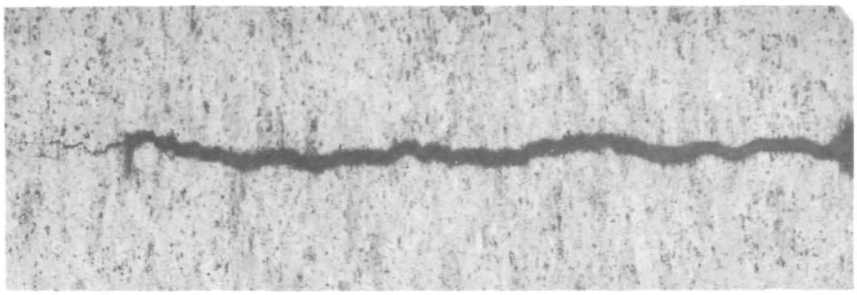

50X

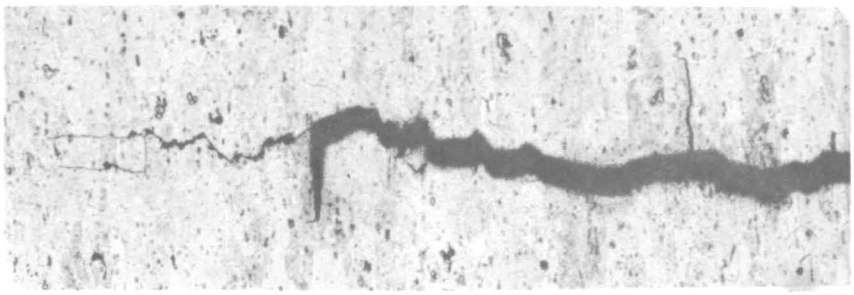

100X

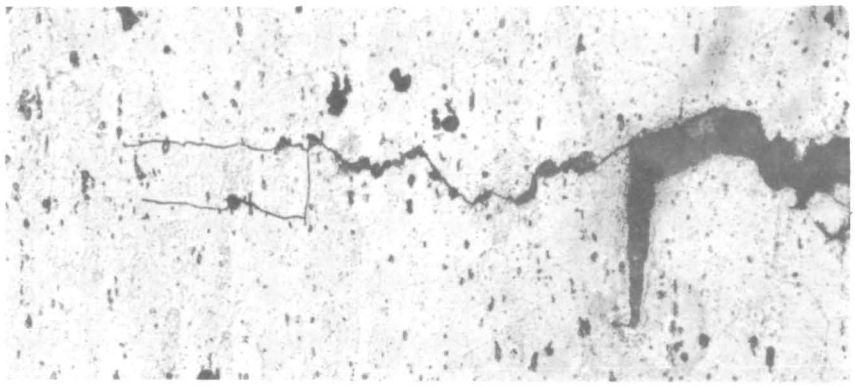

200X

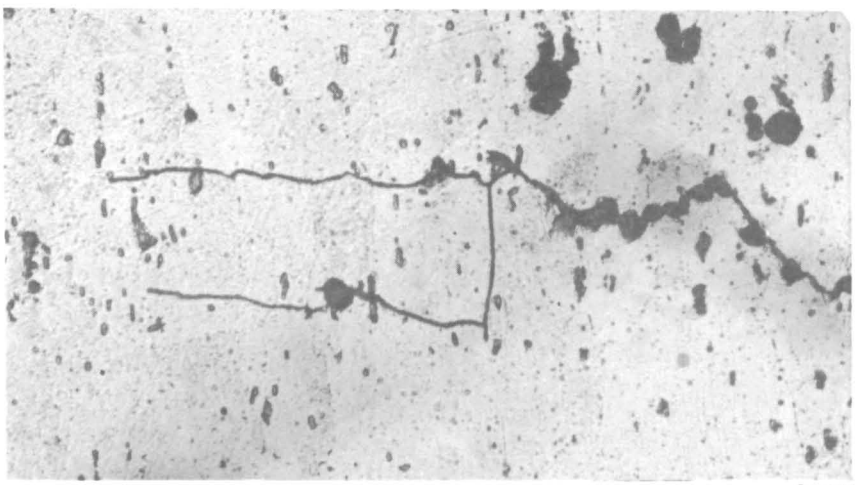

400X

Figure 116. - Base-metal 2219-T87 after 276-MN/m^2 (40-ksi) overload and postoverload fatigue extension (BM-4).

DEEP-SURFACE-FLAW EXTENSION CHARACTERISTICS

This effort was devoted to establishing flaw extension characteristics immediately before failure of the ligament between the flaw front and the back surface of the specimen. The actual nature of the flaw penetration process, i.e., abrupt ligament fracture from a stable ligament condition or a slow steady penetration during monotonic loading, was determined.

Aluminum, titanium, steel (previously described), and welded 2219 aluminum were evaluated.

The approach used was quite similar to that previously described. Both the crack-opening displacement gage and the ultrasonic pitch-catch system were used. The ultrasonic beam was centered on the tip of the defect at the end of the semiminor axis (a depth). To ensure accurate location of the flaw tip, the ultrasonic equipment for centering was adjusted under load. The load used was enough to open the defect but below the load that would permit subcritical growth to occur. Ligament penetration measurements were made with the ultrasonic apparatus fixed in the location previously described.

By fixing the ultrasonic location, crack growth could be measured as a decrease in signal amplitude. Testing was performed using strain rate control and the crack opening displacement gage as the strain sensing transducer. By plotting ultrasonic signal amplitude versus crack-opening displacement, the nature of the crack process was readily apparent. Slow growth during the test was shown by a gradual decrease in the ultrasonic signal amplitude with increasing displacement. Abrupt growth was shown by a sudden decrease in ultrasonic amplitude with little change in displacement.

To study the effects of flaw depth, flaw shape, and crack opening rate, parent-metal aluminum specimens were evaluated. In addition, four specimens each of welded aluminum, parent-metal titanium, and parent-metal steel were evaluated. The results of this study are summarized in the following paragraphs.

Ultrasonic test records showed three types of behavior associated with the ligament penetration process. In five of the parent-metal aluminum specimens, penetration was shown to be stable subcritical growth followed by abrupt growth--usually accompanied by an audible indication of fracture. The through-crack that formed did not propagate catastrophically. One specimen fractured during loading. The remaining specimens (15) exhibited slow growth, then either a rapid, but not abrupt, growth--or a gradual growth to a stable through-crack. Nine of the 15 specimens showed rapid growth, and six showed gradual growth.

Figure 117 is a typical record of ultrasonic signal amplitude versus crack-opening displacement. This specimen (ACC-12) showed rapid penetration. Figure 118 is a companion crack-opening displacement curve.

Table XX summarizes data for parent-metal aluminum specimens. The table gives initial flaw geometry, crack-opening displacement rate, and a description of the type of ligament penetration behavior observed.

Figures 119, 120 and 121 show the penetration portion of the load cycle for the abrupt, rapid, and gradual failures. Categorization into these three groups is somewhat subjective; therefore, the plots are presented for the reader's examination and interpretation.

Crack-opening displacement curves for the rapid and gradual penetration curves showed the characteristic smooth curve of increasing displacement with increasing load. For specimens categorized as abrupt penetrations, three of the five (ALP-1, ACC-5 and ACCO-12) showed discontinuities at the time of ligament failure. The remaining two showed smooth curves. Figures 122, 123 and 124 are curves that show discontinuities.

Parent-metal aluminum tests were prepared and conducted in a manner that attempted to reveal the effects of the following variables:

1) effect of flaw depth;

2) effect of flaw shape;

3) effect of rate.

The effects of the variables were studied by determining the rate of penetration immediately before ligament failure. This was determined from the ultrasonic data plot as the slope of the line (Δ ultrasonic amplitude, measured in volts/Δ crack-opening displacement). Evaluation of the variables showed that ligament penetration behavior appeared to be related only to flaw depth. No relationship between behavior and flaw shape or testing rate was found. Figure 125 gives the data for the depth effect. Note the rapidly increasing rate of penetration for depths of more than 92% of specimen thickness. Specimens that exhibited abrupt penetration were not necessarily the deepest flaws and were of similar depth ($\sim$88% a/t). Whether this is a significant observation cannot be established on the basis of the limited data available.

Specimens of welded 2219 showed only gradual growth to the penetrated condition. Table XXI summarizes the welded data.

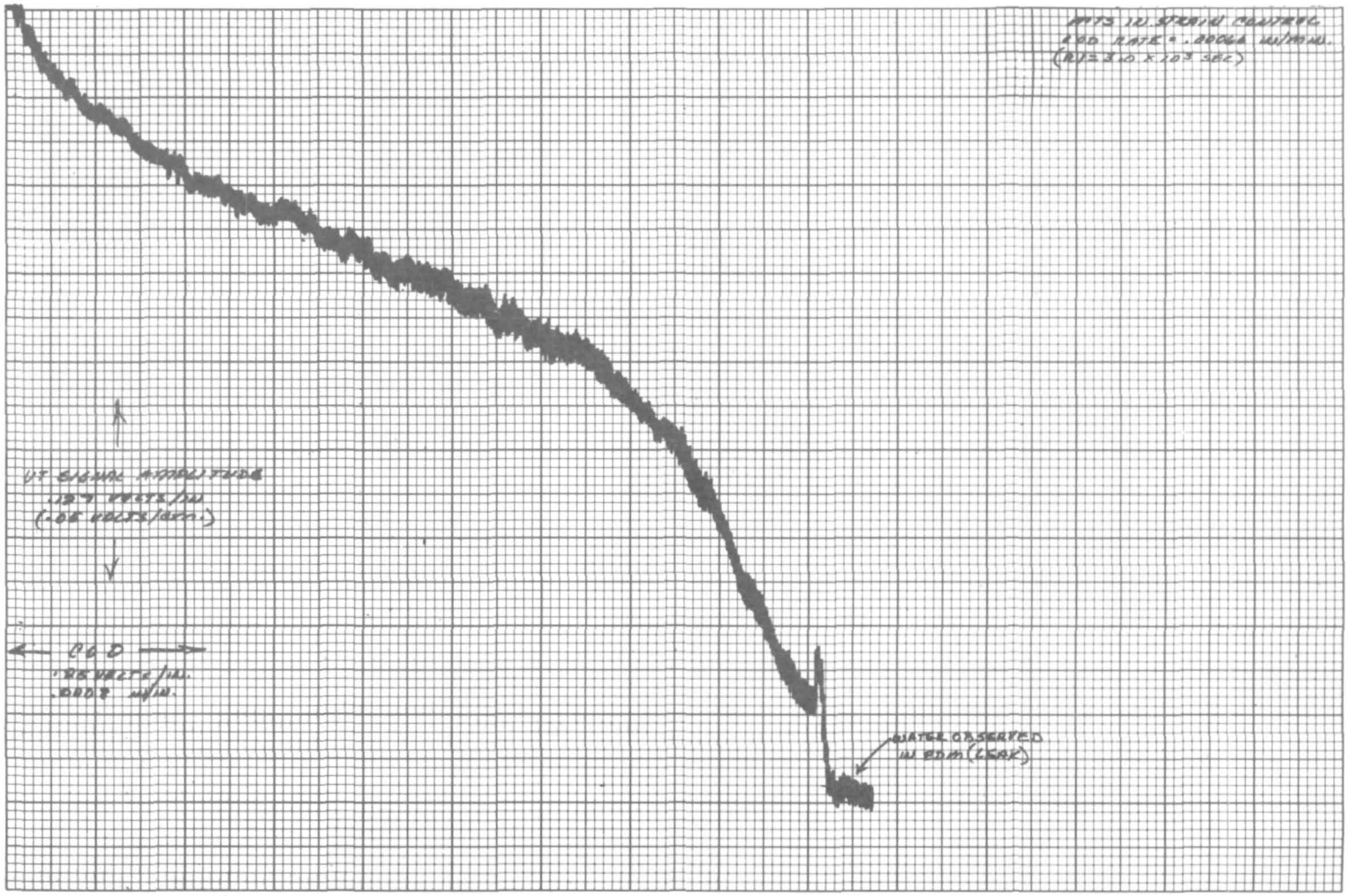

Figure 117. - Ultrasonic data record for ligament penetration of specimen ACC-12.

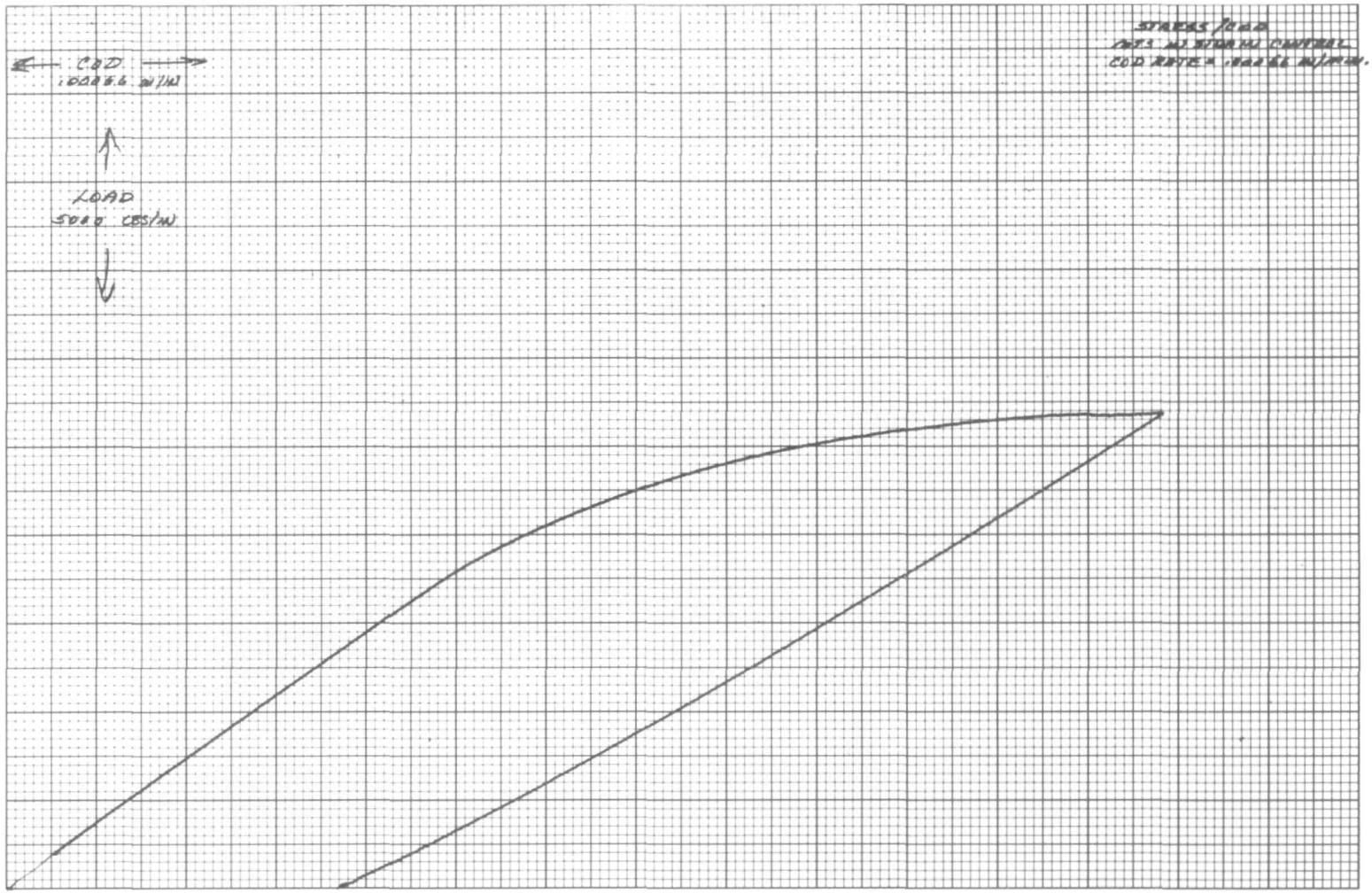

Figure 118. - Crack-opening displacement curve for specimen ACC-12.

Figure 126 summarizes data plots for the four tests. The crack-opening displacement records did not indicate any discontinuities and are therefore not presented.

TABLE XX. - SUMMARY OF PARENT-METAL ALUMINUM PENETRATION DATA

Specimen no.	Flaw geometry						Testing rate		Penetration description
	Depth, a		Width, 2C		a/2C	a/t			
	cm	(in.)	cm	(in.)			nm/min	(in./min)	
ACC-1LP	0.605	(0.238)	1.83	(0.72)	0.33	0.97	0.0019	(0.00033)	Rapid
ACC-4LP	0.531	(0.209)	1.68	(0.66)	0.32	0.85	0.0019	(0.00033)	Specimen fractured
ACC-5LP	0.508	(0.200)	1.14	(0.45)	0.44	0.81	0.038	(0.0066)	Abrupt
ACC-8LP	0.546	(0.215)	1.30	(0.51)	0.42	0.87	0.0019	(0.00033)	Rapid
ACC-10LP	0.574	(0.226)	1.50	(0.59)	0.38	0.92	0.075	(0.013)	Rapid
ACC-11LP	0.579	(0.228)	1.50	(0.59)	0.39	0.93	0.038	(0.0066)	Rapid
ACC-12LP	0.564	(0.222)	1.50	(0.59)	0.38	0.91	0.0038	(0.00066)	Rapid
ACCO-1LP	0.579	(0.228)	1.78	(0.70)	0.33	0.93	0.0019	(0.00033)	Rapid
ACCO-6LP	0.531	(0.209)	1.27	(0.50)	0.42	0.85	0.0038	(0.00066)	Gradual
ACCO-8LP	0.561	(0.221)	1.37	(0.54)	0.41	0.89	0.038	(0.0066)	Abrupt
ACCO-9LP	0.584	(0.230)	1.45	(0.57)	0.40	0.95	0.0038	(0.00066)	Rapid
ACCO-10LP	0.572	(0.225)	1.52	(0.60)	0.38	0.92	0.151	(0.026)	Gradual
ACCO-11LP	0.531	(0.209)	1.35	(0.53)	0.39	0.85	0.038	(0.0066)	Rapid
ACCO-12LP	0.541	(0.213)	1.37	(0.54)	0.39	0.87	0.038	(0.0066)	Abrupt & audible
ALP-1	0.541	(0.213)	2.57	(1.01)	0.21	0.87	0.038	(0.0066)	Abrupt & audible
ALP-3	0.536	(0.211)	1.09	(0.43)	0.49	0.86	0.038	(0.0066)	Rapid
ALP-4	0.554	(0.218)	1.12	(0.44)	0.50	0.89	0.038	(0.0066)	Abrupt
ALP-5	0.574	(0.226)	1.42	(0.56)	0.40	0.92	0.038	(0.0066)	Gradual
ALP-6	0.589	(0.232)	1.52	(0.60)	0.39	0.94	0.038	(0.0066)	Gradual
ALP-7	0.513	(0.202)	1.17	(0.46)	0.44	0.83	0.038	(0.0066)	Gradual
ALP-8	0.572	(0.225)	1.47	(0.58)	0.39	0.93	0.011	(0.0020)	Rapid

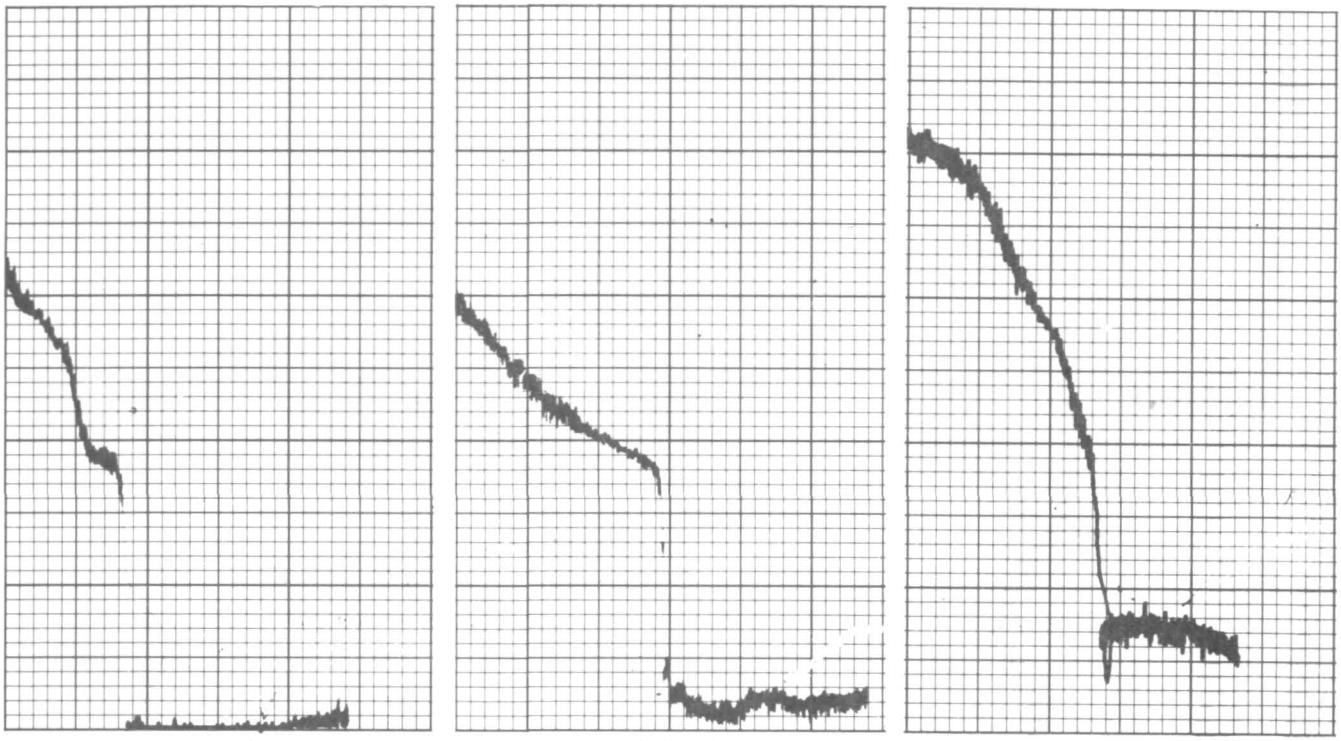

ACC-5 ACCO-8 ACCO-12

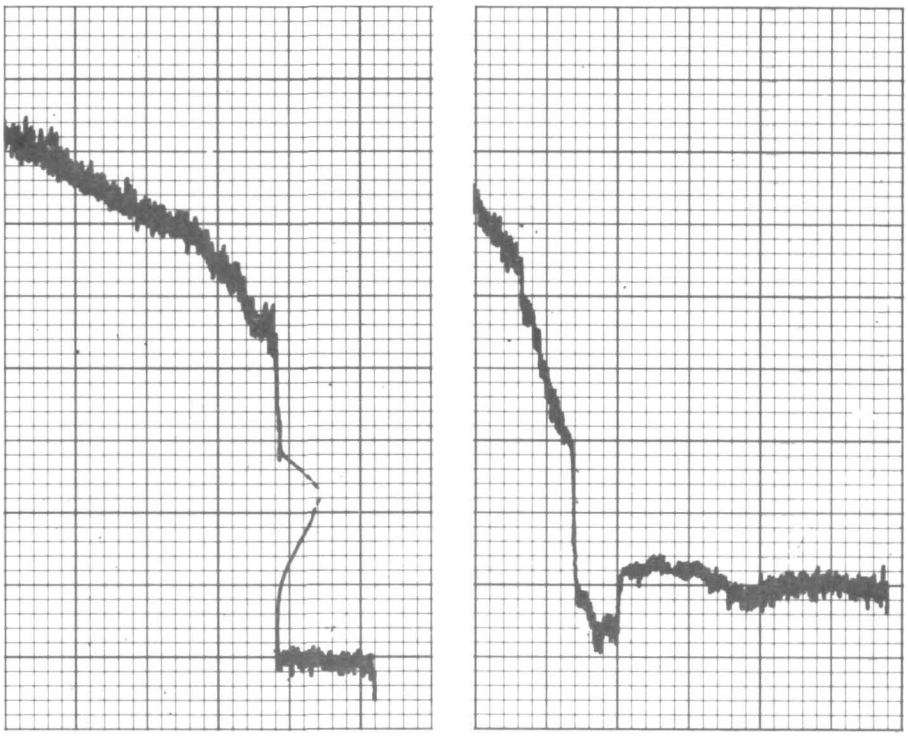

ALP-1 ALP-4

Figure 119. - Ultrasonic records for aluminum specimens exhibiting abrupt penetration

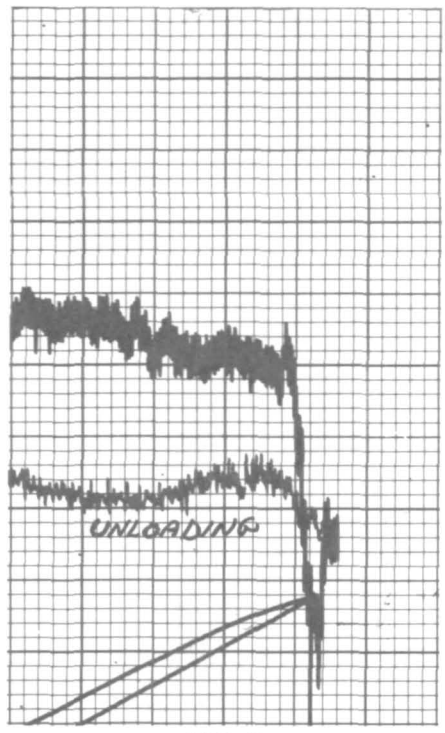

ACC-1

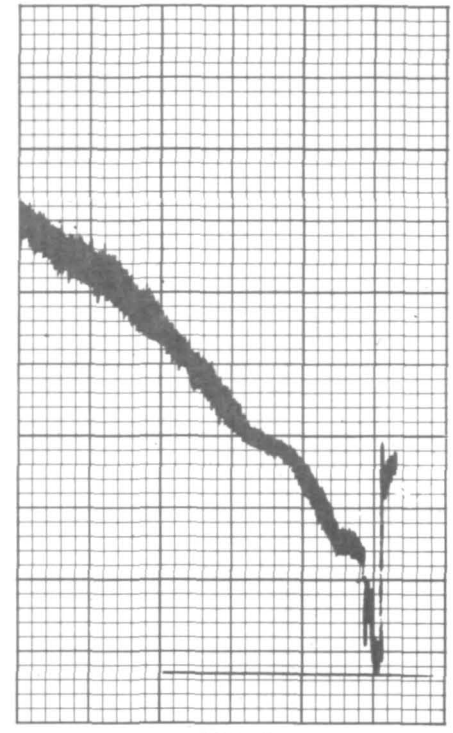

ACC-8

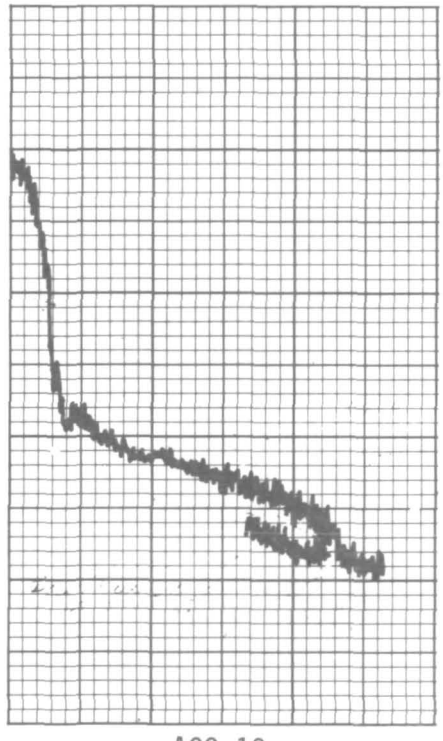

ACC-10

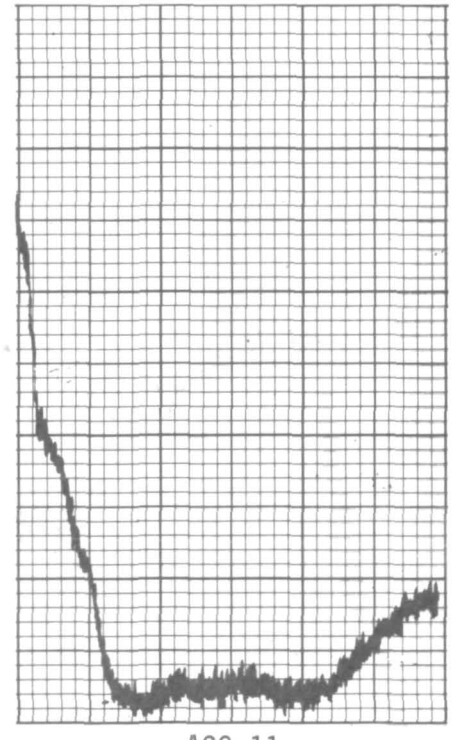

ACC-11

Figure 120. - Ultrasonic records for aluminum specimens exhibiting rapid penetration.

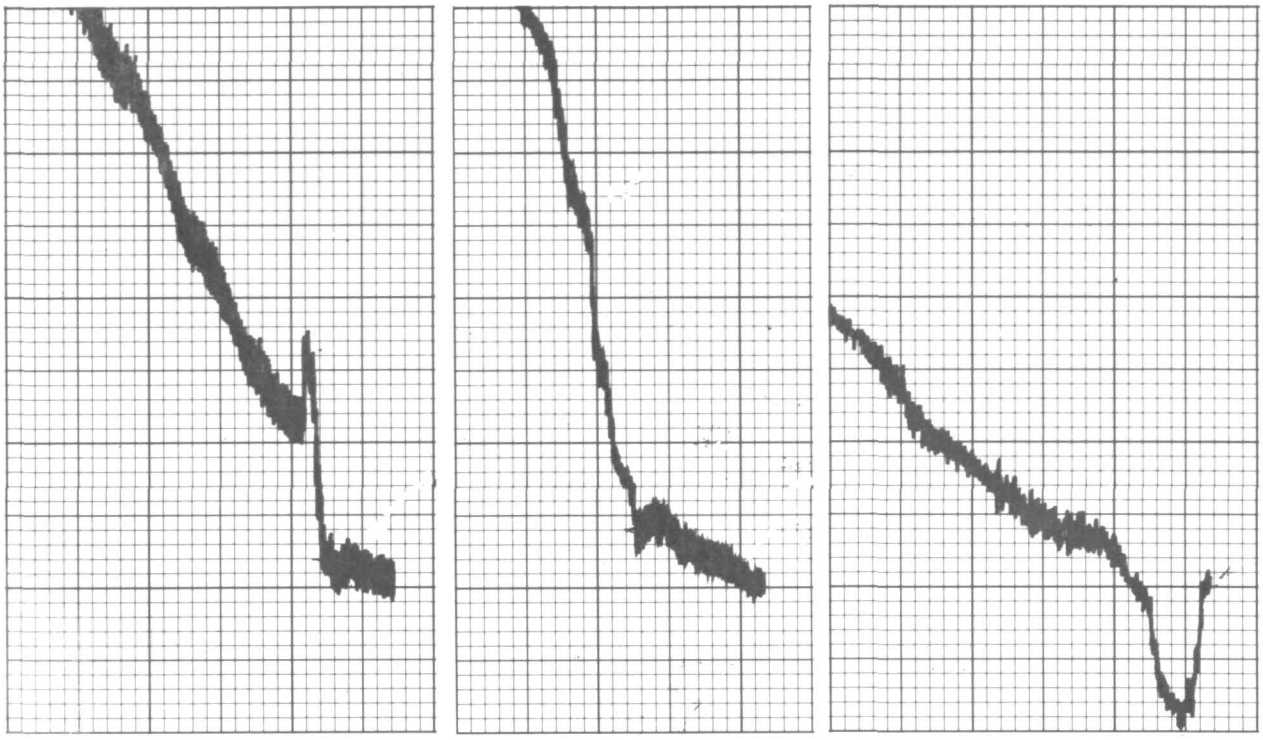

ACC-12 ACCO-1 ACCO-11

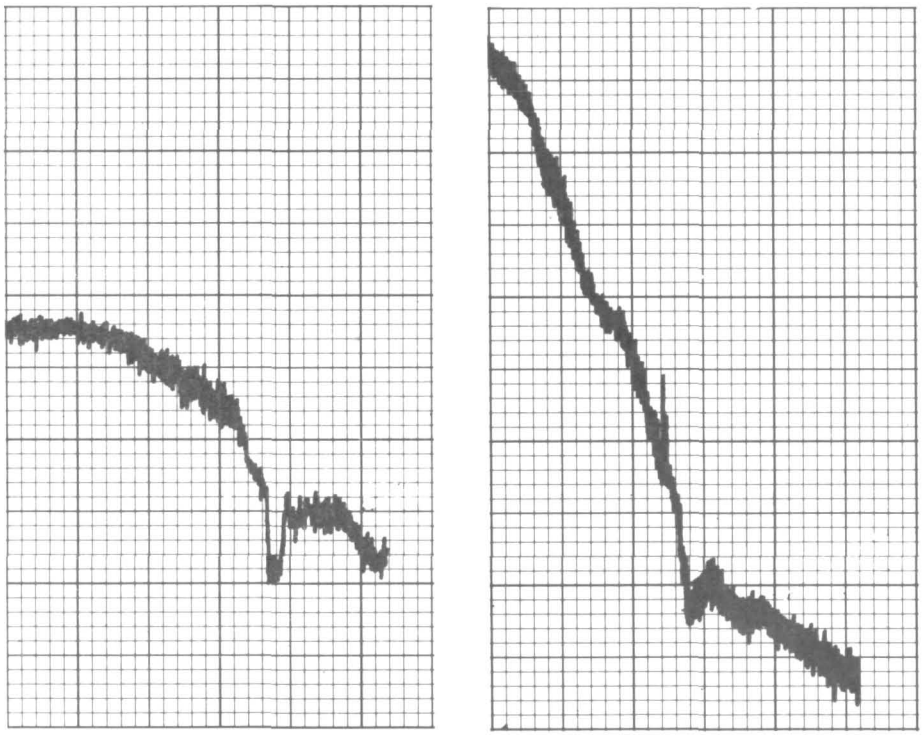

ALP-3 ALP-8

Figure 120. - Concluded.

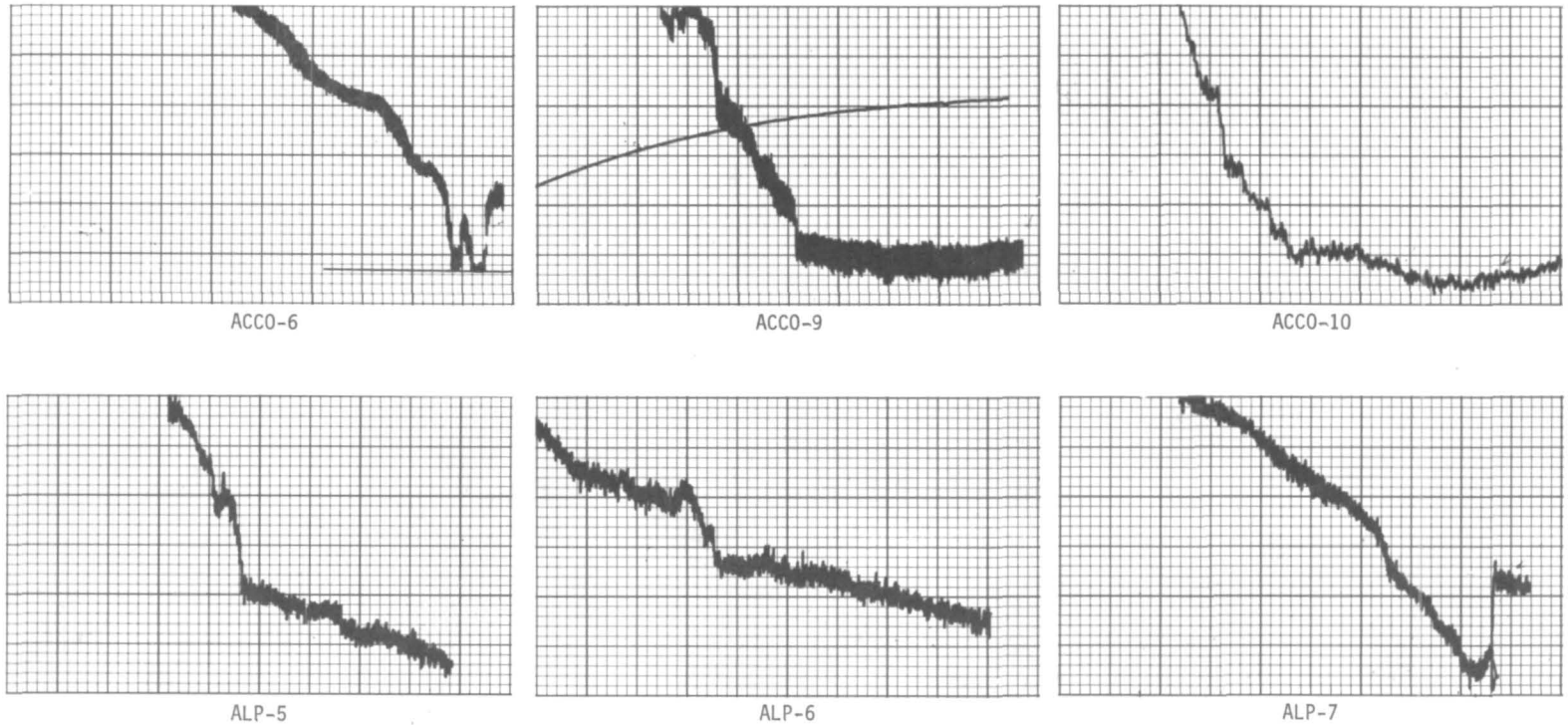

Figure 121. - Ultrasonic records for aluminum specimens exhibiting gradual penetration.

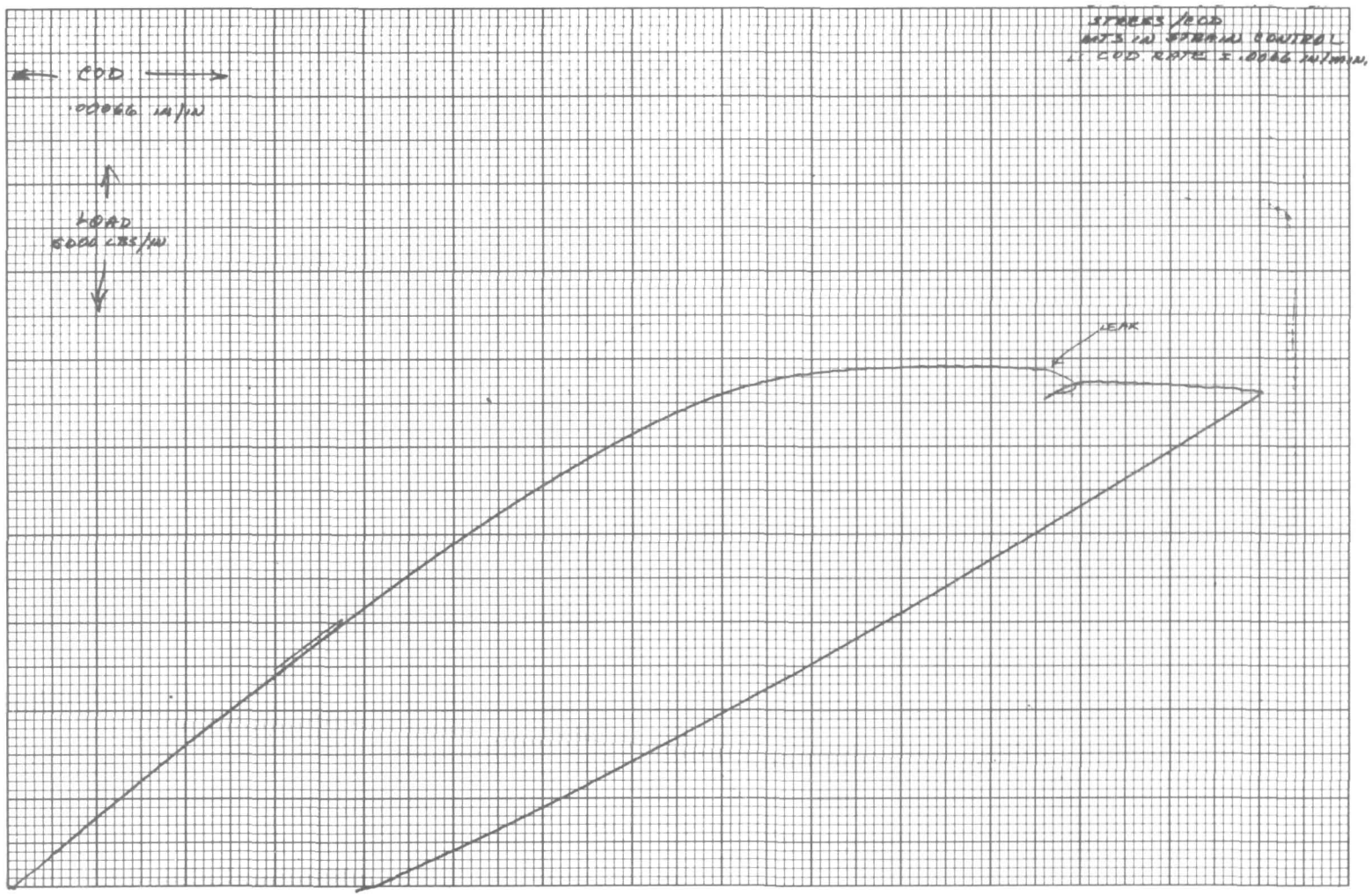

Figure 122. - Crack-opening displacement curve for specimen ACC-5.

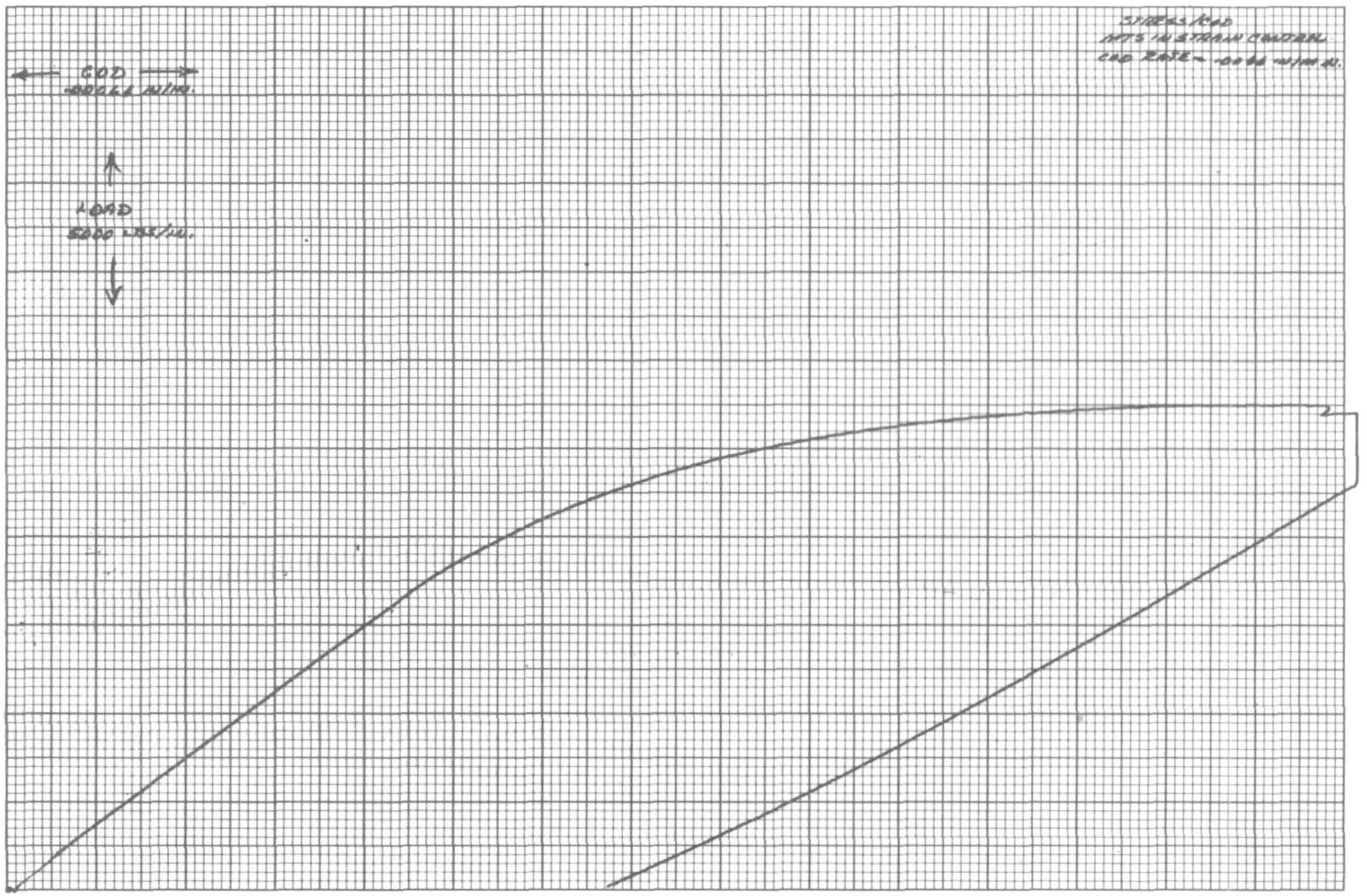

Figure 123. - Crack-opening displacement curve for specimen ACCO-12.

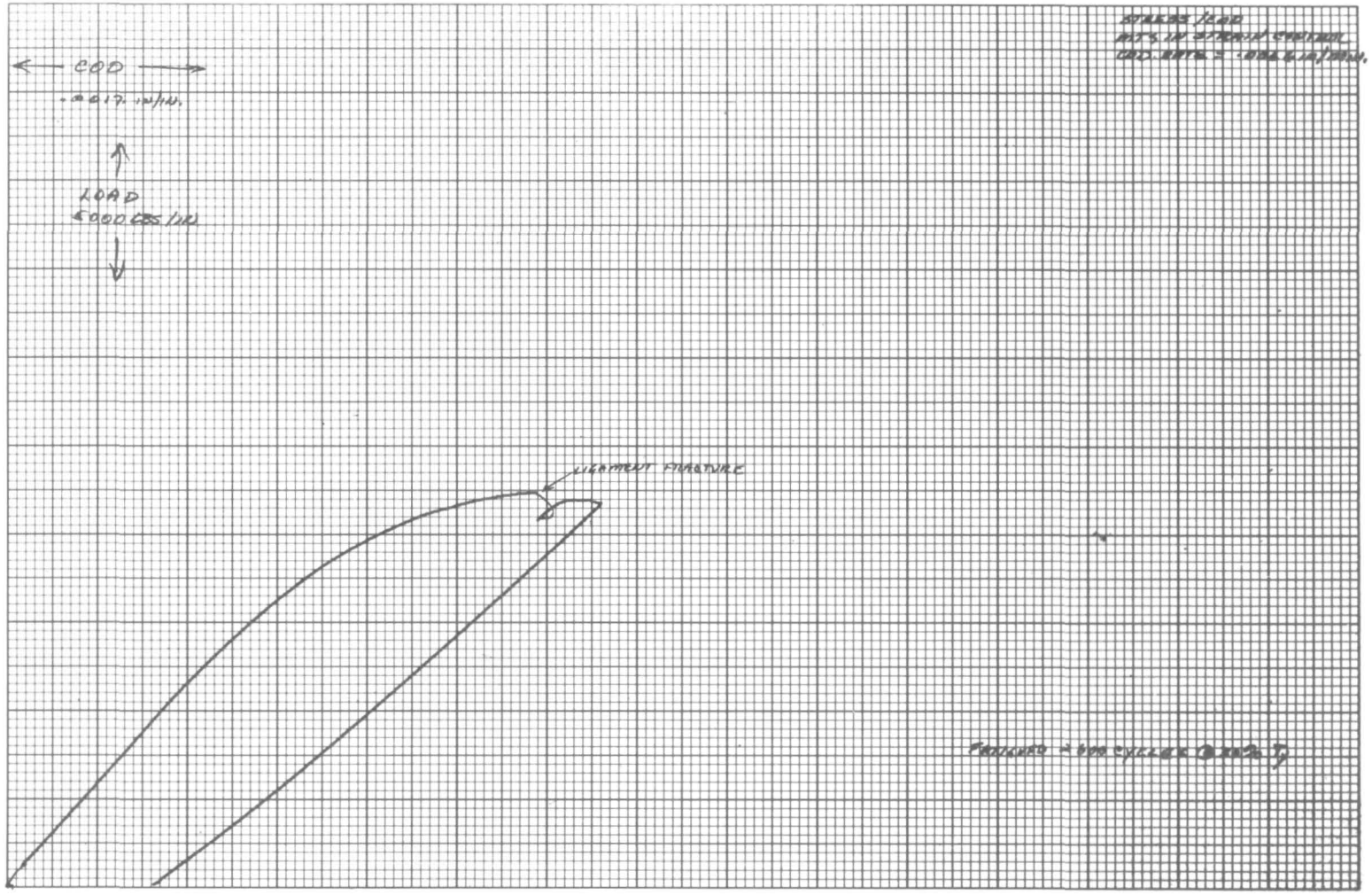

Figure 124. - Crack-opening displacement curve for specimen ALP-1.

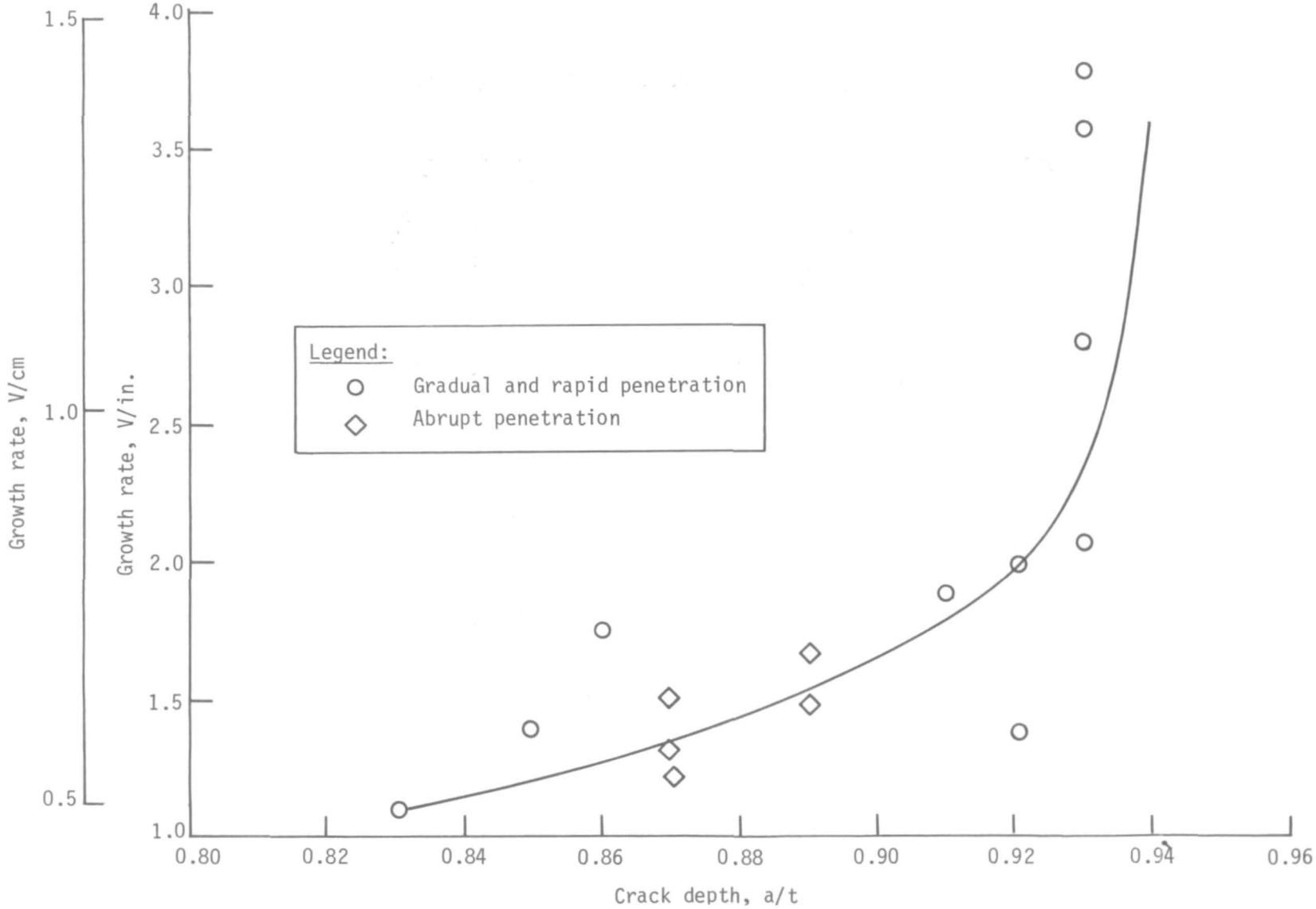

Figure 125. - Effect of crack depth on growth rate before penetration in aluminum.

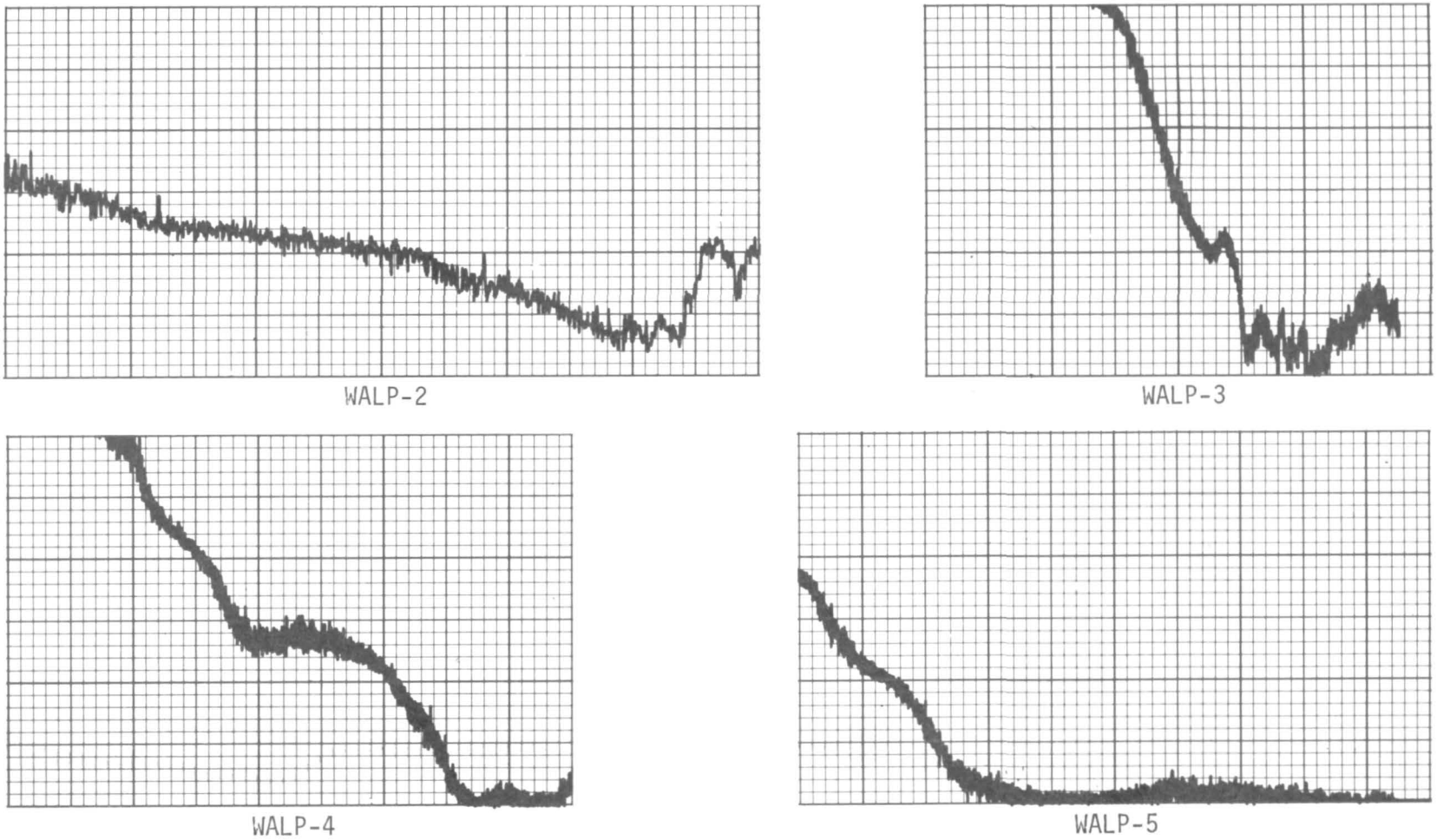

Figure 126. - Ultrasonic penetration records for welded aluminum specimens.

TABLE XXI. - SUMMARY OF WELDED ALUMINUM-LIGAMENT PENETRATION DATA

Specimen no.	Flaw geometry							Penetration Description
	Depth, a,		Width, 2C,		a/2C	a/t	a/Q	
	cm	(in.)	cm	(in.)				
WALP-2	0.513	(0.202)	1.32	(0.52)	0.39	0.85		Gradual
WALP-3	0.485	(0.191)	1.37	(0.54)	0.35	0.79		Gradual
WALP-4	0.467	(0.184)	1.21	(0.48)	0.39	0.77		Gradual
WALP-5	0.427	(0.168)	0.98	(0.39)	0.44	0.67		Gradual
* Testing rate - 0.038 nm/min (0.0066 in./min).								

Tests of four titanium parent-metal specimens showed abrupt penetrations in all cases; two of the penetrations were accompanied by an audible signal. Table XXII summarizes specimen geometry and rate data. Figure 127 is a composite presentation of data plots for the four specimens. Crack opening displacement curves showed an abrupt decrease in load associated with the penetration process. Figures 128 and 129 present two of the curves.

TABLE XXII. - SUMMARY OF PARENT-METAL TITANIUM-LIGAMENT PENETRATION DATA

Specimen no.	Flaw geometry							Penetration Description
	Depth, a,		Width, 2C,		a/2C	a/t	a/Q	
	cm	(in.)	cm	(in.)				
TCC-1LP	0.251	(0.099)	0.75	(0.30)	0.33	0.79		Abrupt
TCC-2LP	0.241	(0.095)	0.68	(0.27)	0.36	0.75		Abrupt & audible
TCCO-1LP	0.246	(0.097)	0.74	(0.29)	0.33	0.77		Abrupt & audible
TCCO-2LP	0.254	(0.100)	0.74	(0.29)	0.34	0.79		Abrupt
* Testing rate - 0.038 nm/min (0.0066 in./min).								

Tests of steel specimens showed very gradual penetration. Figure 130 and Table XXIII summarize the data.

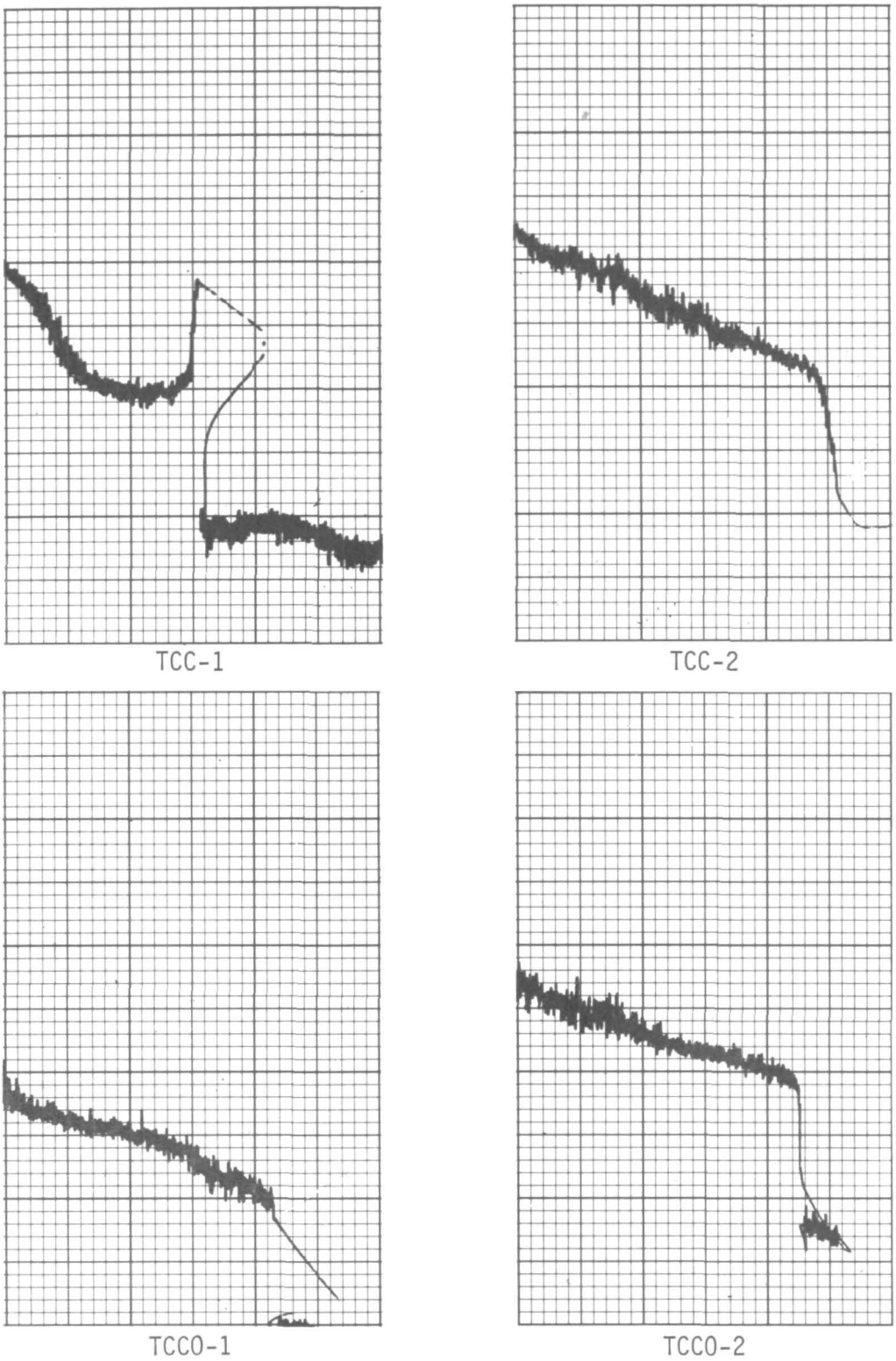

Figure 127. - Ultrasonic penetration records for titanium specimens.

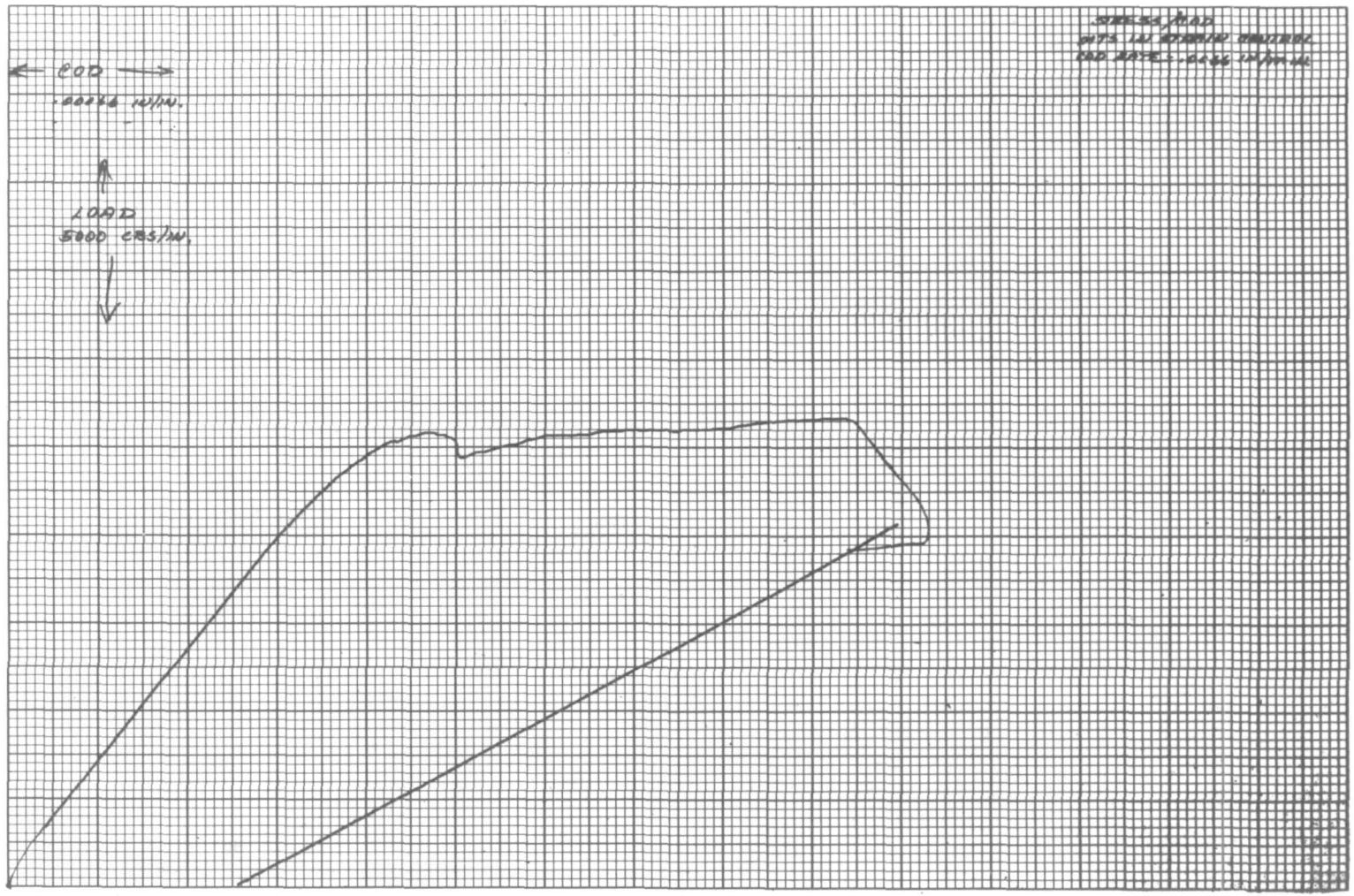

Figure 128. - Crack-opening displacement curve for titanium specimen TCCO-1.

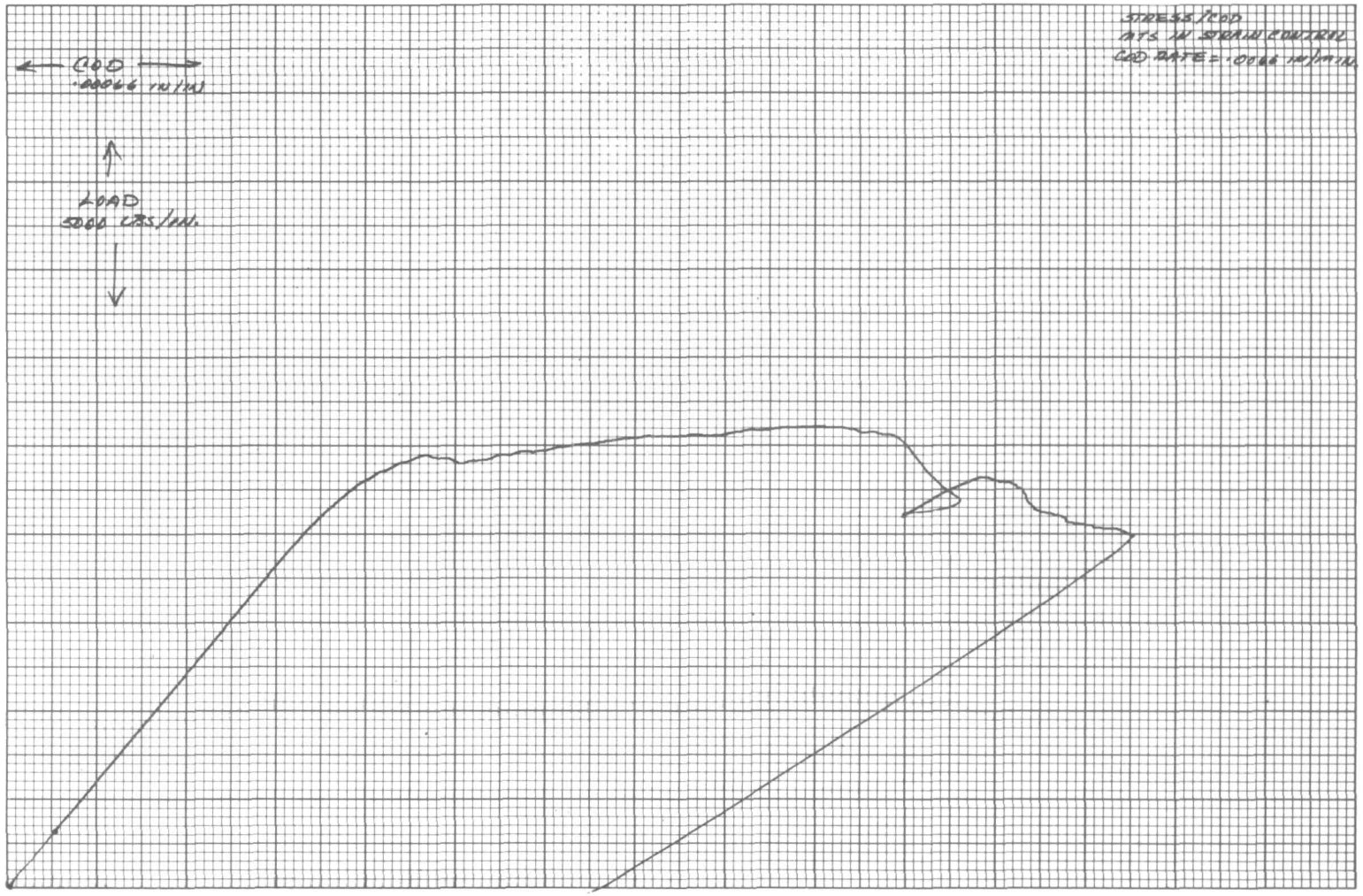

Figure 129. - Crack-opening displacement curve for titanium specimen TCC-1

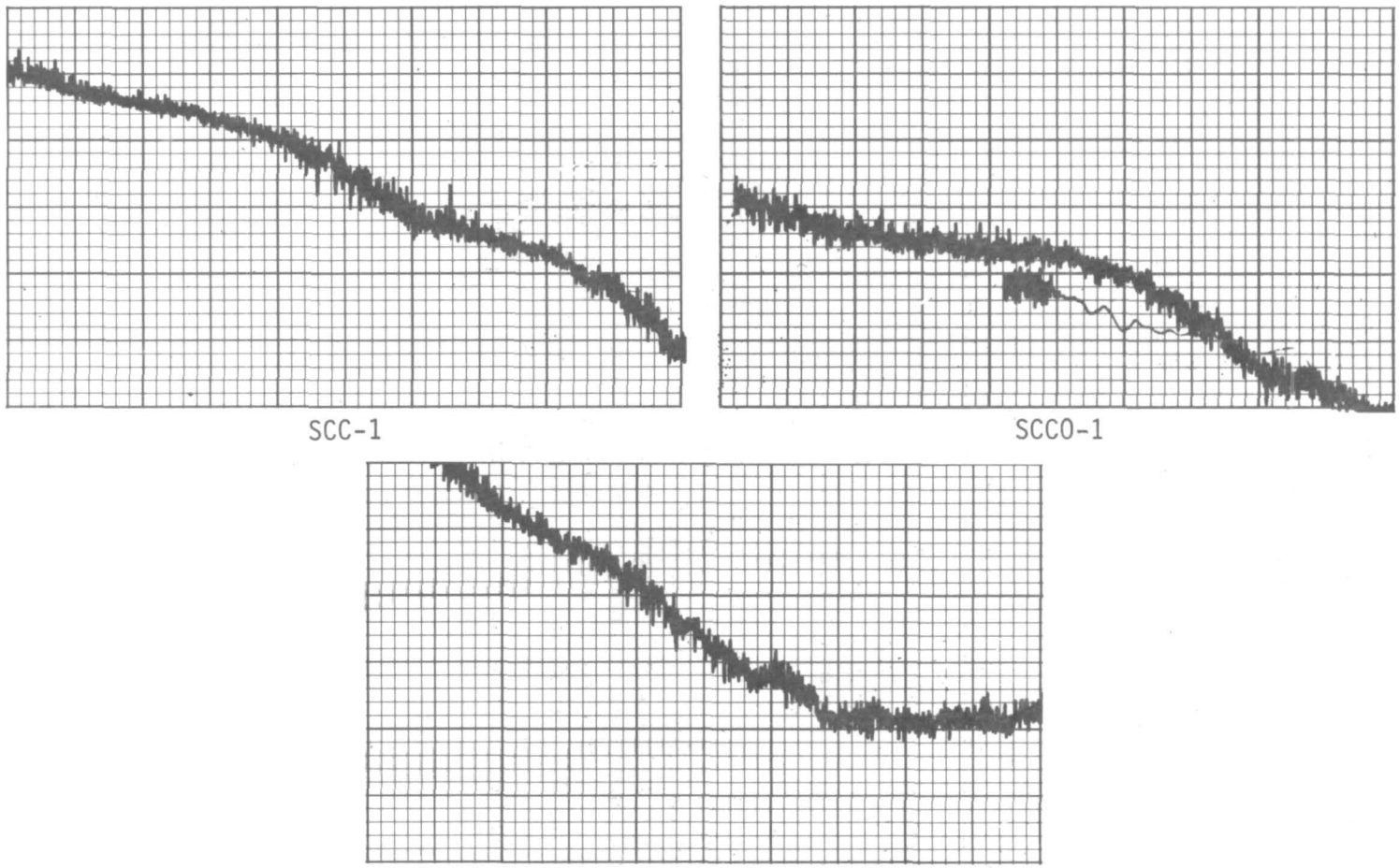

Figure 130. - Ultrasonic penetration records for steel specimens.

TABLE XXIII. - SUMMARY OF PARENT-METAL STEEL-LIGAMENT PENETRATION DATA

Specimen no.	Flaw geometry							Penetration Description
	Depth, a,		Width, 2C,		a/2C	a/t	a/Q	
	cm	(in.)	cm	(in.)				
SCC-1LP	0.257	(0.101)	0.72	(0.28)	0.36	0.83		Gradual
SCC-2LP	0.279	(0.110)	0.79	(0.31)	0.35	0.92		Gradual
SCCO-1LP	0.257	(0.101)	0.71	(0.28)	0.36	0.83		Gradual
SCCO-2LP	0.203	(0.080)	0.60	(0.24)	0.34	0.66		Specimen failed in grip

* Testing rate - 0.038 nm/min (0.0066 in./min).

Results of ligament tests clearly illustrate that the nature of the penetration process varies. Penetration can occur by an abrupt fracturing after subcritical growth or by continuous growth. Continuous growth can be at a rather steady rate until penetration occurs, or by an increasing rate at the critical flaw depth.

Differences in the nature of the penetration process appeared to be closely tied to the properties of the various materials. The titanium alloy, which showed the lowest toughness-to-strength ratio, penetrated the ligament abruptly. The parent-metal aluminum alloy, somewhat tougher, showed a transitional behavior that included the extremes of abrupt penetration and relatively slow growth. Welded aluminum, significantly tougher than the parent metal, showed only gradual penetration. The steel, also very tough, showed behavior comparable to that of the welded aluminum.

CONCLUSIONS

The results of this phase of the experimental program clearly demonstrated that the collimated ultrasonic pitch-catch inspection technique is a powerful tool that can be used in fracture-related studies. Certain behavioral aspects associated with fracture and crack extension that cannot be studied using other techniques have been evaluated with the ultrasonic method.

The first part of the effort pertaining to performance characteristics and optimization of the collimated beam demonstrated that beam width could be reduced by at least 50%. Evaluation of various collimator designs, combinations, and frequencies showed that the combination of a cone collimator and cone receiver was the most effective in terms of maximizing signal strength. A study of the effect of surface roughness showed that the amplitude of a reflected signal was sensitive to the degree of roughness; however, even for the highest roughness levels (300 μin.), the effect on the amplitude was minor compared to that produced by the presence of a defect. The final part of the effort associated with performance characteristics was to determine the effectiveness of the technique to sense the shape and location of small defects in thin materials. It was found that defects as small as 0.25-mm (0.01-in.) deep could be readily detected, but not mapped.

After the characterization effort, three studies were performed to determine;

1) crack-opening displacement-gage correction factors;

2) crack-closure characteristics of surface flaws under cyclic loading;

3) flaw extension characteristics of deep surface flaws.

The following paragraphs discuss the conclusions drawn from each study.

The crack-opening displacement gage correction-factor study showed that displacement resulting from crack opening and that from plasticity could be readily differentiated. To achieve this, it was necessary to obtain the displacement unload curve. Comparison of the slopes of the linear segment of the loading curve and initial segment of the unloading curve can be used to determine the magnitude of subcritical growth. It was shown that there appeared to be a threshold level for the initiation of subcritical growth in the three materials evaluated (aluminum, titanium, and steel). Plastic displacement of approximately 0.025 mm (0.001 in.) appeared to be required before subcritical growth was found.

The agreement between data obtained using the ultrasonic technique and a unique high-sensitivity crack-opening displacement gage was quite satisfactory and agreed well with visual observations by fractographic techniques.

Threshold data for the three materials was obtained and is presented.

A preliminary analysis of data obtained by Boeing (NAS3-19697) indicated that the sensitivity of crack-opening displacement curves was high enough to permit load-unload analysis to determine the degree of subcritical growth.

Crack closure studies using both ultrasonic and crack-opening displacement measurements showed an opening and closing behavior associated with load-unload curves. The results of this work were in general agreement with the closure concepts of Elber (ref. 6 and 7). Ultrasonic measurements showed that changes in crack depth associated with loading and unloading occurred at the crack tip and would confirm the validity of Elber's contention of an effective stress intensity range. Elber's speculation that crack closing stresses would exceed opening stresses was not borne out by our measurements.

Ultrasonic measurements used to study the nature of flaw extension characteristics associated with failure of the ligament between the flaw front and back surface showed that penetration could occur by an abrupt fracturing after subcritical growth or by continuous growth. Differences in the nature of the process appear to be related to the toughness of the materials.

This program showed that the ultrasonic technique can readily be used to study crack growth and fracture-related phenomena in surface-flawed specimens with improved accuracy. Some of these measurements could not be made in any other way. The technique is particularly valuable in studies of flaw-front phenomena. Although the value of the crack-opening displacement gage has been criticized because it only measures surface compliance, the results of our studies show that a high-sensitivity gage can provide reliable information in many types of studies.

The information regarding fracturing behavior should be of general interest to those concerned with surface flaw behavior and serve as the base for more detailed studies.

REFERENCES

1. McElroy, J. T.: "Identification and Measurement of Ultrasonic Search Unit Characteristics," *Materials Evaluation*, Vol XXV, No. 6, p. 129, 1967.

2. Pandall, R. H.: *Introduction to Acoustics*, Wesley Press, 1951.

3. Wheeler, O. E.: "Spectrum Loading and Crack Growth," *Journal of Basic Engineering, Trans. ASME*, Vol 94, Series D, No. 1, March 1972.

4. Willenborg, J. D.; Engle, R. M., Jr.; and Wood, H. A.: *A Crack Growth Retardation Model Using an Effective Stress Concept*, AFFDL-TM-71-1-FBR, Air Force Flight Dynamics Laboratory, January 1971.

5. Gallagher, J. P.: *A Generalized Development of Yield Zone Models*, AFFDL-TM-FBR-74-28, Air Force Flight Dynamics Laboratory, January 1974.

6. Elber, W.: "Fatigue Crack Closure Under Cyclic Tension." *Engineering Fracture Mechanics*, 1970, Vol 2, p 37.

7. Elber, W: "The Significance of Fatigue Crack Closure," *Damage Tolerance in Aircraft Structures*, ASTM, STP 486, 1971.

"Page missing from available version"

"Page missing from available version"

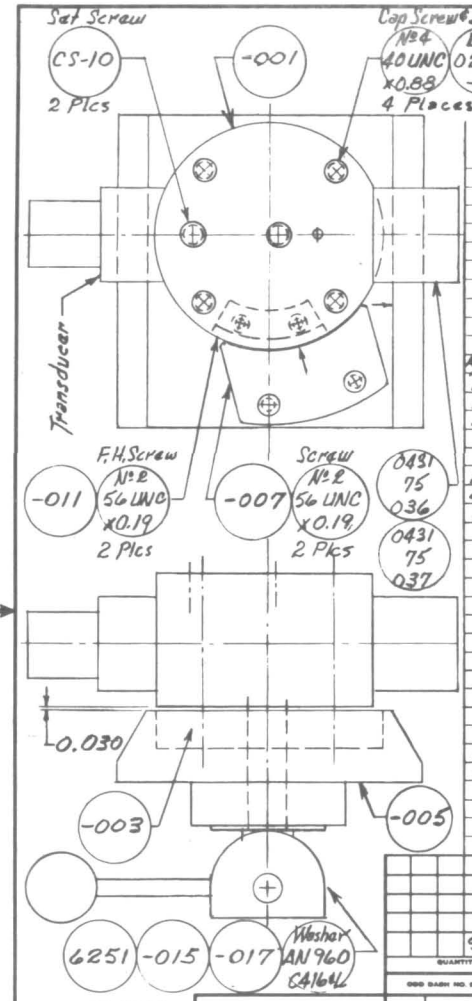

QUANTITY/DASH NO.				PART NO.	ZONE	DESCRIPTION	STOCK SIZE	MATERIAL OR VENDOR	MATERIAL SPECIFICATION	FINISH OR MFR CODE	CHG
			A/R	0431 75 036		Columnator, Trans.					
			A/R	0431 75 037		Columnator, Rec					
			3			Cross Roller Slides; X, Y & Z					
			1			Angle Bracket					
			3			Bolt, Nut & Washer	1/2 -20UNF x 1.5				
			3			Bolt & Washer	1/4 - 28UNF x 1.5	CRES			
		8				Set Screw	Nº6-32UNC x 7/8				(AN565E632H14)
A/R	A/R					Washer					(AN960-C416 & C416L)
2	2					Screw	Nº2-56UNC x 3/16				(MS35275-202)
2	2					Screw, Flat Head	Nº2-56UNC x 3/16		100° CSK		(NAS662-2R3
4	4					Cap Screw	Nº4-40UNC x 7/8	CRES			(NAS1352C04-14)
		4				Screw	Nº4-40UNC x 3/16	CRES			(MS35275-212)
2	2			CS-10		Set Screw	Nº6-32 x 5/32	"No-mar" PIC Design Corp, Van Nuys, Ca. 91405			
4	4			LC-029B-4		Spring		Lee Spring Co. Inc, Brooklyn, N.Y.			
1	1			6251		Eccentric		Vlier Engr Corp Los Angeles, Ca. 90069			
			2	-037		Pin	1/4 Dia x 1.00	Drill Rod			
			1	-035		Bracket	1/2 PL	CRES	303		
			1	-033		Ring	1 1/2 PL	Alum Alloy			
			1	-031		Bracket	1/2 PL	CRES	303		
			2	-027		Pin	1/2 Dia x 0.75	Drill Rod			
		2		-025		Rule					
		1		-023		Strip, Containing	1/4 PL	Brass			
		1		-021		Frame	3/4 PL	CRES			
1	1			-017		Pin	3/16 Dia x 0.5	CRES	Press Fit into Eccentric		
1	1			-015		Post		M/F Vlier Nº 5405			
1				-013		Drum Segment		M/F PIC Design Corp Nº AX-1-D			
	1			-011		Drum Segment		(See -013)			
1	1			-007		Venier		M/F PIC Design Corp Nº AW-1-V			
1				-006		Block	3/4 PL	CRES	303		
	1			-005		Block	3/4 PL				
1	1			-003		Plate					
1				-002		Transducer Holder					
	1			-001		Transducer Holder		CRES	303		
				-							
		1		-030		Transducer Holder Assy					
		1		-029		Transducer Holder Assy					
			1	-019		Frame Assy					
030	029	019	009	-009		Sonic Transducer Assy					

LIST OF MATERIAL

ODD DASH NO. SHOWN — EVEN DASH NO. OPP

-029 SHOWN
-030 OPP HAND

REVISIONS

SYM	ZONE	DESCRIPTION	DATE	APPROVED

DIMENSIONING REF MIL-STD-8 UNLESS OTHERWISE SPECIFIED
DIMENSIONS ARE IN INCHES AND ARE AFTER PLATING
TOLERANCES ON: FRACTIONS ±1/32; DECIMALS .X ±.1, .XX ±.05, .XXX ±.010; ANGLES ±1/2°
MACHINED SURFACES REF: MIL-STD-10
MIL-1-8500 STATUS
INTERCHANGEABLE
REPLACEABLE
UNCONTROLLED

DRAWN BY wlb — DEPT 0437 — DATE 12/20/75
CHECKER
STRESS ENGR
WT ENGR
MATL ENGR
RELIABILITY
QR ENGR
PROJECT
CUST SPECIFICATION

MARTIN MARIETTA CORPORATION
MARTIN MARIETTA AEROSPACE, DENVER DIVISION, P.O. BOX 179, DENVER, COLORADO 80201

SONIC TRANSDUCER ASSY

SIZE C — CODE IDENT NO. 04236 — 0431 75 035
SCALE 2/1 — SHEET 1 of 6

EFFECTIVE ON — CALC WT — DASH NUMBER — NEXT ASSY — USED ON — FINAL ASSY — TEST — APPLICATION — QTY REQD

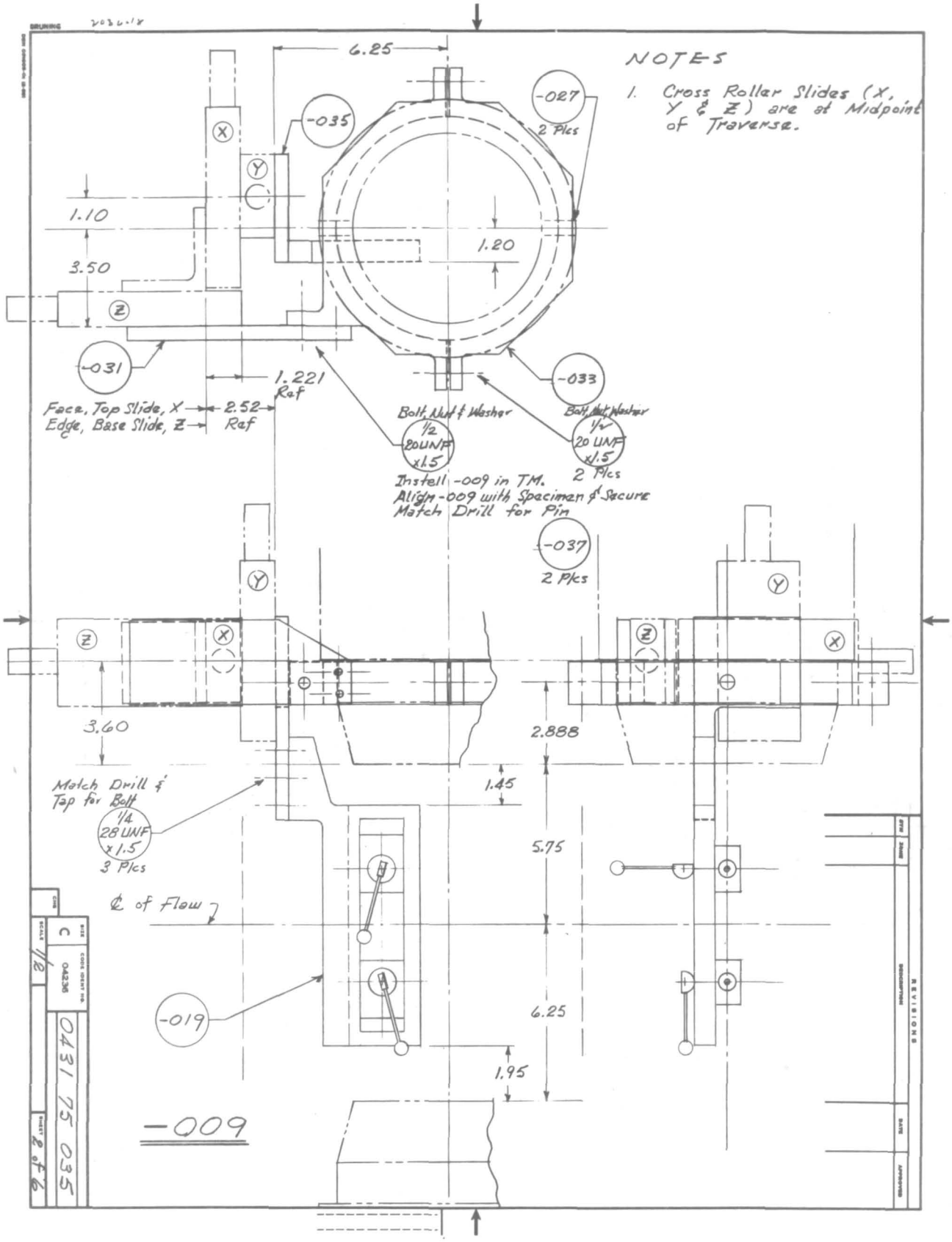
NOTES
1. Cross Roller Slides (X, Y & Z) are at Midpoint of Traverse.
6.25
-027
2 Plcs
-035
1.10
3.50
1.20
-031
1.221 Ref
-033
Face, Top Slide, X
Edge, Base Slide, Z
2.52 Ref
Bolt, Nut & Washer
1/2 20UNF x1.5
Bolt, Nut, Washer
1/2 20 UNF x1.5
2 Plcs
Install -009 in TM.
Align -009 with Specimen & Secure
Match Drill for Pin
-037
2 Plcs
3.60
2.888
1.45
Match Drill & Tap for Bolt
1/4 28 UNF x1.5
3 Plcs
5.75
℄ of Flow
-019
6.25
1.95
-009
C
04236
0431 75 035
1/2
2 of 6
REVISIONS

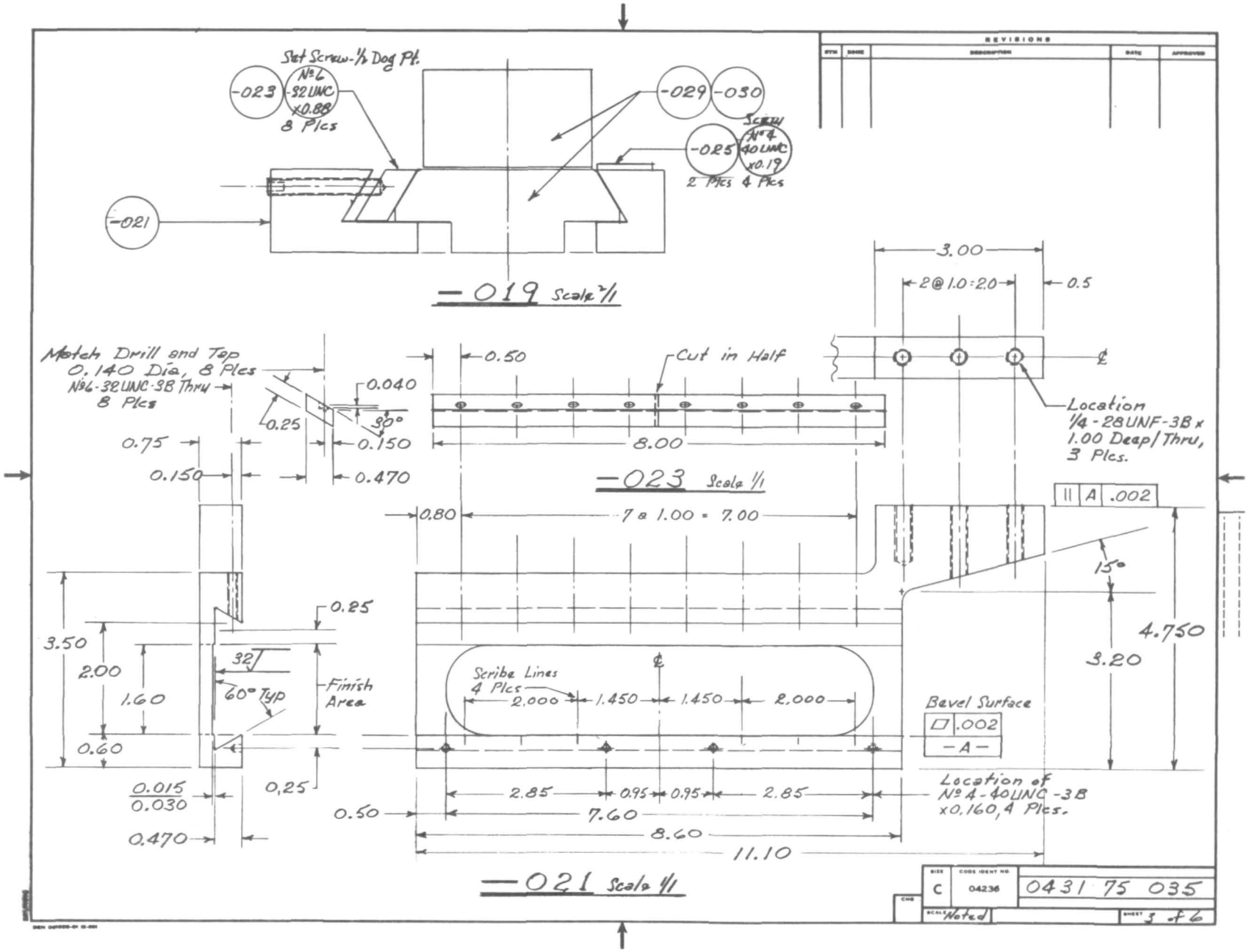
Set Screw-1/2 Dog Pt.
-023
№6-32UNC x0.88
8 Plcs
-029
-030
-025
Screw №4-40UNC x0.19
2 Plcs 4 Plcs
-021
-019 Scale 2/1
3.00
2@1.0=2.0
0.5
Match Drill and Tap 0.140 Dia, 8 Plcs №6-32UNC-3B Thru 8 Plcs
0.040
30°
0.25
0.75
0.150
0.470
0.50
Cut in Half
8.00
-023 Scale 1/1
Location 1/4-28UNF-3B x 1.00 Deep/Thru, 3 Plcs.
0.80
7 @ 1.00 = 7.00
.002
A
15°
4.750
3.20
3.50
2.00
1.60
0.60
32
60° Typ
Finish Area
Scribe Lines 4 Plcs
2.000
1.450
1.450
2.000
Bevel Surface
.002
-A-
0.015
0.030
2.85
0.95
0.95
2.85
7.60
8.60
11.10
Location of №4-40UNC-3B x0.160, 4 Plcs.
-021 Scale 1/1
REVISIONS
C
04236
0431 75 035
Noted
3 of 6

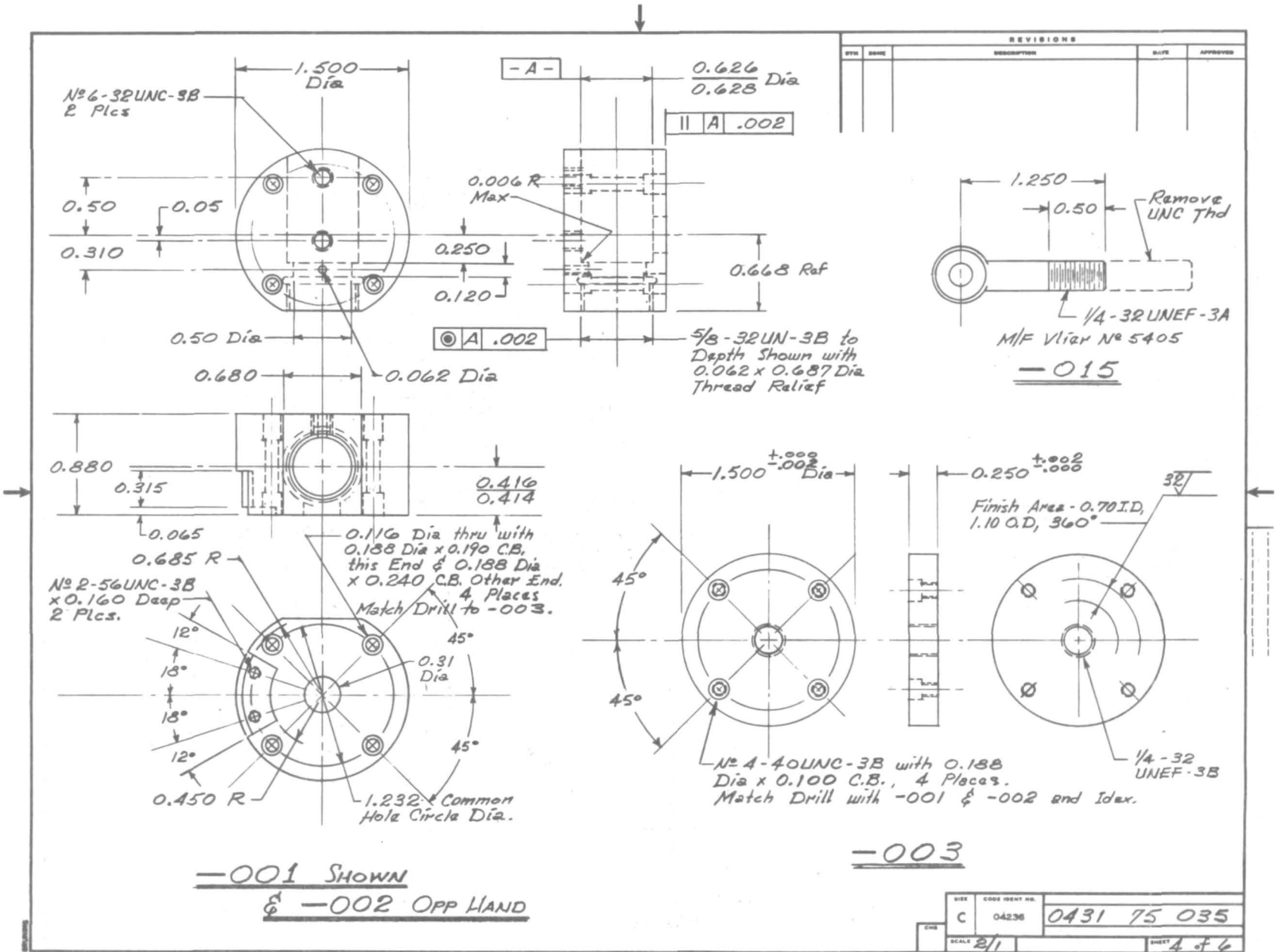
REVISIONS
SYM
ZONE
DESCRIPTION
DATE
APPROVED
1.500 Dia
Nº 6-32UNC-3B 2 Plcs
0.50
0.05
0.310
0.250
0.120
0.50 Dia
0.680
0.062 Dia
-A-
0.626 / 0.628 Dia
|| A .002
0.006 R Max
0.668 Ref
A .002
5/8-32UN-3B to Depth Shown with 0.062 x 0.687 Dia Thread Relief
1.250
0.50
Remove UNC Thd
1/4-32UNEF-3A
M/F Vlier Nº 5405
-015
0.880
0.315
0.065
0.416 / 0.414
0.685 R
Nº 2-56UNC-3B x 0.160 Deep 2 Plcs.
12°
18°
18°
12°
0.450 R
0.116 Dia thru with 0.188 Dia x 0.190 C.B. this End & 0.188 Dia x 0.240 C.B. Other End. 4 Places Match Drill to -003.
45°
0.31 Dia
45°
1.232 ℄ Common Hole Circle Dia.
1.500 +.000 -.002 Dia
0.250 +.002 -.000
32
Finish Area - 0.70 I.D, 1.10 O.D, 360°
45°
45°
Nº 4-40UNC-3B with 0.188 Dia x 0.100 C.B., 4 Places. Match Drill with -001 & -002 and Idex.
1/4-32 UNEF-3B
-003
-001 SHOWN
& -002 OPP HAND
SIZE
C
CODE IDENT NO.
04236
0431 75 035
SCALE 2/1
SHEET 4 of 6

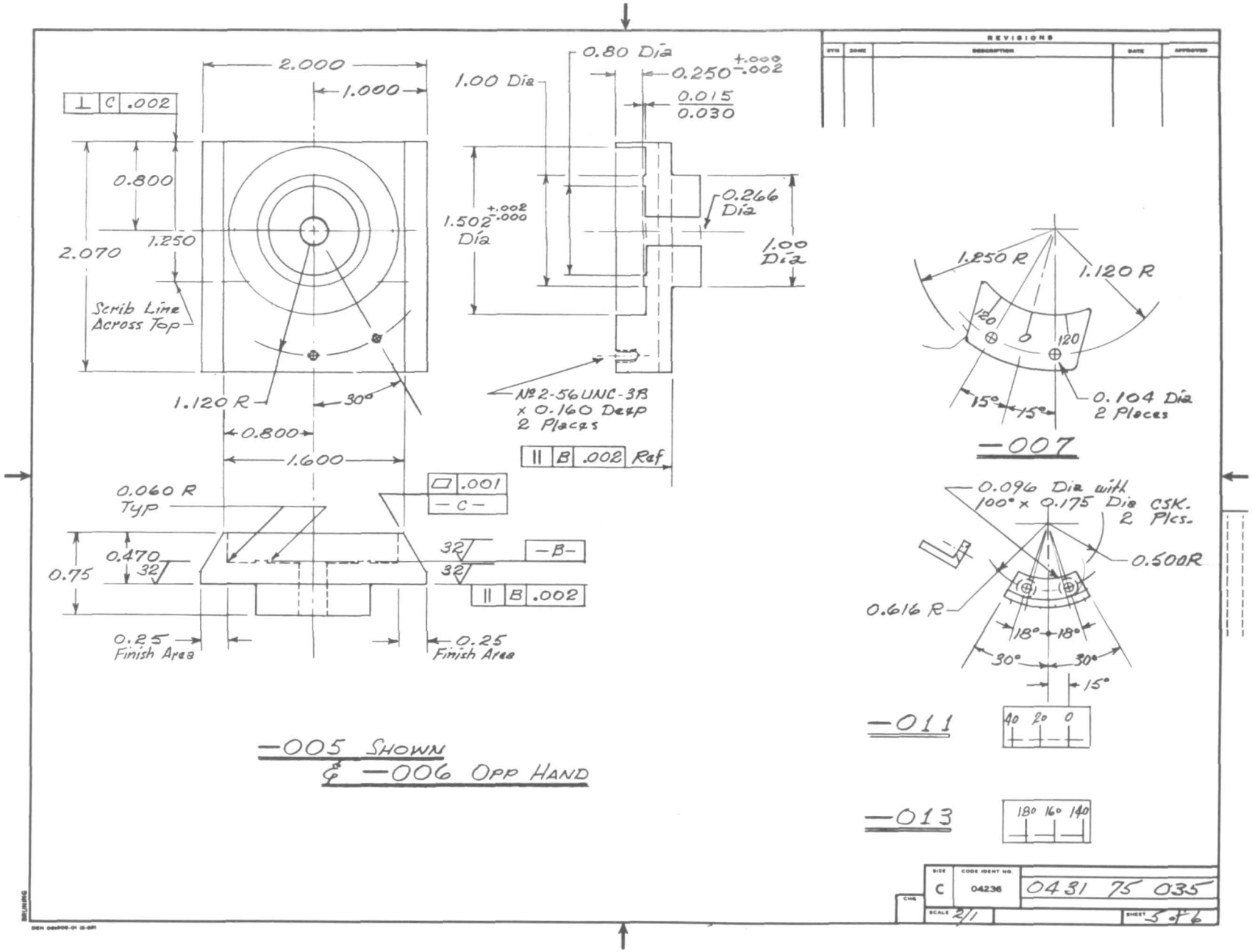
REVISIONS
2.000
1.000
⊥ C .002
0.800
2.070
1.250
Scrib Line Across Top
1.120 R
30°
0.800
1.600
0.060 R Typ
0.470
0.75
32
0.25 Finish Area
0.25 Finish Area
0.80 Dia
1.00 Dia
0.250 +.000 -.002
0.015
0.030
0.266 Dia
1.502 +.002 -.000 Dia
1.00 Dia
№2-56 UNC-3B x 0.160 Deep 2 Places
∥ B .002 Ref
□ .001 — C —
— B —
∥ B .002
—005 SHOWN
& —006 OPP HAND
1.250 R
1.120 R
120
120
15°
15°
0.104 Dia 2 Places
—007
0.096 Dia with 100° x 0.175 Dia CSK. 2 Plcs.
0.500R
0.616 R
18°
18°
30°
30°
15°
—011
40 20 0
—013
180 160 140
SIZE C
CODE IDENT NO. 04236
0431 75 035
SCALE 2/1
SHEET 5 of 6

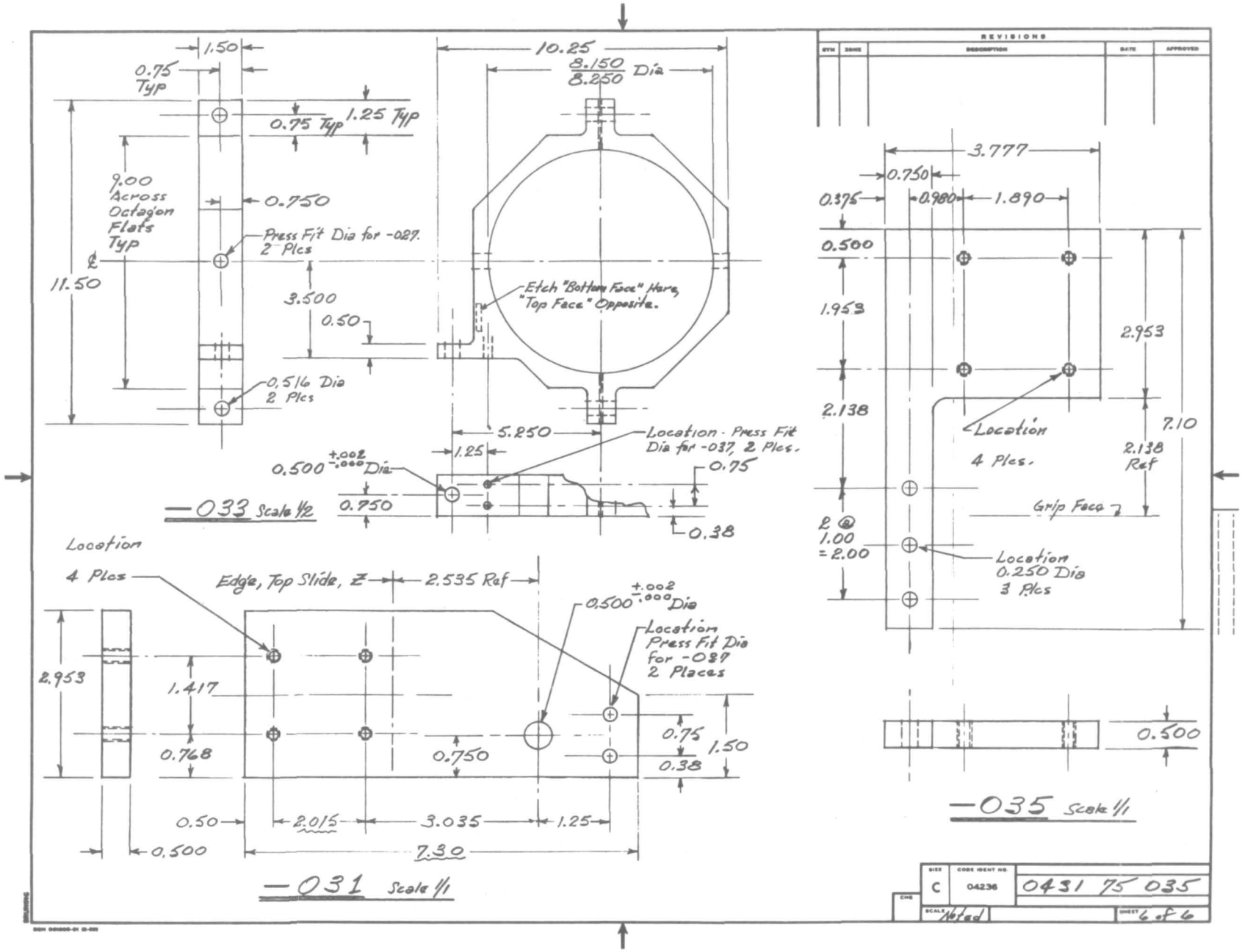
REVISIONS
SYM
ZONE
DESCRIPTION
DATE
APPROVED
1.50
0.75 Typ
10.25
8.150
8.250 Dia
0.75 Typ
1.25 Typ
9.00 Across Octagon Flats Typ
0.750
Press Fit Dia for -027. 2 Plcs
11.50
3.500
0.50
Etch "Bottom Face" Here, "Top Face" Opposite.
0.516 Dia 2 Plcs
5.250
1.25
Location - Press Fit Dia for -037, 2 Plcs.
0.500 +.002 -.000 Dia
0.75
0.750
0.38
-033 Scale 1/2
Location 4 Plcs
Edge, Top Slide, Z
2.535 Ref
0.500 +.002 -.000 Dia
Location Press Fit Dia for -027 2 Places
2.953
1.417
0.768
0.750
0.75
0.38
1.50
0.50
2.015
3.035
1.25
0.500
7.30
-031 Scale 1/1
3.777
0.750
0.375
0.980
1.890
0.500
1.953
2.953
2.138
7.10
Location 4 Plcs.
2.138 Ref
Grip Face
2 @ 1.00 = 2.00
Location 0.250 Dia 3 Plcs
0.500
-035 Scale 1/1
SIZE
C
CODE IDENT NO.
04236
0431 75 035
SCALE
Noted
SHEET
6 of 6

DISTRIBUTION LIST FOR FINAL REPORTS

CONTRACT NAS3-17790

"DEFINITION OF MUTUALLY OPTIMUM NDI AND PROOF TEST CRITERIA FOR 2219 ALUMINUM PRESSURE VESSELS"

Vol. I : Methods, NASA CR-135445
Vol. II : Optimization and Fracture Studies, NASA CR-135446
Vol. III: Applications to Rail Defect Evaluation, NASA CR-135447

	Copies	Vol's
NASA-Lewis Research Center 21000 Brookpark Road Cleveland, OH 44135		
Attn: Contracting Officer, M.S. 500-312	1	1+2+3
Technical Report Control Officer, M.S. 5-5	1	1+2+3
Technology Utilization Office, M.S. 3-16	1	1+2+3
AFSC Liaison Office, M.S. 501-3	1	1+2+3
M&S Division Contract File, M.S. 49-1	1	1+2+3
Library, M.S. 60-3	1	1+2+3
R. H. Johns, M.S. 49-3	1	1+2+3
G. T. Smith, M.S. 49-3	32	1+2+3
J. E. Srawley, M.S. 105-1	1	1+2+3
J. C. Freche, M.S. 49-1	1	1+2+3
R. L. Davies, M.S. 106-1	1	1+2+3
National Aeronautics & Space Administration Washington, DC 20546		
Attn: NHS-22/Library	2	1+2+3
RTM-3/Dr. L. Harris	1	1+2+3
NASA-Ames Research Center Moffett Field, CA 94035		
Attn: Library, M.S. 202-3	1	1+2+3
NASA-Goddard Space Flight Center Greenbelt, MD 20771		
Attn: 252/Library	1	1+2+3
NASA-John F. Kennedy Space Center Kennedy Space Center, FL 32931		
Attn: Library, M.S. AD-CSO-1	1	1+2+3
NASA-Langley Research Center Hampton, VA 23665		
Attn: Library, M.S. 185	1	1+2+3
H. F. Hardrath, M.S. 188M	1	1+2
W. Elber, M.S. 231	1	1+2
J. C. Newman, M.S. 188E	1	1+2
C. M. Hudson, M.S. 441	1	1+2

	Copies	Vol's
NASA-Lyndon B. Johnson Space Center Houston, TX 77001		
Attn: JM6/Library	1	1+2+3
ES5/R. G. Forman	1	1+2
ES5/W. L. Castner	1	1+2+3
NASA-George C. Marshall Space Flight Center Marshall Space Flight Center, AL 35812		
Attn: AS61/Library	1	1+2+3
EP41/C. E. Lifer	1	1+2
EL44/C. D. Crockett	1	1+2
EP01/H. R. Coldwater	1	1+2
Jet Propulsion Laboratory 4800 Oak Grove Drive Pasadena, CA 91103		
Attn: Library	1	1+2+3
Acquisition Department NASA S&T Information Facility P.O. Box 8757 Baltimore-Washington International Airport, MD 21240	10	1+2+3
Air Force Systems Command Aeronautical Systems Division Wright-Patterson Air Force Base, OH 45433		
Attn: Library, Code ENF	1	1+2+3
Wright-Patterson Air Force Base Wright-Patterson Air Force Base, OH 45433		
Attn: AFML	1	1+2+3
D. M. Forney	1	1+2
AFFDL	1	1+2+3
H. A. Wood	1	1+2
Air Force Systems Command Andrews Air Force Base Washington, DC 20332		
Attn: Library	1	1+2
Air Force Systems Command Arnold Engineering Development Center Tellahoma, TN 37389		
Attn: Library	1	1+2+3

	Copies	Vol's
Aerospace Corporation 2400 E. El Segundo Blvd. Los Angeles, CA 90045		
Attn: Library-Documents	1	1+2+3
Air Force Office of Scientific Research Washington, DC 20333		
Attn: Library	1	1+2+3
Department of the Army U.S. Army Material Command Washington, DC 20315		
Attn: AMCRD-RC	1	1+2+3
U.S. Army Missile Command Redstone Scientific Information Center Redstone Arsenal, AL 35808		
Attn: Document Section	1	1+2+3
Commanding Officer U.S. Army Research Office (Durham) Box CM, Duke Station Durham, NC 27706		
Attn: Library	1	1+2+3
Bureau of Naval Weapons Department of the Navy Washington, DC 20360		
Attn: RRRE-6	1	1+2+3
Commander U.S. Naval Ordnance Laboratory White Oak Silver Springs, MD 20910		
Attn: Library	1	1+2+3
Director, Code 6180 U.S. Naval Research Laboratory Washington, DC 20390		
Attn: Library	1	1+2+3
H. W. Carhart	1	1+2
J. M, Krafft	1	1+2
Atomic Energy Commission Division of Reactor Development & Technology Washington, DC 20767	1	1+2+3

	Copies	Vol's
National Science Foundation Engineering Division 1800 G Street, NW Washington, DC 20540		
Attn: Library	1	1+2+3
Denver Federal Center U.S. Bureau of Reclamation P.O. Box 25007 Denver, CO 80225		
Attn: P. M. Lorenz	1	1+2+3
National Technical Information Service Springfield, VA 22151	2	1+2+3
Brown University Providence, RI		
Attn: Technical Library	1	1+2+3
J. R. Rice	1	1+2
Case Western Reserve University 10090 Euclid Avenue Cleveland, OH 44115		
Attn: Technical Library	1	1+2+3
Carnegie Institute of Technology Department of Civil Engineering Pittsburgh, PA 15213		
Attn: Library	1	1+2+3
Colorado State University Department of Mechanical Engineering Ft. Collins, CO 80521		
Attn: F. Smith	1	1+2
Cornell University Department of Materials Science & Engineering Ithaca, NY 14830		
Attn: Library	1	1+2+3
Massachusetts Institute of Technology Cambridge, MA		
Attn: Library	1	1+2+3

	Copies	Vol's
Pennsylvania State University State College, PA		
Attn: Library	1	1+2+3
Purdue University West Lafayette, IN 47907		
Attn: Library	1	1+2+3
C. T. Sun	1	1+2
University of Denver Denver Research Institute P.O. Box 10126 Denver, CO 80210		
Attn: Security Office	1	1+2+3
University of Illinois Department of Theoretical & Applied Mechanics Urbana, IL 61801		
Attn: Prof. Su Su Wang	1	1+2
Washington University St. Louis, MO 63130		
Attn: Prof. P. C. Paris	1	1+2
Aerojet Liquid Rocket Company P.O. Box 15847 Sacramento, CA 95813		
Attn: Technical Library, 2484-2115A	1	1+2+3
Aluminum Company of America 1200 Ring Building Washington, DC 20036		
Attn: G. B. Bauthold	1	1+2
Bell Aerosystems, Inc. P.O. Box 1 Buffalo, NY 14240		
Attn: J. Davis	1	1+2
Brunswick Corporation Defense Products Division P.O. Box 4594 43000 Industrial Avenue Lincoln, NE		
Attn: Library	1	1+2+3

	Copies	Vol's
Chrysler Corporation Space Division P.O. Box 29200 New Orleans, LA 70129		
Attn: P. Munafo	1	1+2
Library	1	1+2+3
Del West Associates, Inc. 6324 Variel Avenue Suite C Woodland Hill, CA 91364		
Attn: M. Creager	1	1+2
Garrett Corporation AiResearch Manufacturing Division 2525 West 190th Street Torrence, CA 90509	1	1+2+3
General American Transportation Corporation General American Research Division 7449 N. Natches Avenue Niles, IL 60648		
Attn: R. N. Johnson	1	1+2+3
General Dynamics P.O. Box 748 Fort Worth, TX 76101		
Attn: Library	1	1+2+3
C. D. Little	1	1+2
General Dynamics/Convair Aerospace P.O. Box 1128 San Diego, CA 92112		
Attn: Library	1	1+2+3
J. Jensen	1	1+2
W. Witzell	1	1+2
J. Haskins	1	1+2
General Electric Company Missiles and Space Systems Center Valley Forge Space Technology Center P.O. Box 8555 Philadelphia, PA 19101		
Attn: Library	1	1+2+3
Grumman Aircraft Engineering Corporation Bethpage, Long Island, NY		
Attn: Library	1	1+2+3
W. Ludwig	1	1+2

	Copies	Vol's
IIT Research Institute Technology Center Chicago, IL 60616		
Attn: Library	1	1+2+3
I. M. Daniel	1	1+2
Martin-Marietta Corporation P.O. Box 29304 New Orleans, LA 70189		
Attn: D. Bolstad	1	1+2+3
McDonnell Douglas Aircraft Corp. P.O. Box 516 Lambert Field, MO 63166		
Attn: Library	1	1+2+3
Northrop Space Laboratories 3401 West Broadway Hawthorne, CA		
Attn: Library	1	1+2+3
North American Rockwell, Inc. Rocketdyne Division 6633 Canoga Avenue Canoga Park, CA 91304		
Attn: Library, Dept. 596-306	1	1+2+3
G. Vroman	1	1+2
North American Rockwell, Inc. Space & Information Systems Division 12214 Lakewood Blvd. Downey, CA		
Attn: Library	1	1+2+3
Republic Aviation Fairchild Hiller Corp. Farmington, Long Island, NY		
Attn: Library	1	1+2+3
Stanford Research Institute 3333 Ravenswood Avenue Menlo Park, CA 94025		
Attn: Library	1	1+2+3

	Copies	Vol's
Thiokol Chemical Corporation Wasatch Division P.O. Box 524 Brigham City, UT 84302		
Attn: Library Section	1	1+2+3
TRW Systems, Inc. One Space Park Redondo Beach, CA 90278		
Attn: Technical Library, Document Acquisition	1	1+2+3
United Aircraft Corporation Corporate Library 400 Main Street East Hartford, CT 06108		
Attn: Library	1	1+2+3
T. Cruse	1	1+2
United Aircraft Corporation Pratt & Whitney Division Florida Research & Development Center P.O. Box 2691 West Palm Beach, FL 33402		
Attn: Library	1	1+2+3
Westinghouse Research Laboratories Beulah Road, Churchhill Borough Pittsburgh, PA 15235		
Attn: Library	1	1+2+3
W. K. Wilson	1	1+2
E. T. Wessell	1	1+2
McDonnell Douglas Astronautics 5301 Bolsa Avenue Huntington Beach, CA 92647		
Attn: Library	1	1+2+3
R. A. Rawe	1	1+2
H. W. Babel	1	1+2
Boeing Aerospace Company P.O. Box 2999 Seattle, WA 98124		
Attn: Library	1	1+2+3
J. N. Masters	1	1+2
L. R. Hall	1	1+2

	Copies	Vol's
Boeing Wichita Company 3801 S. Oliver Wichita, KS 67210		
Attn: C. F. Tiffany, M.S. K-16-36	1	1+2
U.S. Department of Transportation Kendall Square Cambridge, MA 02142		
Attn: P. Tong, DTS-744	1	1+2+3
P. Tong, DTS-744	42	3